Doctoral Dissertation

博士論文

Geochemical carbon cycle and climate of ocean terrestrial planets in the habitable zone

(ハビタブルゾーンにおける海洋を持つ地球型惑星の炭素循環と気候)

A Dissertation Submitted for the Degree of Doctor of Philosophy
November 2019

令和元年 11 月博士（理学）申請

Department of Earth and Planetary Science, Graduate School of Science
The University of Tokyo

東京大学大学院理学系研究科地球惑星科学専攻

Akifumi Nakayama

中山　陽史

ABSTRACT

What made the Earth habitable? This is a long-standing issue in planetary science. At present, in addition to the Earth, we have to generalize the comparative theory of planetary habitability for the Solar-system planets toward extra-solar planets because many exoplanets including similar in size to the Earth have been detected. In this doctoral thesis, we explore the climate of terrestrial exoplanets and the detectability of the climate by near-future observations in order to gain a deeper understanding of climate and habitability of terrestrial planets.

Most previous theoretical studies of planetary habitability assume Earth-like terrestrial planets characterized by active plate tectonics and coexistence with oceans and continents. They also assume that a carbonate-silicate geochemical carbon cycle (called carbon cycle hereafter) stabilizes the climate of Earth-like planets, as in the Earth, because removal of the greenhouse gas CO_2 from the atmosphere via weathering on continents strongly depends on the surface temperature. However, planet formation theories predict that Earth-like exoplanets are not necessarily abundant and the habitable zones around other stars are populated by planets retaining much more water than the Earth's oceans, meaning continental weathering never works. Thus, the carbon cycle in water-rich, continental-free planets is a crucial issue for planetary habitability.

The purpose of this doctoral thesis is to explore the effects of water amount on the planetary climate of terrestrial exoplanets in the habitable zone. To do so, we develop a new theoretical model for the carbon cycle in water-rich terrestrial planets in the habitable zone (Part **I**). Furthermore, we propose a new way to verify our theoretical prediction regarding their climate features with near-future observations (Part **II**).

Previous studies inferred that terrestrial planets covered globally with thick oceans (termed ocean planets) in the habitable zone have extremely hot climates, because H_2O high-pressure ice on the seafloor prevents chemical weathering and, thus, removal of atmospheric CO_2. Those studies, however, ignored melting of the high-pressure ice and horizontal variation of the heat flux from the oceanic crust. In Part **I**, we develop integrated climate models of an Earth-size ocean planet with plate tectonics for different ocean masses, which include the effects of high-pressure ice melting, seafloor weathering, and the carbon cycle. We find that the heat flux near the mid-ocean ridge is high enough to melt the high-

pressure ice, enabling seafloor weathering. In contrast to the previous theoretical prediction, we show that the climates of terrestrial planets with massive oceans lapse into extremely cold ones (or snowball states) with CO_2-poor atmospheres. Such extremely cold climates are achieved mainly because the high-pressure ice melting results in fixing the seafloor temperature at the melting temperature, thereby keeping a high weathering flux regardless of surface temperature. However, seafloor weathering would be limited the supply of cation from the oceanic crust. Including the supply-limit for seafloor weathering, we also find the climate of the ocean planet with a massive ocean lapses into an extremely hot one with a CO_2-rich atmosphere because seafloor weathering is ineffective in compensating massive degassing. Consequently, the ocean planets with several tens of the Earth's ocean mass no longer maintain temperate climates.

In Part II, we explore the way to distinguish between such extremely hot and cold climates of ocean planets with a massive ocean predicted in Part I. The CO_2 abundance strongly affects the temperature of the upper atmosphere. The upper atmosphere with a low mixing ratio of CO_2 is significantly expanded. On the other hand, the Russian space telescope World Space Observatory—Ultraviolet (WSO-UV) to be launched in 2025 plans to observe exoplanets transiting in front of relatively low temperature stars (or M-type stars) with the emission lines of oxygen (OI lines), enabling us to detect expanded atmospheres. Thus, we investigate the effects of the CO_2 abundance and the planetary mass on the absorption depth of OI lines. To do so, we develop the upper atmosphere model and transmission model, which estimates the absorption of OI lines in the expanded planetary atmosphere during transit, for an ocean planet around an M-type star. The upper atmosphere model self-consistently includes the effects of variations of atmospheric composition and stellar spectrum, considering thermo-chemical and photo-chemical reactions, chemical and thermal diffusions, absorption of stellar infrared irradiation, and radiative cooling. We find that hydrodynamic escape proceeds and the expanded atmosphere is formed in the Earth-sized planets with small or moderate CO_2 abundance around quiet M-type stars. Thus, expanded atmospheres with hydrodynamic escape results in significant absorption of OI lines. Otherwise, CO_2 dominant atmosphere achieved in an extremely hot climate absorbs a small portion of stellar light because of efficient radiative cooling of CO_2. In contrast, there is no dependence of the absorption depth on CO_2 abundance in a low-mass planet of about Mars mass because hy-

drodynamic escape proceeds regardless of CO_2 abundance, even around quiet M-type stars. Those results suggest that the difference in the planetary climate of Earth-sized ocean planets with massive oceans coming from the difference in the planetary degassing rate of CO_2 is distinguishable from near future UV observations, provided poorly-constrained properties of ocean planet atmospheres such as turbulent diffusion are similar to what we assume here. This is a milestone for understanding what makes a habitable planet and what made the Earth habitable.

Contents

Chapter 1

General Introduction

What made the Earth habitable? This is a long-standing issue in planetary science. In our Solar system, four terrestrial planets exist: Mercury, Venus, the Earth, and Mars. The terrestrial planets are mainly composed of a metallic core and a rocky mantle. Only the Earth has oceans. Additionally, warm climate and life exist only in the Earth. Such a fact raises one big question: Are there life-supporting planets, like the Earth, beyond the Solar system?

Since the first discovery of a planet beyond the Solar system (Mayor & Queloz, 1995), about 6000 exoplanets (including planetary candidates) have been detected so far (http://exoplanets.org, Oct. 23, 2019). Some of them are arguably terrestrial rocky ones, according to their observed mass-radius relationships (e.g., Dressing & Charbonneau, 2015). Also, the exoplanet statistics obtained from the observation with the *Kepler* space telescope show the vast majority of exoplanets with short orbital distances (or short orbital periods) are planets with radii between 0.5 and 2 times the Earth's radius ($R_\oplus$) (e.g., Petigura et al., 2013; Batalha et al., 2013); such small-sized planets are sometimes termed "Earth-sized planets" in the exoplanet science community.

Characterization of Earth-sized planets is a central issue in exoplanet science which began with the discovery and characterization of gas giants like Jupiter and Saturn because of their large sizes and masses. While most Earth-sized exoplanets detected so far are orbiting close to their central star and, therefore, too warm to be habitable, temperate terrestrial planets in the habitable zone are expected to be detected and characterized thanks to the advance in observational technologies. Indeed, some Earth-sized exoplanets receiving Earth-like stellar insolation have been detected to date (e.g., Kaltenegger, 2017; Gillon et al., 2017). Thus, this is the right time to extend and generalize the comparative

theory of planetary habitability for the Solar-system planets toward extra-solar planets.

1.1 Climate of terrestrial planets in the habitable zone

Habitability of terrestrial exoplanets has been hottly debated. The main focus has been on the stability and evolution of liquid water on the planetary surface, namely oceans (e.g., Kasting et al., 1993; Lammer et al., 2009). This is because liquid water is thought to be essential for terrestrial life to emerge and evolve (e.g., Maruyama et al., 2013). Additionally, H_2O is abundant in our Galaxy: it can be found in various environments from molecular clouds to planetary atmospheres (e.g., Cernicharo & Crovisier, 2005).

1.1.1 Carbon cycle

The presence of oceans is also important for planetary climate. The Earth's climate system is generally thought to be stabilized by a carbonate-silicate geochemical cycle of carbon (hereafter simply called the *carbon cycle*), which is driven by the plate tectonics. The carbon cycle is the circulation of carbon between the mantle and the atmosphere-ocean system. Figure 1.1 shows a schematic illustration of the present Earth's carbon cycle: CO_2 is degassed from the planetary interior to the atmosphere-ocean system through volcanic activity and, then, absorbed by the carbonate formation involving chemical weathering. After that, the carbonate returns to the planetary interior through the plate motion. On geological timescales, the amount of the greenhouse gas, CO_2, is determined by a balance between degassing flux through volcanism and sinking flux through chemical weathering which occurs on the continental crust and the oceanic crust. In the present Earth, weathering occurs mainly on continents (Caldeira, 1995). The carbon cycle needs a large water reservoir such as an ocean because chemical weathering involves a water-rock reaction (Walker et al., 1981). Since the degassing flux is determined mainly by the volcanic activity and CO_2 concentration in the mantle (e.g., Tajika & Matsui, 1992), the degassing flux is insensitive to the climate (or surface temperature). Meanwhile, the chemical weathering becomes more efficient with temperature. Thus, a negative-feedback mechanism operates to keep the CO_2 partial pressure, P_{CO_2}, at low levels and, thus, to maintain the temperate climate (Walker et al., 1981). Indeed, in addi-

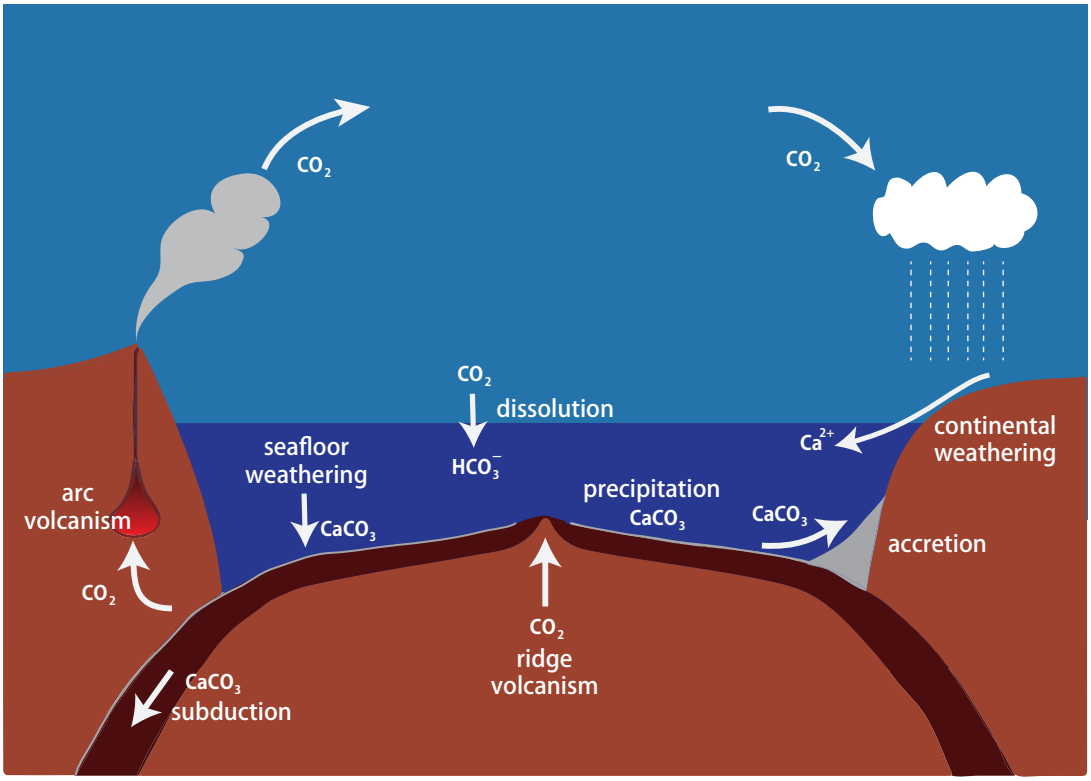

Figure 1.1: Schematic illustration of the Earth's carbon cycle. Arrows represent the flow of cations and CO_2 with dominant mechanisms. For drawing this figure, we use Fig. 1 of Tajika & Matsui (1992) as a reference.

tion to Venus and Mars, a theoretical study (Tosi et al., 2017) suggested that planets without plate tectonics and Earth-like carbon cycle have CO_2-rich hot climates.

Theoretically because of the carbon cycle, the partial pressure of CO_2 decreases with age, as stellar luminosity increases (Kasting, 1987; Tajika & Matsui, 1992). Indeed, geochemical evidence indicates a high CO_2 partial pressure in the Earth's paleo-atmosphere (e.g., Krissansen-Totton et al., 2018a). In the early Proterozoic and late Archean, high P_{CO_2} 10–100 times the today's level is observationally inferred (Rye et al., 1995; Driese et al., 2011). Furthermore, oxygen and silicon isotopes in old sediments indicate that the climate in the Archean was warmer than the present, in spite of the faint young Sun (Knauth & Lowe, 2003; Blake et al., 2010). Such a high temperature condition implies a high level of CO_2 with some additional greenhouse gases such as CH_4 (Sagan & Mullen, 1972; Pavlov et al., 2000; Charnay et al., 2017). According to recent global climate and carbon cycle simulations, the warm early Earth with high P_{CO_2} by an order of 0.1 bars is achieved with or without any other greenhouse

gas (Charnay et al., 2017). These facts support that the carbon cycle has regulated the CO_2 partial pressure and thereby the surface temperature across the Earth's history (Krissansen-Totton et al., 2018a). Thus, terrestrial exoplanets with an ocean and plate tectonics are expected to have the carbon cycle that stabilizes the climate with such a negative feedback mechanism.

1.1.2 Habitable zone

The habitable zone, which is an important concept to discuss planetary habitability, is defined as the circumstellar region where a warm climate is maintained and liquid water can exist on the planetary surface (Kasting et al., 1993). The classical concept of the habitable zone, in which life-supporting planets can exist, was first proposed by Huang (1959). Then, several studies investigated the habitable zone constrained by the climatic condition and the presence of liquid water on the planetary surface, mainly focusing on the evolution of the planets in the Solar system (e.g., Ingersoll, 1969; Rasool & de Bergh, 1970; Hart, 1978). Kasting et al. (1993) generalized and expressly defined the concept of the habitable zone for terrestrial exoplanets, including the negative-feedback mechanism of the carbon cycle, which adjusts the CO_2 abundance in the atmosphere to the stellar insolation to keep a warm climate. Their definition has been so far used as the conventional habitable zone. Then several researches revealed that the habitable zone depends on several factors: atmospheric composition, atmospheric pressure, atmospheric dynamics, water amount, and so on (e.g., Forget & Leconte, 2014). In this thesis, we refer to the conventional habitable zone for terrestrial planets with a $H_2O/CO_2/N_2$ atmosphere as the habitable zone (Kasting et al., 1993). In this case, the inner edge of the habitable zone is determined by the runaway greenhouse effect of H_2O (Nakajima et al., 1992). On the other hand, the outer edge is determined by the maximum greenhouse effect of CO_2, in which an increase of CO_2 reduces the surface temperature as a consequence of enhanced Rayleigh scattering (Kasting, 1991). Based on 1-D radiative-convective models, the conventional habitable zone ranges from 0.34 to 1.06 times the present solar insolation at the Earth's orbit (Kasting et al., 1993; Kopparapu et al., 2013).

1.1.3 Effects of water amount on planetary climate

Beyond the solar system, however, there must be continent-free terrestrial planets completely covered with oceans in the habitable zone. Given diverse water-supply processes and their stochastic nature, terrestrial exoplanets must be diverse in ocean mass. At least, five different ideas have been proposed so far for the source of water on terrestrial planets. The first one is that water-containing small bodies (i.e., planetesimals and/or pebbles) come to the terrestrial planet region from the asteroid belt and beyond (Raymond et al., 2004; Quintana & Lissauer, 2014; Gomes et al., 2005; Sato et al., 2016). The second one is the migration of planets beyond the snowline (Ogihara & Ida, 2009; Tian & Ida, 2015; Alibert & Benz, 2017). The third one is that the protoplanetary disk is so optically thick in the radial direction that the snowline is located in the terrestrial planet formation region (Oka et al., 2011; Machida & Abe, 2010). The fourth one is that hydrogen from the atmosphere of nebula origin is oxidized by magma ocean oxides to produce water (Ikoma & Genda, 2006). The fifth one is the adsorption of water on rocky dust in the inner protoplanetary disk (Stimpfl et al., 2006; Muralidharan et al., 2008). Indeed, many recent theories of planet formation predict that terrestrial exoplanets could have much more water than the Earth (see recent reviews by O'Brien et al. (2018) and Ikoma et al. (2018)), unless the subsequent water escape is intense. As an example, N-body simulations of late-stage terrestrial planet accretion including the supply of water-rich planetesimals beyond the snowline demonstrate that terrestrial planets with oceans of ten to several hundred Earth's ocean masses are populated in the habitable zone (Raymond et al., 2004, 2007). On the Earth, there would be no lands if the ocean mass were three times larger than the present (i.e., 0.023 % of the Earth's mass) (Maruyama et al., 2013; Kodama et al., 2018).

What is the climate of terrestrial planets completely covered with oceans and what influence does ocean mass have on the climate? Such terrestrial planets are called *ocean planets*, hereafter, whereas ones covered partially with oceans like the Earth are called *partial ocean planets* (Kuchner, 2003; Léger et al., 2004). The roles of weathering and carbon cycle in climates for terrestrial planets with different ocean masses are of interest in this thesis.

Previous studies of climates of terrestrial exoplanets primarily focused on those of partial ocean planets (e.g., Abbot et al., 2012). On partial ocean plan-

ets, continental weathering controls the planetary climate (e.g., Tajika & Matsui, 1992). However, water amount is important for the planetary climate of partial ocean planets because land fraction depends on water amounts (Kodama et al., 2018). The effect of land fraction on the continental weathering flux is firstly pointed out by Tajika & Matsui (1993): Motivated by the evolution of continents in the Earth, they discussed the relationship between land fraction and surface temperature. They found that changes in land fraction over several orders of magnitude strongly affects the surface temperature. Then, Abbot et al. (2012) investigated the sensitivity of continental weathering to land fraction in detail, to discuss the planetary climate of partial ocean planets in the habitable zone. Since continental weathering strongly depends on surface temperature, the planetary climate of partial ocean planets is insensitive to land fraction as long as the land fraction is larger than 1% (Abbot et al., 2012). Consequently, in the habitable zone, Earth-like planets with a sufficiently large land fraction have a warm climate due to CO_2 greenhouse effect in most cases (Abbot et al., 2012; Kadoya & Tajika, 2014). Based on the outcome of the carbon cycle, most theoretical studies of the planetary climate of terrestrial exoplanets in the habitable zone focused on stellar spectra and other effects (e.g., tidally locking), assuming the planet is an Earth-like planet (e.g., Shields et al., 2013a; Edson et al., 2012).

On the other hand, planet formation theories predict the frequency of ocean planets in the habitable zone (e.g., Raymond et al., 2007). As for ocean planets, seafloor weathering, instead of continental weathering, would control the planetary climate (Abbot et al., 2012). The role of seafloor weathering in climate is of interest in this thesis. In particular, we focus on the influence of high-pressure (HP) ice of H_2O such as ice VI and VII on seafloor weathering. Planets with larger water amounts than a certain threshold have the HP ice on the seafloor, provided the ocean has a steady, isothermal or adiabatic structure (Léger et al., 2004). Since the HP ice is a solid heavier than its counterpart liquid, a solid layer is formed between the ocean and oceanic crust and prevents seafloor weathering (Alibert, 2014; Kaltenegger et al., 2013).

For ocean planets without the HP ice, the relationship between seafloor weathering rate and CO_2 partial pressure or surface temperature strongly affects the planetary climate (Abbot et al., 2012; Höning et al., 2019). Those studies suggest that the seafloor weathering without surface temperature dependence results in CO_2-rich hot climates, even for the planet with the Earth-like

plate tectonics. However, experimentally and observational studies infer that the seafloor weathering strongly depends on the surface temperature (Brady & Gíslason, 1997; Coogan & Dosso, 2015; Krissansen-Totton & Catling, 2017). Thus, ocean planets without the HP ice would have warm climates with the carbon cycle playing a negative feedback mechanism.

Previous studies of ocean planets with the HP ice simply thought that the geochemical carbon cycle never acts as a thermostat with a negative-feedback mechanism, unlike partial ocean planets (e.g., Alibert, 2014). In this case, the planetary climate of ocean planet in the habitable zone would be controlled by the partitioning CO_2 between the atmosphere and ocean (Wordsworth & Pierrehumbert, 2013). Then, the climate were inferred to have extremely hot climate (Kitzmann et al., 2015). However, they ignore the melting of the HP ice due to heat flow from the planetary interior (Noack et al., 2016; Choblet et al., 2017).

1.2 The planetary climate on terrestrial planets beyond the Solar system constrained by observations

It is hard to obtain information about distant exoplanets. There are some observational methods to constrain the planetary properties using photons from the host star and/or planet. Radial velocity measurement and transit photometry are commonly used. The radial velocity technique constrains the mass of the planet. It detects stellar wobbling, which arises from planetary gravity, by observation of Doppler shifts in the star's spectrum. In contrast, transit photometry constrains the radius of the planet. It observes apparent dimming of stellar brightness during a planetary transit. Thus, planetary parameters of mass and radius are relatively easily estimated. The observed diversity of mass and semimajor axis distribution of exoplanets significantly promotes the planet formation theory (e.g., Ida & Lin, 2004). Only from the mass and radius, however, we cannot constrain the properties of the thin atmosphere on terrestrial planets.

Transit spectroscopy is a powerful tool to estimate the atmospheric composition (e.g., Brown, 2001; Kreidberg et al., 2014). During a planetary transit, a part of the stellar incident light passes through the planetary atmosphere. Since different molecules have different optical properties, the amount of the absorption and scattering by the atmospheric gas depends on wavelength and atmospheric

composition. Thus, transit observations at multiple wavelengths, ranging visible to infrared wavelengths, can infer the atmospheric composition. Indeed, the transit spectroscopy has revealed the diversity of transit spectra and atmospheric compositions including features of clouds and haze in the atmosphere of hot Jupiters (Sing et al., 2016). Furthermore, recent multi-wavelength transit observations detect water vapour in the atmosphere of K2-18b, which is a planet of eight Earth masses in the habitable zone around an M-type star (Tsiaras et al., 2019). Since planets around M-type star has a small stellar to planetary radius ratio and M-type stars are abundant in our galaxy, planets orbiting M-type stars are primary targets for the present and near future observations. Although advancement of the observational technology promotes the detection of the atmospheric molecules via multi-wavelength transit observations, we still need some new strategy to constrain the planetary climate because the transit method only observes the optically thin upper atmosphere.

1.2.1 Constraining CO_2 abundance of terrestrial exoplanet atmospheres

Constraining the CO_2 abundance in planetary atmospheres observationally is of major concern in exoplanet science because CO_2 is a major greenhouse gas for terrestrial planets and the carbon cycle is thought to be regulating the CO_2 abundance in the habitable zone if the Earth-like carbon cycle works. In addition, the CO_2 abundance would be an indicator how the carbon cycle acts on terrestrial exoplanets. Using the transit spectroscopy, several theoretical studies attempt to assess the feasibility of constraining the CO_2 abundance with the future space telescope of James Webb Space Telescope (*JWST*) (Morley et al., 2017; Krissansen-Totton et al., 2018b). Their simulations show that direct detection of CO_2 absorption in the infrared and visible wavelengths and constraining their abundance need much observational time (or number of transits), even if the planet nearby the Earth has a clear-sky condition. Furthermore, cloud and/or haze significantly prevent the feasibility because infrared and visible absorption occurs in the lower atmosphere owing to small pressure scale height (Lustig-Yaeger et al., 2019; Arney et al., 2017). Consequently, constraining the CO_2 abundance by transit spectroscopy in the infrared and visible wavelength would be difficult practically.

On the other hand, the transit spectroscopy in the UV wavelength can eas-

ily detect features of atomic species because the upper atmosphere composed of atomic species is significantly expanded for planets receiving high EUV irradiation (e.g., Vidal-Madjar et al., 2003). So far, this method has been applied to the observation of the hydrodynamic escape from hot Jupiters and warm Neptunes using the absorption of hydrogen Ly α (Vidal-Madjar et al., 2003; Ehrenreich et al., 2015).

Tavrov et al. (2018) demonstrated that the UV absorption by atomic oxygen lines (OI triplet) would be a useful tool for constraining the planetary climate on terrestrial planets. They focused on the difference in atmospheric composition between Venus and the Earth, in particular in CO_2 abundance, because CO_2 is the dominant coolant for terrestrial upper atmospheres. The lower the mixing ratio of CO_2, the higher the exospheric temperature is, for the same EUV irradiation environment. Thus, a planet with a low mixing ratio of CO_2 has a much expanded upper atmosphere. Using the atmospheric model of Kulikov et al. (2007) and Tian et al. (2008b), they found that the upper atmosphere on an Earth-like planet around an M-type star causes significant absorption of the OI lines. Under the condition of high EUV irradiation, the absorption fraction at the line center for the Earth-like planet is 76%, while that for the Venus-like planet is 0.7%. This is much larger than the absorption fraction due to molecular absorption in the visible and infrared wavelengths ($< 1\%$). Thus, high dispersion observations resolving the absorption feature in the OI lines would distinguish Earth-like planets with CO_2-poor atmospheres from the Venus-like planets with CO_2-rich atmospheres.

Furthermore, space telescope missions including the measurement of UV spectroscopy are scheduled within a decade: World Space Observatory-UltraViolet (WSO-UV) (Tavrov et al., 2018) and Large UV/Optical/IR surveyor (LUVOIR) (France et al., 2017). Those space telescopes have the advantage in UV observations in comparison with ground-based telescopes because their high orbits reduce the contamination by the Earth's geocorona. Additionally, they have high spectral resolving powers enough to resolve the OI lines. Thus, the absorption of OI lines during planetary transits will be readily observed when the upper atmosphere of the planet is significantly expanded.

1.3 Purpose of this thesis

Previous researches of the planetary climate and habitability of terrestrial exoplanets assume highly idealized planets. In order to gain a more deeper understanding of the planetary climate and habitability of terrestrial exoplanets, we have to examine the comparison between theoretical estimates and observed actual exoplanets. In this doctoral thesis, we explore the planetary climate of water-rich terrestrial exoplanets, which termed ocean planets, and the detectability of their planetary climate by near-future observations.

In this doctoral thesis, we focus on the amount of ocean water on the planet, which has a crucial role in the planetary climate and habitability of the terrestrial exoplanets as mentioned above. Previous studies of the planetary climate of ocean planets inferred that ocean planets have extremely hot climate partly because the HP ice prevents weathering processes (e.g., Kitzmann et al., 2015). We revisit the carbon cycle on water-rich ocean planets in the habitable zone and investigate the effect of water amount on the planetary climate. In particular, this study is aimed at evaluating the role of the HP ice in seafloor weathering and climate and classifying the planetary climate of terrestrial planets. Then, we explored the UV absorption of OI lines of the atmosphere during planetary transits to discuss the possibility distinguishing the planetary climatic feature estimated theoretically.

The rest of this doctoral thesis is organized as follows. In Part I (chapter 2), we describe the methodology of the carbon cycle modelling for ocean planets, including the effects of HP ice. Then, we theoretically explore the planetary climate of ocean planets with plate tectonics. In Part II (chapter 3), we describe the methodology of the upper atmosphere modelling and apply to planets around M-type stars. Then, we discuss the detectability of planetary climates obtained in Part I. Finally, we conclude this thesis in chapter 4.

Chapter 2

Part I: Theoretical Study of Planetary Climate of Ocean Terrestrial Planets in the Habitable Zone

2.1 Introduction of Part I

As described in Section 1.1.3, an ocean planet with the HP ice is thought to lack weathering processes and geochemical carbon cycle. Climates of ocean planets without geochemical interaction and carbon cycle between the ocean-atmosphere system and silicate mantle were previously investigated. Wordsworth & Pierrehumbert (2013) and Kitzmann et al. (2015) explored the effect of dissolution of CO_2 into an ocean and found that the CO_2 pressure increases with increasing temperature for a given carbon inventory in the atmosphere-ocean system. This suggests that such a climate system is an unstable one with a positive feedback cycle. Kitzmann et al. (2015) also showed that a positive feedback cycle leads to hot planetary climate for a large CO_2 inventory ($\sim$ 100 bars) in the atmosphere-ocean system even for stellar insolation comparable to the present Earth.

However, whether the layer of HP ice really exists and prevents seafloor weathering completely must be verified through a detailed consideration of heat transfer and rheology in the HP ice layer. Noack et al. (2016) examined the stability of the HP ice layer by performing non-steady, one-dimensional simulations of heat transfer, including the melting of HP ice, in the layer (liquid H_2O + HP ice) above the oceanic crust (collectively called the *H_2O layer,* hereafter). They found that the heat flux from the oceanic crust is too high for steady heat transport in the HP ice and, thus, the heat is temporarily stored near the bottom of the H_2O layer, which results in melting the HP ice. Since the resultant melt is lighter than its surroundings, an upwelling flow of partially molten HP ice occurs. Such a possibility has been investigated also in studies of large icy moons in the solar system, in particular, Ganymede, which propose that solid and liquid coexist via melt production within the HP ice layer, bringing about a melt-buoyancy-driven upwelling flow in the interior.

To evaluate the efficiency of heat transport by the melt-buoyancy-driven flow, Choblet et al. (2017) performed 3-D simulations of thermal convection in the HP ice layer, including the effect of melting of the HP ice. In their simulations, they assumed and mimicked a permeable flow in the HP ice by extracting the generated melt instantaneously to the above ocean. Then, they demonstrated that melt is mostly generated on the oceanic crust and the permeable flow dominates the heat transport. Recently, Kalousová et al. (2018) performed 2-D convection

simulation of a water-ice mixture to investigate the behavior of the generated melt in the HP ice layer. They demonstrated that heat is efficiently transported by the melt-buoyancy-driven convective and permeable flows and water is exchanged throughout the HP ice layer. In this study, we call those flows the *sorbet flow*, since they are flows of a water-ice mixture. The sorbet flow occurs for the small thickness of the HP ice ($\lesssim 200$ km) and large heat flow ($\gtrsim 20$ mW m^{-2}) for Ganymede-like icy bodies. Nusselt–Rayleigh number scaling supports that such a sorbet flow likely occurs also for ocean planets with Earth-like geothermal heats (80 mW m^{-2} in the present Earth's mean mantle heat flow) and thicker HP ice. Hence, seafloor weathering likely occurs for ocean planets with the HP ice.

Horizontal variation is another important effect ignored previously. In particular, for planets where plate tectonics works, the heat flow from oceanic crusts is highest at mid-ocean ridges and decreases with distance from there. The heat flow near mid-ocean ridges can be high enough to melt the HP ice. Then, the seafloor temperature is fixed close to the melting temperature for the pressure at the seafloor (hereafter, the seafloor pressure). This temperature is much higher than one obtained from inward integration of the adiabat from the oceanic surface to the seafloor. Higher seafloor temperature results in more efficient seafloor weathering, according to the temperature dependence of seafloor weathering inferred based on dissolution experiments of basalt (Brady & Gíslason, 1997; Gudbrandsson et al., 2011) and geological evidence (Coogan & Dosso, 2015; Krissansen-Totton & Catling, 2017). Hence, the seafloor weathering can remove atmospheric CO_2 efficiently, provided such a molten region is sufficiently wide.

We theoretically explore the planetary climate on ocean planets with plate tectonics in the habitable zone. This study is aimed at evaluating the role of the HP ice in seafloor weathering and climate for ocean planets with a focus on the effects of the liquid-solid coexistence region maintained by the sorbet flow and the horizontal variation in heat flux from the oceanic crust.

The rest of this part is organized as follows: In Section 2.2, we describe our model to simulate the ocean layer structure and planetary climate. In Section 2.3, we show the behavior of the HP ice with a focus on the area where melting occurs and the impacts of seafloor weathering with the HP ice on the planetary climate. In Section 2.4, we discuss surface environments of ocean planets, caveats of the model, and implication of our results for terrestrial exoplanets. In Section 2.5,

we summarize this part.

2.2 Climate model

We consider an Earth-size ocean planet with various amounts of H_2O and CO_2. Of special interest in this study is the impact of ocean mass, M_{oc}, on the planetary climate including surface temperature, T_s, and CO_2 partial pressure, P_{CO_2}. We assume that the planet is almost Earth-like, namely, a terrestrial planet with the Earth's mass and internal composition orbiting at 1 AU far from a Sun-like star, except for the ocean mass. Our climate model consists of four components: (1) internal structure integration that determines the thickness of the HP ice layer (section 2.2.1); (2) seafloor environment modeling that determines the area where seafloor weathering works when the HP ice is present (section 2.2.2); (3) carbon cycle modeling that calculates P_{CO_2} (section 2.2.3); (4) atmospheric modeling that calculates T_s (section 2.2.4).

2.2.1 Ocean structure model

We develop a radially one-dimensional, hydrostatic internal structure mode, based on Valencia et al. (2007b). We consider a differentiated solid rock-metal body of 1 Earth mass covered with various amounts of H_2O. Note that the planetary mass is the sum of the rock-metal body and ocean masses (i.e., $1M_\oplus + M_{oc}$). We assume (1) the mass ratio of iron core to silicate-mantle is 7 : 3, (2) the mass ratio of the inner to outer core is the same as that of the Earth (35 : 65), (3) phase transitions occur at the same pressures as in the Earth's interior, and (4) thermal expansion of the mantle and core never occurs. These assumptions have little influence on the surface gravity, which affects the structure of the ocean layer and thus on our conclusion in this study.

The hydrostatic structure of the ocean is determined by

$$\frac{dP}{dr} = -g\rho, \tag{2.1}$$

$$\frac{dm}{dr} = 4\pi r^2 \rho, \tag{2.2}$$

where r is the radial distance from the planetary center, P and ρ are the pressure and density, respectively, m is the cumulative mass, and g is the gravity ($g = Gm/r^2$; G being the gravitational constant). Its thermal structure is assumed to be adiabatic:

$$\frac{dT}{dr} = -\frac{\alpha g T}{C_P}, \tag{2.3}$$

where T is the temperature, α is the thermal expansivity, and C_P is the heat capacity.

The equations of state (EOSs) and parameter values that we adopt are summarized in Table 2.1. The temperature effect on density of the HP ice follows expressions from Bezacier et al. (2014) for ice VI and Fei et al. (1993) for ice VII. The thermal capacity of liquid water is taken from Waite et al. (2007). The phase transition from water to HP ice occurs where the adiabat crosses the phase boundaries in the P-T plane. given by Eq. 2.4. For the melting point temperature $T^{\rm mel}$ at a given pressure, we use the formula from Dunaeva et al. (2010),

$$T^{\rm mel} = a_1 + a_2 P + a_3 \ln P + a_4 P^{-1} + a_5 \sqrt{P}, \tag{2.4}$$

where P is the pressure in bar and the values of coefficients are summarized in Table 2.2. We assume that the phase transition from ice VI to VII occurs at the triple point of liquid/ice VI/ice VII, the pressure of which is 22160 bars. We assume the thermal structure of the iron core and the rocky mantle are the same as the Earth. The phase transitions and the pressures at the transitions are summarized in Table 2.3.

Two of the three boundary conditions are $T = T_{\rm s}$ and $P = P_{\rm s}$ at $r = R_{\rm p}$, where $P_{\rm s}$ is the surface pressure and $R_{\rm p}$ is the planet radius. Here $P_{\rm s}$ is the sum of the background pressure ($P_{\rm n} = 1 \times 10^5$ Pa) and vapor pressure $P_{\rm H_2O}$ for $T_{\rm s}$, which is taken from Nakajima et al. (1992); $P_{\rm CO_2}$ is relatively small. The inner boundary condition is $m = 0$ at $r = 0$. This means that we must continue the integration until the planet's center, although we are interested only in the ocean layer.

The red line of Fig. 2.1 shows the calculated relationship between the surface temperature and critical ocean mass beyond which HP ice exists (see section 2.2.5 for the numerical procedure), which is abbreviated to COM-HP hereafter. It turns out that HP ice exists for an Earth-like planet with an ocean of more than $\sim$20 to $\sim$100 $M_{\rm oc,\oplus}$, depending on surface temperature. To see the sensitivity to the thermal structure of the ocean, we also show the result for an isothermal ocean. The difference in COM-HP between the isothermal and adiabatic cases is $\sim$ 1–30$M_{\rm oc,\oplus}$ for $T_{\rm s}$ = 280–400 K. Even for the two extreme cases, the difference is small enough not to change our conclusions.

Table 2.1: Data for EOS parameters

Layer	Composition	ρ_0 (kg m^{-3})	B_0 (GPa)	B_0'	EOS	Reference
H_2O	Liquid water					(1)
	Ice VI	1270	14.05		BME	(2)
	Ice VII	1240	5.02	7.51	Vinet	(3)
Upper mantle	ol	3347	126.8	4.274	Vinet	(4)
	wd + rw	3644	174.5	4.274	Vinet	(4)
Lower mantle	pv + fmv	4152	223.6	4.274	Vinet	(4)
	ppv + fmv	4270	233.6	4.524	Vinet	(4)
Outer core	$Fe_{0.8}(FeS)_{0.2}$	7171	150.2	5.675	Vinet	(4)
Inner core	Fe	8300	150.2	5.675	Vinet	(4)

ρ_0 is the reference density, B_0 is the bulk modulus and B_0' is the pressure derivative of the bulk modulus. BME represents second-order Birch-Murnaghan EOS (ref. Birch, 1978), Vinet is represented Vinet EOS (ref. Vinet et al., 1989).

(1) Levi et al. (2014) and references therein; (2) Bezacier et al. (2014); (3) Sugimura et al. (2008); (4) Valencia et al. (2007b) and references therein.

Table 2.2: Coefficients for ice melting curve given by Eq. (2.4) from Dunaeva et al. (2010)

Ice phase	a_1	a_2	a_3	a_4	a_5
Ice VI	4.2804	-0.0013	21.8756	1.0018	1.0785
Ice VII	-1355.42	0.0018	167.0609	-0.6633	0

Table 2.3: Phase boundaries of rocky material

Phase transition	Boundary pressure	Reference
ol $\rightarrow$ wd + rw	13.5 GPa	(1)
rw $\rightarrow$ pv + fmv	23.1 GPa	(1)
pv + fmv $\rightarrow$ ppv + fmv	125 GPa	(2)

(1)Turcotte & Schubert (2002); (2)Murakami et al. (2004)

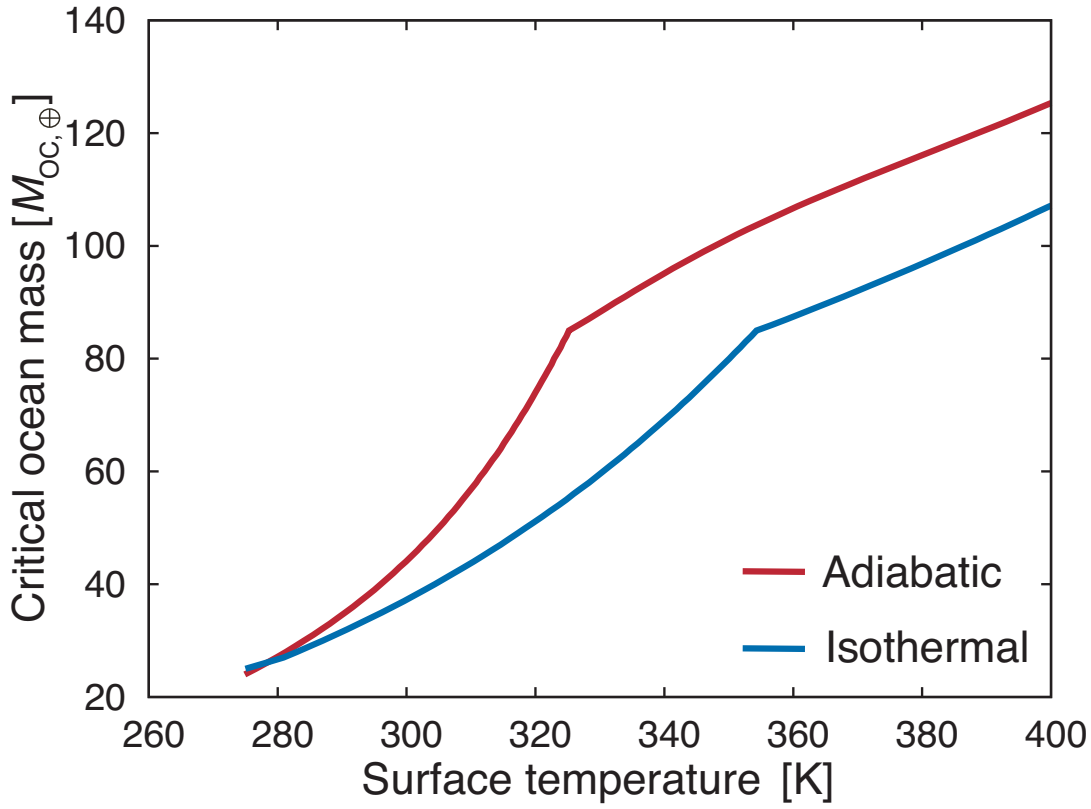

Figure 2.1: The critical ocean mass (COM-HP) in the unit of the Earth's ocean mass ($M_{oc,\oplus}$), beyond which high-pressure (HP) ice appears deep in the ocean is shown as a function of surface temperature (red line). Note that the result for an isothermal liquid ocean is also shown (blue line) to confirm that our calculation reproduces the result of Kitzmann et al. (2015) well.

2.2.2 Seafloor environment model

Near a mid-ocean ridge, heat flow from below is so high that the HP ice would be incapable of transporting the heat by thermal conduction nor convection and consequently become molten. If liquid water exists together with ice, the heat can be transported efficiently by a sorbet flow, as described in Introduction. The HP ice far from a mid-ocean ridge remains solid because of low heat flow. Hence, there is a *critical distance* beyond which or a *critical heat flow*, q_{cr}, below which the HP ice remains solid.

A schematic illustration of our seafloor environment model is shown in Fig. 2.2. Here we assume that (1) the heat transport is steady and vertically one dimensional, (2) the composition and phase of H_2O are vertically homogeneous in the HP ice region, and (3) the sorbet flow dominates the heat transport in the solid-

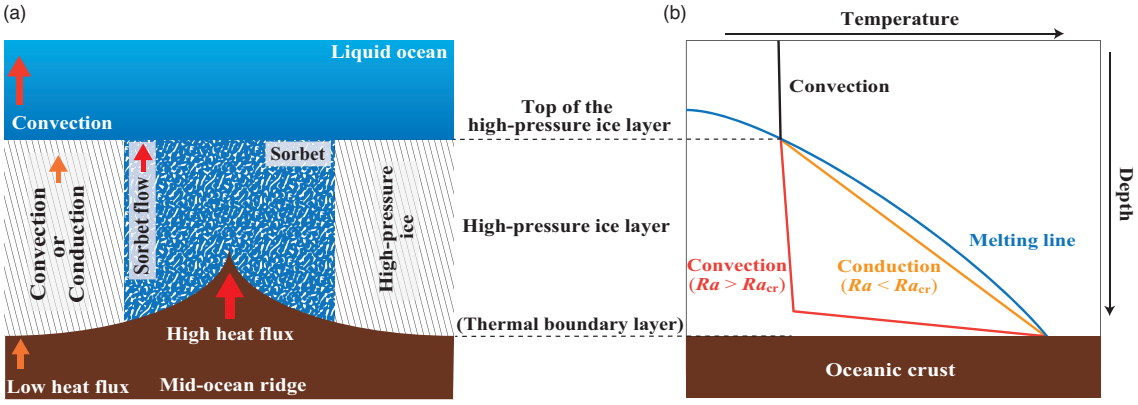

Figure 2.2: Seafloor environment model—(*a*) schematic illustration of the seafloor environment and (*b*) qualitative temperature profiles in the infinitesimally thin layer on the side of the high-pressure ice at the boundary between the "sorbet" and "high-pressure ice" regions. In panel (*a*), arrows represent the direction and dominant mechanisms of heat transport. In the sorbet region, ice and liquid coexist and thus the temperature is fixed at the melting point of H_2O. In panel (*b*), Ra and Ra_{cr} represent the Rayleigh number and the critical Rayleigh number, respectively. The red and orange solid lines represent thermal structure when the high-pressure ice layer is convective and conductive, respectively. The blue and black solid lines represent the melting line of H_2O and adiabatic thermal structure of the liquid ocean, respectively.

liquid coexistence region (called the *sorbet region*, hereafter), whereas solid-state convection or conduction occurs in the HP ice region. These assumptions are consistent with results of previous hydrodynamical simulations (Choblet et al., 2017; Kalousová et al., 2018). We discuss their validity and impact on our conclusion in section 2.4.3.1.

2.2.2.1 Critical heat flow

First, we determine the critical distance or critical heat flow. Namely, according to its definition, we find the point at which convection nor conduction can hardly transport the heat inside the HP ice region. Figure 2.2*b* shows qualitative temperature profiles in the HP ice: At the critical distance, since the ice-liquid mixture on the oceanic crust is in phase equilibrium, the temperature is equal to the melting temperature. Also, the temperature at the top of the HP layer is the melting one, by definition.

To determine the thermal structure of the HP ice region, we adopt a similar

approach with that used by Fu et al. (2010) who investigated the structure of the icy mantle of an ocean planet with a frozen surface, although they ignored horizontal variation in heat flux. Unlike Fu et al. (2010), we take into account the case where the HP ice layer is wholly conductive, ignore the upper thermal boundary layer, and consider the different boundary condition for the bottom of the HP layer. The details are described below.

The mechanism of heat transport depends on the Rayleigh number, Ra, which is defined as (Turcotte & Schubert, 2002)

$$Ra = \frac{g\alpha\rho D^3 \Delta T_{\rm HP}}{\kappa\eta}, \tag{2.5}$$

where D is the thickness of the HP ice layer, κ is the coefficient of thermal diffusivity, η is the viscosity, $\Delta T_{\rm HP} = T_{\rm BB}^{\rm mel} - T_{\rm TB}^{\rm mel}$ and $T_{\rm TB}^{\rm mel}$ and $T_{\rm BB}^{\rm mel}$ are the melting point temperatures for the pressures at the top and bottom of the HP ice layer, respectively. For the melting point temperature $T^{\rm mel}$, we use Eq. 2.4. The thermal diffusivity is defined by $\kappa = k/\rho C_P$, where k is the thermal conductivity. For C_P of ice VI and VII, we use the expression derived by Fei et al. (1993). For k, we adopt a constant value of 3.8 $\mathrm{Wm^{-1}K^{-1}}$, which is its typical value for ice VII under 2.5 GPa and 300 K (Chen et al., 2011), for simplicity. For η of ice VII, which is poorly constrained, we adopt a dislocation model for the viscosity of phase VI, which is the highest phase of the HP ice measured so far (Durham et al., 1997) :

$$\eta(P_\eta, T_\eta) = B\zeta^{-3.5} \exp\left[\frac{(E^* + P_\eta V^*)}{RT_\eta}\right], \tag{2.6}$$

where B ($= 6.7 \times 10^{19}$ $\mathrm{Pa^{4.5}}$ s) is a constant, ζ ($= 2.0 \times 10^6$ Pa) is a characteristic shear stress (Fu et al., 2010), R is the ideal gas constant, E^* ($= 110$ kJ $\mathrm{mol^{-1}}$) and V^* ($= 1.1 \times 10^{-5}$ $\mathrm{m^3\ mol^{-1}}$) are the activation energy and volume (Durham et al., 1997), respectively, and T_η and P_η are the temperature and pressure at deformation, respectively. Because the viscosity contrast in the HP ice layer is relatively small, the small viscosity contrast prescription can be used (Fu et al., 2010). For P_η and, T_η, we use the averaged values for the HP ice layer (Dumoulin et al., 1999). In this study, we assume the value of the critical Rayleigh number, $Ra_{\rm cr}$, is 2000.

When $Ra < Ra_{\rm cr}$, conduction dominates heat transport and, thus, $q_{\rm cr}$ is given as

$$q_{\rm cr} = k\frac{\Delta T_{\rm HP}}{D}. \tag{2.7}$$

When $Ra > Ra_{\rm cr}$, since convection occurs, we assume the adiabatic temperature gradient (i.e., Eq.[2.3]). Near physical boundaries, however, since convective motion is prevented, thermal boundary layers are formed, where conduction transports heat. In this study, we consider the presence of a boundary layer only on the bottom of the HP ice layer (BBL), where the temperature gradient is given by

$$\frac{dT}{dr} = -\frac{q}{k} \tag{2.8}$$

and q is the heat flux. Integrating Eq. (2.3) inwards from the top of the HP ice layer and Eq. (2.8) outwards from the surface of the oceanic crust, we determine the BBL's thickness, δ, and the temperature difference in the BBL, $\Delta T_{\rm BBL}$ at the crossover point for a given q (see Fig. 2.2*b*).

Given that the BBL is marginally stable against convection, $Ra = Ra_{\rm cr}$ in the BBL, namely, $Ra_{\rm cr} = g\alpha\rho\delta^3\Delta T_{\rm BBL}/\kappa\eta_{\rm BBL}$, which comes to be

$$\delta = \left(\frac{\kappa\eta_{\rm BBL}Ra_{\rm cr}}{g\alpha\rho\Delta T_{\rm BBL}}\right)^{1/3}, \tag{2.9}$$

where $\eta_{\rm BBL}$ is the viscosity of the HP ice in the BBL and calculated with the intermediate values of temperature and pressure between the top and bottom of the BBL. If the set of δ and $\Delta T_{\rm BBL}$ for a given q satisfies Eq. (2.9), the value of q corresponds to $q_{\rm cr}$, which is also written as

$$q_{\rm cr} = k\frac{\Delta T_{\rm BBL}}{\delta} = \frac{k\kappa Ra_{\rm cr}}{g\alpha\rho}\cdot\frac{\eta_{\rm BBL}}{\delta^4}. \tag{2.10}$$

Note that Fu et al. (2010) considered a boundary layer under the top of the HP ice layer in addition to BBL. We discuss the difference in temperature structure in the HP ice layer between this study and Fu et al. (2010) and its impacts on our conclusion in section 2.4.3.1.

2.2.2.2 Effective weathering area

Same as in the Earth, the oceanic crust is assumed to form via eruption of hot mantle rock only at the mid-ocean ridge. As it moves away from the mid-ocean ridge toward the trench, the oceanic crust is cooled by seawater. Here we define a non-dimensional *effective weathering area*, $f_{\rm oc}$, as the area of the sorbet region (i.e., $q > q_{\rm cr}$) relative to the whole area of oceanic crust. A constant rate of oceanic crust production being assumed, $f_{\rm oc}$ is equivalent to the ratio of the period during which $q \geq q_{\rm cr}$ to the residence time of the oceanic crust, τ.

To calculate $f_{\rm oc}$, we model the cooling of the oceanic crust, adopting the semi-infinite half-space cooling model (Turcotte & Schubert, 2002): This model assumes that the crust cools only by vertical heat conduction. The heat flux from the oceanic crust is given by (Turcotte & Schubert, 2002)

$$q(t) = \frac{k_{\rm rock}(T_{\rm sol} - T_{\rm floor})}{\sqrt{\pi \kappa_{\rm rock} t}} \equiv \frac{\mathscr{A}}{\sqrt{t}}, \tag{2.11}$$

where t is time, $k_{\rm rock}$ ($= 3.3$ W m^{-1} K^{-1}) and $\kappa_{\rm rock}$ ($= 1.0 \times 10^{-6}$ m^2 s^{-1}) are the thermal conductivity and thermal diffusivity of the oceanic crust, respectively, $T_{\rm floor}$ is the seafloor temperature, and $T_{\rm sol}$ is the potential temperature of the mantle, for which we assume the peridotite dry solidus at the seafloor pressure, which was parameterized by Hirschmann et al. (2009). This assumption is made just for simplicity. The influence of the assumption on planetary climate is discussed in section 2.4.2.

From Eq. (2.11), the length of time required for q to decrease to $q_{\rm cr}$, which is denoted by $t_{\rm cr}$, is given by $t_{\rm cr} = \mathscr{A}^2/q_{\rm cr}^2$. Also, if the mean mantle heat flow, $\bar{q}$, is defined as $\bar{q} \equiv \tau^{-1} \int_0^\tau q \, {\rm d}t$, the residence time τ is given as a function of $\bar{q}$ as $\tau = 4\mathscr{A}^2/\bar{q}^2$. Thus, the effective weathering area is given as

$$f_{\rm oc} \equiv \frac{t_{\rm cr}}{\tau} = \frac{1}{4}\left(\frac{\bar{q}}{q_{\rm cr}}\right)^2. \tag{2.12}$$

In some cases, calculated $t_{\rm cr}$ happens to be larger than τ, which means the oceanic crust is fully covered with the solid-liquid mixture (i.e., the sorbet). In such cases, we set $f_{\rm oc} = 1$. From Eq. (2.12), it turns out that when $q_{\rm cr} > \bar{q}/2$, solid HP ice appears near the trench. In the next section, we use $f_{\rm oc}$ in the carbon cycle model.

In this study, the mean mantle heat flow $\bar{q}$ is a free parameter. As the fiducial value, we use $\bar{q} = 80$ mW m^{-2}, which is the value for the present Earth. Note that $q_{\rm cr}$ is independent of $\bar{q}$, according to Eq. (2.12).

2.2.3 Carbon cycle model

In order to investigate planetary climate, we develop a carbon cycle model by modifying the Earth's carbon cycle model of Tajika & Matsui (1992). Since we focus on continent-free terrestrial planets, we add the effect of seafloor weathering and neglect the continental reservoir of carbon and the effect of continental weathering. In addition, we consider the presence of the HP ice and pressure-dependent degassing. Same as Tajika & Matsui (1992) and Sleep & Zahnle

(2001), we perform box-model calculations of carbon circulation among reservoirs and find the equilibrium states.

2.2.3.1 Carbon reservoirs

We consider four reservoirs, which include the atmosphere, ocean (liquid water plus HP ice), oceanic crust (basalt), and mantle. Between the atmosphere and ocean, however, the carbon partition is assumed to be always in equilibrium, which is described in detail in section 2.2.3.3. The equilibrium value of the CO_2 partial pressure P_{CO_2} depends on the number of cations dissolved in the ocean (e.g., Zeebe & Wolf-Gladrow, 2001), for which we assume the present Earth's value, although the supply of cations via continental weathering never occurs in ocean planets. We have confirmed that overall results are insensitive to the number of dissolved cations (even in the case with no cations in the ocean). This is because the ocean reservoir is much small relative to the whole planetary carbon reservoir.

Carbon dissolved in the ocean is carried to the seafloor in the form of CO_2 ice, into which aqueous CO_2 is converted in the sorbet region (Bollengier et al., 2013). We assume that the carbon circulation in the sorbet region occurs quickly enough that it never affects the mass balance and also planetary climate. Detailed discussion of the CO_2 circulation is given in section 2.4.3.1.

The origin of volatiles in terrestrial planets has been highly debated so far, even for the Earth (e.g., O'Brien et al., 2018). Since possible candidates such as carbonaceous chondrites and comets include both carbon compounds and water, we assume that the total mole number of carbon contained in the whole planet, $C_{\rm total}$, is proportional to ocean mass, namely

$$C_{\rm total} = \gamma n_{\rm oc,\oplus} \frac{M_{\rm oc}}{M_{\rm oc,\oplus}}, \tag{2.13}$$

where γ is the CO_2/H_2O molar ratio in the source of volatiles of the planet, $n_{\rm oc,\oplus}(= 7.6 \times 10^{22}$ mol) is the molar quantity of H_2O in the Earth ocean mass, and $M_{\rm oc,\oplus}$ $(= 1.37 \times 10^{21}$ kg) is the Earth's ocean mass. Using the data and estimation published, we can estimate γ is to be 0.22 for carbonaceous chondrites (Jarosewich, 1990), 0.71 for comae of comets (Marty et al., 2016), and 0.19 for Earth composition (Tajika & Matsui, 1992). We use the Earth-like value ($\gamma = 0.19$) as the fiducial value. Dependence of planetary climate on γ is discussed in sections 2.3.2.

2.2.3.2 Carbon budget

The mass balance among those reservoirs is expressed as

$$\frac{d(C_{\rm atm}+C_{\rm oc})}{dt} = F_{\rm D}+F_{\rm M}-F_{\rm SW}, \tag{2.14}$$

$$\frac{dC_{\rm bs}}{dt} = F_{\rm SW}-F_{\rm R}-F_{\rm M}, \tag{2.15}$$

$$\frac{dC_{\rm man}}{dt} = F_{\rm R}-F_{\rm D}, \tag{2.16}$$

$$C_{\rm total} = C_{\rm atm}+C_{\rm oc}+C_{\rm bs}+C_{\rm man}, \tag{2.17}$$

where $C_{\rm atm}$, $C_{\rm oc}$, $C_{\rm bs}$, and $C_{\rm man}$ are the mole numbers of carbon contained in the atmosphere, ocean, oceanic basalt, and mantle, respectively, and $F_{\rm SW}, F_{\rm D}, F_{\rm R}, F_{\rm M}$ are the carbon fluxes due to seafloor weathering, degassing from the mid-ocean ridge, regassing via subduction into mantle and metamorphism that leads to degassing from volcanic arc, respectively. Those equations are solved for a given value of $C_{\rm total}$.

We adopt the degassing, regassing, and metamorphism models from Tajika & Matsui (1992), where each flux is expressed as

$$F_{\rm D} = K_{\rm D}A_{\rm S}C_{\rm man}, \tag{2.18}$$

$$F_{\rm R} = \frac{\beta}{\tau}C_{\rm bs}, \tag{2.19}$$

$$F_{\rm M} = \frac{1-\beta}{\tau}C_{\rm bs}. \tag{2.20}$$

Here $K_{\rm D}$ is the molar fraction of carbon degassing as CO_2 from the erupting magma per unit area. We take into account the dependence of $K_{\rm D}$ on seafloor pressure (i.e., ocean mass), the detail of which is described in section 2.2.3.4. β is the regassing ratio defined as the molar fraction of carbonate regassed into the mantle in the total subducting carbonate. We adopt the present Earth's value of β ($= 0.4$) estimated by Tajika & Matsui (1992). $A_{\rm S}$ is the seafloor spreading rate, which is simply given by

$$A_{\rm S} = \frac{A_0}{\tau}, \tag{2.21}$$

where A_0 is the whole area of the seafloor. We assume that A_0 is the present Earth's value ($= 3.1\times10^{14}$ m^2) from McGovern & Schubert (1989) and calculate τ from the relation $\tau = 4\mathscr{A}^2/\bar{q}^2$ for a given $\bar{q}$.

The seafloor weathering rate $F_{\rm SW}$ depends on seafloor temperature $T_{\rm floor}$ as (Brady & Gíslason, 1997)

$$F_{\rm SW} = F^*_{\rm SW} f_{\rm oc} \exp\left[\frac{E_{\rm a}}{R}\left(\frac{1}{T_0}-\frac{1}{T_{\rm floor}}\right)\right], \tag{2.22}$$

where F^*_{SW} is the present Earth's seafloor weathering rate, f_{oc} is the effective weathering area given by Eq. (2.12), E_{a} is the activation energy, and T_0 (= 289 K) is the reference seafloor temperature that corresponds to the surface temperature obtained by the atmospheric model with the present Earth's condition. F^*_{SW} estimated from deep-sea cores has a large variation with an order of magnitude (Coogan & Gillis, 2018). However, many estimations show the value about 2.0×10^{12} mol yr^{-1} (Alt & Teagle, 1999; Staudigel et al., 1989; Gillis & Coogan, 2011). In this study, thus, we use $F^*_{\mathrm{SW}} = 2.0 \times 10^{12}$ mol yr^{-1} as a nominal value and we vary it over the range between 2.0×10^{11} and 2.0×10^{13} mol yr^{-1}.

The activation energy E_{a} is uncertain and its reported value ranges between 30 and 92 kJ mol^{-1}. Brady & Gíslason (1997) firstly determined E_{a} experimentally to be 41 kJ mol^{-1}. Recent inversion methods using geological evidence support a relatively high value of E_{a}: Precisely, strontium and oxygen isotopes in carbonates indicated $E_{\mathrm{a}} = 92 \pm 7$ kJ mol^{-1} (Coogan & Dosso, 2015). Also, several proxies reflecting the surface and seafloor temperatures, atmospheric $\mathrm{CO_2}$, and oceanic pH showed $E_{\mathrm{a}} = 75^{+22}_{-21}$ kJ mol^{-1} (Krissansen-Totton & Catling, 2017). Those values are also consistent with estimates from laboratory experiments for the dominant minerals in the oceanic crust (Brantley & Olsen, 2013). In contrast, an experimental study of basalt dissolution in the moderate pH range reported the relatively small E_{a} of 30 kJ mol^{-1} (Gudbrandsson et al., 2011). In this study, we use $E_{\mathrm{a}} = 41$ kJ mol^{-1} as the fiducial value according to previous studies (e.g., Foley, 2015) and vary it over the range between 30 and 92 kJ mol^{-1}. We ignore the pH dependence of seafloor weathering since it is known to be small in the pH range between 4 and 10 (Gudbrandsson et al., 2011).

The seafloor temperature also depends on the surface temperature, T_{s}, because we assume that the temperature structure of the ocean is adiabatic (see also § 2.2.1). We calculate T_{s} as a function of $P_{\mathrm{CO_2}}$, as described in detail in section 2.2.4. On the area of the seafloor beneath the sorbet region, T_{floor} is equal to the melting temperature at the seafloor pressure.

2.2.3.3 Partitioning of $\mathrm{CO_2}$ between atmosphere and ocean

The partial pressure of $\mathrm{CO_2}$, $P_{\mathrm{CO_2}}$, depends on the carbon budget of the surface reservoirs ($C_{\mathrm{atm}} + C_{\mathrm{oc}}$), oceanic pH and ocean volume, V_{oc}. Here we describe the calculation method of carbon partitioning between the atmosphere and ocean, which is almost the same as that described in Tajika & Matsui (1990) and Kitz-

mann et al. (2015).

Chemical equilibrium among $CO_2(g)$, carbonic acid (H_2CO_3), carbonate ion (CO_3^{2-}), and bicarbonate ion (HCO_3^-) is determined by the following reactions

$$CO_2(g) + H_2O \rightleftharpoons H_2CO_3, \tag{2.23}$$

$$H_2CO_3 \rightleftharpoons HCO_3^- + H^+, \tag{2.24}$$

$$HCO_3^- \rightleftharpoons CO_3^{2-} + H^+, \tag{2.25}$$

$$H_2O \rightleftharpoons H^+ + OH^-, \tag{2.26}$$

with equilibrium constants

$$K_0 = \frac{[H_2CO_3]}{P_{CO_2}}, \tag{2.27}$$

$$K_1 = \frac{[H^+][HCO_3^-]}{[H_2CO_3]}, \tag{2.28}$$

$$K_2 = \frac{[H^+][CO_3^{2-}]}{[HCO_3^-]}, \tag{2.29}$$

$$K_w = [H^+][OH^-]. \tag{2.30}$$

We have assumed the Henry's law is valid. We use the values of K_0 from Weiss (1974), K_1 and K_2 from Millero et al. (2006), and K_w from Millero (1995), which were obtained experimentally for temperature of 300 K and salinity of 35 ‰. We use those values at all temperatures, because those equilibrium constants have not been experimentally measured for the temperature range of interest in the study.

Since Equations (2.27)–(2.30) contain six unknowns, we need at least two additional equations. One is the equation of charge conservation:

$$[OH^-] + [HCO_3^-] + 2[CO_3^{2-}] = [H^+] + [M^+], \tag{2.31}$$

where $[M^+]$ represents the concentration of all the cations in the ocean. In this study, we use the average value of $[M^+]$ measured in the present Earth ocean (i.e., $[M^+] = 2.2 \times 10^{-3}$ mol L^{-1}). Even a constant value of $[M^+]$ has little influence on conclusions (see also section 2.2.3). Also, the total number of carbon $C_{atm} + C_{oc}$, which is determined from the carbon cycle model (section 2.2.3), must be conserved in the atmosphere-ocean system. Since the solubility of CO_2 in liquid water increases rapidly with pressure (Duan & Sun, 2003) and mixing occurs in the ocean on a timescale much shorter than that of interest in this

study, we assume C_{oc} to be equal to the surface concentration of CO_2. Thus, the total number of carbon is expressed as

$$C_{atm} + C_{oc} \approx \frac{4\pi R_p^2 P_{CO_2}}{m_{CO_2} g_s} + ([H_2CO_3] + [HCO_3^-] + [CO_3^{2-}])V_{oc}, \tag{2.32}$$

where the first term on the right-hand side corresponds to C_{atm}, and m_{CO_2} is the molecular weight of CO_2 ($= 44$ g mol^{-1}) and g_s is the surface gravity. We obtain R_p, g_s, and V_{oc} for given T_s and M_{oc} from the internal structure model in section 2.2.1. For C_{atm}, we assume that the molecular weight of the atmospheric gas is equal to the molecular weight of CO_2, which overestimates P_{CO_2}. However, the approximation has no influence on the overall results of the study.

Finally, solving Eqs. (2.27)-(2.32), we determine P_{CO_2} and the mole fractions of ions.

2.2.3.4 Dependence of degassing coefficient on seafloor pressure

Here we introduce the dependence of degassing coefficient, K_D, on seafloor pressure. According to Tajika & Matsui (1992), the degassing coefficient is given by

$$K_D = f_{CO_2} \frac{d_m}{V_{man}}, \tag{2.33}$$

where f_{CO_2} is the degassing fraction, which is defined as the molar fraction of the CO_2 degased from the upwelling magma at the ridge, d_m is the degassing depth, which is defined as the melt generation depth of mantle, and V_{man} is the volume of the mantle. For V_{man} and d_m, we use the values for the present Earth, namely $V_{man} = 8.0 \times 10^{20}$ m^3 and $d_m = 40$ km (Tajika & Matsui, 1992).

The degassing fraction f_{CO_2} depends on the ocean mass, because of pressure dependence of CO_2 solubility into magma (Kite et al., 2009). In this study, we take it into account, following Tajika & Matsui (1992), who considered the solubility equilibrium of CO_2 with solid/liquid silicate. We incorporate the pressure dependence on the solubility of CO_2 into silicate melts, $K^{G/L}$, and the molar volume of CO_2, V_M, in calculating f_{CO_2} as (Tajika & Matsui, 1992)

$$f_{CO_2} = \left\{ 1 + \frac{(f_{melt}^{-1} - 1)K^{L/S}}{1 + (w^G/w^L)} \right\}^{-1}, \tag{2.34}$$

where f_{melt} is the melt fraction, $K^{L/S}$ is the partition coefficient of CO_2 between solid and liquid, and w^G/w^L represents the mass ratio of CO_2 partitioned into

the gas phase to that into the liquid phase (liquid phase meaning CO_2 dissolved in melt); w^G/w^L is defined as

$$\frac{w^G}{w^L} = \frac{\phi m_{CO_2} n_{CO_2}}{\rho_{rock} V_M K^{G/L}}, \tag{2.35}$$

where ϕ is the vesicularity of melt, ρ_{rock} is the density of oceanic crust, and n_{CO_2} is the molar concentration of CO_2 gas in the vesicles. We adopt values of $f_{melt}, K^{L/S}, \phi$, and n_{CO_2} from Tajika & Matsui (1992)

Recent molecular dynamics simulations (Guillot & Sator, 2011) predict higher solubility of CO_2 for > 2 GPa than that obtained according to Henry's law. Those simulations found an almost linear dependence on pressure and weakly correlation with temperature. We have estimated the relationship between $K^{G/L}$ and P based on tabular data for $T = 1673$ K and MORB composition presented in Guillot & Sator (2011):

$$K^{G/L} = \begin{cases} 0.008P & P < 2\text{GPa} \\ 0.035(P-2.0)+0.016 & P \geq 2\text{GPa}. \end{cases} \tag{2.36}$$

Here P is the pressure in the unit of GPa. We evaluate V_M at the seafloor pressure using the EOS based on molecular dynamics simulations (Duan & Zhang, 2006), which is of wide application (i.e., up to 10 GPa and 2573.15 K). The temperature in the EOS corresponds to the solidus of anhydrous peridotite at the seafloor pressure, which is parameterized by Hirschmann et al. (2009).

Figure 2.3 shows the degassing fraction f_{CO_2} as a function of ocean mass M_{oc} for $T_s = 300$ K. f_{CO_2} is found to decrease with M_{oc}, because the solubility of CO_2 increases with pressure. f_{CO_2} varies from 0.23 to 0.1 between 1 to 200 $M_{oc,\oplus}$. At $M_{oc} = 77\ M_{oc,\oplus}$, the slope of f_{CO_2} changes because seafloor pressure becomes higher than 2 GPa. Kite et al. (2009) proposed that degassing could be completely suppressed (i.e., $f_{CO_2} = 0$) for a 100 km ocean (roughly 40 $M_{oc,\oplus}$ in our model) because of higher solubility of CO_2. In contrast, Fig. 2.3 indicates that degassing also occurs for larger M_{oc}. Higher solubility would lead to no partitioning into the gas phase ($w^G/w^L \to 0$). In this case, degassing fraction would be determined by two-phase partitioning between solid and liquid and consequently f_{CO_2} becomes 0.096. Therefore, our model results in degassing that mainly occurs as the liquid phase at high pressures.

Also, in Fig. 2.3, f_{CO_2} is estimated to be 0.23 for $M_{oc} = 1\ M_{oc,\oplus}$ corresponding to seafloor pressure of 27 MPa, which is relatively smaller than the value

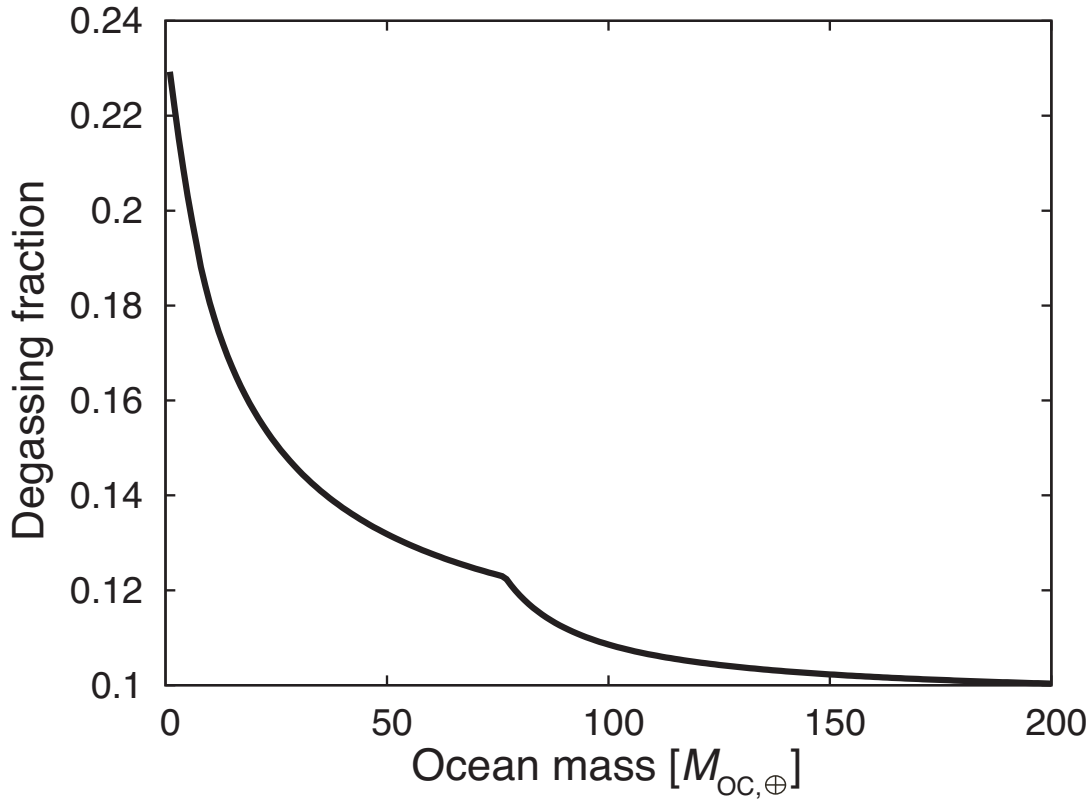

Figure 2.3: Degassing fraction f_{CO_2} (see Eq.[2.34]) as a function of ocean mass for surface temperature $T_s = 300$ K. $M_{oc,\oplus}$ means the Earth's ocean mass.

(0.32) estimated according to the Henry's law, by Tajika & Matsui (1992). This difference is due to higher solubility (216 ppm at 27 MPa) than that (100 ppm) of Tajika & Matsui (1992). Note that low-pressure experiments suggest higher solubility than our model (Jendrzejewski et al., 1997). In any case, because a pressure range much higher than 27 MPa is of special interest in this study, we neglect this difference.

2.2.4 Atmospheric model

In this study, we use the open-source code for 1-D radiative-convective climate models, *Atmos*[1], developed by Kasting and his collaborators (Kasting et al., 1993; Kopparapu et al., 2013; Ramirez et al., 2014). This code calculates radiative fluxes in vertically spacing layers of the atmosphere, using the two-stream approximation with the coefficients for radiative absorption and scattering by gaseous molecules updated by Kopparapu et al. (2013). We assume a 1-bar N_2 atmosphere with various partial pressures of CO_2. The distribution of the relative

[1]https://github.com/VirtualPlanetaryLaboratory/atmos

Table 2.4: Variables and their values.

Parameter	Symbol	Value
Ocean mass	$M_{\rm oc}$	1–200 $M_{\rm oc,\oplus}$
Mean mantle heat flow	$\bar{q}$	40, 60, 80, 100, 120 mW $\rm m^{-2}$
Activation energy of seafloor weathering	$E_{\rm a}$	30, 41, 92 kJ $\rm mol^{-1}$
Normalized constant of seafloor weathering	$F^*_{\rm SW}$	2.0×10^{11}–2.0×10^{13} mol $\rm yr^{-1}$
CO_2/H_2O molar ratio	γ	1.0×10^{-3}–10

humidity of water vapor is treated according to the empirical Manabe-Wetherald model which assumes the surface relative humidity of 0.8, based on the present Earth's atmosphere (Manabe & Wetherald, 1967; Pavlov et al., 2000). According to Kopparapu et al. (2013), we use the surface albedo of 0.32, which implicitly includes the cloud radiative effect. We use the present insolation flux at the Earth's orbit $S_\odot$ (=1360 W $\rm m^{-2}$) and the present Sun's spectrum as the fiducial value and spectrum model, respectively. The other model settings are the same as those adopted in Ramirez et al. (2014). Then, we calculate equilibrium values of $T_{\rm s}$ as a function of $P_{\rm CO_2}$ for given stellar insolation, using a time-stepping approach with moist convective adjustment (Pavlov et al., 2000). We have confirmed that our calculated $T_{\rm s}$ is almost the same with sufficient accuracy as that from Ramirez et al. (2014). We discuss the uncertainties and impacts of stellar insolation, surface albedo, and relative humidity in sections 2.3.2.2, 2.4.3.2, and 2.4.4.

2.2.5 Numerical procedure

In summary, for given values of ocean mass $M_{\rm oc}$ and mean mantle heat flow $\bar{q}$, we determine the climate of the ocean planet by the following procedure.

(i) For trial values of surface temperature $T_{\rm s}$ and surface pressure $P_{\rm s}$, we integrate Eqs. (2.1)–(2.3) inward from the surface to determine temperature as a function of pressure in the ocean (see § 2.2.1). We find a level where the adiabat crosses the melting temperature of ice. The layer between the crossover level and the oceanic crust surface consists of HP ice. Then, the seafloor pressure $P_{\rm floor}$ and the thickness of the HP ice layer D are determined. If the adiabat reaches the oceanic crust surface before crossing the

Table 2.5: Parameters and their values.

Parameter	Symbol	Value
Earth ocean mass	$M_{\mathrm{oc},\oplus}$	1.37×10^{21} kg
Molar quantity of H_2O in the Earth ocean mass	$n_{\mathrm{oc},\oplus}$	7.6×10^{22} mol
Thermal conductivity of the HP ice	k	3.8 W m^{-1} K^{-1}
Constant for the viscosity of the HP ice	B	6.7×10^{19} $Pa^{4.5}s$
Characteristic shear stress of the HP ice	ζ	2.0×10^{6} Pa
Activation energy for the viscosity of the HP ice	E^*	110 kJ mol^{-1}
Activation volume for the viscosity of the HP ice	V^*	1.1×10^{-5} m^3 mol^{-1}
Critical Rayleigh number	Ra_{cr}	2000
Thermal conductivity of the oceanic crust	k_{rock}	3.3 W m^2 s^{-1}
Thermal diffusivity of the oceanic crust	κ_{rock}	1.0×10^{-6} m^2 s^{-1}
Reference seafloor temperature	T_0	289 K
Area of the oceanic floor	A_0	3.1×10^{14} m^2
Regassing ratio	β	0.4

ice melting curve, the planet has no ice in the deep ocean. The numerical integration is performed with a 4th-order Runge-Kutta method. The size of the interval is chosen so that the pressure at the crossover point is determined with < 0.1 % accuracy.

(ii) When the HP ice is present, from the seafloor environment model, we determines the critical heat flow q_{cr} (or the area of the sorbet region) from Eq. (2.7) or (2.10), depending on Ra (§ 2.2.2). Then, we obtain the effective weathering area f_{oc} by substituting q_{cr} and $\bar{q}$ in Eq. (2.12). Also, we obtain the seafloor temperature T_{floor} in the sorbet region by substituting P_{floor} in Eq. (2.4).

(iii) In the carbon cycle model (§ 2.2.3), using T_{floor} and f_{oc} obtained above, we perform a time integration of Eqs. (2.14)–(2.16) and determine the carbon partition among the atmosphere, ocean, oceanic crust, and mantle. Then, from the calculated $P_{\mathrm{CO_2}}$, we obtain a new value of T_{s} (and thereby P_{s}) from the atmospheric model (§ 2.2.4). If the new value of T_{s} differs by

> 0.01 K from the trial value of T_s, we return to Step (i) and repeat the above procedures with the new T_s. The time integration is performed with a Euler method and the interval size is chosen so that the time difference in the molar number of carbons is smaller than 0.1 % for all the reservoirs.

(iv) Once all the time derivatives in Eqs. (2.14)–(2.16) become zero, we judge the solution as an equilibrium state. If the surface temperature drops below 273 K, we also stop the time integration and regard the solution as a snowball state.

We start time-stepping calculations at arbitrarily high P_{CO_2} (i.e., in a warm condition) for finding equilibrium solutions. We have confirmed that the results are insensitive to choice of the initial condition, provided a sufficiently high CO_2 pressure ($P_{CO_2} > 10$ bars) is adopted. (The carbon cycle and climate stability in the snowball state are discussed in section 2.4.3.3.) In most of our simulations, an equilibrium state is achieved on a timescale of the order of Gyr, which is consistent with results shown in Foley (2015). In Appendix A, we discuss details of response times for carbon cycle model.

The parameters and constants with their values adopted in this study are summarized in Tables 2.4 and 2.5, respectively. The upper limit for ocean mass M_{oc} that we consider is 200 $M_{oc,\oplus}$. The reasoning is as follows: We suppose that plate tectonics is working on the planet. Although still not fully understood, an increase in water has negative effects on plate tectonics. In particular, it leads to reducing crustal production and degassing, since the solidus temperature of the mantle material increases with pressure (Kite et al., 2009; Noack et al., 2016). According to Noack et al. (2016), crustal production completely ceases for an Earth-mass planet with the ocean layer thicker than approximately 400 km, if plate tectonics operates. The ocean mass of 200 $M_{oc,\oplus}$ that we adopt here corresponds to the ocean layer of $\sim$350 km for $T_s = 300$ K. We do not consider ocean planets with more massive oceans because such planets are expected to have no geochemical cycle. For planetary climates with no geochemical cycle, see Kitzmann et al. (2015) and Kite & Ford (2018).

Note that we assume a spherically symmetric structure in the internal structure modeling, while we consider the presence of the sorbet and HP ice regions in the deep ocean in the seafloor environment modeling. Such self-contradiction, however, has little influence on our whole modeling. This is because only the

thermal structure above the HP ice layer is of interest in this study and the equations of state of water, rock, and iron are rather insensitive to temperature.

2.3 Results

2.3.1 Melting of the HP ice

We first investigate the behavior of the HP ice with a focus on the effective weathering area, which is a controlling factor for seafloor weathering. Here we do not use the carbon cycle model, but, instead, perform calculations for fixed values of the surface temperature T_s. Figure 2.4 shows the calculated thickness of the HP ice layer D (left column), the critical heat flow q_{cr} (middle column) and effective weathering area f_{oc} (right column) as a function of ocean mass M_{oc} for $T_s = 300$ K (top) and as a function of T_s for $M_{oc} = 200M_{oc,\oplus}$ (bottom). In those calculations, the mean mantle heat flow $\bar{q}$ is assumed to be 80 mW m^{-2}.

2.3.1.1 Dependence on Ocean Mass

The overall dependence on ocean mass is as follows. As shown in Fig. 2.4*a*, the HP ice is present, if $M_{oc} \gtrsim 45M_{oc,\oplus}$. Its thickness increases almost linearly with ocean mass and reaches 247 km at $M_{oc} = 200M_{oc,\oplus}$. In Fig. 2.4*b*, the critical heat flow is found to be zero for $M_{oc} \lesssim 45M_{oc,\oplus}$, because of no HP ice, and then increase with ocean mass, up to about 80 mW m^{-2} ($\simeq \bar{q}$) at $M_{oc} = 200M_{oc,\oplus}$. In Fig. 2.4*c*, the effective weathering area is found to be unity until $M_{oc} \simeq 139M_{oc,\oplus}$ and rapidly decrease to about 0.2 at $M_{oc} = 200M_{oc,\oplus}$.

A jump in q_{cr} is found at $M_{oc} \simeq 74M_{oc,\oplus}$ in Fig. 2.4*b*. At that point, the heat transport mechanism in the HP ice above the critical point (i.e., $q = q_{cr}$) changes from conduction to convection. For $M_{oc} \lesssim 74M_{oc,\oplus}$ ($D \simeq 55$ km), the HP ice layer is thin enough and, therefore, the temperature difference ΔT_{HP} ($= T_{BB}^{mel} - T_{TB}^{mel}$) is small enough for conduction to transport the heat flux from the oceanic crust. However, as shown in Fig 2.4*c*, $q_{cr} \simeq 10$ mW m^{-2} $< \bar{q}/2$ at $M_{oc} \lesssim 74M_{oc,\oplus}$, meaning that the HP ice is entirely molten (i.e., $f_{oc} = 1$), that is, the seafloor is covered entirely with the sorbet for $M_{oc} \lesssim 74M_{oc,\oplus}$ (see the text just below Eq. [2.12]). Note that discontinuities in q_{cr} or dq_{cr}/dM_{oc} found at $M_{oc} \simeq 86$ and $103M_{oc,\oplus}$ come from those in the melting curve of H_2O at the phase boundaries of ice VI/VII.

The critical heat flow exceeds $\bar{q}/2$ at $M_{oc} \simeq 139\ M_{oc,\oplus}$ ($D \simeq 160$ km), until which the effective weathering area is unity, and then increases further with ocean mass. Such an increase in q_{cr} occurs because the Rayleigh number in the HP ice layer increases. Thus, the effective weathering area decreases with ocean

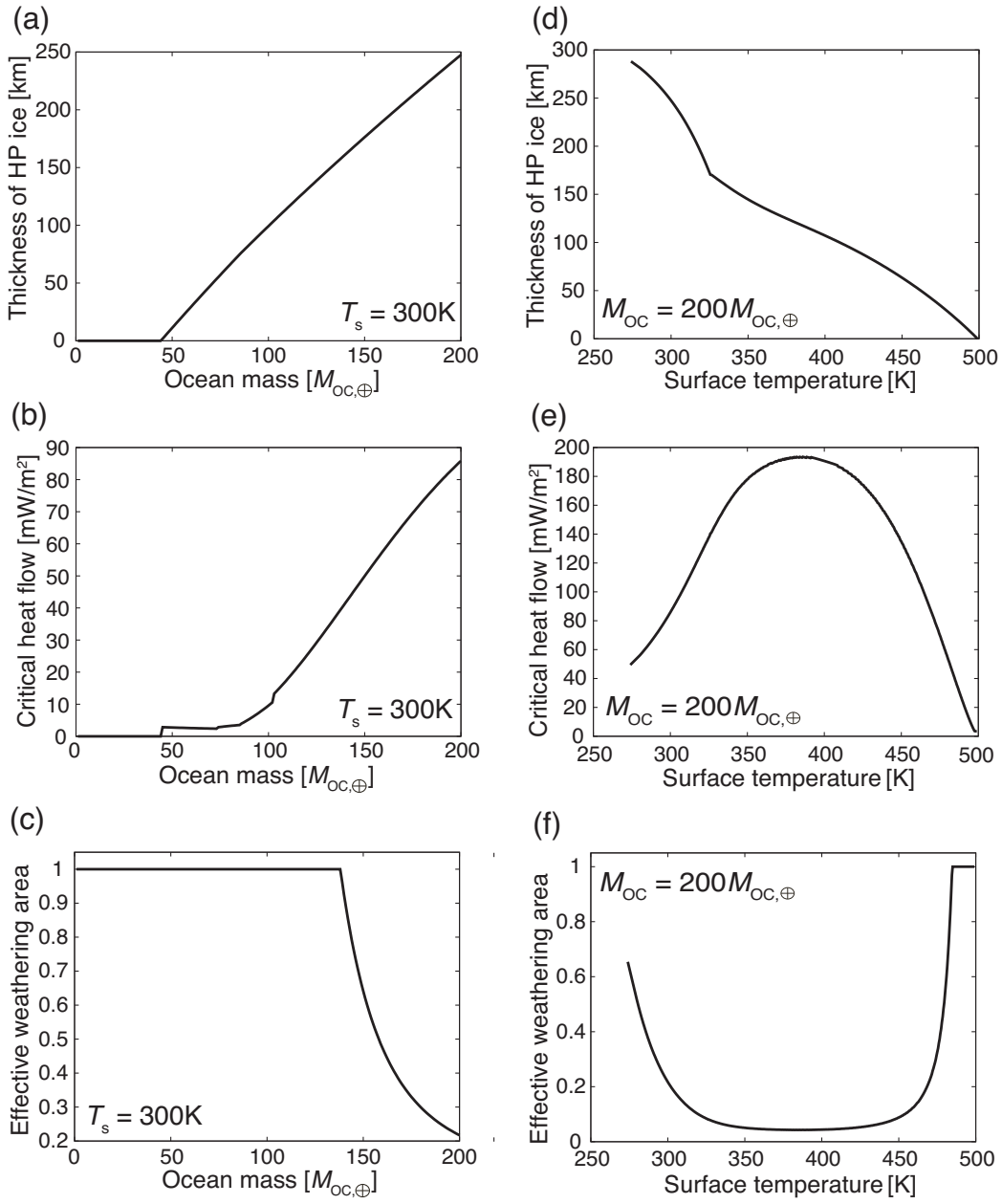

Figure 2.4: Formation of high-pressure (HP) ice and its impacts on the seafloor condition. Thickness of the HP ice layer (panels *a* and *d*), critical heat flow (panels *b* and *e*), and effective weathering area (panels *c* and *f*) are shown as a function of ocean mass M_{oc} for surface temperature $T_s = 300$ K (top) and as a function of T_s for $M_{oc} = 200M_{oc,\oplus}$ (bottom). $M_{oc,\oplus}$ represents the present Earth's ocean mass. Note that we have not used the carbon cycle model for determining T_s here, but performed calculations for given values of T_s, instead.

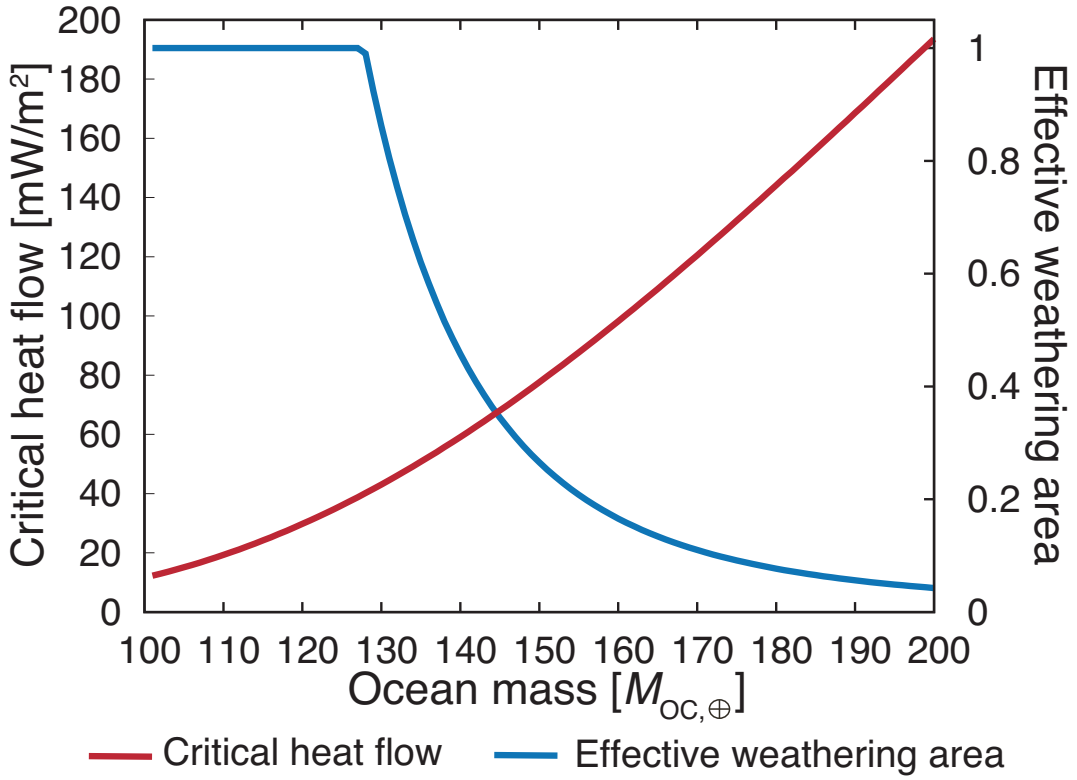

Figure 2.5: The maximum of critical heat flow (red solid line) and the minimum of effective weathering area (blue solid line) found in the surface temperature range considered in this study are shown as a function of ocean mass. In these calculations, we have assumed the mean mantle heat flux $\bar{q} = 80$ mW m^{-2}.

mass, but never becomes zero until $M_{oc} = 200 M_{oc,\oplus}$. This means that water-rock reactions between water and rock including the seafloor weathering are possible, despite the presence of the thick HP ice, because the sorbet region also exists near the mid-ocean ridge.

2.3.1.2 Dependence on Surface Temperature

The three lower panels of Fig. 2.4 show the dependence on the surface temperature for $M_{oc} = 200 M_{oc,\oplus}$. The HP ice thickness decreases, as the surface temperature increases, as shown in Fig. 2.4*d*. At $T_s \simeq 320$ K, the curve is a bit inflected. This is due to the phase change of HP ice from ice VI to ice VII.

In Figs. 2.4*e* and 2.4*f*, we find a maximum of the critical heat flow and a minimum of the effective weathering area, respectively, at $T_s \simeq 390$ K. As indicated in Eq. (2.10), q_{cr} depends on η_{BBL} and δ, both of which decrease with T_s. For $T_s \lesssim 390$ K, δ^4 decreases more rapidly than η_{BBL} and, thus, q_{cr} increases

with T_s. In contrast, for $T_s \gtrsim 390$ K, the latter dominates over the former, so that q_{cr} decreases. At $T_s \simeq 390$ K, $\partial(\eta_{BBL}/\delta^4)/\partial T_s = 0$. The behavior of the effective weathering area can be readily understood from Eq. (2.12), namely, $f_{oc} \propto q_{cr}^{-2}$. The minimum is $f_{oc} \simeq 0.04$.

In Fig. 2.5, we show the maximum of critical heat flow $q_{cr,max}$ and minimum of effective weathering area $f_{oc,min}$ as a function of ocean mass for $\bar{q} = 80$ mW m^{-2}. Here we show only the results for the case of convective HP ice for $M_{oc} > 100 M_{oc,\oplus}$ because the critical heat flow due to conduction is small. While $q_{cr,max}$ is found to monotonically increase with M_{oc}, $f_{oc,min}$ begins to drop with M_{oc} at $M_{oc} \simeq 128 M_{oc,\oplus}$, which is smaller than in the case of $T_s = 300$ K because of difference in T_s. The blue line in Fig. 2.5 indicates that even the minimum of f_{oc} is unity for $M_{oc} \lesssim 128 M_{oc,\oplus}$, which means that the HP ice is entirely molten and the seafloor is completely covered with the sorbet, regardless of surface temperature, in such an ocean mass range for the Earth-like mean mantle heat flow ($\bar{q} = 80$ mW m^{-2}). Also, $f_{oc,min} > 0$, meaning that seafloor weathering works, even if $M_{oc} = 200 M_{oc,\oplus}$.

2.3.2 Seafloor weathering enhanced by the HP ice

2.3.2.1 Consequence of carbon cycle

Here we examine the planetary climate based on the carbon cycle including the effective weathering area obtained above. The calculation results for $\bar{q} = 80$ mW m^{-2}, $\gamma = 0.19$, and $S = S_\odot$ and $0.9S_\odot$ are shown in Fig. 2.6, where (a) the surface and seafloor temperatures, (b) the seafloor weathering flux and effective weathering area, and (c) the partial pressure of atmospheric CO_2 are plotted as functions of the ocean mass. In Fig. 2.6a, two obviously different states are found: One is the state with $T_s > 273$ K, where the carbon cycle is in a steady state, the other, as indicated by a shaded area, is the state with $T_s = 273$ K, where the carbon cycle calculation is artificially stopped at $T_s = 273$ K because the surface ice is expected to form (see also § 2.2.5). The former is called the *equilibrium state* and the latter is called the *snowball state* in this study. In this case, the HP ice begins to form at $M_{oc} = 86M_{oc,\oplus}$. It turns out that the formation of the HP ice has a drastic effect on the carbon cycle and determines which state is achieved.

In the case of no HP ice (i.e., $M_{oc} < 86M_{oc,\oplus}$), both the surface temperature and CO_2 partial pressure increase with ocean mass. An equilibrium state is achieved for a given ocean mass via a negative feedback loop such that an increase in P_{CO_2} raises the surface temperature, which leads to a rise in seafloor temperature, which enhances seafloor weathering flux, which finally reduces the atmospheric CO_2. The larger the ocean mass, the larger the total carbon inventory C_{total} is (see Eq. [2.13]). Since an increase in C_{total} enhances the degassing flux of CO_2 (see Eq. [2.18]), the surface temperature consequently raises with ocean mass. This is, in other words, because the enhancement of the degassing flux dominates over the increase in seafloor temperature in the case of $\gamma = 0.19$. While the outcome depends on γ, we have confirmed that this trend is the same also in the case of one-tenth of the Earth-like value γ (= 0.019) and comet-like γ (= 0.71) higher than the Earth's: The equilibrium values of T_s and P_{CO_2} for $M_{oc} < 86M_{oc,\oplus}$ are increased up to 326 K and 2.4×10^{-1} bars for $\gamma = 0.19$ and $S_\odot$, respectively (see Figs. 2.6a and 2.6c).

In contrast, when the HP ice is present ($M_{oc} \geq 86M_{oc,\oplus}$), the negative feedback never works and, consequently, the snowball state is attained. This is because the seafloor temperature on the area under the sorbet region, where seafloor

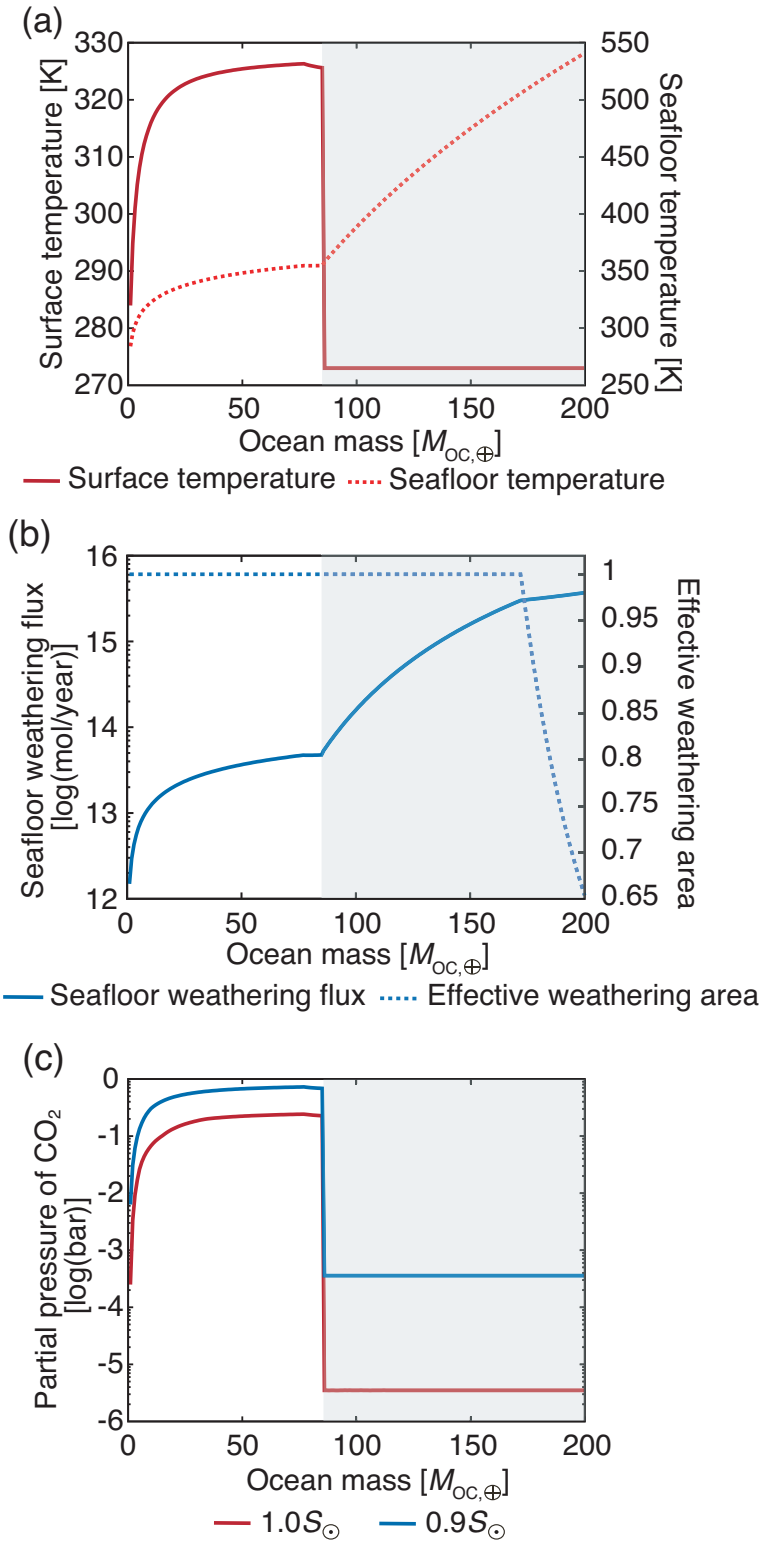

Figure 2.6: Surface and seafloor conditions obtained from the carbon cycle model: (*a*) Surface temperature (red sold line) and seafloor temperature (red dashed line), (*b*) seafloor weathering flux (blue solid line) and effective weathering area (blue dashed line), and (*c*) partial pressure of CO_2 are shown as a function of ocean mass in the unit of the Earth's ocean mass $M_{oc,\oplus}$. Shaded is the range for the snowball state. In this calculation, the mean mantle heat flow is assumed to be 80 mW m^{-2}. The symbol $S_\odot$ represents the solar insolation received by the present Earth.

weathering works, is fixed at the melting temperature of ice and, thus, insensitive to the surface temperature. Although the reduction in effective weathering area reduces seafloor weathering rate (see Fig.2.6*b*), it is found to have little impact on surface temperature because the seafloor weathering flux is significantly higher than the degassing flux.

2.3.2.2 Dependence on stellar insolation

We examine the dependence of planetary climate on stellar insolation. Since the runaway greenhouse limit, which controls the inner edge of the habitable zone, is only slightly higher than $S_\odot$ (e.g., $1.06S_\odot$ Kopparapu et al., 2013), we show only the results for smaller stellar insolation of $0.9S_\odot$ than the fiducial value of $1.0S_\odot$. As shown in Fig. 2.6*c*, stellar insolation affects CO_2 partial pressure both in the equilibrium and snowball states: the smaller the stellar insolation, the higher the CO_2 pressure is, as a whole: P_{CO_2} for $S = 0.9S_\odot$ is higher by a factor of $\sim$ 3 and by two orders of magnitude than that for $S = 1.0S_\odot$ in the equilibrium and snowball states, respectively. The other quantities are almost unaffected by stellar insolation. This is because the increase in CO_2 pressure compensates for the decline in stellar insolation so as not to change the surface temperature which controls weathering behavior and COM-HP in our climate model. Thus, variation in stellar insolation has little impact on planetary climate, provided the planet is located in the habitable zone.

2.3.2.3 Dependence on mean mantle heat flow

Next, we examine what impact the mean mantle heat flow $\bar{q}$ has on the surface and seafloor conditions. Figure 2.7 shows (*a*) the surface temperature, (*b*) effective weathering area, and (*c*) seafloor weathering flux for five different choices of $\bar{q}$. The variation in mean mantle heat flow turns out to yield no change on the overall behavior, but quantitative modifications to the ocean mass dependence.

First, as seen in Fig. 2.7*a*, when no HP ice is present, the larger the mean mantle heat flow, the higher the surface temperature is for a given ocean mass. The variation in $\bar{q}$ leads to a large difference in the surface temperature (up to 40 K). Also, the surface condition lapses into the snowball state at larger ocean mass for a larger $\bar{q}$. That is because as $\bar{q}$ increases, the seafloor spreading rate A_S increases (see Eq. [2.21]) and, thus, the degassing flux increases (see Eq. [2.18]),

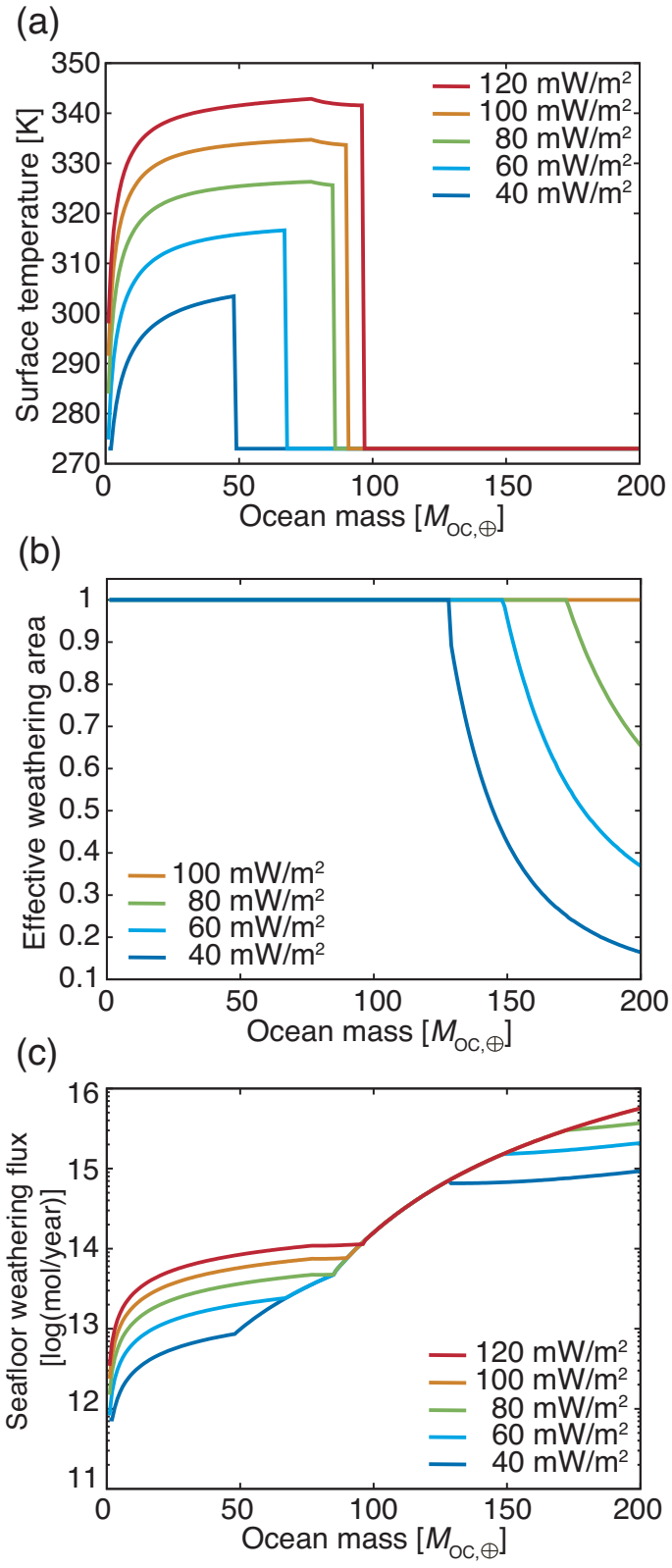

Figure 2.7: Surface and seafloor conditions obtained from the carbon cycle model for five different values of the mean mantle heat flow. (*a*) Surface temperature, (*b*) effective weathering area and (*c*) seafloor weathering flux are shown as functions of ocean mass.

leading to higher surface temperature and larger critical ocean mass for forming the HP ice (COM-HP, see also Fig. 2.1). In Fig. 2.7*c*, the seafloor weathering flux is also found to increase by approximately an order of magnitude in response to the rise in the degassing flux.

As shown in Fig. 2.7*b*, the effective weathering area $f_{\rm oc}$ starts to decrease from unity at larger ocean mass for larger mean mantle heat flow and is always unity until $M_{\rm oc} = 200 M_{\rm oc,\oplus}$ for $\bar{q} \geq 100$ mW m^{-2}. While the seafloor weathering flux changes with $\bar{q}$ (i.e., $f_{\rm oc}$) in the case with HP ice, the reduction in $f_{\rm oc}$ turns out to have only a small effect on the surface temperature, because of significantly high seafloor weathering rate for any value of $\bar{q}$ (see Fig. 2.7*c*).

2.3.2.4 Dependence on CO_2/H_2O ratio and formulation of seafloor weathering

As described in section 2.2.3, the carbon cycle depends on the total carbon inventory and seafloor weathering rate. The former may differ greatly from planet to planet, as suggested, for example, by a difference in the CO_2/H_2O molar ratio γ (Eq. [2.13]) between comets and the Earth. Also, the seafloor weathering rate is in general uncertain, mainly because the activation energy $E_{\rm a}$ (Eq. [2.22]) and the present Earth's weathering rate $F^*_{\rm SW}$ are poorly determined observationally. Here we investigate the sensitivities of the planetary climate to γ, $F^*_{\rm sw}$ and $E_{\rm a}$ with focus on the critical ocean mass, beyond which the planetary climate is in the snowball state (hereafter, abbreviated to COM-SB and denoted by $M_{\rm oc}^{\rm cr(sb)}$).

In Fig. 2.8, we plot the relationships between $M_{\rm oc}^{\rm cr(sb)}$ and total degassing flux, $F_{\rm D} + F_{\rm M}$, for various values of γ between 7.4×10^{-3} and 2.1; both $M_{\rm oc}^{\rm cr(sb)}$ and $F_{\rm D} + F_{\rm M}$ are obtained from the carbon cycle calculations. Here we assume $\bar{q} = 80$ mW m^{-2}. Fig. 2.8 shows the fiducial case with $E_{\rm a} = 41$ kJ mol^{-1}; For reference, in Fig. 2.8, we show the relationships between $F_{\rm D} + F_{\rm M}$ and not $M_{\rm oc}^{\rm cr(sb)}$ but $M_{\rm oc}$ for three different values of γ by dashed lines (the result for $\gamma = 0.19$ is also shown in Fig. 2.6*b*). In Fig. 2.8, we can see that the total degassing flux increase almost linearly with γ for a given ocean mass. For $\gamma < 7.4 \times 10^{-3}$, the COM-SB is absent because the snowball state is achieved in all the ocean mass range due to low degassing flux.

As shown in Fig. 2.8, the total degassing flux has a peak at $M_{\rm oc}^{\rm cr(sb)} = 128 M_{\rm oc,\oplus}$. For $M_{\rm oc}^{\rm cr(sb)} \leq 128 M_{\rm oc,\oplus}$, the COM-SB increases from 24 to 128 $M_{\rm oc,\oplus}$ and the total

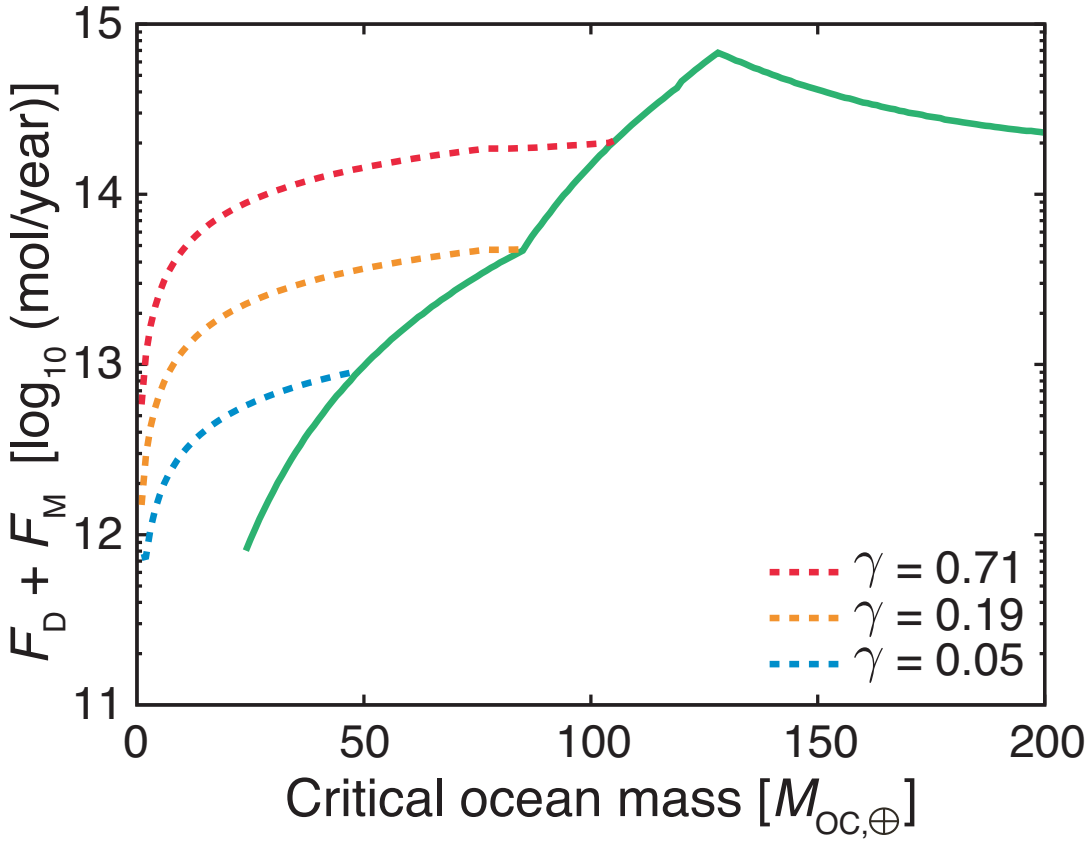

Figure 2.8: Relationship between the critical ocean mass for the snowball state (COM-SB) and the total-degassing flux $F_D + F_M$ (solid lines) for different choices of the CO_2/H_2O molar ratio in the source of volatiles, γ (see Eq. [2.13]). The figure shows the fiducial case with $E_a = 41$ kJ mol^{-1}. For reference, dashed lines represent the relationship between $F_D + F_M$ and not the COM-SB, but just the ocean mass for three different values of γ when the planetary climate is in an equilibrium state. On the right side of the solid lines, the sorbet is present in the deep ocean. In these calculations, we have assumed the mean mantle heat flux $\bar{q} = 80$ mW m^{-2}.

degassing flux, which is determined by $F_{SW}(T_{floor}, f_{oc}) = F_{SW}(T^{mel}_{floor}, 1)$, increases from 8.1×10^{11} to 6.8×10^{14} mol yr^{-1} with increase in γ from 7.4×10^{-3} to 2.1. Despite order-of-magnitude variation in $F_D + F_M$, the COM-SB varies moderately by a factor of $\sim$5 (see section 2.4.1 for an analytical interpretation). On the other hand, for $M^{cr(sb)}_{oc} > 128 M_{oc,\oplus}$, the total degassing flux is determined by the minimum weathering flux with the HP ice, namely $F_{SW}(T_{floor}, f_{oc}) = F_{SW}(T^{mel}_{floor}, f_{oc,min})$ (see Fig. 2.5 for $f_{oc,min}$). Thus, the COM-SB increases from 128 to $200 M_{oc,\oplus}$ and the total degassing flux decreases from 6.8×10^{14} to 2.3×10^{14} mol yr^{-1} with

decrease in γ from 2.1 to 5.2×10^{-1}. In this diagram, equilibrium climates ($F_{\rm SW} = F_{\rm D} + F_{\rm M}$) are achieved on the side above the solid line, whereas the planetary surface condition lapses into snowball states ($F_{\rm SW} > F_{\rm D} + F_{\rm M}$), because of the presence of the sorbet region, on the side below the solid line. Note the curve of $M_{\rm oc}^{\rm cr(sb)}$ is a bit inflected at $M_{\rm oc} = 85 M_{\rm oc,\oplus}$ because of a phase change of the HP ice.

In Fig, 2.9, we show the impact of $F_{\rm SW}^*$ and $E_{\rm a}$ on $M_{\rm oc}^{\rm cr(sb)}$. Fig. 2.9*a* shows cases with three different values of $F_{\rm SW}^*$. As expected, the smaller $F_{\rm SW}^*$ is, the larger $M_{\rm oc}^{\rm cr(sb)}$ is. This is because small $F_{\rm SW}^*$ results in small minimum weathering flux with the HP ice for a given ocean mass. However, the overall shapes of curves are similar. Furthermore, the figure shows that the dependence of $M_{\rm oc}^{\rm cr(sb)}$ on $F_{\rm SW}^*$ is almost opposite dependence of the total degassing flux (see section 2.4.1). Thus, $M_{\rm oc}^{\rm cr(sb)}$ is rather insensitive to $F_{\rm SW}^*$ and choice of $F_{\rm SW}^*$ is a small influence on results.

In Fig. 2.9*b*, we show cases with three different values of $E_{\rm a}$. The curve for larger $E_{\rm a}$ is found to be steeper. The three curves cross each other at $F_{\rm D} + F_{\rm M} = 2.0 \times 10^{12}$ mol yr^{-1}, where the seafloor temperature $T_{\rm floor}$ is equal to T_0 (=289 K), so that $F_{\rm SW}$ is independent of $E_{\rm a}$ (see Eq. [2.22]). Above the crossover point, the higher the activation energy, the smaller the COM-SB is; its dependence is opposite below the crossover point. Although being large relative to that on γ, the dependence of $M_{\rm oc}^{\rm cr(sb)}$ on $E_{\rm a}$ is at most linear. Thus, it would be fair to say that $M_{\rm oc}^{\rm cr(sb)}$ is rather insensitive to $E_{\rm a}$. We further discuss the nature of the COM-SB analytically in section 2.4.1.

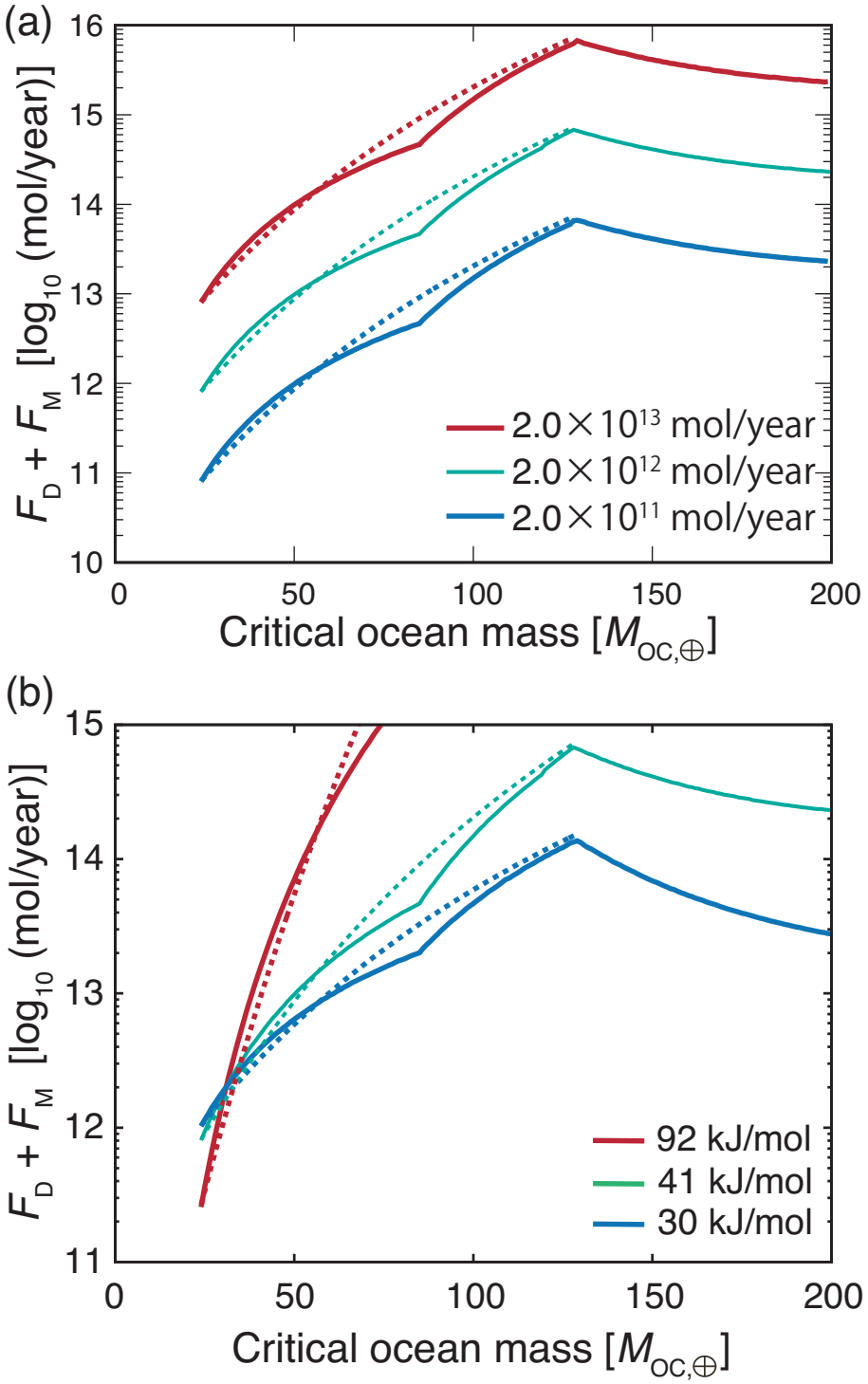

Figure 2.9: Relationship between the critical ocean mass for the snowball state (COM-SB) and the total-degassing flux $F_D + F_M$ for different choices of the normalized constant of the seafloor weathering, F^*_{SW}, and the seafloor weathering activation energy, E_a (see Eq. [2.22]). Panel (*a*) shows the critical ocean masses with $E_a = 41$ kJ mol^{-1} for there different values of F^*_{SW}. Panel (*b*) compares the results with $F^*_{SW} = 2.0 \times 10^{12}$ mol yr^{-1} for three different values of E_a. Dashed lines represent the analytical solutions of COM-SB (see Eq. [2.39]). On the right side of the solid lines, the sorbet is present in the deep ocean. In these calculations, we have assumed the mean mantle heat flux $\bar{q} = 80$ mW m^{-2}.

2.4 Discussion

2.4.1 Critical ocean mass for snowball state

One of the most important findings in this study is that there is a critical ocean mass, beyond which an ocean terrestrial planet has an extremely cold climate (i.e., the snowball state). Furthermore, we have found that the COM-SB, $M_{\rm oc}^{\rm cr(sb)}$, falls into a relatively narrow range between 20 and 100 $M_{\rm oc,\oplus}$. Here we give an interpretation to the low sensitivity of $M_{\rm oc}^{\rm cr(sb)}$ to the planetary mass $M_{\rm p}$, the total degassing flux $F_{\rm D}+F_{\rm M}$, and the activation energy of seafloor weathering $E_{\rm a}$, by deriving an approximate solution for $M_{\rm oc}^{\rm cr(sb)}$. This could help us obtain an integrated view of planetary climate on ocean planets under our idealized seafloor environments.

As demonstrated in section 2.3.2, the planetary climate lapses into the extremely cold one, when HP ice is formed on the seafloor. Then, the seafloor temperature $T_{\rm floor}$ is fixed at the melting temperature $T^{\rm mel}$ and thus determined uniquely by the seafloor pressure $P_{\rm floor}$. Since the ocean mass and depth are negligibly small relative to the planetary mass and radius, respectively, under hydrostatic equilibrium, the seafloor pressure is given approximately by

$$P_{\rm floor} \approx \frac{GM_{\rm p}}{4\pi R_{\rm p}^4} M_{\rm oc} = \frac{G\bar{\rho}_{\rm p}}{3R_{\rm p}} M_{\rm oc}, \tag{2.37}$$

where $R_{\rm p}$ and $\bar{\rho}_{\rm p}$ are the planetary radius and mean density, respectively. For $M_{\rm oc} = M_{\rm oc}^{\rm cr(sb)}$, $P_{\rm floor}$ corresponds to the crossover pressure between the adiabat and the melting curve, both of which are independent of planetary mass. Thus, from Eq. (2.37), $M_{\rm oc}^{\rm cr(sb)} \propto R_{\rm p}^4/M_{\rm p}$. According to Valencia et al. (2007a), the mass-radius relationship for Earth-like planets is $R_{\rm p} \propto M_{\rm p}^{0.262}$, which yields $M_{\rm oc}^{\rm cr(sb)} \propto M_{\rm p}^{0.048}$. This indicates that the COM-SB is insensitive to planetary mass; indeed, between $M_{\rm p} = 1M_\oplus$ and $10M_\oplus$, for example, $M_{\rm oc}^{\rm cr(sb)}$ differs only by ∼12%.

To derive the dependence of $M_{\rm oc}^{\rm cr(sb)}$ on $F_{\rm D}+F_{\rm M}$ and $E_{\rm a}$, we consider seafloor weathering. In the equilibrium state, since $F_{\rm SW}(T_{\rm floor}) = F_{\rm D}+F_{\rm M}$, $T_{\rm floor}$ is given as a function of $F_{\rm D}+F_{\rm M}$ (see Eq. [2.22]). Also, $T_{\rm floor} = T^{\rm mel}$, when $M_{\rm oc} = M_{\rm oc}^{\rm cr(sb)}$: From Eq. (2.4),

$$T^{\rm mel} \simeq c_1 + c_2 P_{\rm floor}, \tag{2.38}$$

where $c_1 = 236$ K, $c_2 = 6.09\times10^{-8}$ K Pa^{-1}. From Eqs. (2.22)–(2.38), $M_{\rm oc}^{\rm cr(sb)}$ is

expressed as

$$M_{\rm oc}^{\rm cr} = \frac{3R_{\rm p}}{c_2 G\bar{\rho}_{\rm p}} \left\{ \frac{T_0}{1 - \frac{RT_0}{E_{\rm a}} \ln\left(\frac{F_{\rm D}+F_{\rm M}}{f_{\rm oc}F_{\rm SW}^*}\right)} - c_1 \right\}. \tag{2.39}$$

This equation confirms that the COM-SB depends on $F_{\rm D}+F_{\rm M}$ and $F_{\rm SW}^*$ only weakly. Also, since the denominator of the first term must be positive, the sensitivity of $M_{\rm oc}^{\rm cr(sb)}$ to $E_{\rm a}$ turns out to be small. In Fig. 2.9, we plot the relationships between $M_{\rm oc}^{\rm cr(sb)}$ and $F_{\rm D}+F_{\rm M}$ calculated from Eq. (2.39), which is found to reproduce the numerical results well, except for the effect of phase change of the HP ice.

2.4.2 Effect of supply limit of cations

As shown in section 2.3.2, without any limit to seafloor weathering, the presence of the HP ice (exactly to say, the sorbet) always enhances seafloor weathering, resulting in extremely cold climates (i.e., the snowball states). In reality, however, the seafloor weathering rate is limited by the number of cations available in the oceanic crust. This is because seafloor weathering occurs through hydrothermal circulation in the oceanic crust and thus the amount of cations available depends on the depth of hydrothermal circulation. This limit to seafloor weathering rate, which we call the supply limit, $F_{\rm SW}^{\rm limit}$, can be given by (Sleep et al., 2001; Foley, 2015)

$$F_{\rm SW}^{\rm limit} = \frac{x}{m_{\rm c}} \rho_{\rm rock} d_{\rm hy} A_{\rm S}, \tag{2.40}$$

where x is the number fraction of cations (Ca^{2+}, Mg^{2+}, and Fe^{2+}) in the oceanic crust, $m_{\rm c}$ is the averaged molar mass of cation, $\rho_{\rm rock}$ is the density of the oceanic crust, $d_{\rm hy}$ is the depth at which hydrothermal carbonation occurs, and $A_{\rm S}$ is the seafloor spreading rate. In the present Earth condition, where $x = 0.3$, $m_{\rm c} = 55$ g mol^{-1}, $\rho_{\rm rock} = 2800$ kg m^{-3} and $d_{\rm hy} = 500$ m (Sleep et al., 2001), $F_{\rm SW}^{\rm limit} = 7.6 \times 10^6 A_{\rm S}$.

If the total degassing flux is higher than the supply limit, the atmospheric CO_2 continues to increase with age. Qualitatively, the more the atmospheric CO_2, the higher the surface temperature is. While climate sensitivity to the amount of CO_2 is unclear for high P_{CO_2} because of poor understanding of radiative forcing of water vapor for hot atmospheres, recent 1-D radiative-convective calculations show that $T_{\rm s} > 350$ K for $P_{CO_2} >$ several bars, provided the stellar

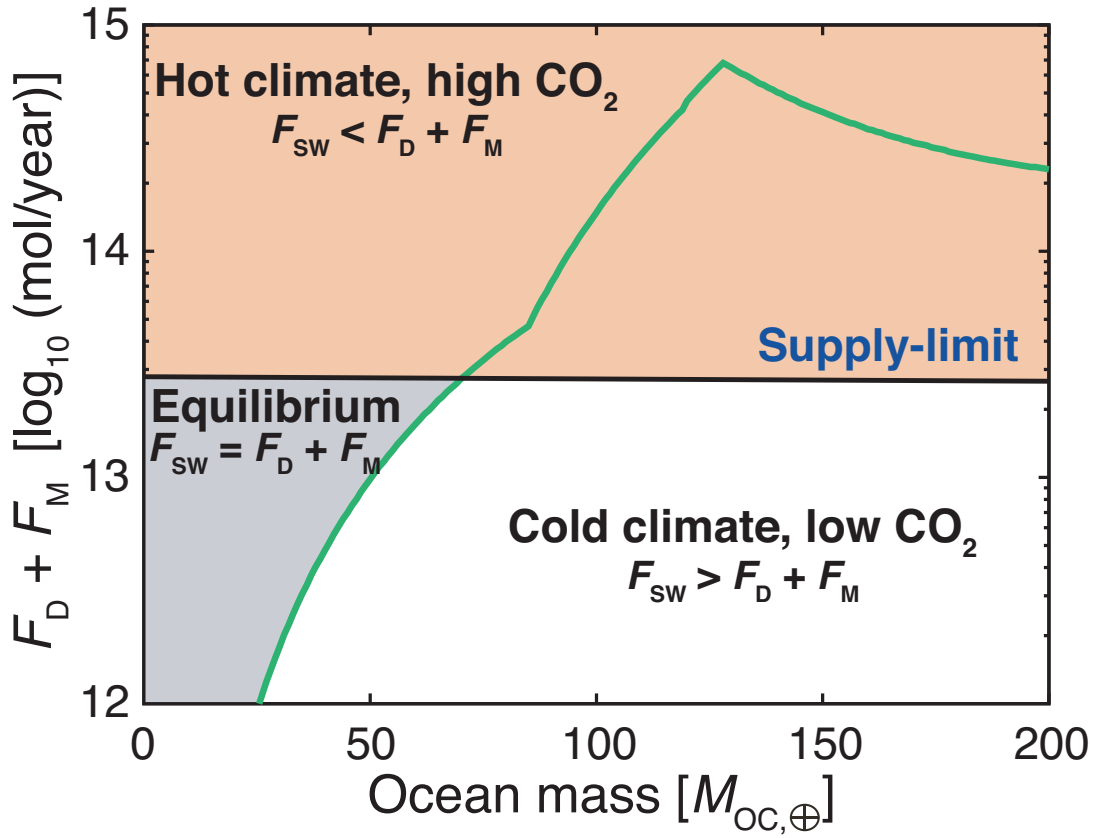

Figure 2.10: Climate diagram that shows different climate regimes on the plane of the total degassing flux ($F_{\rm D}+F_{\rm M}$) vs. ocean mass. The horizontal black solid line represents the supply limit above which seafloor weathering $F_{\rm SW}$ is limited by the insufficient supply of cations (see Eq. [2.40]). The green solid line corresponds to the critical ocean mass (COM-SB), namely, the boundary between the equilibrium states and the extremely cold (snowball) states that would be achieved if no supply limit were assumed, same as that in Fig. 2.8 *a*. In this calculation, we have assumed the mean mantle heat flux $\bar{q}=80$ mW m^{-2} and activation energy $E_{\rm a}=41$ kJ mol^{-1}.

insolation is equal to that for the present Earth (Wordsworth & Pierrehumbert, 2013; Ramirez et al., 2014).

Figure 2.10 is the climate diagram for $\bar{q}=80$ mW m^{-2} and $E_{\rm a}=41$ kJ mol^{-1}, where we indicate three different climate regimes, which include the equilibrium climates, the extremely cold climates (or the snowball states), and the extremely hot climates. The extremely hot climate is a state such that $F_{\rm SW}<F_{\rm D}+F_{\rm M}$, because of supply limit so that CO_2 accumulates in the atmosphere. The supply limit (horizontal black solid line) is calculated from Eq. (2.40). The bound-

ary between the equilibrium-climate and cold-climate regimes (green line) corresponds to the COM-SB shown in Fig. 2.8*a*. Of importance here is that the total degassing flux at the COM-SB is always higher than the supply limit for $M_{\rm oc} > 70 M_{\rm oc,\oplus}$. Thus, for $M_{\rm oc} > 70 M_{\rm oc,\oplus}$, the planet has no equilibrium climate (i.e., extremely hot or cold climate) because of the enhanced seafloor weathering and the supply limit.

Here we give a brief discussion about the uncertainty in the supply limit. Although the mean mantle heat flow $\bar{q}$, which determines the seafloor spreading rate $A_{\rm S}$ and thus the supply limit $F_{\rm SW}^{\rm limit}$, decreases with age during planetary evolution, its decrement on a timescale of billion years is known to be similar to the mean mantle flow for Earth-like planets with age of several billion years (McGovern & Schubert, 1989). Also, we have adopted the solidus temperature of rock for $T_{\rm sol}$ in Eq. (2.11), instead of the potential temperature of the mantle, which leads to overestimating the supply limit approximately by a factor of 2 in the case of $T_{\rm sol} = 2000$ K, which corresponds to the potential temperature at hot initial states (e.g., Tajika & Matsui, 1992). In addition, in the equilibrium states, the effects of variation in seafloor spreading rate are canceled out, because both of the supply limit and degassing flux have a linear dependence on seafloor spreading rate (Eqs. [2.18] and [2.40]). Thus, the uncertainty in $\bar{q}$ has a small influence on the climate diagram for ocean planets.

The hydrothermal carbonation depth $d_{\rm hy}$ would depend on ocean mass. Some experiments suggest that the hydrothermal carbonation depth decreases with increasing seafloor pressure because thermal cracking becomes weaker (Vance et al., 2007). Thus, the supply limit is expected to decrease with ocean mass, which would extend the domain of the extremely hot climate in Fig. 2.10.

In conclusion, the enhanced seafloor weathering due to the formation of the sorbet region and the supply limit narrow the range of ocean mass of terrestrial planets with the equilibrium climates. This implies the difficulty of clement climates, like the present Earth, on ocean planets with plenty of water.

2.4.3 Caveats

2.4.3.1 Ocean Layer Model

Here we discuss the validity of our assumptions regarding the ocean layer, which include: (1) No boundary layer exists at the top of the HP ice layer; (2) The

carbon partitioning between the atmosphere and ocean is always in equilibrium and the CO_2 content is constant through the sorbet region; and (3) The heat transport occurs in the vertically one dimension.

(1) Regarding convective transport in the HP ice, we have considered the presence of a thermal boundary layer at the bottom, but not at the top. To evaluate the effect of the top boundary layer (TBL) on the effective weathering area f_{oc}, we have calculated f_{oc} in the same settings as in Fu et al. (2010), who considered TBL in addition to a bottom boundary layer (BBL). Then, we have found that TBL leads to reducing the effective weathering area in the low surface temperature domain for a given ocean mass (e.g., $T_s \lesssim 390$ K for $M_{oc} = 200 M_{oc,\oplus}$, see also Fig. 2.4*f*). This is because BBL is cooler and thicker without TBL than in the case with TBL. As discussed in section 2.3.1.2, in this domain, the reduced thickness of BBL, δ, increases the critical heat flow (Eq. [2.10]) and, thus, reduces the effective weathering area (Eq. [2.12]). However, we have also found that the presence of TBL brings about little change in the maximum of q_{cr} at a given ocean mass (Fig. 2.5). This is because the same temperature gradient in BBL is achieved by a change in T_s, given that TBL is assumed to follow the melting line of ice (see Fig.2 in Fu et al., 2010). Hence, the climate diagram for ocean planets is almost unaffected by the presence of TBL.

(2) We have assumed that the CO_2 circulation in the sorbet region occurs efficiently enough that carbon partitioning between the atmosphere and ocean remains in equilibrium. However, the CO_2 circulation (not the seafloor weathering) limits the consumption of atmospheric CO_2, if being slower than the response of the carbon budget in the ocean-atmosphere system. The latter is controlled by regassing in the environments of interest in this study, although depending on degassing, in general (Tajika & Matsui, 1992); thus, its timescale is $\sim \tau/\beta$.

The CO_2 circulation occurs in the following way: Aqueous CO_2 converts to CO_2 ice quickly within the HP ice (Bollengier et al., 2013) and, then, the CO_2 ice moves together with the HP ice. In the HP ice layer, since the upward sorbet flow transports mass (and heat), the HP ice sinks accordingly for mass conservation. Below we estimate the sinking speed of the

HP ice and the overturn timescale of the HP ice layer from energy balance and mass conservation.

When heat is transported by thermal diffusion and sorbet flow, the energy balance is expressed as

$$Q = -k\frac{dT}{dr} + \chi\rho_{\rm l}(L + C_{\rm P}\Delta T_{\rm HP})w_{\rm l}, \tag{2.41}$$

where Q is the heat flux from the oceanic crust, χ is the melt fraction, L is the latent heat of HP ice, and $\rho_{\rm l}$, $C_{\rm P}$, and $w_{\rm l}$ are the density, specific heat, and flow speed of liquid water in the sorbet, respectively. The first and second terms on the right side represent the thermal conduction and melt advection, respectively. Note that we have assumed that permeable flow of liquid dominates the sorbet flow and, namely, neglected upwelling solid flow, which results in underestimating the sinking flux of the HP ice. From mass conservation and Eq. (2.41), the sinking speed of the HP ice, $w_{\rm HP}$, against the upwelling sorbet flow is given by

$$w_{\rm HP} = \frac{\chi\rho_{\rm l}}{(1-\chi)\rho_{\rm HP}}w_{\rm l} = \frac{Q + k\frac{dT}{dr}}{(L + C_{\rm P}\Delta T_{\rm HP})(1-\chi)\rho_{\rm HP}}, \tag{2.42}$$

where $\rho_{\rm HP}$ is the density of the HP ice. The thermal conduction flux along the melting curve is $-kdT/dr \approx 10$ mW m^2 (see Fig. 2.4*b*). The heat flux from the oceanic crust of 80 mW m^{-2} being added, $Q + kdT/dr \approx$ 70 mW m^{-2}. The material properties of liquid water and HP ice are $\rho_{\rm HP}$ = 1400 kg m^{-3}, $L = 4.2 \times 10^5$ J kg^{-1} (at 300 K from Dunaeva et al., 2010), and $C_{\rm P} = 4.1 \times 10^3$ J kg^{-1} K^{-1} (at 300 K from Waite et al., 2007).

For terrestrial sea ice, permeability decreases abruptly for melt fraction below $\chi = 5$ % (Golden et al., 1998). Although not known well for the HP ice, we assume that the HP ice behaves in a similar way and use χ = 5 %. According to our calculation results, $\Delta T_{\rm HP} = 78$ K and $D = 99$ km for $M_{\rm oc} = 100\ M_{\rm oc,\oplus}$ and $T_{\rm s} = 300$ K. Then, the overturn timescale of the HP ice ($\equiv D/w_{\rm HP}$) comes out to be 44 Myr. Even for the $M_{\rm oc} = 200 M_{\rm oc,\oplus}$, $D/w_{\rm HP} = 203$ Myr. On the other hand, $\tau/\beta \sim 250$ Myr for the present Earth's condition, using the value of τ for the present Earth (~ 100 Myr) (Turcotte & Schubert, 2002). Thus, the CO_2 circulation occurs faster than the response of the carbon budget in the atmosphere-ocean system.

The above estimate may remain to be refined. For example, using the relation between the Nusselt number (Nu) and the Rayleigh number, $Nu \propto$

$Ra^{1/3}$, (Turcotte & Schubert, 2002), the semi-infinite half-space cooling model shows that the residence timescale τ is $\propto \eta_{\rm man}^{2/3}$, where $\eta_{\rm man}$ is a viscosity of the mantle material, and, thus, depends strongly on mantle temperature and water content in the mantle. Indeed, the residence timescale is thought to have varied by an order of magnitude during the thermal evolution of the Earth (Tajika & Matsui, 1992). Also, seafloor weathering would be limited, if the planet has a thick HP ice and vigorous convective mantle. However, it is emphasized here that given a weak dependence of the COM-SB even a sluggish circulation of CO_2 in the HP ice could yield no significant change in COM-SB.

(3) We have assumed a vertically one-dimensional structure of the ocean and thus considered only vertical heat transport. In reality, the thermal structure of the ocean is more complicated because of convective patterns and inhomogeneous phase change. First, since the distance between the mid-ocean ridge and trench ($\gtrsim$ 10000 km) is much larger than the thickness of the HP ice (100 km), with which the size of convective cells is comparable (e.g., Turcotte & Schubert, 2002), detailed convective patterns matter little for the overall heat transfer in the HP ice layer. In addition, hydrodynamical simulations show a heat-pipe structure of the HP ice layer for high heat fluxes from the oceanic crust, which means phase change rarely occurs vertically throughout the ocean (Choblet et al., 2017; Kalousová et al., 2018).

2.4.3.2 Atmospheric model

Our climate modeling has demonstrated that the runaway cooling due to atmospheric CO_2 drawdown generally occurs on ocean planets with plate tectonics, provided $M_{\rm oc} > M_{\rm oc}^{\rm cr(sb)}$. Although we assume the runaway cooling ends up with the snowball state with $T_{\rm s} < 273$ K, it is to be examined more carefully whether the global snowball state is achieved or not. Here we discuss some uncertainties of the atmospheric model.

We have assumed a constant surface albedo of 0.32. Planetary albedo depends on cloud radiative forcing that generally depends on $T_{\rm s}$ (e.g., Wolf & Toon, 2013, 2015). As far as partially ice-covered planets are concerned, simulations based on 3-D general circulation models (GCMs) for the Archean Earth (Wolf &

Toon, 2013) and ocean planets (Charnay et al., 2017) demonstrate that planetary albedo increases rapidly with decreasing T_s due to the ice-albedo feedback, although the contribution of clouds to planetary albedo declines. This means that the assumed surface albedo of 0.32 is an underestimate for the planetary albedo for cold climates of interest in this study and thereby leads to overestimating T_s. This indicates that the runaway cooling results in the snowball state, even if the planet receives high stellar insolation comparable to the present Earth.

Also, we have assumed that the distribution of relative humidity in the atmosphere is the same as that in the present Earth's atmosphere. Wordsworth & Pierrehumbert (2013) and Ramirez et al. (2014) found multiple equilibrium solutions for a CO_2-free, almost water-saturated atmosphere, including a hot solution with the surface temperature of $\sim$ 500 K, even if stellar insolation is comparable to the present Earth's stellar insolation. This suggests that the snowball state is not always achieved. However, GCM simulations show that atmospheric circulation leads to precipitation and thereby to removing water vapor from the atmosphere, namely, making unsaturated regions even if stellar insolation is close to the runaway greenhouse limit (Wolf & Toon, 2015). This suggests that such a hot state would be unlikely to occur, although more work is needed to confirm so.

2.4.3.3 Carbon cycle model

In this study we have ignored the situation where the atmosphere is so cold that the surface of the ocean is frozen and, instead, have stopped calculations once the surface temperature reaches 273 K. Here we discuss the effect of surface ice on the carbon cycle and warming process in the snowball state. When the surface ice is convectively stable, which is appropriate for Earth-like high heat fluxes and moderately low surface temperatures (Fu et al., 2010), molecular diffusion in the surface ice would control the exchange of CO_2 between the atmosphere and ocean. Performing molecular dynamics simulations, Ikeda-Fukazawa et al. (2004) estimated that CO_2 molecular diffusion coefficient in H_2O ice is $\sim 10^{-10}$ m^2 s^{-1} at 270 K. For the thickness of surface ice of 1 km, for example, the diffusion timescale is on the order of Gyr. This means that even for a degassing flux higher than the critical value shown in Fig.2.8, CO_2 accumulation in the atmosphere proceeds too slowly for the climate to escape from the snowball state. This indicates that the snowball state we have found is maintained on a timescale of

Gyr. We have to keep in mind, however, that it still remains a matter of debate how past Earth escaped from the snowball state.

On the other hand, the seafloor weathering is thought to be insensitive to the existence of surface ice, as follows. The seafloor temperature is fixed at the melting temperature of the ice in the snowball solutions. Since surface ice has a steep conductive temperature gradient and thus the thickness is small relative to the whole ocean, the T-P structure below the surface ice is rather insensitive to the surface temperature, thereby having little effect on the seafloor pressure and temperature. Thus, the seafloor weathering flux is proportional to the effective weathering area. The latter increases with decreasing the surface temperature in the low surface temperature regime shown in Figure 2.4f. Thus, beyond the critical ocean mass, the seafloor weathering would be higher than the degassing flux, even if the surface ice is formed. Thus, once being achieved by the runaway cooling, the snowball state is maintained.

2.4.4 Exoplanet

Finally, we discuss an application of our findings to terrestrial exoplanets. Although we have no enough knowledge of the degassing flux of exoplanets, which depends on several uncertain factors such as planetary carbon budget, thermal structure of planetary interior, and ocean mass, we have found that the COM-SB is less sensitive to the degassing flux. As shown in Fig. 2.8a, terrestrial exoplanets with oceans of more than several tens of $M_{\mathrm{oc},\oplus}$ in the habitable zone have extremely cold climates. Cold climates are also suggested for Earth-like planets with low degassing flux in the habitable zone (e.g., Kadoya & Tajika, 2014). Thus, terrestrial planets with CO_2-poor cold climates would not be uncommon in the habitable zone around Sun-like stars, provided plate tectonics is common for those planets.

Recently, habitability for planets around ultra cool stars (e.g., Proxima Centauri and TRAPPIST-1) are actively debated (e.g., Ribas et al., 2016a; Turbet et al., 2018; Valencia et al., 2018). Since the snowline is located near the habitable zone and ice-rich planets readily migrate from beyond, ocean planets would be abundant in the habitable zone around cool stars (e.g., Tian & Ida, 2015). Cool stars emit their radiation at a longer wavelength, which can strongly affect the planetary albedo (e.g., Shields et al., 2013b). We performed the additional simulation of the atmospheric model for the planet around cool stars, using a

spectrum of M-type star of AD Leo (Segura et al., 2005). The simulation is performed for $S = 0.8S_{\odot}$ because the runaway greenhouse limit for cool stars is lower than the Sun's (Kopparapu et al., 2013). Other settings are the same those used in § 2.2.4. Fig. 2.11 shows the relationship between the surface temperature and the partial pressure of CO_2. The relationship for M-type stars is plotted in the red line. As a reference, we also plot the relationship for G-type stars (blue and green lines) used in the carbon cycle calculations (§ 2.3.2). This figure realizes that the spectrum shift has no influence on the surface temperature because the spectrum shift does not alter the trend of T_s as a function of P_{CO_2}. Thus, spectrum shift only affects P_{CO_2} in equilibrium and snowball states, as discussed in § 2.3.2.2 for dependence on the stellar insolation. This suggests that the runaway cooling is insensitive to the boundary conditions such as stellar insolation and spectrum type, provided the ocean planet is located in the habitable zone.

Moreover, planets in the habitable zone of cool stars, which orbit close to the central star, are synchronously rotating, which results in a large difference in surface temperature between the day and night sides (e.g., Pierrehumbert, 2011). This might result in a different H_2O-phase structure and flow pattern in the ocean layer from our model and CO_2 might condense on the night side (Turbet et al., 2018). In this case, the HP ice would be easily formed on the cool night side.

However, provided all our assumptions are valid also for synchronously rotating planets and both the dayside and nightside have the same thickness of the ocean layer, the weathering flux on the dayside is always higher than that on the nightside, because of high surface temperature due to the concentration of all the stellar insolation. Thus, an equilibrium climate could be achieved on the dayside, whereas the nightside is extremely cold, unless efficient heat transport occurs. Then, the COM-SB for such a planet can be defined in the same way as we have done above and its value is equivalent to the estimate given in the previous sections. This implies a low probability of exoplanets with temperate climates in the habitable zone also around cool stars. Note that even if they have massive oceans with a mass larger than the COM-SB, synchronously rotating planets never become snowballs, because the local climate around the substellar point could be always temperate (Checlair et al., 2017).

The large temperature contrast between the dayside and nightside would be diminished by the horizontal heat transportation by flows in the atmosphere

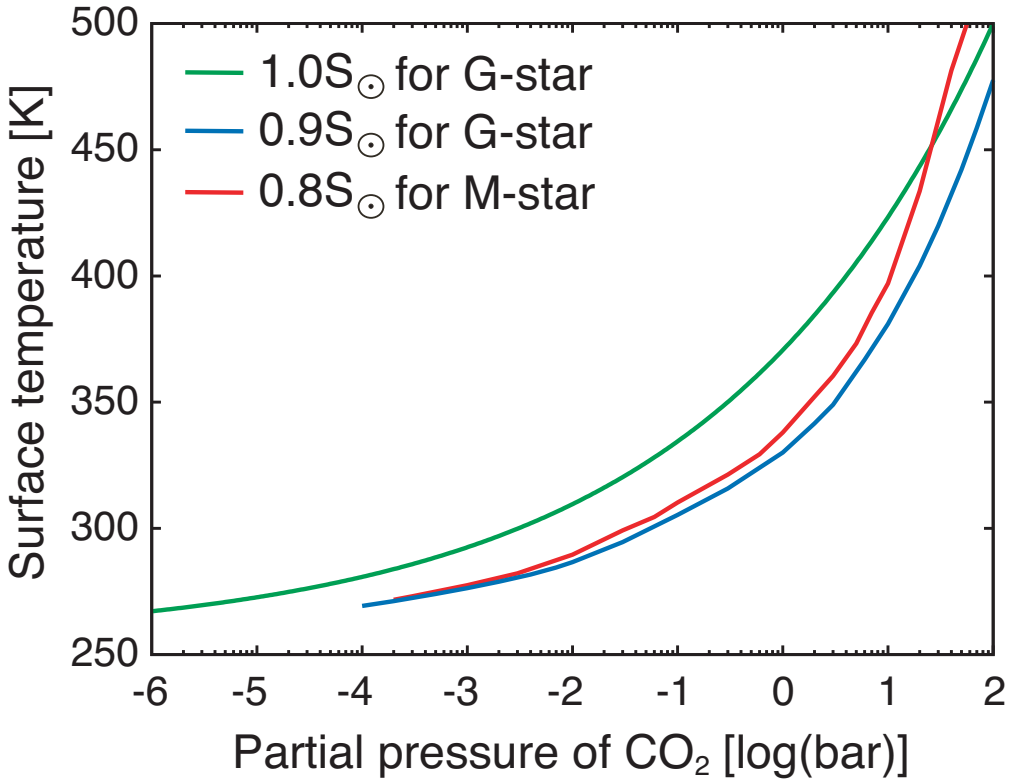

Figure 2.11: Relationship between the surface temperature and partial pressure of CO_2 for different stellar luminosities and spectral type. The red line indicates the relationship for M-type stars with stellar insolation of $0.8S_\odot$, where $S_\odot$ represents the solar insolation received by the present Earth. Blue and green lines indicate the relationship for G-type stars with stellar insolation of $0.9S_\odot$ and $1.0S_\odot$, respectively.

and the ocean. The atmospheric mean zonal circulation from the dayside to nightside is effective for fast rotating planets with the orbital period of about 10 days or shorter because the Rossby deformation radius is larger than the planetary radius because of a significant Coriolis force (Yang et al., 2014; Haqq-Misra et al., 2018; Komacek & Abbot, 2019). Such a short orbital period is achieved for tidally locked planets within the habitable zone around cool M-type stars. A large atmospheric pressure also enhances horizontal heat transportation (e.g., Komacek & Abbot, 2019). Furthermore, the presence of an ocean generally buffers the day-night temperature contrast (Hu & Yang, 2014; Yang et al., 2019). On the other hand, there is a possibility that planets with a high eccentricity are captured into 3:2: spin-orbit resonance (Ribas et al., 2016b). For the non-synchronous case, the difference in the surface temperature is significantly

suppressed (Turbet et al., 2016). Although the efficiency of horizontal heat transport for planets orbiting M-type stars has been still debated, the global averaged model like in our model is valid when horizontal heat transport is effective. In this case, the COM-SB derived in this study can be directly applied to planets around M-type stars.

2.5 Summary of Part I

The Earth's climate is stabilized by temperature-dependent, efficient continental weathering. Beyond the solar system, however, there must be continent-free terrestrial planets covered with global oceans (called ocean planets). Only with inefficient seafloor weathering, the Earth's climate would be much warmer. Furthermore, previous studies suggest that ocean planets have extremely hot climates, if they have massive oceans of 20 to $\sim 100 M_{\mathrm{oc},\oplus}$, because the HP ice present in the deep ocean completely prevents chemical weathering on the oceanic crust (Alibert, 2014; Kitzmann et al., 2015). However, those studies oversimplify the heat transfer in the HP-ice layer and ignore horizontal variation from heat flow from the oceanic crust. Thus, in this study, we have revisited the climate of ocean planets with plate tectonics in the habitable zone, by incorporating the effects of the liquid/solid coexistence region (called the sorbet region) near the mid-ocean ridge in the carbon cycle (Fig. 2.2). The main findings of this study are summarized as follows.

Our seafloor environment model without the effect of the carbon cycle (i.e., fixed surface temperature) has shown that even if pressures in the deep ocean are high enough for HP ice to form, heat flux from the crust is too high to be transferred by solid convection, making the HP ice molten and forming a sorbet region, at least, near the mid-ocean ridge (section 2.3.1). Although reduced with increasing ocean mass or decreasing mean mantle heat flow, the effective weathering area never becomes zero for $M_{\mathrm{oc}} \leq 200 M_{\mathrm{oc},\oplus}$. This means that seafloor weathering remains possible and subsequent material circulation (e.g., carbon cycle) will sufficiently occur through the sorbet region.

Modeling the carbon cycle with the effect of seafloor weathering under the sorbet region, we have found that the climate on the ocean planet is destabilized and lapses into a CO_2 poor, extremely cold state, which is called the snowball state (section 2.3.2). Such destabilization is triggered because seafloor temperature is fixed at the melting temperature of the HP ice and, thus, a high seafloor weathering flux is kept regardless of surface temperature, unlike continental weathering which is dependent on surface temperature. This indicates the existence of a critical ocean mass, beyond which an ocean planet no longer maintains a temperate climate. We have demonstrated that the critical ocean mass is less sensitive to planetary mass, degassing flux, and the detailed de-

pendence of seafloor weather flux on seafloor temperature (i.e., the activation energy E_a), and is several tens of $M_{oc,\oplus}$. Also, because of the supply limit of cations, seafloor weathering is ineffective in compensating massive degassing, not achieving equilibrium climates, but yielding extremely hot ones.

As demonstrated in this paper, thermal and chemical interaction between the ocean and rocky interior significantly alters the planetary climate of ocean planets even in the habitable zone. We have found that temperate equilibrium climates are achieved in limited ranges of ocean mass and degassing flux. This suggests that a certain proportion of terrestrial exoplanets in the habitable zone are frozen ocean planets, provided they are Earth-like ones with plate tectonics. In any case, our findings indicate that ocean mass has a crucial role in the planetary climate of terrestrial planets with a massive ocean. While the characterization of terrestrial exoplanets will be performed for detecting habitable planets in the next decade, we should discuss their climates carefully because those exoplanets would be diverse in surface water amount.

Chapter 3

Part II: Observational Features of Planetary Climate on Terrestrial Planets in the Habitable Zone

3.1 Introduction of Part II

Our theoretical models for the climates of ocean planets developed in Part I show that the planetary climate depends greatly on ocean mass and CO_2 degassing rate. Moreover, the planetary climate for massive oceans lapses into extreme states such as extremely hot ones with CO_2-rich atmospheres or extremely cold (or snowball) ones with CO_2-poor atmospheres (see Fig. 2.10). Those conclusions are, however, based on several assumptions such as operation of plate tectonics and geochemical carbon cycle including a weathering process and would therefore need some observational verification. The most promising among observation methods so far proposed would be transit spectroscopy, by which one detects the line absorption of stellar radiation passing through the upper atmosphere of a planet being in front of its central star.

As described above, the different climate states are characterized by different amounts of atmospheric CO_2. As is well known, CO_2 plays a crucial role in the thermal state of planetary atmospheres. In the upper atmospheres of the terrestrial planets, Venus, the Earth, and Mars, CO_2 is an important coolant emitting radiation mainly at 4.3 and 15 μm, and controls the atmospheric thermal structure (e.g., Kulikov et al., 2007). Indeed, while Venus receives an EUV flux higher only by ∼90 % than the Earth, the former and latter have significantly different exospheric temperatures, which are ~ 300 and ~ 1000 K, respectively (e.g., Jacchia, 1977; Hedin et al., 1983). Such a difference in exospheric temperature is due to the difference in the amount of coolants, namely, CO_2. High exospheric temperature results in an extended upper atmosphere, which is more readily detected by transit observations.

Tavrov et al. (2018) investigated how the absorption during planetary transit varies with the abundance of CO_2 in the upper atmosphere of Earth-like and Venus-like planets orbiting a small-size, low-temperature star (or an M star), as discused in Chapter 1. Such an investigation was carried out in the context of the future space mission *World Space Observatory - UltraViolet (WSO-UV)* to be launched in 2025. Its on-board instruments include a UV-spectrograph (called UVSPEX) with spectral range of 115 to 310 nm. In the spectral range, the atomic oxygen (OI) line around 130 nm causes strong absortion of stellar radiation. Therefore Tavrov et al. (2018) quantified the absorption at the OI line.

To do so, they used the theoretical models from Kulikov et al. (2007) and Tian et al. (2008b). In their models, the exospheric temperatures are ~ 10000 and ~ 600 K for the Earth-like CO_2 abundance (330 ppm) and Venus-like CO_2 abundance (96%), respectively, when the planet receives five times higher EUV flux than the present Earth. In addition, the altitudes at the exobase are ~ 10000 and 300 km for the Earth-like atmosphere and Venus-like atmosphere, respectively. This difference causes a dramatically large difference in the absorption of the OI lines during a planetary transit. Then, the absorption feature of the OI lines was predicted to be observable only for Earth-like planets. Thus, Tavrov et al. (2018) concluded that Earth-like exoplanets can be potentially distinguished from Venus-like exoplanets, because of a large difference in absorption during transits.

While Tavrov et al. (2018) examined only the Venus- and Earth-like planets, terrestrial exoplanets must be more diverse, in reality, as predicted in Part I. Thus, we need to know the dependence of the absorption fraction of the stellar OI line radiation during transits on several factors such as CO_2 abundance and planetary mass. Furthermore, the upper atmospheric models used in Tavrov et al. (2018) are the ones simply extrapolated from the numerical results obtained for the planet around our Sun to those for a M-type star. The chemistry and temperature structure of upper atmospheres are, however, controlled by the stellar spectral energy distribution such as its shape and absolute flux (or intensity). In particular, the shape and intensity of EUV spectra of M-type stars are quite different from those for the Sun (e.g., France et al., 2016). Additionally, the bolometric fluxes of M-type stars are red-shifted because of the low effective temperatures. Thus, CO_2 absorb a larger fraction of the stellar irradiation in the visible to neat-IR and, thereby, heats up the atmosphere. Thus, CO_2 would act as not only a coolant but also a heating agent in the case of M stars, in contrast to solar-type stars.

Therefore, in this study, we newly develop an upper atmosphere model that can be applied to planets around M-type stars. Then, we investigate the effects of the CO_2 abundance and planetary mass on the temperature and density structure of the upper atmosphere. After that, we quantify how large fraction of the stellar cross section is occulted by the ocean planet with the extended oxygen corona when observed at the OI line wavelength, and whether such observations provide observational constraints on the climatic feature of extrasolar

ocean planets in the habitable zone.

The rest of this part is organized as follows: In § 3.2, we describe the details of our upper atmospheric modelling for simulating the temperature and oxygen density structure and our transmittance modelling for simulating the absorption of OI lines in the oxygen corona during a planetary transit. In § 3.3, we show our numerical results regarding the upper atmospheric structure and the occultation degree during a transit (which is termed the transit depth) and its implication for planetary climate for different CO_2 abundances and planetary masses. In § 3.4, we discuss how to constrain the ocean masses observationally, some caveats to our model, and implication for atmospheric escape. In § 3.5, we summarise this part.

3.2 Method

We first simulate the thermal, photo-chemical structure of the upper atmosphere of an aqua planet, in particular, to derive the vertical distribution of atomic oxygen. Then, we model the absorption line profile of atomic oxygen (OI lines) during a transit of the planet, using the obtained OI number density as a function of altitude. In this chapter, we give a detailed description of the methods for modelling the upper atmospheric properties (§ 3.2.1) and the OI absorption line profile (§ 3.2.2).

Before that, we first describe key assumptions made in this modelling. Here, we assume that (1) the atmosphere is in hydrostatic equilibrium and composed of ideal gases, (2) the effect of the magnetic field is negligibly small, and (3) the atmospheric structure is spherically symmetric. Assumption (1) is a reasonable one, when UV irradiation is not intense enough to drive atmospheric escape; such a condition is of interest in this study. Assumption (2) is just for simplicity. While magnetic fields affect motion of charged gases (e.g., Shinagawa & Cravens, 1989), they have never been directly observed around exoplanets so far. Instead, recent observation of the Lyman-α emission from the Earth's geocorona (Kameda et al., 2017) and observation of the occultation by the extended hydrogen atmosphere of the exoplanet GJ436b, which is a Neptune-sized planet around an M-type star, during transits (Ehrenreich et al., 2015) suggest that magnetic fields have only a small influence on the density structure of, at least, the upper part of the atmosphere. Assumption (3) is also for simplicity. In reality, the atmospheric structure would become spherically asymmetric because the planet is thought to be tidally locked in the habitable zone around M-type stars, which is located close to the central star. These assumptions are commonly adopted in theoretical research of the upper atmospheric structure of exoplanets. While these assumptions are commonly adopted in theoretical research of the upper atmospheric structure of exoplanets, we discuss their validity and impact on our conclusion in § 3.4.2.

3.2.1 Upper Atmospheric Model

We develop a simulation code for investigating the 1D steady-state structure of the upper atmosphere. So far, several 1D models of the upper atmospheres have been developed for the terrestrial planets in the solar system (e.g. Roble et al.,

1987) and for close-in giant planets beyond the solar system (e.g., García Muñoz, 2007). Many of them adopt the so-called heating efficiency approach (e.g., Tian et al., 2008a), which assumes a constant value of or a simple formula for the fraction of absorbed stellar UV available for heating the atmosphere, which is termed the heating efficiency. Instead, we give a more precise treatment to the heating efficiency by considering

1. Thermo-chemical reactions (§ 3.2.1.3),
2. Photo-chemical reactions (§ 3.2.1.4),
3. Chemical and thermal diffusions (§ 3.2.1.5),
4. Heating by absorption of stellar infrared irradiation (§ 3.2.1.6), and
5. Radiative cooling (§ 3.2.1.7),

in a similar way to Johnstone et al. (2018). In addition to the key assumptions above, we assume that all the gaseous species share the same temperature, for simplicity. However, the effects of this simplification would have small influence on our results, because ionization fraction is relatively small. Below, we give a detailed description of the components and procedure of the simulation.

3.2.1.1 Basic equations

Under the hydrostatic condition (i.e., no bulk motion), the basic equations that determine the structure of the upper atmosphere include equations of continuity, momentum conservation, and energy conservation (e.g., Banks & Kockarts, 1973):

$$\frac{\partial n_{\rm j}}{\partial t} + \frac{1}{r^2}\frac{\partial (r^2 \Phi_{\rm j})}{\partial r} = S_{\rm j}, \tag{3.1}$$

$$\frac{dP}{dr} = -\rho g, \tag{3.2}$$

$$\frac{\partial e}{\partial t} = Q^{\rm diff} + Q^{\rm chem} + Q^{\rm uv} + Q^{\rm pe} - Q^{\rm rad}, \tag{3.3}$$

where r is the radial distance measured from the planet's center, t is the time, n_j is the number density of species j, P is the pressure, ρ is the density, g is the gravitational acceleration, Φ_j is the diffusive flux of species j, S_j is the source/sink term of species j, which includes thermo-chemical and photo-chemical reactions,

e is the energy density, $Q^{\rm diff}$ is the heating rate of thermal diffusion, $Q^{\rm chem}$ is the rate of heating via chemical reactions, $Q^{\rm uv}$ is that by photo-dissociation, $Q^{\rm pe}$ is that by collision with photo-electrons, and $Q^{\rm rad}$ is the rate of IR cooling. In this chapter, the subscripts n, i, and e mean neutrals, ions, and electrons, respectively.

The temperature, T, is obtained as

$$T = \frac{e}{NC_{\rm v}} \tag{3.4}$$

where N is the total number density and $C_{\rm v}$ is the specific heat. For simplicity, we assume that the specific heats are $3k_{\rm B}/2$ and $5k_{\rm B}/2$ for atoms and molecules, respectively ($k_{\rm B}$ is the Boltzmann constant). For the gas mixture, we use a number density averaged value of the specific heat.

We integrate the temperature and compositional structure from the lower boundary to the exobase. The exobase is defined by the altitude where the mean free path of gas species is the same as the pressure scale height. This condition is also written by use of the Knudsen number, Kn, defined as

$$Kn = \frac{l_{\rm mfp}}{\bar{H}}, \tag{3.5}$$

where $l_{\rm mfp}$ is the mean free path and $\bar{H}$ is the pressure scale height. The mean pressure scale height is defined as

$$\bar{H} = \frac{k_{\rm B}T}{\bar{m}g}, \tag{3.6}$$

where $\bar{m}$ is the mean molecular weight. The mean free path is written by $l_{\rm mfp} = 1/(\sigma N)$, where σ is the collisional cross section and N is the total number density. Although σ depends on gas species and temperature, we adopt σ as a constant value of 2.0×10^{15} cm^2, which is the typical value for an oxygen atom in low energy levels ($\sim$ eV) (Tully & Johnson, 2001), because the difference in σ between different gas species is small (Johnson et al., 2002). Beyond the exobase, the gases behave the collisionless particles and fluid approximation would be no longer valid.

3.2.1.2 Hydrostatic density structure

We obtain the equation of density structure, using the procedure given in Tian et al. (2008a). Using the ideal equation of state, the density is given by $\rho =$

$\bar{m}/Pk_{\rm B}T$ and the radial derivative of ρ is written as

$$\frac{d\rho}{dr} = -\frac{\rho}{\bar{m}}\frac{d\bar{m}}{dr} + \left(\frac{1}{v^{\rm t}}\right)^2 \frac{dP}{dr} - \frac{\rho}{T}\frac{dT}{dr}, \tag{3.7}$$

where $v^{\rm t}(=\sqrt{k_{\rm B}T/\bar{m}})$ is the thermal velocity. Putting Eq. (3.2) into Eq. (3.7), we obtain the equation for the density structure :

$$\frac{1}{\rho}\frac{d\rho}{dr} = \frac{1}{\bar{m}}\frac{d\bar{m}}{dr} - \frac{g}{(v^{\rm t})^2} - \frac{1}{T}\frac{dT}{dr}, \tag{3.8}$$

$$g = \frac{GM_{\rm p}}{r^2}, \tag{3.9}$$

where G is the gravitational constant and $M_{\rm p}$ is the planetary mass. We radially integrate Eq.(3.8) from the lower boundary for known mean molecular weight and temperature profiles, using the 4th order Runge-Kutta method.

3.2.1.3 Thermo-chemical reactions

We consider thermo-chemical reactions among neutrals and ions, and electrons. Our chemical network, which contains 417 reactions, is listed in Tables C.1 and C.2 in Appendix C. We consider 63 chemical species composed of the seven elements, H, He, C, O, N, Ar, and Cl. The chemical network is mostly taken from Johnstone et al. (2018), which compile chemical reactions used in several atmospheric models previously published. Note that we exclude reaction No. 387 in the appendix of Johnstone et al. (2018) because they doubly counted the same reaction. This chemical network can be applied to a range of terrestrial atmospheric composition.

The rate of the kth reaction, $R_{\rm k}$, can be calculated using the rate coefficient, k_k. The reaction rate for both chemical and photochemical reactions is given by

$$R_{\rm k} = k_{\rm k}\prod_{\rm j} n_{\rm j}, \tag{3.10}$$

where the RHS means the reaction coefficient times the product of the number densities of all reactants. For chemical reactions, $k_{\rm k}$ depends on the temperature and reaction and their values are given in Tables C.1 and C.2. We calculate source/sink term in Eq.(3.1) by summing all the reactions including chemical and photochemical reactions.

We include the heating due to exothermic reactions, which release the chemical potential energy as heat. The heating rate is simply given by

$$Q^{\rm chem} = \sum_{\rm k} E_{\rm k} R_{\rm k}, \tag{3.11}$$

where E_k is the released energy per reaction for the kth reaction, which is tabulated in Tables C.1 and C.2. The chemical network also includes radiative-recombination and de-excitation reactions by spontaneous emission for photo-chemically exited species. We assume that those emissions directly escape to space (i.e., no absorption).

3.2.1.4 Photo-chemical reactions

The photo-chemical reactions are important not only for heating sources but also for driving sources for subsequent chemical reactions. Although we use the photo-chemical network shown in Johnstone et al. (2018), we slightly modified the network because absorption cross-sections or quantum yields for some reactions are unavailable in their references. In particular, we exclude reactions No.446, 447, 454, 455, 459, and 468 in the appendix of Johnstone et al. (2018). Our photochemical network includes 50 reactions, which are listed in Table C.3 in Appendix C. For all of the reactions, we take the wavelength-dependent absorption cross-sections from the PHIDRATES database (Huebner & Mukherjee, 2015). Our model covers the wavelength range of 1–400 nm to resolve the oxygen chemistry.

For photo reactions, k_k is given by

$$k_k = \int_{\lambda_k^{cr}}^{\infty} \sigma_k(\lambda) I_\lambda(r) d\lambda, \tag{3.12}$$

where λ_k^{cr} is the threshold wavelength for the kth reaction given in Table C.3, $\sigma(\lambda)$ is the absorption coefficient for a given wavelength, and $I_\lambda(r)$ is the irradience per photon, quadratic cm, wavelength and second for a given wavelength at altitude r. $I_\lambda(r)$ is calculated by the radiative transfer equation:

$$I_\lambda(r) = I_\lambda(\infty) \exp\left(-\left\{ \sum_k \int_r^{\infty} \sigma_k(\lambda) n_k dr \right\} / \mu \right), \tag{3.13}$$

where $I_\lambda(\infty)$ is the irradiance at the top of the atmosphere and μ is the stellar zenith angle. As done in Johnstone et al. (2018), we assume $\mu = 66°$ to evaluate the global averaged structure of the upper atmosphere. This assumption is partly supported by GCM simulations including photo-chemistry (Chen et al., 2018). They suggested that day-to-nightside mixing ratio differences on tidally locaked planets remain small because dynamics transports photo-chemically produced species from the dayside toward the terminator, which is probed by the transit

observation. We should note that the upper boundary of their simulations is, however, the altitude of 100 Pa.

The absorbed photon energy is largely consumed by the chemical reactions. For photo-dissociative reactions, the remaining energy converts into kinetic energy of molecules, which is subsequently dissipated as heat through the collisional relaxation. We assume the remaining energy quickly converts into heat. Thus, the heating rate due to photo-dissociative reactions is given by

$$Q^{\rm uv} = \sum_{\rm k} \int_0^{\lambda_{\rm k}^{\rm cr}} \left(\frac{hc}{\lambda} - \frac{hc}{\lambda_{\rm k}^{\rm cr}} \right) n_{\rm k} \sigma_{\rm k}(\lambda) I_\lambda(r) d\lambda, \tag{3.14}$$

where h is the planck constant and c is the velocity of light. The terms of (hc/λ) and $(hc/\lambda_{\rm k}^{\rm cr})$ mean the absorbed photon energy for a given wavelength and the energy required to cause the kth reaction, respectively.

For photoionization reactions, the remaining energy is consumed in a complicated way. The remaining energy firstly goes to the kinetic energy of electrons. These electrons, termed photoelectron, have higher energy than the ambient thermal electrons. Because of their high energy, collisions with photoelectrons result in chemical reactions of neutral species, including secondary photoionization, and heating thermal electrons. Since calculating the full physics of photoelectrons is time-consuming, we adopt the simple heating efficiency approach given in Smithtro & Solomon (2008). To parameterized the photoelectron heating rate, they repeatedly performed photochemical reactions including the effect of photoelectrons for a variety of conditions, using the *GLOW* model (Solomon et al., 1988). The photoelectron heating rate can be expressed as

$$Q^{\rm pe} = \chi \sum_{\rm k} R_{\rm k}, \tag{3.15}$$

where χ is the heating efficiency. The parameterization of χ in eV is given by (Smithtro & Solomon, 2008)

$$\begin{aligned} \chi = \exp(&5.342 + 1.056x - 4.392 \times 10^{-2} x^2 - 5.900 \times 10^{-2} x^3 \\ &-9.346 \times 10^{-3} x^4 - 5.755 \times 10^{-4} x^5 - 1.249 \times 10^{-5} x^6), \end{aligned} \tag{3.16}$$

where x is the ionization fraction. We adopt $x = \ln(n_{\rm e}/\{n_{\rm N_2} + n_{\rm O_2} + n_{\rm O} + n_{\rm CO_2} + n_{\rm CO}\})$, although Smithtro & Solomon (2008) adopted $x = \ln(n_{\rm e}/\{n_{\rm N_2} + n_{\rm O_2} + n_{\rm O}\})$. This is because Smithtro & Solomon (2008) considered a CO_2-poor Earth-like atmosphere. However, this modification would be valid because inelastic collisions

with neutrals (i.e., neutral concentration) reduce the available photoelectron energy to heating and inelastic cross-sections of CO_2 and CO are not so different from other species (Sawada et al., 1972a,b; Jackman et al., 1977). Indeed, Johnstone et al. (2018) showed that a change in CO_2 abundance by five order of magnitude results in a variation of the heating flux due to photoelectron within a factor of four. Thus, the modification of the ionization fraction has a small influence on results.

We use the stellar spectrum observed previously as the input irradiance at the top of the atmosphere. The UV emission spectrum differs geratly from star to star, depending on stellar spectral type, age, and activity (e.g., Linsky et al., 2014; Ribas et al., 2005). In this study, we adopt the observed UV spectrum of GJ1214 from MUSCLES Treasury Survey (France et al., 2016) for the irradiance at the top of the atmosphere. GJ 1214 is a M-type star having a super-Earth planet outside the habitable zone (Charbonneau et al., 2009). The intensity of EUV spectrum is adjusted so that the bolometric flux at visible wavelength recieved by the planet is 0.9 times that of Earth's. Figure 3.1 shows the EUV spectrum used in our model (red solid line). For comparison, we also show the modern Sun's spectrum (blue solid line) taken from Claire et al. (2012), which represents the Sun at the maximum activity level. In the EUV wavelength region (≤ 91 nm), the intensity for GJ1214 is much larger than that for the Sun. In contrast, in near-UV (≥ 170 nm), the former is much weaker than the latter. This trend is similar to other M-type stars (France et al., 2016).

3.2.1.5 Diffusion

We take into account both molecular and eddy diffusion. The eddy diffusion mixes the lower region (i.e., homosphere), in which number density profiles for all species mostly follow the same pressure scale height. On the other hand, the molecular diffusion dominates in the upper region (i.e., heterosphere). In the heterosphere, gravitational separation occurs faster than mixing, so that number densities of heavy species decrease with altitude.

The diffusion (momentum) equation follows the equation developed by Chapman & Cowling (1991) and Banks & Kockarts (1973). The diffusive flux of the jth species is written by

$$\Phi_j = v_j n_j, \tag{3.17}$$

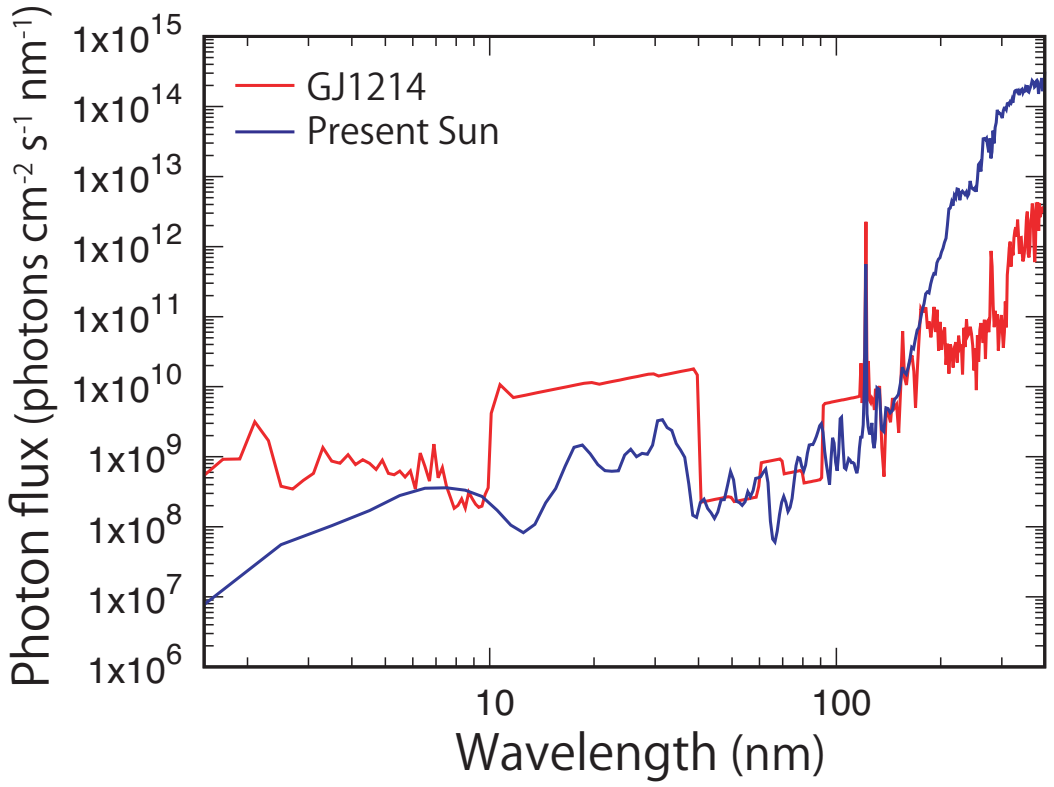

Figure 3.1: The host-stellar spectrum model used in this study. The red solid line is the photon flux of GJ1214 at the distance where the bolometric flux is equivalent to stellar insolation 0.9 times the solar insolation recieved by the present Earth. The blue solid line is the photon flux of the present sun at 1AU.

where v_j is the diffusion speed and can be split into molecular and eddy diffusion terms: $v_j = v_j^{mol} + v_j^{eddy}$. The diffusion speed due to molecular diffusion is given by (e.g., Banks & Kockarts, 1973)

$$v_j^{mol} = -D_j \left(\frac{1}{n_j} \frac{dn_j}{dr} + \frac{1}{H_j} + \frac{(1+\alpha_j)}{T} \frac{dT}{dr} \right), \tag{3.18}$$

where α_j is the thermal diffusion factor, H_j is the scale height of species j, and D_j is the molecular diffusion coefficient of the jth species. In the scale height of the jth species, $\bar{m}$ is replaced with the mass of the jth species, m_j, in Eq. (3.6). The thermal diffusion factor is assumed to be zero for all species expect for H, H_2, and He. We set the thermal diffusion factor of 0.38 for H, H_2, and He (Banks & Kockarts, 1973). The diffusion coefficient D_j for the gas mixture depends on several factor: composition of the background gas, temperature, and the species itself. We assume that the background gas is N_2, which has small influence on the results because the diffusion coefficients are similar for other background

Table 3.1: Parameters for diffusion coefficient

Species	H	H_2	He	Ar	CO	CO_2	O
a_j	4.87	2.80	2.94	6.64×10^{-1}	9.28×10^{-1}	6.58×10^{-1}	9.69×10^{-1}
b_j	0.698	0.740	0.718	0.752	0.710	0.752	0.774

gases. We use the relation (Banks & Kockarts, 1973)

$$D_j = \frac{a_j \times 10^{17} T_j^b}{N}. \tag{3.19}$$

For H, H_2, Ar, CO, CO_2, and O, we use the tabulated values in Banks & Kockarts (1973), which are given in table 3.1. For the other species, we use $a_j = 1$ and $b_j = 0.75$, as done in Johnstone et al. (2018).

For eddy diffusion, the diffusion speed is given by (e.g., Banks & Kockarts, 1973)

$$v_j^{\rm eddy} = -K_E \left(\frac{1}{n_j}\frac{dn_j}{dr} + \frac{1}{\bar{H}} + \frac{1}{T}\frac{dT}{dr} \right), \tag{3.20}$$

where K_E is the eddy diffusion coefficient. We use the eddy diffusion coefficient in the usual form of

$$K_E = A_E N^{B_E}, \tag{3.21}$$

where $A_E = 10^8$ and $B_E = -0.1$ for the Earth (Johnstone et al., 2018). These values were chosen so as reproduce the current Earth's number density profiles, using their model. This functional form was also used for some models for the Venus and Mars and coefficients are given by $A_E = 2\times10^{13}$ and $B_E = -0.5$ (Fox, 2015). We adopt the Earth-like eddy diffusion coefficient as the fiducial value. As noticed from the significant difference in diffusion coefficient between the Earth and Venus-like value, eddy diffusion is quite uncertain. Thus, we discuss the effect of the eddy diffusivity on the upper atmosphere structure in § 3.4.2.5

For the diffusion of electrons, we assume that the atmosphere maintains the local electrical neutrality. Assuming no magnetic field, the electron diffusive flux is equal to the sum of ion's diffusive fluxes (e.g., Shinagawa & Cravens, 1989):

$$v_e n_e = \sum_j v_j n_j. \tag{3.22}$$

Heat transport occurs via thermal conduction. We separately evaluate the thermal conduction in neutral, ion, and electron components. Then, we evaluate the heating rate due to diffusion, summing each component :

$$Q^{\rm diff} = Q_n^{\rm diff} + Q_i^{\rm diff} + Q_e^{\rm diff}. \tag{3.23}$$

For neutral species, thermal conduction is caused by molecular and eddy conduction:

$$Q_{\rm n}^{\rm diff} = \kappa_{\rm mol}\frac{dT}{dr} + \kappa_{\rm eddy}\left(\frac{dT}{dr} + \frac{g}{C_{\rm P}}\right), \tag{3.24}$$

where $\kappa_{\rm mol}$ and $\kappa_{\rm eddy}$ are the thermal conductivity due to molecular and eddy diffusion, respectively, and $C_{\rm p}$ is the specific heat at constant pressure. The eddy conductivity is related to eddy diffusion coefficient (Hunten, 1974): $\kappa_{\rm eddy} = \rho C_{\rm P} K_{\rm E}$.

For molecular conductivity, we consider only N_2, O_2, CO_2, CO, O, He, H, and Ar. The molecular conductivity of neutral species is given by (Banks & Kockarts, 1973)

$$\kappa^{\rm j} = A_j^{\kappa} T^{B_{\rm j}^{\kappa}}, \tag{3.25}$$

where $A_{\rm j}^{\kappa}$ and $B_{\rm j}^{\kappa}$ are constants for species j and values taken from Bauer & Lammer (2004) for Ar and Schunk & Nagy (2000) for the others. For the mixture of neutral species, we use the expression of total conductivity given by Banks & Kockarts (1973):

$$\kappa_{\rm mol} = \sum_{\rm k}\frac{n_{\rm k}\kappa_k}{\sum_{\rm j} n_{\rm j}\phi_{\rm kj}}, \tag{3.26}$$

where

$$\phi_{\rm kj} = \frac{[1+(\kappa_{\rm k}/\kappa_{\rm j})^{1/2}(m_{\rm j}/m_{\rm k})^{1/4}]}{2\sqrt{2}[1+m_{\rm j}/m_{\rm k}]^{1/2}}. \tag{3.27}$$

For the ions, the heating transport due to conduction is simply given by

$$Q_{\rm i}^{\rm diff} = \kappa_{\rm i}\frac{dT}{dr}, \tag{3.28}$$

where $\kappa_{\rm i}$ is the thermal conductivity of ions. For single ion species, thermal conductivity is expressed as (Banks & Kockarts, 1973)

$$\kappa_{\rm j} = 4.6\times10^4 n_{\rm j}(\mathscr{M}_{\rm j})^{-1/2}T^{5/2}, \tag{3.29}$$

where $\mathscr{M}_{\rm j}$ is the atomic mass of species. For the conductivity of the mixture of ions, we use the number density weighted average recommended by Banks & Kockarts (1973):

$$\kappa_{\rm i} = \frac{\sum_{\rm j} n_{\rm j}\kappa_{\rm j}}{\sum_{\rm j} n_{\rm j}}. \tag{3.30}$$

For the electrons, the conduction equation is the same as that for ion's given in Eq.(3.28), but subscript i replaced with e; thermal conductivity of electrons is given by (Banks & Kockarts, 1973)

$$\kappa_{\rm e} = \frac{7.7\times10^5 T^{5/2}}{1+3.22\times10^4(T^2/n_{\rm e})\sum_{\rm j} n_{\rm j}\bar{Q}_{\rm j}^{\rm D}}, \tag{3.31}$$

where $\bar{Q}_j^D$ is the average momentum transfer cross-section of species j. This formula includes a reduction in conductivity caused by collisions with neutral species. For the sum in the denominator, we consider only the effects of N_2, O_2, O, H, and He. The expression of $\bar{Q}_j^D$ is given in Banks & Kockarts (1973). Note that conductivities of ions and electron are in units of eV cm^{-1} s^{-1} K^{-1}, although that for neutrals in units of erg cm^{-1} s^{-1} K^{-1}.

To solve the diffusion equations, boundary conditions are need. In the compositional part, we assume that there is no gradient in composition at the lower boundary because eddy diffusion mixes the lower atmosphere efficiently. For the upper boundary, we adopt the Jeans escape flux as the outward diffusion flux for the species with mass up to 4 times the mass of a hydrogen atom because we assume no bulk motion and hydrostatic equilibrium. We use the Jeans escape flux given in Öpik (1963) :

$$\Phi_j = 4\pi n v_j^t \frac{(1+\zeta_j)\exp(-\zeta_j)}{2\sqrt{\pi}}, \tag{3.32}$$

where $v_j^t (= \sqrt{k_B T/m_j})$ is the thermal velocity of gas species and ζ_j is the Jeans escape parameter. The Jeans escape parameter is defined by

$$\zeta_j = \frac{r_{exo} g_{exo} m_j}{k T_{exo}}, \tag{3.33}$$

where the subscript exo means the exobase. Otherwise, we adopt no compositional diffusion for heavier species. In the thermal part, we adopt the Dirichlet boundary condition and no diffusion flux for the lower and upper boundaries, respectively.

3.2.1.6 Absorption of stellar infrared irradiation

We consider the absorption of stellar irradiation by H_2O and CO_2, which are strong absorbers in the infrared (IR) region and important heating sources for the CO_2-rich atmosphere like Venus and Mars ones (e.g., Bougher & Dickinson, 1988). We perform radiative transfer calculation in the IR band between 500 and 12850 cm^{-1} (i.e., 0.78 and 20 μm in wavelength). We consider only gaseous absorption because Rayleigh scattering is negligible in the infrared band. We assume that absorbed radiative energy quickly converts into heat. For the stellar IR spectrum, we assume the black-body spectrum of 3000K, which is equivalent to the effective temperature of GJ1214. The integrated stellar intensity is as-

sumed to be 1.2×10^6 erg cm^{-2}, which is 0.9 times that received by the present Earth, as done in UV spectrum.

The spectral absorption coefficient varies irregularly with wavenumber, ν, because radiatively active gases have a large number of absorption lines. For that reason, the integration of the radiative transfer equation requires very small wavenumber intervals, which is computationally enormous. Therefore, we use the k-distribution method, which is widely adopted in radiative transfer calculations (e.g., Mlawer et al., 1997). The k-distribution method has much faster speed with comparable accuracy (within 1%) than the line-by-line integration technique (Fu & Liou, 1992). In the k-distribution method, the spectrum is divided into small bands and the absorption probability distribution in each band is described by a small number of k-coefficients and corresponding weights. Namely, the mean absorption cross-section in each band, $\sigma^{\Delta\nu}$, is expressed by

$$\sigma^{\Delta\nu} = \sum_{\mathrm{i}}^{N_\mathrm{q}} k^\mathrm{i} w^\mathrm{i}, \tag{3.34}$$

where N_q is the total number of quadrature points, k^i is the k-coefficient, and w^i is corresponding weight parameter. We divide the spectrum into 21 spectral intervals and the range of each band follows rapid radiative transfer model (RRTM) (Mlawer et al., 1997), which is given in Table 3.2. Then, heating by stellar irradiation, Q^IR, is derived by summing the absorption of all the gas species over the whole wavenumber:

$$Q^\mathrm{IR} = \sum_\mathrm{j} Q_\mathrm{j}^\mathrm{IR} = \sum_\mathrm{j} \int_{\nu_0}^{\nu_1} I^{\Delta\nu}(r) \sigma_\mathrm{j}^{\Delta\nu} \Delta\nu d\nu, \tag{3.35}$$

where $I^{\Delta\nu}(r)$ is the band averaged irradiance at r and ν_0 and ν_1 are start (500 cm^{-1}) and end point (12850 cm^{-1}) of whole integration interval, respectively.

The k-coefficients are derived from high-resolution absorption spectrum. We calculate the absorption spectrum using the open-source code *kspectrum* (Eymet et al., 2016). We consider molecular line absorption and all the molecular line parameters are obtained from HITRAN2012 database (Rothman et al., 2013). The shape of the spectral line is calculated by the Voigt profile, which is the convolution of Lorentz and Gaussian profiles. We adopt any cut-off in the line wings. We consider only the main isotopes (i.e., $\mathrm{H_2^{16}O}$ and $^{12}\mathrm{C}^{16}\mathrm{O_2}$), for simplicity. As in Johnstone et al. (2018), we calculate the cross-section only under the condition of 200K and 1Pa and use these values everywhere, for simplicity. Then,

we calculate k-coefficients in each band, using the open-source code *kdistribution* (Eymet et al., 2016). We use 16 quadrature points for accuracy, as in RRTM. Fig. 3.2 shows absorption cross-sections of CO_2 (*a*) and H_2O (*b*). Red lines indicate high-resolution spectrum derived line-by-line method. Blue lines indicate band-averaged absorption cross-section derived by the k-distribution method. Absorption of stellar irradiation is mainly occurred at about 2300 cm^{-1} (band 12) for CO_2. H_2O can absorb stellar irradiation at larger wavenumber (or shorter wavelength) than that of CO_2. However, CO_2 absorption is dominant in our situations because of the small abundance of H_2O.

The method of k-distribution can not treat the effect of absorption overlapping on the transmittance exactly, because the method includes the coordinate transformation from wavenumber to cumulative absorption probability. For the absorption overlapping, we use correlated spectra scheme (e.g., Zhang et al., 2003), which assumes spectral distributions of all overlapping components have the same shape, but their magnitude can be different. This method efficiently calculated band overlapping and produce reasonable error (Shi et al., 2009). Furthermore, since the absorption is important for CO_2-rich atmosphere in our interest situation, single absorber (i.e., CO_2) dominates the transmittance. Thus, the treatment of overlapping does not influence our results. In the correlated spectra scheme, the total transmittance in each band for gaseous mixture at r is

$$\mathscr{T}^{\Delta\nu}(r) = \sum_{\mathrm{i}}^{N_\mathrm{q}} w^{\mathrm{i}} \exp\left(- \left\{ \int_r^\infty \sum_{\mathrm{j}} (k_\mathrm{j}^i n_\mathrm{j}(r')) dr' \right\} / \mu \right). \tag{3.36}$$

Using the transmittance, the irradiance in each band at r is calculated by

$$I^{\Delta\nu}(r) = I^{\Delta\nu}(\infty)\mathscr{T}^{\Delta\nu}(r), \tag{3.37}$$

where $I^{\Delta\nu}(\infty)$ is the stellar irradiance at the top of atmosphere.

Table 3.2: Bands for infrared absorption

Band No.	Spectral range (cm^{-1})
1	500–630
2	630–700
3	700–820
4	820–980
5	980–1080
6	1080–1180
7	1180–1390
8	1390–1480
9	1480–1800
10	1800–2080
11	2080–2250
12	2250–2380
13	2380–2600
14	2600–3250
15	3250–4000
16	4000–4650
17	4650–5150
18	5150–6150
19	6150–7700
20	7700–8050
21	8050–12850

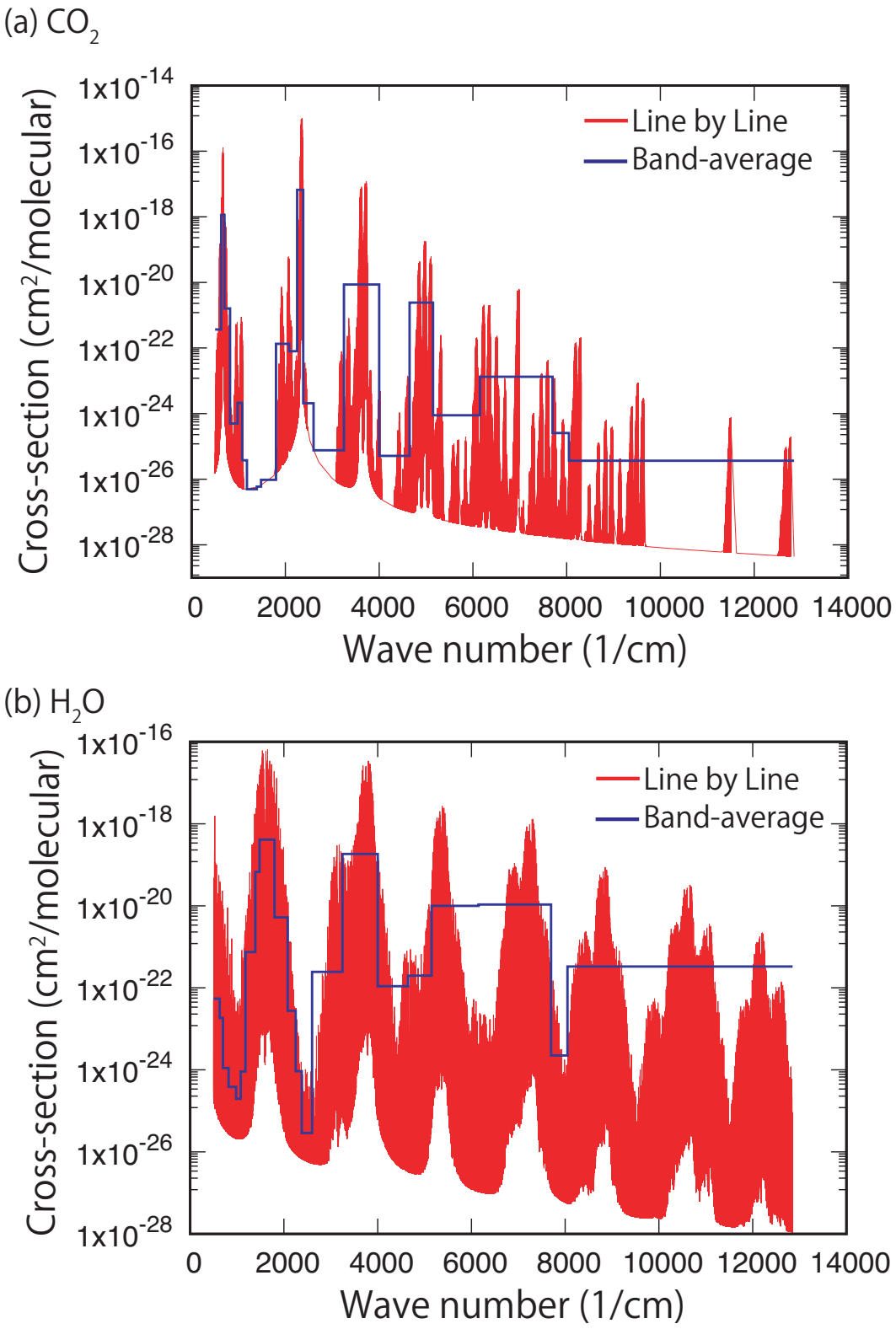

Figure 3.2: Derived absorption cross-sections of CO_2 (*a*) and H_2O (*b*). Red lines indicate high-resolution spectrum. Blue lines indicate band-averaged absorption cross-section derived by k-distribution method.

3.2.1.7 Radiative cooling

We consider radiative cooling by CO_2, NO, O, and H_2O. They are important coolants for terrestrial upper atmosphere (e.g., Roble et al., 1987; Kasting & Pollack, 1983). Radiative cooling occurrs when species are excited by collisions and/or radiation and then emit photon to space. Therefore, to precisely estimate the cooling rate, the population of energy levels (rotational, vibrational and electronic state) and radiative transfer calculation are necessary (e.g., Funke et al., 2012). In this study, we perform a relatively simpler method following Johnstone et al. (2018), which assumes two (or three) level populations with first (and second) excited and ground states, level populations in the steady state, ignoring stimulated emission, and cooling-to-space approximation. The cooling-to-space approximation means that photons emitted from a given point directly escapes to space and escape probability, ε, is determined by the optical depth. This method is a common way to evaluate the radiative cooling (e.g., Roble et al., 1987).

The radiative cooling by CO_2 is dominated by emission at 15 μm band for the Earth-like condition because of small excitation temperature (e.g., Dickinson, 1976). However, radiative excitation due to absorption of stellar insolation and the radiation at 4.3 μm band are important because we focus on an M-type star whose spectrum is red-shitted. Thus, we include the radiation at 4.3 and 15 μm bands. Our model is based on Johnstone et al. (2018), which only consider 15 μm band (i.e., $v_2 = 1$ state), and further includes collisional and radiative excitation/de-excitation of 4.3 μm (i.e., $v_3 = 1$ state) and vibrational-vibrational transition. We assume that absorption of staller insolation at 1–5 bands and 6–21 bands in table 3.2 contribute radiative excitations of 15 and 4.3 μm bands, respectively. Hereafter, $v_2 = 1$ and $v_3 = 1$ states are called as v_2 and v_3, respectively.

The cooling rate at 15 μm band, $Q^{\rm rad}_{\rm CO_2,15\mu m}$, and at 4.3 μm band, $Q^{\rm rad}_{\rm CO_2,4.3\mu m}$, are expressed by

$$Q^{\rm rad}_{\rm CO_2,15\mu m} = (h\nu)_{15\mu m} A^{\rm sp}_{\rm CO_2,15\mu m} [\rm CO_2]_{v_2} \varepsilon_{15\mu m}, \tag{3.38}$$

$$Q^{\rm rad}_{\rm CO_2,4.3\mu m} = (h\nu)_{4.3\mu m} A^{\rm sp}_{\rm CO_2,4.3\mu m} [\rm CO_2]_{v_3} \varepsilon_{4.3\mu m}, \tag{3.39}$$

where $(h\nu)$ is the energy of photon at each bands, $[\rm CO_2]_{v_2}$ is the number density of CO_2 excited v_2 state, $[\rm CO_2]_{v_3}$ is the number density of CO_2 excited v_3 state,

$A^{\rm sp}_{\rm CO_2}$ is the Einstein coefficient for spontaneous emission of each bands, and subscript 4.3μm and 15μm denote the bands. For the 15μm band, $(h\nu) = 1.3\times10^{-13}$ erg and $A^{\rm sp}_{\rm CO_2} = 0.46$ s^{-1} (Curtis & Goody, 1956). For the 4.3μm band, $(h\nu) = 4.5\times10^{-13}$ erg and $A^{\rm sp}_{\rm CO_2} = 400$ s^{-1} (Zahnle et al., 2019).

To estimate the number density of excited species, we consider collisional excitation and de-excitation, vibrational-vibrational transition from ν_3 to ν_2, and radiative excitation and de-excitation. We assume all photons that do not escape to space are reabsorbed locally where the emission took place, as done in Johnstone et al. (2018). Based on these assumptions, excitation rates are given by

$$\frac{d[\mathrm{CO_2}]_{\mathrm{v_2}}}{dt} = \sum_{\rm j} k^{\rm ex}_{\rm j} n_{\rm j}[\mathrm{CO_2}] + \sum_{\rm j} k^{\rm v-v}_{\rm j} n_{\rm j}[\mathrm{CO_2}]_{\mathrm{v_3}} + Q^{\rm IR}_{\rm CO_2}/(h\nu)_{15\mu m} + A^{\rm sp}_{\rm CO_2}(1-\varepsilon)[\mathrm{CO_2}]_{\mathrm{v_2}} - \sum_{\rm j} k^{\rm de}_{\rm j} n_{\rm j}[\mathrm{CO_2}]_{\mathrm{v_2}} - A_{\mathrm{CO_2}}\varepsilon[\mathrm{CO_2}]_{\mathrm{v_2}}, \tag{3.40}$$

$$\frac{d[\mathrm{CO_2}]_{\mathrm{v_3}}}{dt} = \sum_{\rm j} k^{\rm ex}_{\rm j} n_{\rm j}[\mathrm{CO_2}] + Q^{\rm IR}_{\rm CO_2}/(h\nu)_{4.3\mu m} + A^{\rm sp}_{\rm CO_2}(1-\varepsilon)[\mathrm{CO_2}]_{\mathrm{v_3}} - \sum_{\rm j} k^{\rm de}_{\rm j} n_{\rm j}[\mathrm{CO_2}]_{\mathrm{v_3}} - \sum_{\rm j} k^{\rm v-v}_{\rm j} n_{\rm j}[\mathrm{CO_2}]_{\mathrm{v_3}} - A_{\mathrm{CO_2}}\varepsilon[\mathrm{CO_2}]_{\mathrm{v_3}}, \tag{3.41}$$

and mass conservation:

$$[\mathrm{CO_2}] + [\mathrm{CO_2}]_{\mathrm{v_2}} + [\mathrm{CO_2}]_{\mathrm{v_3}} = n_{\mathrm{CO_2}}, \tag{3.42}$$

where $k^{\rm ex}_{\rm j}$ is the rate coefficient for collisional excitation of jth species, $k^{\rm de}_{\rm j}$ is the rate coefficient for collisional de-excitation of jth species, $k^{\rm v-v}_{\rm j}$ is the vibtational-vibrational transition rate of jth species, and $[\mathrm{CO_2}]$ is number density of $\mathrm{CO_2}$ at the ground state. We omit the subscripts of 4.3μm and 15μm above equations from rate coefficients, absorption of stellar insolation, the Einstein coefficients, and escape parameter. Assuming excitation and de-excitation equilibrium state (i.e., stady state), we analytically solve Eqs.(3.41), (3.40), and (3.42) and determine the level population.

For collisional excitation and de-excitation of ν_2, collisions with O, $\mathrm{O_2}$, $\mathrm{N_2}$, $\mathrm{CO_2}$, He, and Ar are considered. Johnstone et al. (2018) fitted the rate coefficients of de-excitation in the form of $k^{\rm de}_{\rm j} = A^{\rm de} T_{\rm n}^{B^{\rm de}}$, using experimentally measured values given by Siddles et al. (1994) and Castle et al. (2012). The values of coefficients are tabulated in table 3.3. The rate of excitation coefficient is related to the de-excitation coefficient (Castle et al., 2006): $k^{\rm ex}_{\rm j} = 2k^{\rm de}_{\rm j}\exp(-960/T)$.

Table 3.3: Fitted coefficients for CO_2 collisional de-excitation of $v_2 = 1$ state

Species	O	O_2	N_2	CO_2	He	Ar
A^{de}	5.10×10^{-11}	4.97×10^{-22}	6.43×10^{-21}	4.21×10^{-17}	4.73×10^{-19}	8.13×10^{-24}
B^{de}	-0.59	2.83	2.30	0.85	2.19	3.19

Table 3.4: Fitted coefficients for CO_2 vibrational-vibrational transition

Species	rate coefficients
O	$2.0 \times 10^{-13}(T/300)^{1/2}$
O_2	$1.82 \times 10^{-15} + 3.1 \times 10^{-11}\exp(-63.3/T^{1/3}) + 2.0 \times 10^{-31}T^6$
N_2	$1.1 \times 10^{-14} + 1.14 \times 10^{-10}\exp(-72.3/T^{1/3}) + 2.3 \times 10^{-40}T^9$
$[CO_2]$	$3.6 \times 10^{-13}\exp(-166/T + 176948/T^2)$

For collisional excitation and de-excitation of v_3, we only consider collision with N_2 and the rate coefficients of de-excitation is $5.0 \times 10^{-13}\exp(300/T)^{1/2}$ (Inoue & Tsuchiya, 1975). The rate coefficient of excitation is given by $k_j^{ex} = k_j^{de}\exp(-3350/T)$. For the vibtational-vibrational transition, we consider O, O_2, N_2, and $[CO_2]$, whose rate coefficients are tabulated in table 3.4 (Funke et al., 2012, and references therein).

The escape probabilities depend on the optical depth of each band. We use similar dependences of the optical depth of escape probability for 4.3μm and 15μm bands, for simplicity. Based on the radiative transfer calculation of 15μm band, Kumer & James (1974) estimated the relationship between optical depth and escape probability. Johnstone et al. (2018) fitted the tabular data estimated by Kumer & James (1974), which is given by

$$\varepsilon = \begin{cases} 0.7202(\tau_{CO_2})^{-0.613} & \text{if } \tau_{CO_2} > 2 \\ 0.4732(\tau_{CO_2})^{-0.0069} & \text{if } \tau_{CO_2} < 2, \end{cases} \tag{3.43}$$

where τ_{CO_2} is the optical depth. The optical is given by $\tau_{CO_2} = \sigma_{CO_2}\int_r^\infty n_{CO_2}dr$, where σ_{CO_2} is the absorption cross-section. For the absorption cross-section, we use 6.43×10^{-15} cm^2 for 15μm band and 2.47×10^{-14} cm^2 for 4.3μm band (Zahnle et al., 2019). Since the radiation filed is isotropic, escape probability in the optically thin limit becomes 0.5.

For radiation cooling of NO, the emission in the vibrational band at 5.3μm dominates. We adopt the model of Oberheide et al. (2013), which considered collisional excitation and de-excitation by O atom and radiative excitation by stellar insolation. The model includes the transition between ground to the first

excited state in the vibrational mode. The cooling rate is given by

$$Q_{\rm NO}^{\rm rad} = (h\nu)_{5.3\mu m} A_{\rm NO}^{\rm sp} [{\rm NO}^*], \tag{3.44}$$

where $(h\nu)_{5.3\mu\rm m}$ is the energy of photon at 5.3 μm ($= 3,75 \times 10^{-13}$ erg), $A_{\rm sp}^{\rm NO}$($=$ 12.54 s^{-1}) is the Einstein coefficient for spontaneous emission, and [NO*] is the number density of excited NO. We assume escape probability is unity as done in Johnstone et al. (2018) because cooling of NO is only significant in the thermosphere. As in CO_2, the number density of exited NO can be written as

$$[{\rm NO}^*] = \frac{k_{\rm O}^{\rm ex} n_{\rm O} + P_{\rm E}}{(k_{\rm O}^{\rm ex} + k_{\rm O}^{\rm de}) n_{\rm O} + A_{\rm NO}^{\rm sp}} n_{\rm NO}, \tag{3.45}$$

where $P_{\rm E}$($= 1.06 \times 10^{-4}$ s^{-1}) is the excitation rate due to earthshine and $k_{\rm O}^{\rm de}$($=$ 2.8×10^{-11} cm^3) s^{-1} and $k_{\rm O}^{\rm ex} = k_{\rm O}^{\rm de} \exp(-2700/T)$ are the collisional de-excitation and excitation rate by O atom, respectively (Oberheide et al., 2013).

For radiative cooling of O, the emission arises from the transition of the fine structure of the electronic state (OI lines). We adopt the parameterization derived by Bates (1951) (see also Banks & Kockarts (1973)), which assume collisional frequency is high enough to ensure the level population according to the Boltzmann distribution. The model considers three level population of ground (^{3}P$_2$) and first (^{3}P$_1$) and second (^{3}P$_0$) excited states. The cooling rate is given by

$$\begin{aligned} Q_{\rm O}^{\rm rad} = & \frac{1.67 \times 10^{-17} \exp(-228/T) n_{\rm O}}{1 + 0.6 \exp(-228/T) + 0.2 \exp(-326/T)} \\ & + \frac{4.59 \times 10^{-20} \exp(-326/T) n_{\rm O}}{1 + 0.6 \exp(-228/T) + 0.2 \exp(-326/T)}. \end{aligned} \tag{3.46}$$

In Eq. 3.46, first term and second term in the right side correspond to the emission at 63μm (^{3}P$_1 \rightarrow ^3$ P$_2$) and 147μm (^{3}P$_0 \rightarrow ^3$ P$_1$), respectively. In this model, escape probability assumes unity. Assumption of the level population also overestimates the radiative cooling rate of O atom because the cooling is effective in the higher region of the upper atmosphere, where the collisional frequency is low.

For cooling by H_2O, we use the analytical formula for rotational bands given by Hollenbach & McKee (1979). Detailed explanation and summary of equations are also found in Kasting & Pollack (1983). In this model, they assumed that excitation arises from collisions with H atom because the model originally applied to interstellar shock. This assumption results in an underestimation of

the cooling rate. However, it is no influence on results because radiation cooling of H_2O is ineffective in our interest situation shown in result sections.

In summary, the total radiative cooling rate is obtained by

$$Q^{\rm rad} = Q^{\rm rad}_{\rm CO_2,15\mu m} + Q^{\rm rad}_{\rm CO_2,4.3\mu m} + Q^{\rm rad}_{\rm NO} + Q^{\rm rad}_{\rm O} + Q^{\rm rad}_{\rm H_2O}. \tag{3.47}$$

We calculate radiative cooling rate in each layer using Eq.3.47.

3.2.1.8 Lower boundary condition and parameters

We assume that temperature and composition are constant with time in the lower boundary. The boundary condition is derived by the lower atmospheric model used in $ 2.2.4. To determine the boundary condition, we perform the following procedure : Firstly, we determine the equilibrium state of the lower atmosphere for a given surface partial pressure of CO_2, O_2, N_2. For the lower boundary, we take the temperature compositions, which are mixing ratios of CO_2, O_2, N_2, and H_2O, at the pressure of 100 Pa from the result of the lower atmospheric model. Finding equilibrium state, we use the inverse method (Kasting et al., 1993), though time forwarding method is used in $ 2.2.4. This is because the forwarding method results in cold stratosphere due to lacking ozone heating effect. The inverse method assumes temperature structure: adiabatic temperature gradient in the convective troposphere and isothermal stratosphere. Given temperature structure, this model finds the radiative equilibrium state, which means that incoming stellar insolation equals outgoing planetary radiation. We assume that the temperature at the stratosphere is 200K, which implicitly assume the heating effect of the ozone. We further assume the intensity of stellar insolation is 0.9 times the present Earth, because the habitable zone is outward for the planet around M-type star. We adopt the visible and IR spectrum of AD Leo, which is originally used in *Atmos* for the spectrum of an M-type star. The surface partial pressure of N_2 and O_2 are assumed to be 0.8 bars and 0.2 bars, respectively. We discuss the effect of partial pressure of O_2 on the structure of the upper atmosphere and the detectability in § 3.4.2.4.

We treat partial pressures of CO_2 as a parameter. The theoretical study in Part 1 shows that ocean planets with a massive ocean larger than the several tens of $M_{\rm oc,\oplus}$ have two extreme climates: CO_2-poor cold one and CO_2-rich hot one. Thus, we investigate the dependence of the CO_2 abundance on the upper atmospheric structure. We vary CO_2 abundance from 10^0 to 10^5 Earth's

Table 3.5: Parameters for upper atmosphere

Parameters	Values
Partial pressure of CO_2	1×10^0–1×10^5 PAL
Planetary mass	$0.1, 0.2, 0.5, 1 M_\oplus$

abundance (PAL: 3.3×10^{-4} bars). We also treat planetary mass as a parameter because the upper atmospheric structure depends on the planetary gravity. We use $M_\mathrm{p} = M_\oplus$ for nominal value and vary it over the range between 0.1 and 1 $M_\oplus$. Parameters used in our model are summarized in table 3.5. Fig. 3.3 shows lower boundary condition as a function of CO_2: (a) Volume mixing ratio of CO_2, O_2, and N_2. (b) Altitude at the lower boundary for four different values of the planetary mass. The volume mixing ratio of CO_2 varies over wide range between 3.3×10^{-6} and 0.97. The mixing ratio of H_2O, which is not shown, is constant value of 4.0×10^{-6} because of the cold trap in the traposphere. The larger partial pressure of CO_2 and/or the small planetary mass, the larger altitude at the lower boundary is, because we assume that lower boundary is defined as the altitude where total pressure is 100 Pa.

The planetary radius, defined at the ocean surface R_s, is calculated by the mass-radius relationship given by Valencia et al. (2007b):

$$R_\mathrm{s} = R_\oplus \left(\frac{M_\mathrm{p}}{M_\oplus}\right)^{0.262}. \tag{3.48}$$

In this formula, we neglect the effect of ocean on the planetary radius, for simplicity.

3.2.1.9 Numerical procedure

We calculate temperature and compositional structure of the upper atmosphere for a given partial pressure of CO_2 and planetary mass. We divide the atmosphere into layers whose thickness increases with altitude. We assume that the thickness of the bottom layer is 2km and the thickness ratio of neighbouring layers is 1.015. The physical quantities in each cells are defined at the center of the cell. We add the layer into the top layer to satisfy Kn of top layer becomes $0.7 \leq Kn \leq 1.3$.

We investigate stedy-state solution of the upper atmosphere from the lower boundary to the exobase. Starting from the arbitrary condition, the time-dependent Eqs. (3.1) and (3.3) are solved until steady-state values are obtained.

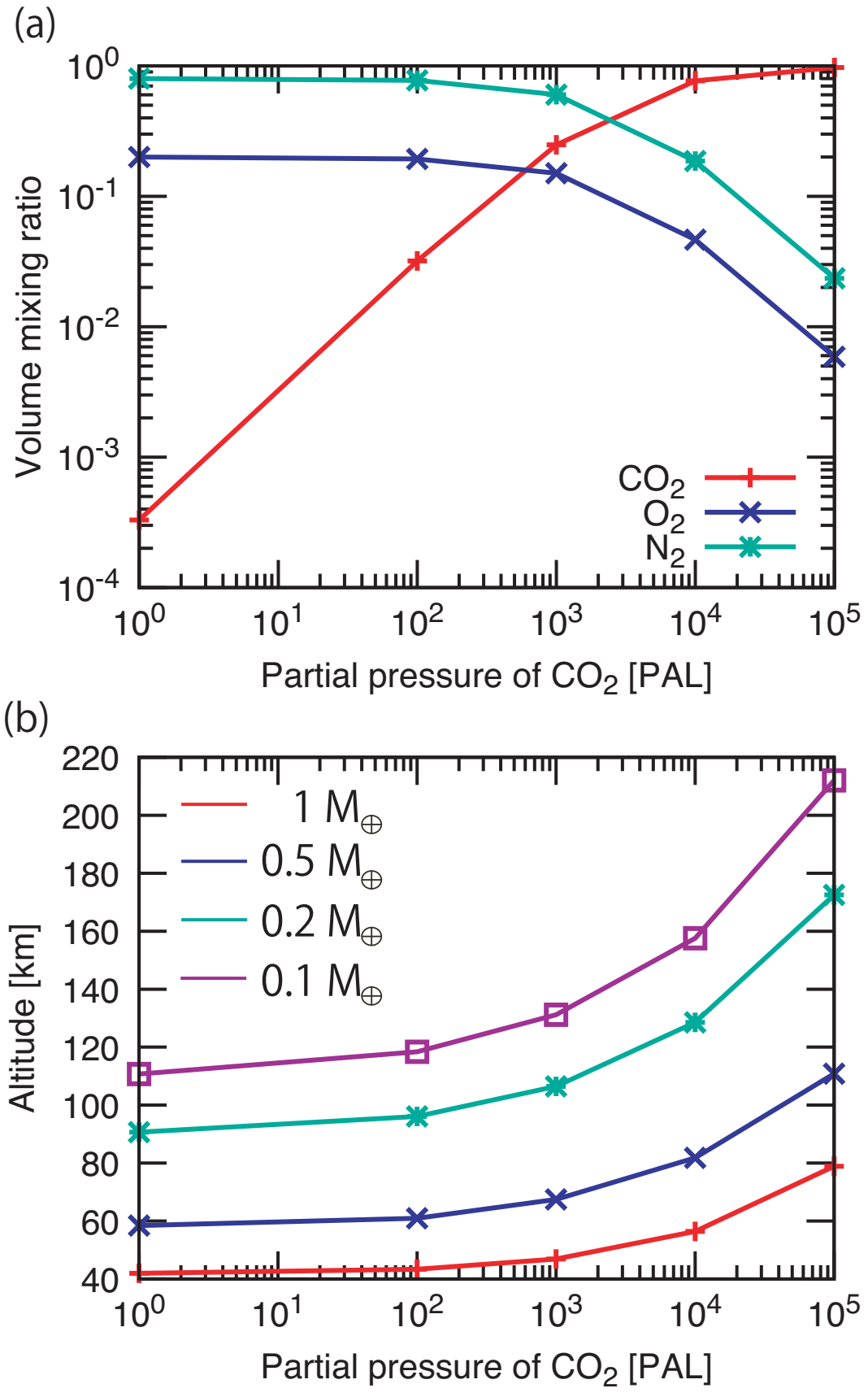

Figure 3.3: Lower boundary condition as a function of partial pressure of CO_2 used in our model. Panel(a) shows volume mixing ratio of CO_2 (red solid line), O_2 (blue solid line), and N_2 (green solid line). Panel(b) shows altitude of lower boundary for four different values of the planetary mass.

For the initial condition, the condition where the atmosphere is perfectly mixed is used: the temperature and mixing ratios of all layers are same as lower boundary conditions. For the criteria of convergence, we introduce variable:

$$\Delta_\Theta = \frac{1}{\Theta}\frac{d\Theta}{dt}, \tag{3.49}$$

where Θ is the physical quantity. When Δ_Θ of all physical quantities become less than 10^{-5} in all layers, we judge that the calculation is converged. We also stop the calculation when the Jeans escape parameter becomes unity because hydrodynamic escape would proceed and the assumption of hydrostatic equilibrium is no longer valid if the Jeans escape parameter is less than 1.5 (e.g., Watson et al., 1981).

Our model is a very stiff system because the temperature and the reaction rate are closely related and the collision frequency (i.e., the reaction rate) changes greatly with the altitude. Thus, we use an implicit solver of *DLSODE* with the backward differential formula (Hindmarsh, 1983) for the time integration. It is a suitable solver for a stiff ODE system, like the chemical network (e.g., Grassi et al., 2014). We adopt that the relative and absolute tolerances for solver are 10^{-3} and 10^{-12}, respectively. Allowing the hydrostatic condition, we calculate the density structure from Eq.(3.8) using obtained temperature and mean molecular weight structure from time-dependent equations. Then, we update the number density of each species at each location every time step, satisfying $\rho = \sum_j m_j n_j$.

The diffusion fluxes are calculated from the finite volume method. Thus, we estimate diffusion fluxes at the cell boundary. To stabilize diffusion fluxes, we estimate physical quantities and their radial derivatives at the cell boundary using the natural cubic spline function with third-order accuracy. We have confirmed that our model reproduces the upper atmosphere of the present Earth (Picone et al., 2002) and previous studies attempting to the effect of CO_2 abundance (Johnstone et al., 2018) well. Detailed comparison is given in Section B.

3.2.2 Transmission Spectrum Model

In this section, we give the procedure to estimate the absorption line profile for OI during the transit of the planet, using the oxygen number density and temperature at the exobase obtained in 3.2.1. First, we show the model of the density structure of the oxygen corona (§ 3.2.2.1). Next, we show the method to estimate absorption profiles of OI line, using the density structure of the oxygen geocorona (§3.2.2.2).

3.2.2.1 Density structure of the oxygen corona

We assume the oxygen corona is spherically symmetric. This assumption is supported by the observation of hydrogen geocorona around the Earth (Kameda et al., 2017). The observation also suggest that the magnetic field has a small influence on the density structure of the geocorona. Thus, we adopt the analytical model presented by Chamberlain (1963) which does not consider magnetic effects. We neglect the effect of stellar radiation pressure, which overestimates the number density in outer corona and absorption of OI line, for simplicity. However, we have confirmed that the radiation pressure is negligible effect, even the radiation pressure is 10 times that of the present Sun received by the Earth.

In this model, the density structure is determined by three parameters: the exobase temperature, density, and altitude. For briefly, we omit the subscript O from the number density (n), mass (m), and escape parameter (ζ) hereafter. The density structure of the oxygen is expressed by

$$n(r) = n_{\rm exo} \exp\left(-\frac{E_{\rm r}}{kT_{\rm exo}}\right) \omega, \tag{3.50}$$

where $E_{\rm r}$ is the difference of the gravitational potential between that at the exobase and that at r and ω is the partition function. $E_{\rm r}$ is given by

$$E_{\rm r} = \frac{GM_{\rm p}m}{r_{\rm exo}} - \frac{GM_{\rm p}m}{r}. \tag{3.51}$$

The partition function is composed of three components (or classes of orbit): the ballistic, $\omega_{\rm bal}$, satellite, $\omega_{\rm sat}$, and escape components $\omega_{\rm esc}$. Each of partition functions are expressed as

$$\omega_{\rm bal} = \frac{2}{\sqrt{\pi}}\left[\gamma\left(\frac{3}{2},\zeta\right) - \frac{\sqrt{\zeta_{\rm exo}^2-\zeta^2}}{\zeta_{\rm exo}} \exp\left(-\frac{\zeta^2}{\zeta+\zeta_{\rm exo}}\right)\gamma\left(\frac{3}{2},\frac{\zeta\zeta_{\rm exo}}{\zeta+\zeta_{\rm exo}}\right)\right], \tag{3.52}$$

$$\omega_{\rm sat} = \frac{2}{\sqrt{\pi}}\frac{\sqrt{\zeta_{\rm exo}^2-\zeta^2}}{\zeta_{\rm exo}} \exp\left(-\frac{\zeta^2}{\zeta+\zeta_{\rm exo}}\right)\gamma\left(\frac{3}{2},\frac{\zeta\zeta_{\rm exo}}{\zeta+\zeta_{\rm exo}}\right), \tag{3.53}$$

Table 3.6: Oxygen transition

Transition	Wavelength (nm)	Oscillator strength
$^3P_2 \rightarrow ^3S_0$	130.2168	5.20×10^{-2}
$^3P_1 \rightarrow ^3S_0$	130.4548	5.18×10^{-2}
$^3P_0 \rightarrow ^3S_0$	130.6029	5.19×10^{-2}

$$\omega_{\rm esc} = \frac{1}{\sqrt{\pi}} \left[\Gamma\left(\frac{3}{2}\right) - \gamma\left(\frac{3}{2}, \zeta\right) - \frac{\sqrt{\zeta_{\rm exo}^2 - \zeta^2}}{\zeta_{\rm exo}} \exp\left(-\frac{\zeta^2}{\zeta + \zeta_{\rm exo}}\right) \left\{ \Gamma\left(\frac{3}{2}\right) - \gamma\left(\frac{3}{2}, \frac{\zeta\,\zeta_{\rm exo}}{\zeta + \zeta_{\rm exo}}\right) \right\} \right], \tag{3.54}$$

where Γ is the complete gamma function and γ is the incomplete gamma function. Consequently, the total partition function used in (3.50) is

$$\omega = \omega_{\rm bal} + \omega_{\rm sat} + \omega_{\rm esc}. \tag{3.55}$$

We calculate the spherically symmetric density structure of the oxygen corona, using Eqs.(3.50), (3.51), and (3.55).

3.2.2.2 Transmission model

Absorption of OI lines are caused by transitions of the electronic state of oxygen among $^3P_2$, $^3P_1$, $^3P_0$, and $^3S_0$. All of the transitions, which are interested, are summarised in table 3.6. In the table, we also show wavelengths of the line center, λ_0, and oscillator strength, f_0, of each absorption line. The values of them are taken from NIST[1].

The absorption cross-section of each line can be characterised by the position of the line center, strength, and profile. The absorption cross-section at wavenumber, ν, is generally written as

$$\sigma(\nu) = \sigma_0 \Psi(\nu), \tag{3.56}$$

where σ_0 is the absorption cross-section at the line center and $\Psi(\nu)$ is the line profile function. We only consider the Doppler broadening which arise from random motion of the gas, because of low pressure. Using the oscillator strength, the absorption cross-section at the line center is given by (e.g., Rybicki & Lightman, 1986)

$$\sigma_0 = \frac{\sqrt{\pi} e^2}{m_e c} \frac{f_0}{\alpha_D}, \tag{3.57}$$

[1] https://www.nist.gov/pml/atomic-spectra-database

where e is the elementary charge, c is the speed of light, and α_D is the Doppler width. α_D is written by

$$\alpha_{\rm D} = \nu_0 \sqrt{\frac{2k_{\rm B}T}{m_{\rm O}c^2}}, \tag{3.58}$$

where $\nu_0 (= 1/\lambda_0)$ is the wavenumber at the line center, The line profile function of the Doppler broadening is

$$\Psi(\nu) = \frac{1}{\alpha_{\rm D}\sqrt{\pi}} \exp\left(-\frac{(\nu-\nu_0)^2}{\alpha_{\rm D}^2}\right). \tag{3.59}$$

We assume that the temperature of the oxygen corona is same as that at the exobase, for simplicity. For the level population of the oxygen, we assume level population does not change within the corona. we also assume that the Boltzmann distribution is achieved because of high collisional frequency within the exobase. Thus, number density of each level is given by

$$[{\rm O}]_{^3{\rm P}_0} = \frac{0.2\exp(-326/T)n_{\rm O}}{1+0.6\exp(-228/T)+0.2\exp(-326/T)}, \tag{3.60}$$

$$[{\rm O}]_{^3{\rm P}_1} = \frac{0.6\exp(-228/T)n_{\rm O}}{1+0.6\exp(-228/T)+0.2\exp(-326/T)}, \tag{3.61}$$

$$[{\rm O}]_{^3{\rm P}_2} = \frac{n_{\rm O}}{1+0.6\exp(-228/T)+0.2\exp(-326/T)}. \tag{3.62}$$

We simulate the transmission spectra following the method given by Brown (2001). Without planetary transit, light emitted from the star is directly observed because emission from the planet is quiet small for OI lines. Observed luminosity without planetary transit is the disk-integrated luminosity, $L_{\rm s}$, which is given by

$$L_{\rm s}(\lambda) = \int_0^{R_{\rm s}} F_{\rm s}(\lambda) 2\pi r dr, \tag{3.63}$$

where $R_{\rm s}$ is stellar radius and $F_{\rm s}$ is the stellar flux. Here we assume incident stellar light rays to the planet are parallel because planetary orbital distance in the habitable zone is much larger than the stellar radius. During the planetary transit, observed stellar luminosity at wavelength, λ, is given as

$$L_{\rm obs}(\lambda) = \int_0^{R_{\rm s}} F_{\rm s}(\lambda)\exp(-\tau(r,\lambda)) 2\pi r dr, \tag{3.64}$$

where $\tau(r,\lambda)$ is the tangential optical depth. $\tau(r,\lambda)$ is defined by

$$\tau(r,\lambda) = 2\int_0^{\infty} \sigma(r,s,\lambda) n_{\rm o} ds, \tag{3.65}$$

where ds is the line element along the line of sight. Since individual absorption line is clearly separated, we separately calculate the optical depth of absorption lines. The transit depth at wavelength, λ, can be written as

$$D_{\rm transit} = \frac{L_{\rm s}(\lambda) - L_{\rm obs}(\lambda)}{L_{\rm s}(\lambda)}, \tag{3.66}$$

We assume planetary atmosphere below the lower boundary is optically thick enough to shut the stellar flux off. This assumption has a small influence on the results because the absorption bellow the lower boundary is relatively small to the expanded corona.

Stellar radiations of OI lines without planetary transit are observed. Thus, we can use the observed spectrum for the input spectrum in actual comparison. In this model, we adopt observed spectrum of the Proxima Centauri which is an M-type star, as an example. We take the spectrum from StartCAT which is a catalog of high resolution ultraviiolel spectra record by Hubble Space Telescope (Ayres, 2010). Fig. 3.4 shows observed spectrum from 130 to 130.8 nm. Peaks at about 130.2, 130,5, and 130.6 nm correspond to emission lines of OI. The observed spectrum also includes emissions from the Earth's geocorona because the orbit of Hubble Space Telescope is not far from the Earth. As done in Tavrov et al. (2018), we fit the spectrum by Gaussian fitting:

$$f(\lambda) = A \exp\left(-\frac{(\lambda - B)^2}{C^2}\right), \tag{3.67}$$

where A, B, and C are fitting parameters which are tabulated in Table 3.7. Fig. 3.5 shows the observed spectrum and its fitting of $^3\mathrm{P}_0 \rightarrow ^3\mathrm{S}_0$ transition. In the figure, we also show the Gaussian fitting of Earth's emission line. As shown in the figure, the position of line center in the stellar spectrum is shifted from that of gaseous emission line (see Table 3.6) because star has a proper motion against the Earth. Thus, we use the position of line center shown in Table 3.6, instead of the parameter of B. For $R_{\rm s}$, we also use the value of Proxima Centauri ($0.141 R_\odot$) (Boyajian et al., 2012).

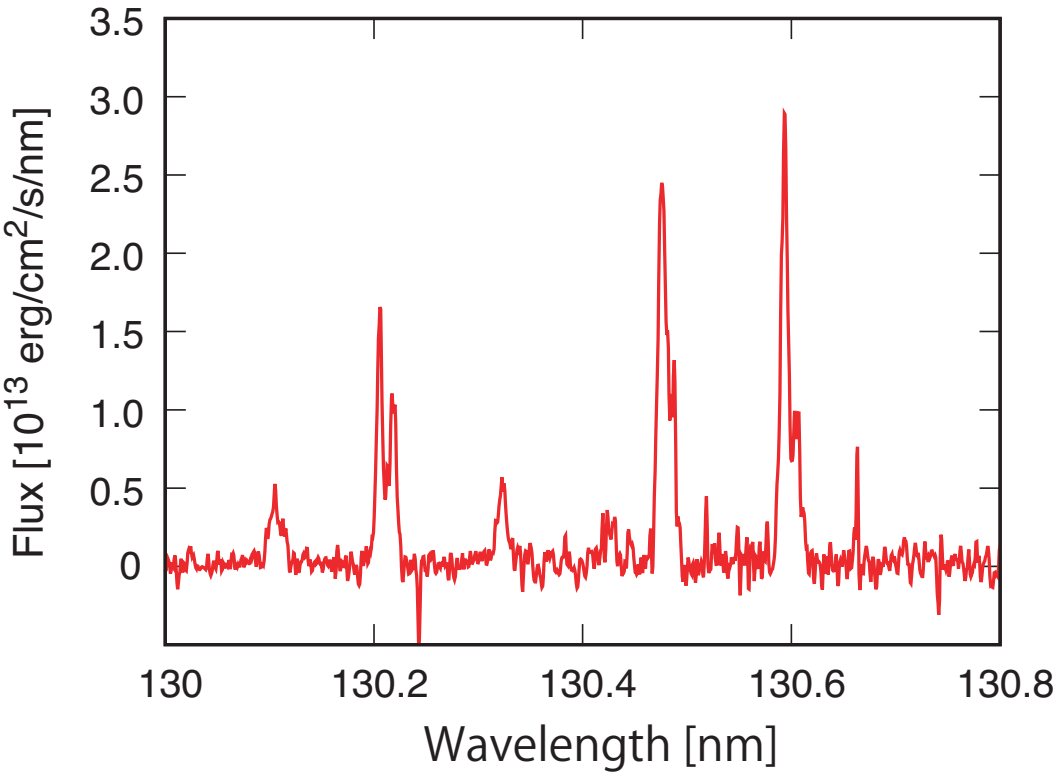

Figure 3.4: Obseved spectrum of Proxima Centauri. Peaks at about 130.2, 130.5, and 130.6 nm correspond to emission lines of OI.

Table 3.7: Fitting parameters of stellar OI lines

Transition	A	B	C
$^3P_2 \rightarrow ^3S_0$	1.7×10^{-13}	130.2056	5.2×10^{-3}
$^3P_1 \rightarrow ^3S_0$	2.5×10^{-13}	130.4759	7.4×10^{-3}
$^3P_0 \rightarrow ^3S_0$	2.8×10^{-13}	130.5933	6.6×10^{-3}

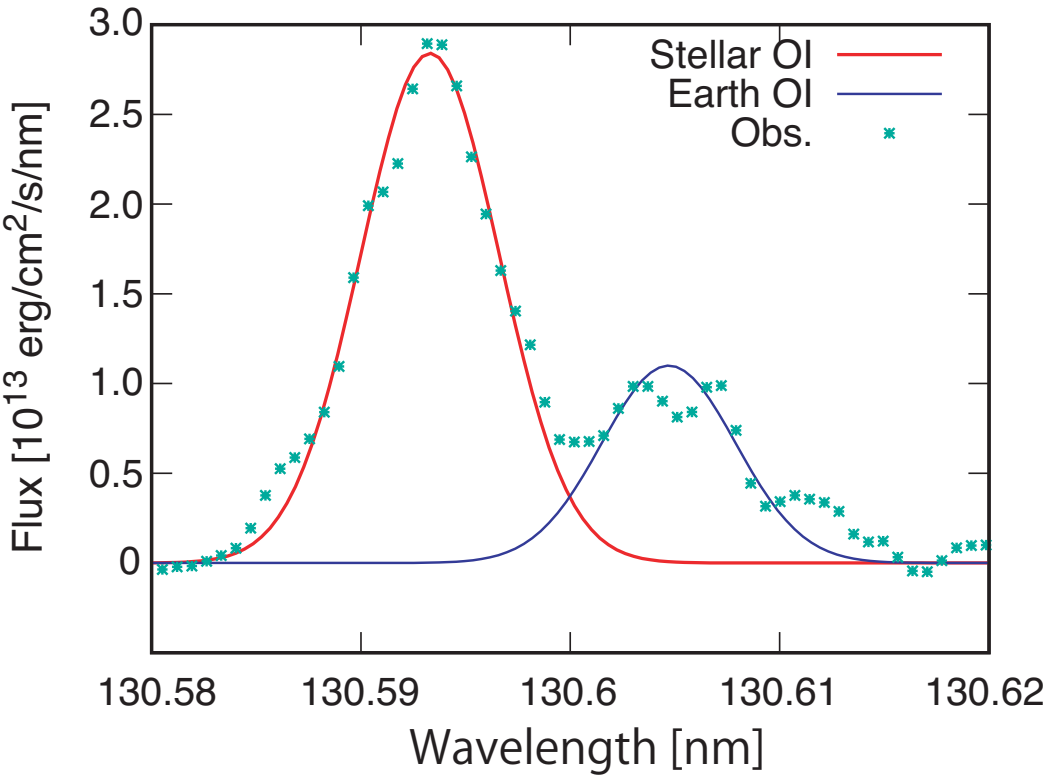

Figure 3.5: Spectrum of OI line around 130.6 nm. The red line is Gaussian fitting for emission from the Proxima Centauri. The blue line is Gaussian fitting for emission from the Earth. The green symbols are observed spectrum by Hubble Space Telescope.

3.3 Results

3.3.1 Structure of Upper Atmosphere

In this section, we show the structure of the upper atmosphere with a focus on the effects of the partial pressure of CO_2, P_{CO_2}, and planetary mass, M_p. First, we detail the structure of the upper atmosphere for an Earth-mass planet with a CO_2-rich atmosphere orbiting an M-type star. Next, we examine the dependence on P_{CO_2} (§ 3.3.1.1) and on M_p (§ 3.3.1.2).

We show the temperature structure of the atmosphere in the steady state in Fig. 3.6. In the calculation, we assume $M_p = 1M_\oplus$ and $P_{CO_2} = 1 \times 10^4$ PAL. The overall structure is as follows. In the lower most part of the atmosphere (or the stratosphere), the temperature inversion occurs and the maximum temperature is about 360 K at the altitude of 60 km. Above the stratopause, the temperature decreases with altitude and reaches a minimum of about 174 K at the altitude of 97 km (mesopause). Above that, the temperature increases rapidly with altitude. The temperature is 911 K at the exobase located at about 200 km, above which the structure is nearly isothermal.

This structure is determined by the heating and cooling processes shown in Fig. 3.7. Although the net heating is balanced with radiative cooling at each altitude in a steady state, the heating/cooling include several different processes, the rates of which change with altitude. Fig. 3.7 shows the overall heat budget at each altitude. The heating involving high-energy photons (i.e., $Q_{chem} + Q_{UV} + Q_{PE}$) occurs mainly above the mesopause. In particular, the chemical heating (blue) is the dominant heating source in the thermosphere where is the region above the mesopause. On the other hand, radiation cooling is most effective around the mesopause and the cooling rate per unit mass decreases with altitude. The thermal conduction transports heat from the thermosphere toward the mesopause, as realized from the fact that $Q_{cond} > 0$ around the mesopause. Thus, the energy balance is archived at the steady state. Below the mesopause, the radiation cooling is balanced with the IR-heating locally because the conduction is ineffective.

Panel(a) in Fig. 3.8 shows contributions of heating processes in detail. The heating of the thermo-chemical reaction of ion species, which is labeled as Chem-Ion, and photo-electron dominants at the thermosphere. Those heating is much larger than the heating due to dissociation and thermo-cheamical reaction of neu-

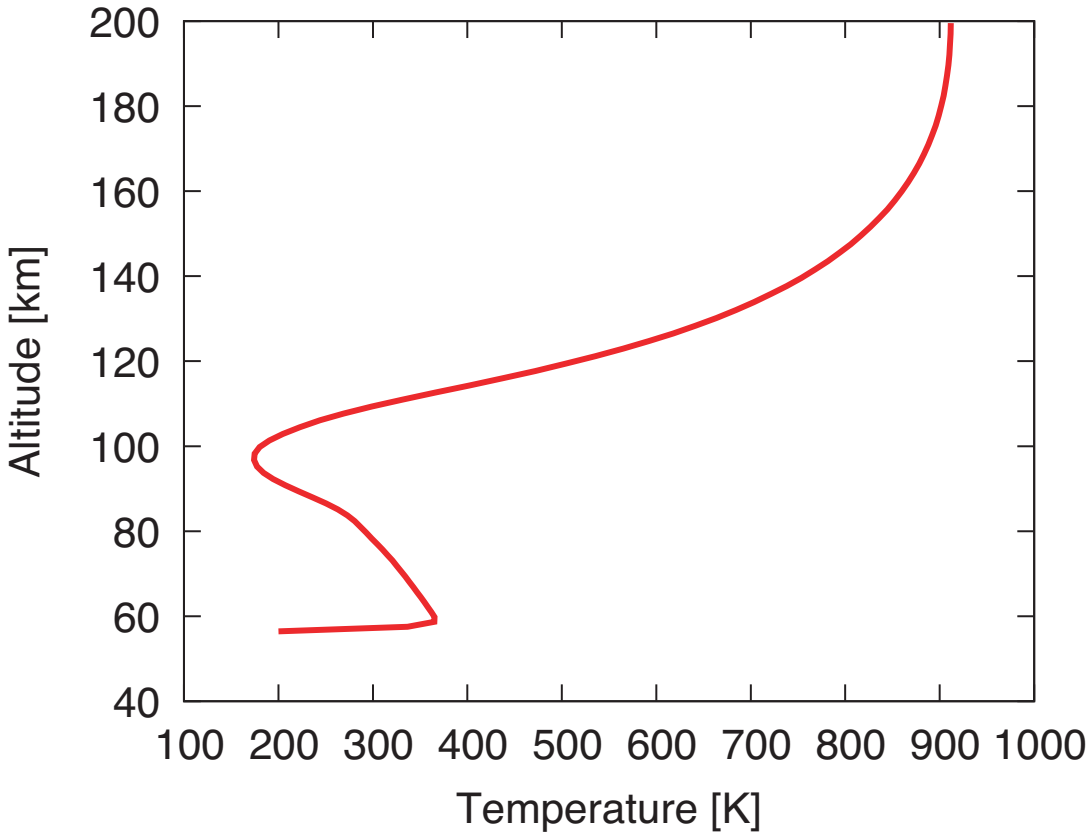

Figure 3.6: Temperature profile in the upper atmosphere for the planet mass $M_{\rm p} = 1 M_{\oplus}$ and the atmospheric CO_2 partial pressure $P_{CO_2} = 1 \times 10^4$ PAL.

tral species, which is labeled as Chem-Neutral, because the photo-reaction resulting ionizations is induced by photons with higher energy (or shorter wavelength) than that of dissociative reaction. However, the heating involving the photo-reaction significantly decreases with decreasing altitude around the mesopause optical depth at almost EUV wavelength becomes unity. Below the mesopause, IR-heating is much larger than $Q_{\rm chem} + Q_{\rm UV}$, while $Q_{\rm chem} + Q_{\rm UV}$ involving oxygen chemistry is the dominant heating source in the present Earth (e.g., Johnstone et al., 2018). This arises from three reasons. One is that an M-type star has a red-shifted spectrum at the visible and IR wavelength, which enhances the absorption by CO_2. Another is that the intensity of the near-UV spectrum of an M-type star is generally much weaker than that of the Sun (e.g., France et al., 2016), which weakens the dissociation rate of O_2 and O_3. The other is that the mixing ratio of O_2 (CO_2) is smaller (larger) than that of the present Earth because we assume CO_2-rich atmosphere.

Panel(b) in Fig. 3.8 shows contributions of radiative coolants to the radiative

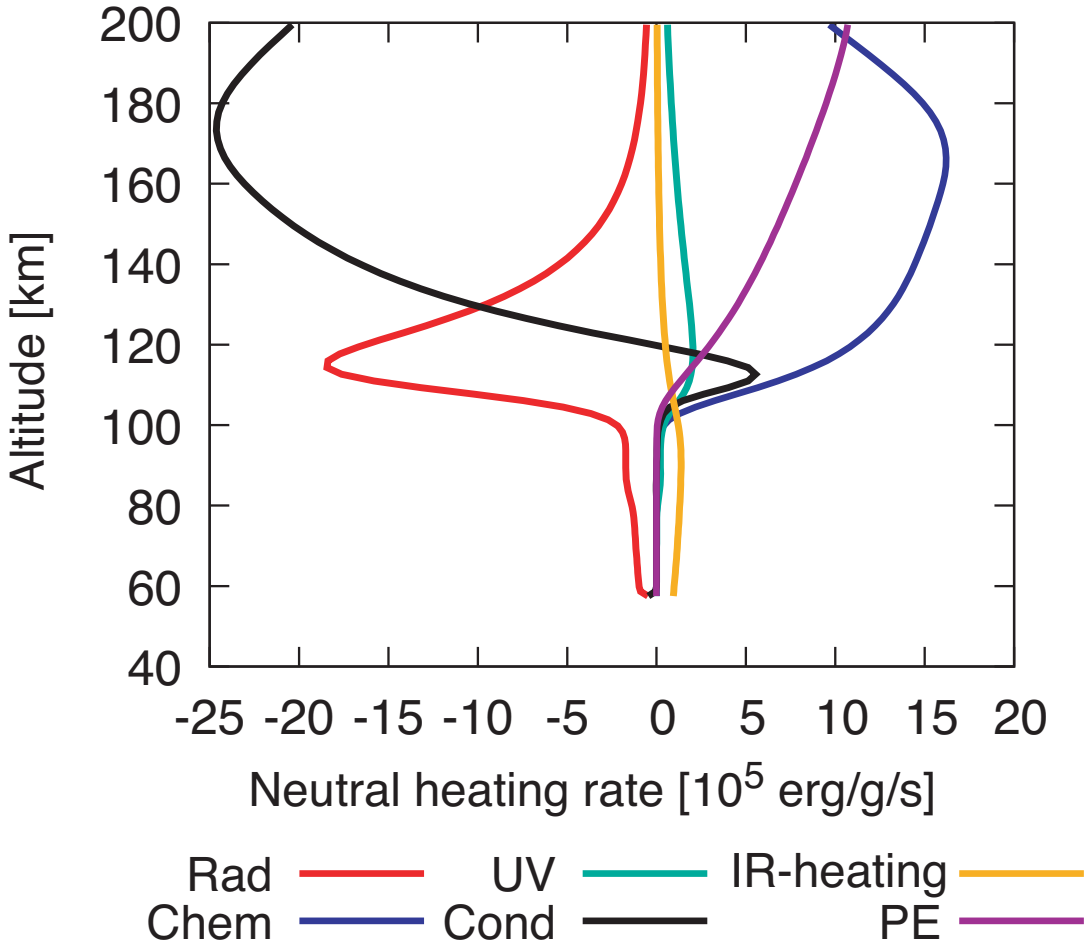

Figure 3.7: Profiles of heating and cooling rates for several processes : those for the radiative cooling (red; "Rad"), heating by thermo-chemical reaction (blue; "Chem"), UV absorption (green; "UV"), thermal conduction (black; "Cond"), heating by absorption of stellar infrared irradiation (yellow; "IR-heating"), and heating by photo-electrons (purple; "PE").

cooling. CO_2 is the dominant cooling source in almost region. The radiative cooling of oxygen is effective only in the top of the atmosphere. The cooling of NO is much smaller than the cooling of CO_2 and its influence on the temperature structure is small, while the cooling of NO dominants in the thermosphere of the present Earth (e.g., Roble et al., 1987). This is because a low mixing ratio of N_2 and O_2 at the lower boundary results in small NO abundance. Likewise, H_2O radiation is negligible because of low abundance. The radiative cooling excepting CO_2 is simply understood by the local abundance and temperature because of no radiative excitation.

The behavior of CO_2 radiation is somewhat complicated because several exci-

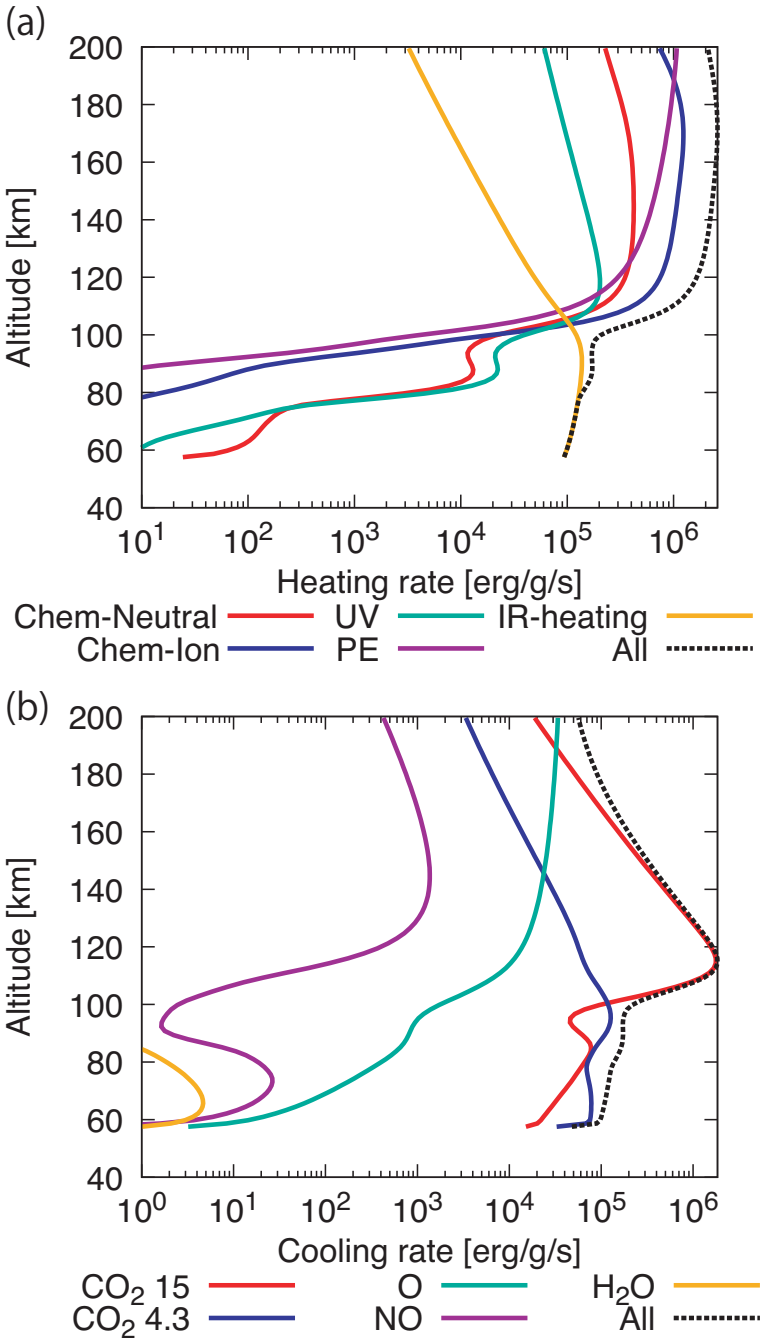

Figure 3.8: Profiles of heating and cooling rates for several processes : (*a*) enlarged view of the profiles only of the heating rates for thermo-chemical reaction of neutral species (red; "Chem-Neutral"), thermo-chemical reactions of ion species (blue; "Chem-Ion"), UV absorption (green; "UV"), reactions with photo-electrons (purple; "PE"), absorption of stellar infrared irradiation (yellow; "IR-heating"), and sum of them (black dashed; "All"); (*b*) enlarge view of the profiles only of the radiative cooling rates for CO_2 emission at 15 μm (red; "CO_2 15"), CO_2 emission at 4.3 μm (red; "CO_2 4.3"), O emission (green; "O"), NO emission (purple; "NO"), H_2O emission (yellow; "H_2O"), and sum of them (black dashed; "All").

tation mechanisms are included. Fig. 3.9 shows absorption and emission of CO_2 in each band. Solid lines and dashed lines indicate the emission and absorption of each band, respectively. The absorption at a longer wavelength (15 μm) is much weaker than the absorption at a shorter wavelength (4.3 μm) and its radiative excitation is negligible. Thus, cooling rates are determined by the balance between the radiative excitation at 4.3 μm, collisional excitation/de-excitation, and the vibtational-vibrational transition. In the thermosphere, the emission at 15 μm is determined by the collisional excitation/de-excitation because the excitation temperature is small. Otherwise, the emission at 4.3 μm is mainly determined by radiative excitation and collisional processes is a small influence because the excitation temperature is large. Below the mesopause, the sum of emission rates is balanced with the absorption rate locally. CO_2 does not radiate all of the absorbed energy at 4.3 μm because collisional de-excitation and the vibrational-vibrational transition are faster than the spontaneous emission. Removed energy via collisional de-excitation converts into heats and, subsequently, results in high temperature. Then, high temperature enhances the collisional excitation and the radiative cooling at 15 μm. The temperature increases until the energy balance is achieved. Thus, the temperature inversion at the stratosphere is formed. Absorption of H_2O, which is not shown, is much smaller than the CO_2 absorption because of low abundance.

Next, we show the number density structure of several important species in Fig. 3.10. Panel(a) shows the number density structure of neutral species. In the lower part of the atmosphere below about the mesopause, eddy diffusion mixes the atmosphere. Thus, major constitutes are the same as the lower boundary condition. Although chemical species resulted from photo-chemical reactions (e.g., atomic species) are present, their mixing ratio is relatively small. Since a large number density leads to efficient thermo-chemical reactions, complex compounds (e.g., O_3) are also formed. Above the mesopause, photo-chemical reactions and molecular diffusion result in lighter species (e.g., atomic species and CO). Their abundance increases with the altitude, as there are the nearly constant number density structures of atomic species. Atomic oxygen becomes the most abundant species, like the present Earth and Venus (e.g., Jacchia, 1977; Hedin et al., 1983).

Panel(b) shows the number density structure of ion species. Major ion constitutes change with the altitude and the structure is determined by ion-neutral

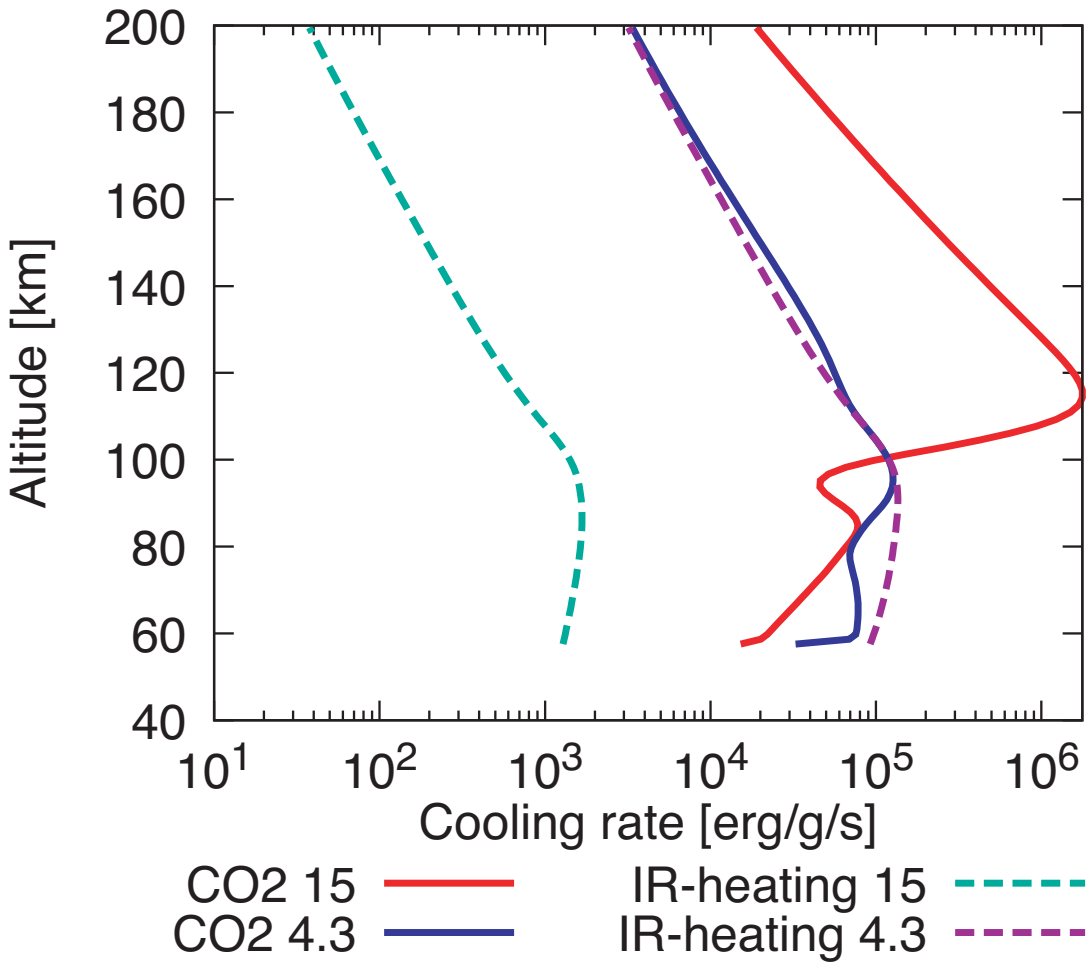

Figure 3.9: Absorption and emission of CO_2. The red and blue solid line mean CO_2 radiation at 15 and 4.3 μm, respectively. The green and purple dashed line mean CO_2 absorption at 15 and 4.3 μm, respectively. Absorption of H_2O is not shown because it is negligible.

reactions, in addition to photo-chemical reactions (e.g., Banks & Kockarts, 1973). Since the high photo-ionization rate and low thermo-reaction rate, ionized atomic species are abundant in the upper part of the atmosphere. In contrast to neutral species, O^+ is relatively small abundance in almost region of the thermosphere. This is because O^+ is quickly lost by the reactions with O_2 and N_2, which produces O_2^+ and NO^+, respectively. Thus, O_2^+ and NO^+ become major ion species. Below the mesopause, O_2^+ abundance decreases with decreasing altitude because of efficient reactions with N and NO, resulting NO^+. Around the lower boundary, H_3O^+ becomes the dominant species, which is formed by the reaction of HCO^+ with H_2O.

Lastly, we examine the source of atomic oxygen in detail because we focus on

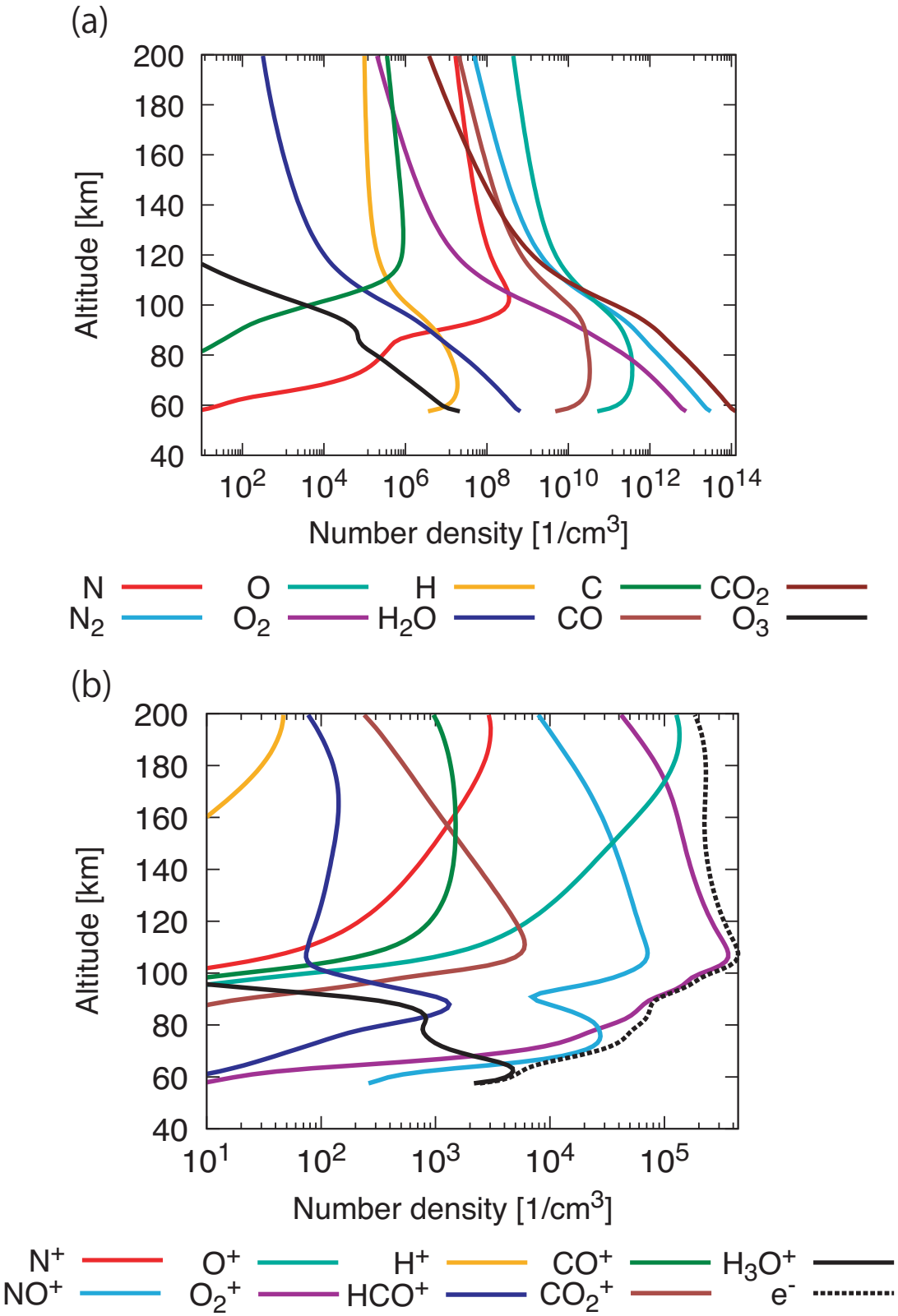

Figure 3.10: Density structure of several important species for the planetary mass $M_p = M_\oplus$ and the partial pressure of CO_2 $P_{CO_2} = 1 \times 10^4$ PAL. Panel (*a*) shows density structure of neutral species. Panel (*b*) shows density structure of ion species.

the oxygen density in the upper atmosphere. In Fig. 3.11, we show production rate of oxygen including O, O(^{1}D), O(^{1}S), and O^+ via photo-chemical reactions. We plot the production rates by three major reactants of O_2, CO, and CO_2. For O_2, production rates are the sum of reactions: No. 2, 3, 5, and 6, which are listed in table C.3. For CO, production rates are the sum of reactions: No. 26, 27, 28, and 29. For CO_2, production rates are the sum of reactions: No. 30, 31, 33, and 34. Production rates have peaks (e.g., $\sim$ 100 km for CO and CO_2), where both of the high number density of a reactant and intense high-energy photon causing dissociation are achieved. In other words, the peak altitude corresponds to the altitude satisfying the optical depth of each reactant at the wavelength to dissociate effectively (e.g., Lyman-α line at 121 nm for CO and CO_2) become about unity. The productions via O_2 reactions are dominant in the lower atmosphere because O_2 can absorb photons at near-UV wavelength. As altitude increases, CO and CO_2 dissociation are effective. Furthermore, those dissociations become the dominant processes for oxygen production in the thermosphere. Thus, the oxygen-rich upper atmosphere can be produced in the CO_2-rich atmosphere. This is also supported by three reasons. One is that absorption cross-sections of CO and CO_2 resulting dissociative ionization are similar to that of O_2 at EUV wavelength (Huebner & Mukherjee, 2015). Another is that the UV spectrum of an M-type star is much weaker than the present Sun's at near-UV wavelength (see Fig. 3.1), which results in O_2 dissociation. The other is that oxygen is the dominant species in Venus's upper atmosphere above about 160 km (Hedin et al., 1983). Further discussion about oxygen production in the condition of a low O_2 mixing ratio is given in § 3.4.2.4.

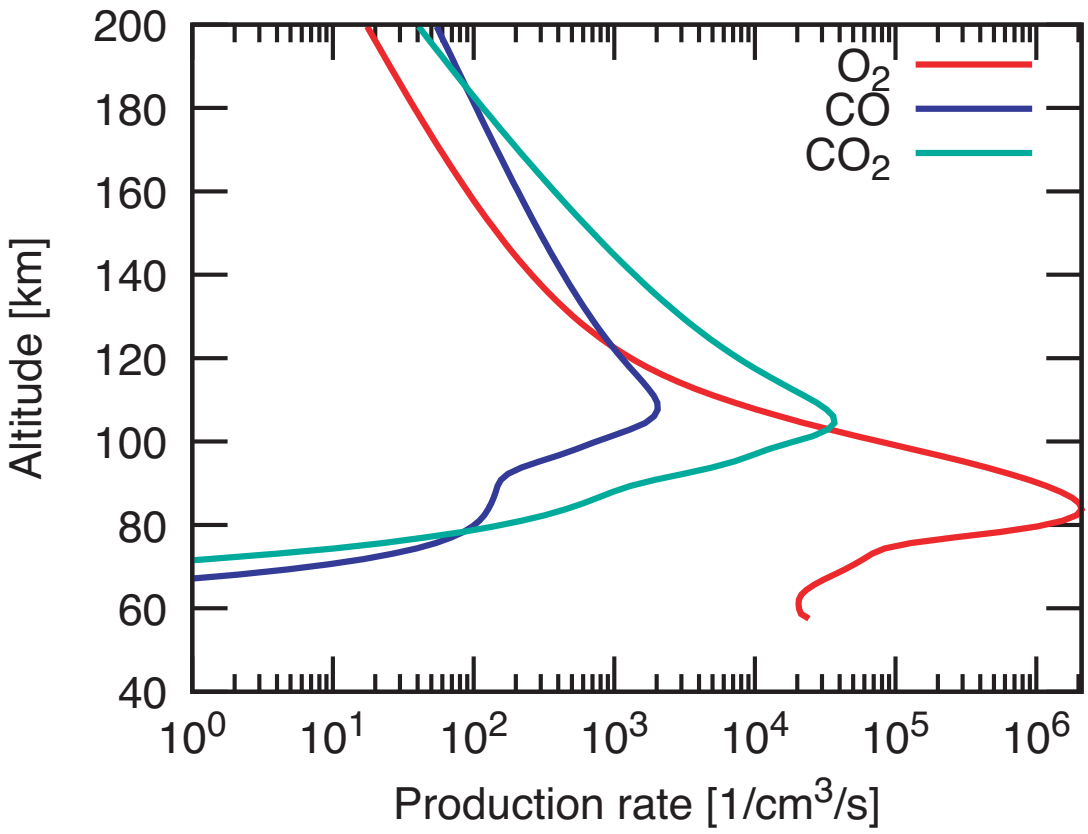

Figure 3.11: Photo reaction rates involving oxygen production for the planetary mass $M_p = M_\oplus$ and the partial pressure of CO_2 $P_{CO_2} = 1 \times 10^4$ PAL. The red, blue, and green lines indicate reactions of O_2, CO, and CO_2, respectively.

3.3.1.1 Dependence on amount of carbon dioxide

Here, we examine the dependence of the upper atmospheric structure on the amount of CO_2. The planetary mass is assumed to be $1M_\oplus$ in calculations shown in this section. The partial pressure of CO_2 is varied over the range between 1×10^2 PAL and 1×10^5 PAL. As shown in Fig. 3.12, decreasing CO_2 abundance leads to a significant increase in the exospheric temperature, which is defined as the temperature at the top of the atmosphere. This is consistent with the previous study attempting to quantify the dependence of the CO_2 abundance on the exospheric temperature (Kulikov et al., 2007). In Fig. 3.12, two different states are found: One is the steady-state with hydrostatic equilibrium for $P_{CO_2} \geq 3 \times 10^2$ PAL, the other is the state with unconverged solution for $P_{CO_2} = 1 \times 10^2$ PAL, where the calculation is artificially stopped because the Jeans escape become unity. In latter, unconverged solution is termed as a hydrodynamic escape regime.

In the case of abundant CO_2 ($P_{CO_2} \geq 3 \times 10^2$ PAL), converged solutions with hydrostatic equilibrium are obtained. As discussed in the above section, converged solutions are achieved by the energy balance between the heating involving high-energy photon and radiative cooling. However, P_{CO_2} affects thermal structure both in the thermosphere and the stratosphere. The exospheric temperature increase from 721 K to 6486 K, as P_{CO_2} decreases from 1×10^5 PAL to 3×10^2 PAL because an decreases in P_{CO_2} weakens the radiation cooling. Then, the altitude at exobase also increases from 1.7×10^2 km to 1.5×10^3 km. P_{CO_2} also affects the maximum temperature of the thermal inversion at the stratosphere, where temperature structure is determined by the balance between the radiative cooling and the IR-heating. This is because the IR-heating rate of CO_2 depends on the number density of CO_2. Thus, local energy balance at the stratosphere is achieved in a lower temperature for a lower P_{CO_2}.

In contrast, when the calculation with CO_2-poor condition ($P_{CO_2} = 1 \times 10^2$ PAL), the energy balance is not achieved and significantly expanded upper atmosphere is formed. The exospheric temperature and the altitude at the exobase become 42715 K and 1.4×10^4 km, respectively. In this case, hydrodynamic escape would be operated and the adiabatic cooling associated with a hydrodynamic flow is effective because the Jeans escape parameter at the top of the atmosphere become unity (e.g., Tian et al., 2008a). We also show the Jeans escape parameter

at the top of the atmosphere as a function of P_{CO_2}, in Fig. 3.13. The Jeans escape parameter gradually decreases from 235 to 14 with decreasing P_{CO_2} for $P_{CO_2} \geq 3 \times 10^2$ PAL. Then, the Jeans escape parameter quickly drops into unity at $P_{CO_2} = 1 \times 10^2$ PAL. Those are consistent with the hydrodynamical calculation of Tian et al. (2008a), who suggested that the hydrodynamic escape is operated for larger EUV intensity than a critical value of 5.3 times that of present Sun recieved by the Earth, when $P_{CO_2} = 1 \times 10^0$ PAL and $M_p = 1 M_\oplus$. The EUV intensity of GJ1214 used in our model is 4.0×10^1 erg cm^{-2} s^{-1} which is 8.5 times the present Sun's level. Consequently, the planet has the upper atmosphere extending to a larger radius than the solid part of the planet. Furthermore, their simulations show that the transition from hydrostatic equilibrium regime to hydrodynamic regime occurs when the exospheric temperature reaches 7000–8000 K. This transition temperature is also consistent with our results because the hydrostatic equilibrium is achieved in the exospheric temperature below 6486 K.

In Fig. 3.14, we show the number density of O as a function of altitude for four different P_{CO_2}. The overall trend is the same for all calculations. However, radial gradient of O number density in the thermosphere increases with decreasing P_{CO_2}. This is because higher temperature and larger radius lead to a larger radial gradient of the density in hydrostatic equilibrium (see Eq.(3.7)). Thus, a higher number density of O is achieved in high altitude for a lower P_{CO_2}. The volume mixing ratio of O at the exobase slightly decreases with decreasing P_{CO_2} because the molecular diffusion, which brings up lighter species than O (e.g., N), is effective in high altitude (i.e., low gravity). However, O is still major constitute of the atmosphere and the mixing ratio of O is larger than the 0.2, even in the significantly expanded atmosphere for $P_{CO_2} = 1 \times 10^2$ PAL.

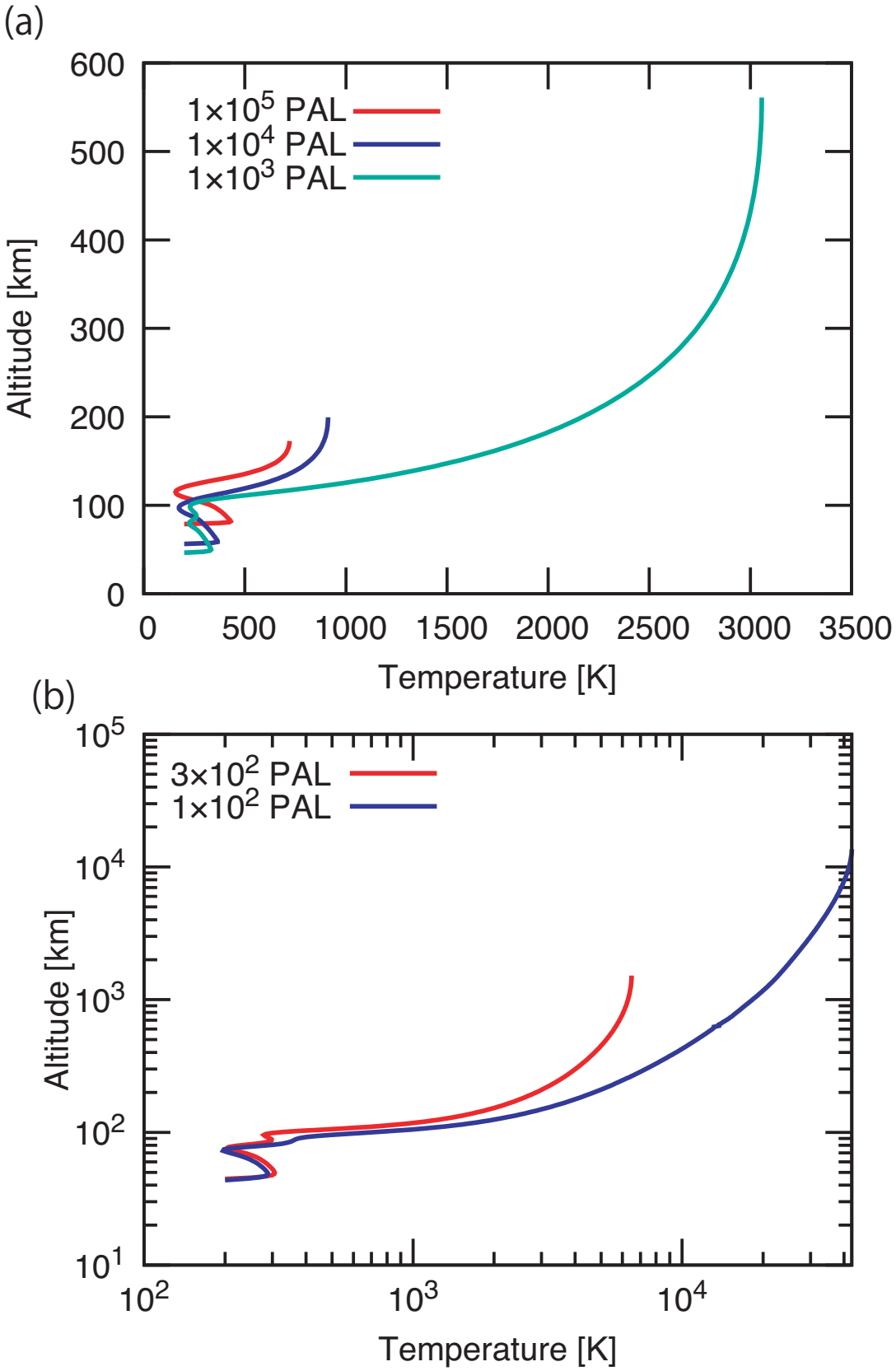

Figure 3.12: Temperature profiles for different partial pressure of CO_2, P_{CO_2}. Panel(a) shows temperature profiles for $P_{CO_2} = 1 \times 10^5$ (red), 1×10^4 (blue), and 1×10^3 PAL (green). Panel(b) shows temperature profiles for $P_{CO_2} = 3 \times 10^2$ (red) and 1×10^2 PAL (blue). For $P_{CO_2} = 1 \times 10^2$ PAL, the calculation is artificially stopped because the Jeans escape parameter becomes unity. Note that (a) and (b) are plotted with linear scale and log scale, respectively.

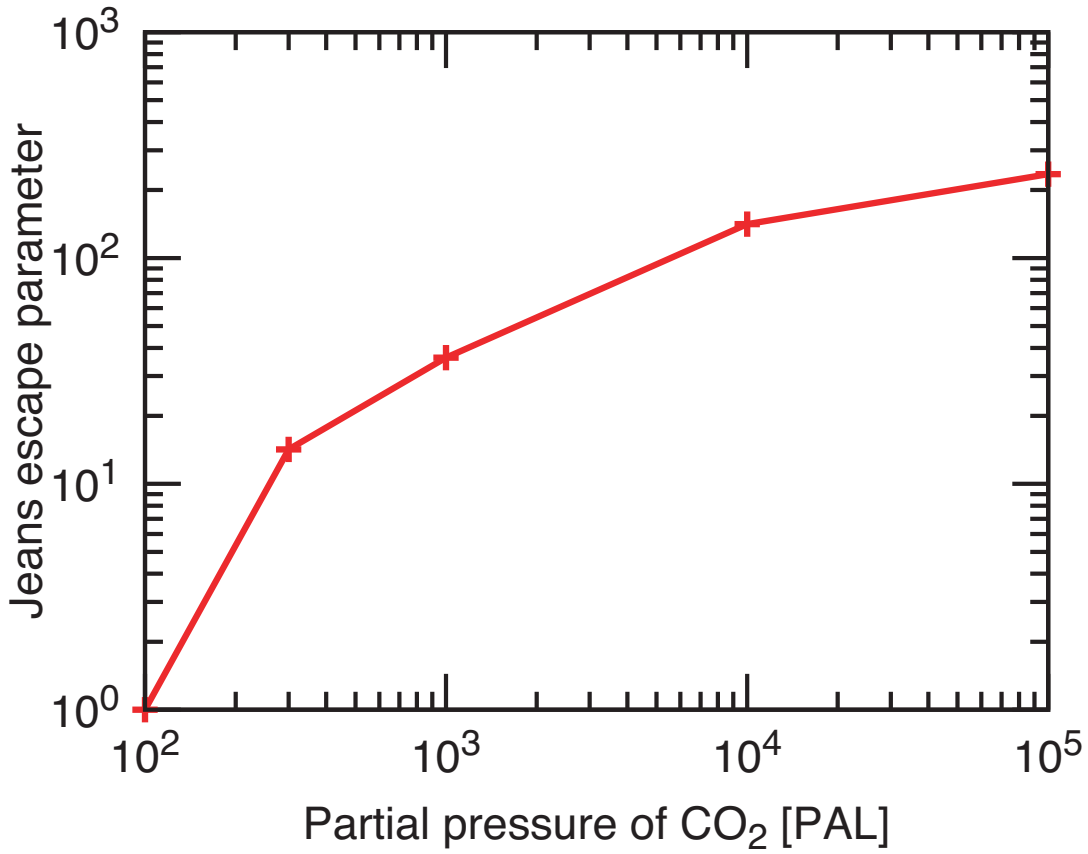

Figure 3.13: The Jeans escape parameters at the top of the atmosphere as a function of the partial pressure of CO_2, P_{CO_2}. For $P_{CO_2} = 1 \times 10^2$ PAL, the calculation is artificially stopped because the Jeans escape parameter becomes unity.

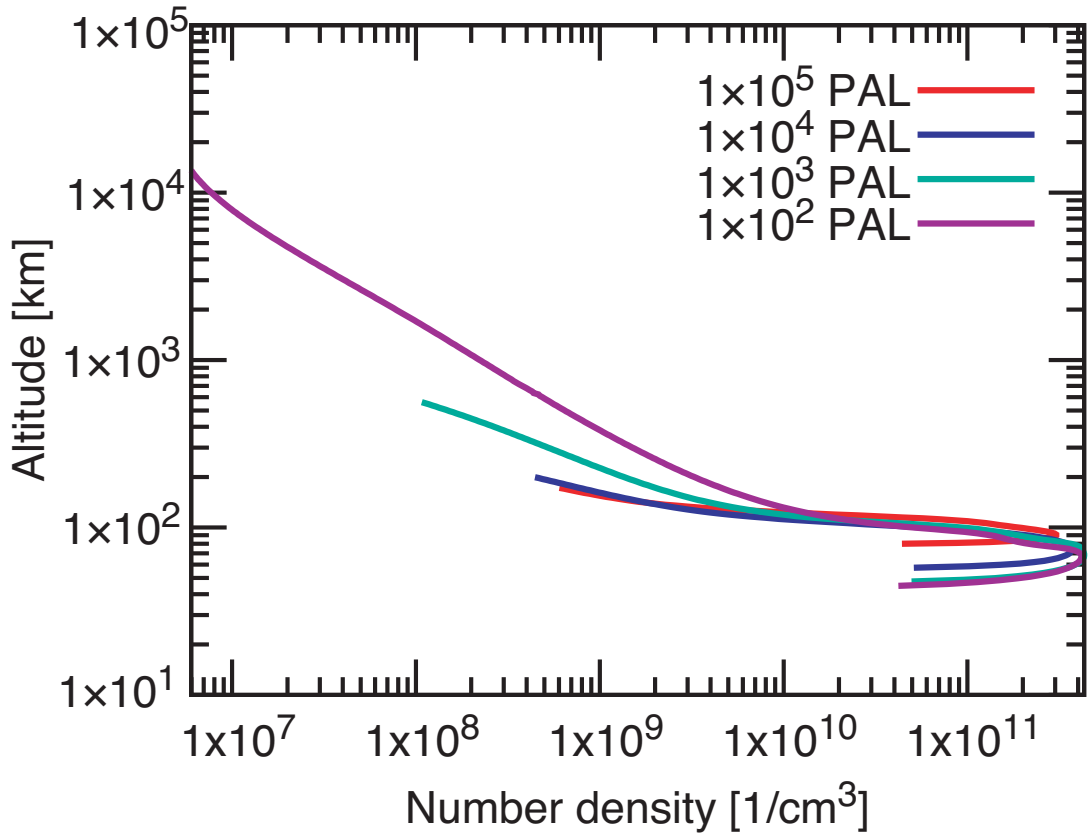

Figure 3.14: Number density profiles of oxygen for different partial pressure of CO_2 $P_{CO_2} = 1 \times 10^5$ PAL (red), 10^4 PAL (blue), 10^3 PAL (green), and 10^2 PAL (purple). For $P_{CO_2} = 1 \times 10^2$ PAL, the calculation is artificially stopped because the Jeans escape parameter becomes unity.

3.3.1.2 Dependence on planetary mass

Lastly, we examine the dependence of the upper atmospheric structure on the planetary mass. The partial pressure of CO_2 is assumed to be $P_{CO_2} = 1 \times 10^4$ PAL in below calculations. The planetary mass is varied over the range between $1M_\oplus$ and $0.1M_\oplus$. As shown in Fig. 3.15, the planetary mass strongly affects the temperature structure. The exospheric temperature increases from 911 K to 16619 K, as the planetary mass decreases from $1M_\oplus$ to $0.1M_\oplus$. For $M_p = 1M_\oplus$ and $0.5M_\oplus$ (Panel(a)), solutions at steady-state with hydrostatic equilibrium are achieved. In contrast, for $M_p = 0.2M_\oplus$ and $0.1M_\oplus$ (Panel(b)), steady-state solutions are never achieved and the Jeans escape parameters becomes unity (i.e., hydrodynamic escape regime). Thus, the significantly expanded upper atmosphere is formed. Note that the Jeans escape becomes unity in lower altitude for lower planetary mass in hydrodynamic escape regime because of lower gravitational energy.

This trend is understood by the difference of the scale height (i.e., gravity). Considering the energy balance between heating of high-energy photons and cooling due to the thermal conduction, Gross (1972) obtained the dependence of exospheric temperature, T_∞:

$$T_\infty \propto (I_{\rm EUV}/g_{\rm exo})^{1/B^\kappa}, \tag{3.68}$$

where B^κ is the temperature dependence of conductive coefficient (see Eq.(3.25)), $I_{\rm EUV}$ is the energy flux at EUV wavelength, and $g_{\rm exo}$ is the gravity at the exobase. B^κ is 0.5–1, depending on the atmospheric composition (e.g., Banks & Kockarts, 1973). Since $g_{\rm exo}$ linearly depends on the planetary mass, exospheric temperature increases with decreasing planetary mass. In addition, low gravity promotes atmospheric escape because of reducing gravitational energy. Thus, the upper atmosphere in low mass planet become hydrodynamic escape regime, even in high P_{CO_2} condition.

In Fig. 3.16, we show the number density profiles of O for different planetary masses. The lower atmosphere below the mesopause, sane behavior is achieved in O number density which increases with the altitude according to the production rate of oxygen via photo-chemical reactions, discussed in the above section. The peak number density slightly increases with decreasing planetary mass because of the difference in the scale height. As shown in the temperature structure of Fig. 3.15, the lower planetary mass, the more expanded atmosphere is in

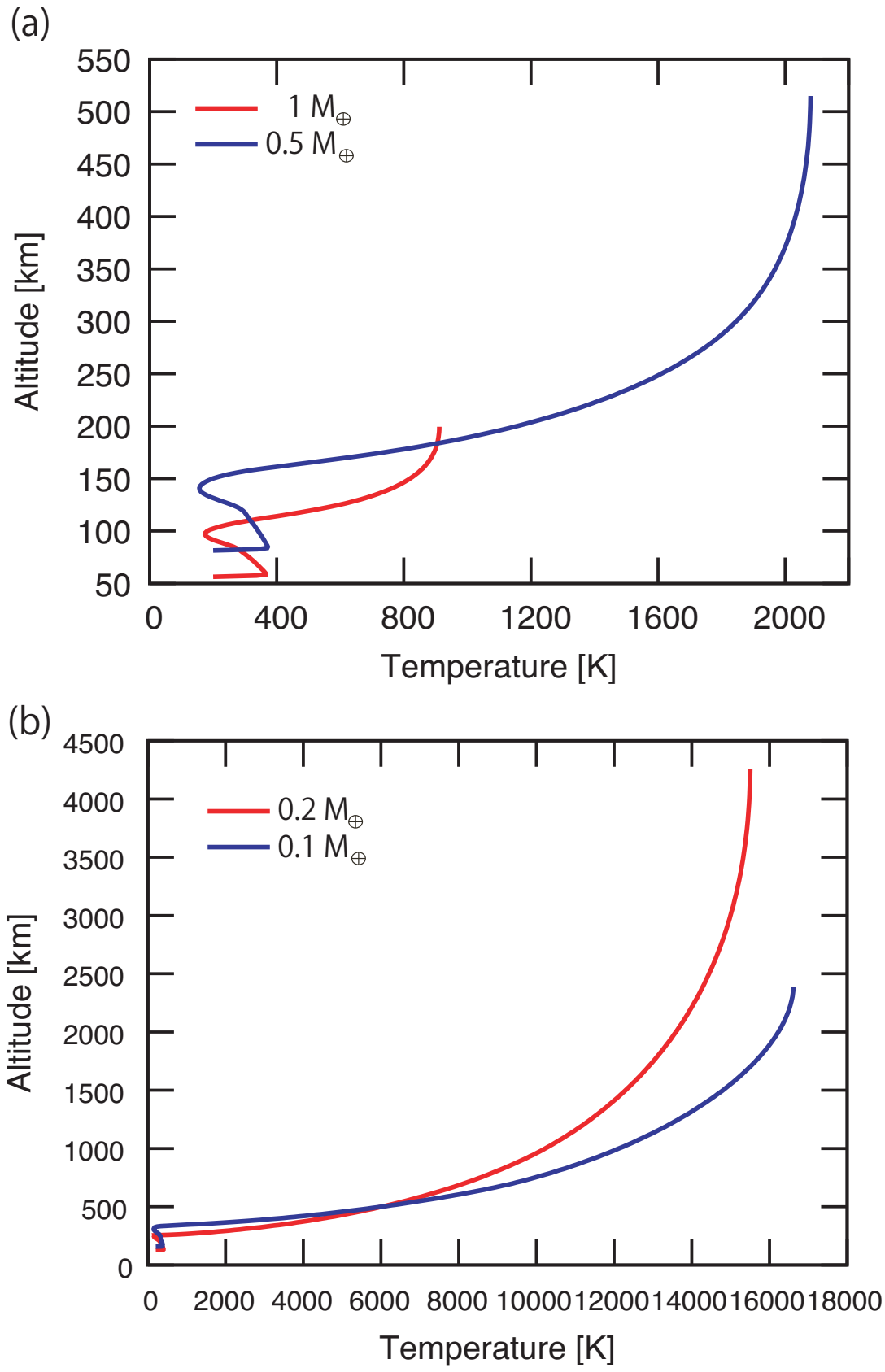

Figure 3.15: Temperature profiles for the partial pressure of CO_2 $P_{CO_2} = 1 \times 10^4$ PAL and different planetary masses, M_p. Panel (a) shows temperature profiles for $M_p = M_\oplus$ (red) and $M_p = 0.5M_\oplus$ (blue). Panel (b) shows temperature profiles for $M_p = 0.2M_\oplus$ (red) and $M_p = 0.1M_\oplus$ (blue), though those calculations are artificially stopped because the Jeans escape parameters becomes unity.

the thermosphere. As a result, the high number density of O is achieved at high altitudes. In particular for planets in hydrodynamic escape regime ($M_{\rm p} \leq 0.2M_{\oplus}$), oxygen number density is still high even in the altitude comparable to the planetary radius.

We summarize the results of the upper atmospheric structure in Fig. 3.17. The exospheric temperature as a function of $P_{\rm CO_2}$ for four different planetary masses are plotted. Solid lines indicate that calculated values from the upper atmospheric model. Dashed lines indicate that extrapolated values toward lower $P_{\rm CO_2}$ because the upper atmosphere is in the hydrodynamic escape regime and detailed dependence can not be investigated in our model. For $M_{\rm p} = 1M_{\oplus}$ and $0.5M_{\oplus}$, exospheric temperatures are extrapolated from $P_{\rm CO_2} = 1 \times 10^2$ and 1×10^3 PAL, respectively. For $M_{\rm p} \leq 0.2M_{\oplus}$, planets are the hydrodynamic escape regime in all $P_{\rm CO_2}$ region. Thus, we plot the values for $P_{\rm CO_2} = 10^4$ PAL. This figure shows that the upper atmospheric structure depends on the partial pressure of CO_2 for larger planetary mass $M_{\rm p} \geq 0.5M_{\oplus}$ in our EUV irradiance environment. Furthermore, the transition from compact atmosphere in hydrostatic equilibrium regime to expanded atmosphere in hydrodynamic escape regime occurs in $P_{\rm CO_2} \sim 10^2$ PAL ($\sim 1 \times 10^{-1}$ bars) and $P_{\rm CO_2} \sim 10^3$ PAL ($\sim 1 \times 10^0$ bars) for $M_{\rm p} = 1M_{\oplus}$ and $0.5M_{\oplus}$, respectively. Our theoretical estimation of the planetary climate shows that such moderate $P_{\rm CO_2}$ is never achieved in ocean planets with a massive ocean.

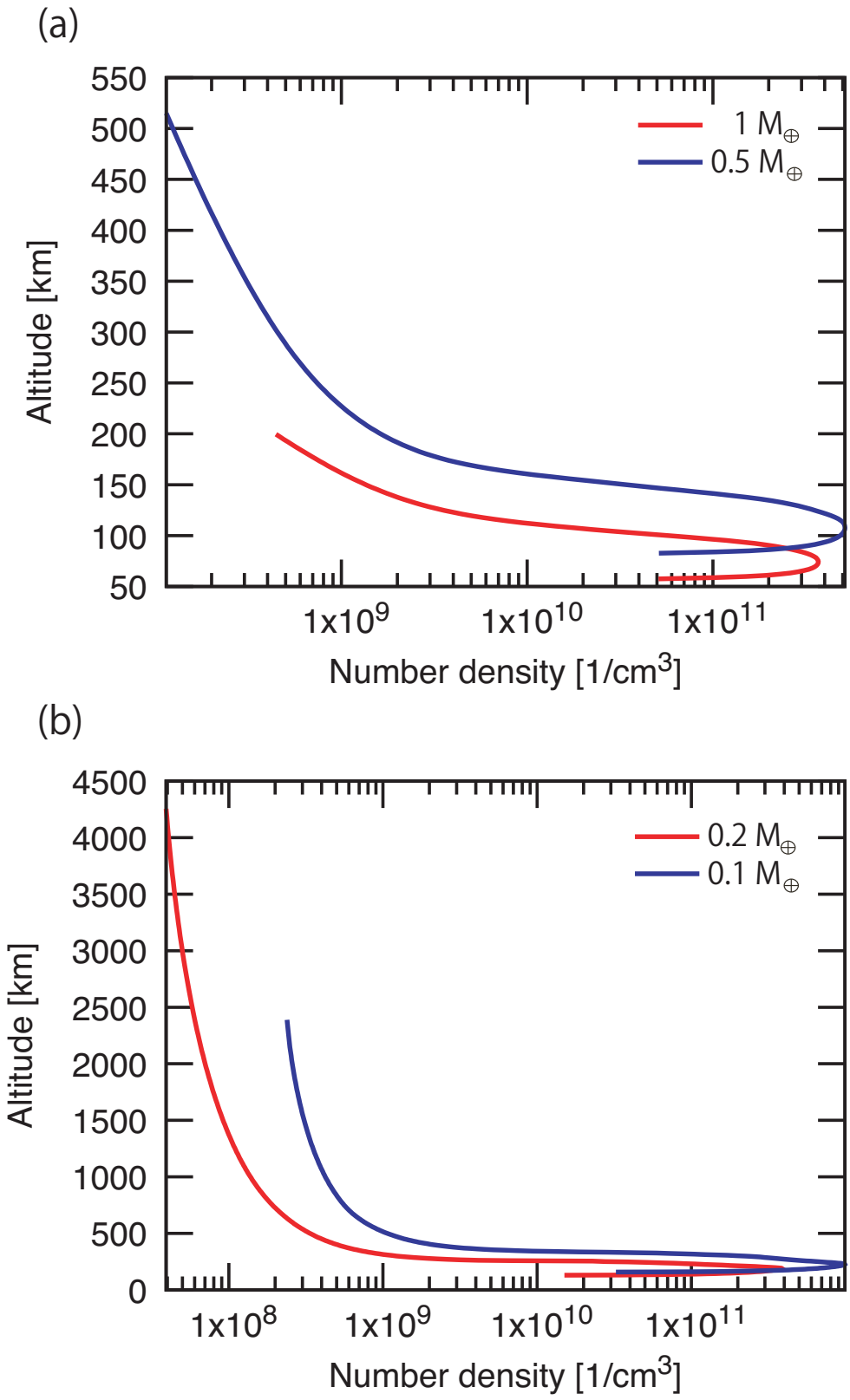

Figure 3.16: Number density profiles of oxygen for the partial pressure of CO_2 $P_{CO_2} = 1 \times 10^4$ PAL and different planetary masses, M_p. Panel (*a*) shows number density profiles for $M_p = M_\oplus$ (red) and $M_p = 0.5M_\oplus$ (blue). Panel (*b*) shows number density profiles for $M_p = 0.2M_\oplus$ (red) and $M_p = 0.1M_\oplus$ (blue), though those calculations are artificially stopped because the Jeans escape parameters becomes unity.

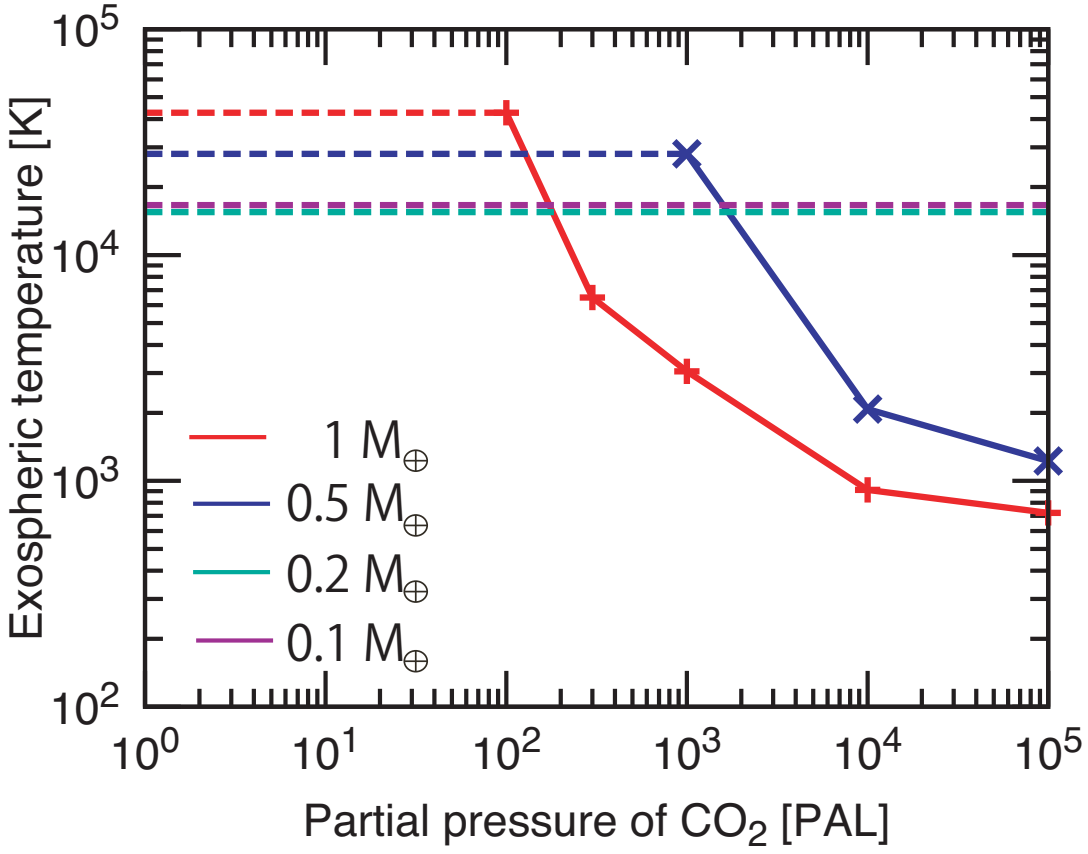

Figure 3.17: Exospheric temperatures as a function of the partial pressure of CO_2 for different planetary masses, $M_{\rm p}$. The red, blue, green, and purple lines indicate the exospheric temperature for $M_{\rm p} = 1M_{\oplus}$, $M_{\rm p} = 0.5M_{\oplus}$, $M_{\rm p} = 0.2M_{\oplus}$, and $M_{\rm p} = 0.1M_{\oplus}$, respectively. Solid lines indicate calculated values. Dashed lines indicate extrapolated values and detailed description is in the main text.

3.3.2 Detectability of oxygen and planetary climate

Here, we examine the detectability of the oxygen corona and planetary climate, using the obtained upper atmospheric profiles. First, we show the density structure of the oxygen corona and absorption feature of OI lines during planetary transit for the Earth-mass planet with different partial pressure of CO_2, P_{CO_2} (§ 3.3.2.1), as an example. Then, we show the dependence of planetary mass on results (§ 3.3.2.2).

3.3.2.1 Dependence of partial pressure of CO_2 on transit depth

We first show the number density structure of the oxygen corona. Fig. 3.18 shows number density profiles of oxygen for $M_p = 1M_\oplus$ and three different P_{CO_2}. Solid lines indicate the profiles derived by the upper atmospheric model (§ 3.2.1). Dashed lines indicate the profiles derived by the oxygen corona model (§ 3.2.2.1). Boundary altitudes where the model switches are 5.6×10^2, 1.5×10^3, and 1.4×10^4 km for 1×10^3, 3×10^2, and 1×10^2 PAL, respectively. For the cases of 1×10^3, the number density significantly decreases with the altitude. Above the altitude equivalent to the planetary radius ($\sim 6 \times 10^3$ km), there is almost no oxygen. In contrast, for the case of 3×10^2 PAL and 1×10^2 PAL, the oxygen corona is expanded to the stellar radius ($\sim 10^5$ km). In particular for $P_{CO_2} = 1 \times 10^2$ PAL, there is abundant oxygen, even in the stellar radius. The difference arises from the higher exospheric temperature and smaller Jeans escape parameter at the top of the upper atmosphere. This is because the density in the corona is simply determined by the kinetic energy (i.e., the temperature) and the gravitational potential energy, without the magnetic field and stellar wind. The exospheric temperature increases from 3056 to 42715 K and the Jeans escape parameter decreases from 36 to 1, as the partial pressure of CO_2 decreases from 1×10^3 to 1×10^2 PAL.

In Fig.3.19, we plot the absorption cross-section of OI line around 130.6 nm. Each lines correspond to absorption cross-section for different P_{CO_2}. We use the exospheric temperature of 3056, 6486 and 42715 K for 1×10^3, 3×10^2, and 1×10^2 PAL. Although the Doppler width is slightly different for each lines, Doppler width of the line around 130.6 nm are 1.6×10^{-3}, 1.6×10^{-3}, and 2.3×10^{-3} nm for 1×10^3, 3×10^2, and 1×10^2 PAL, respectively. The higher temperature, weaker absorption cross-section at the line center is, because of larger Doppler

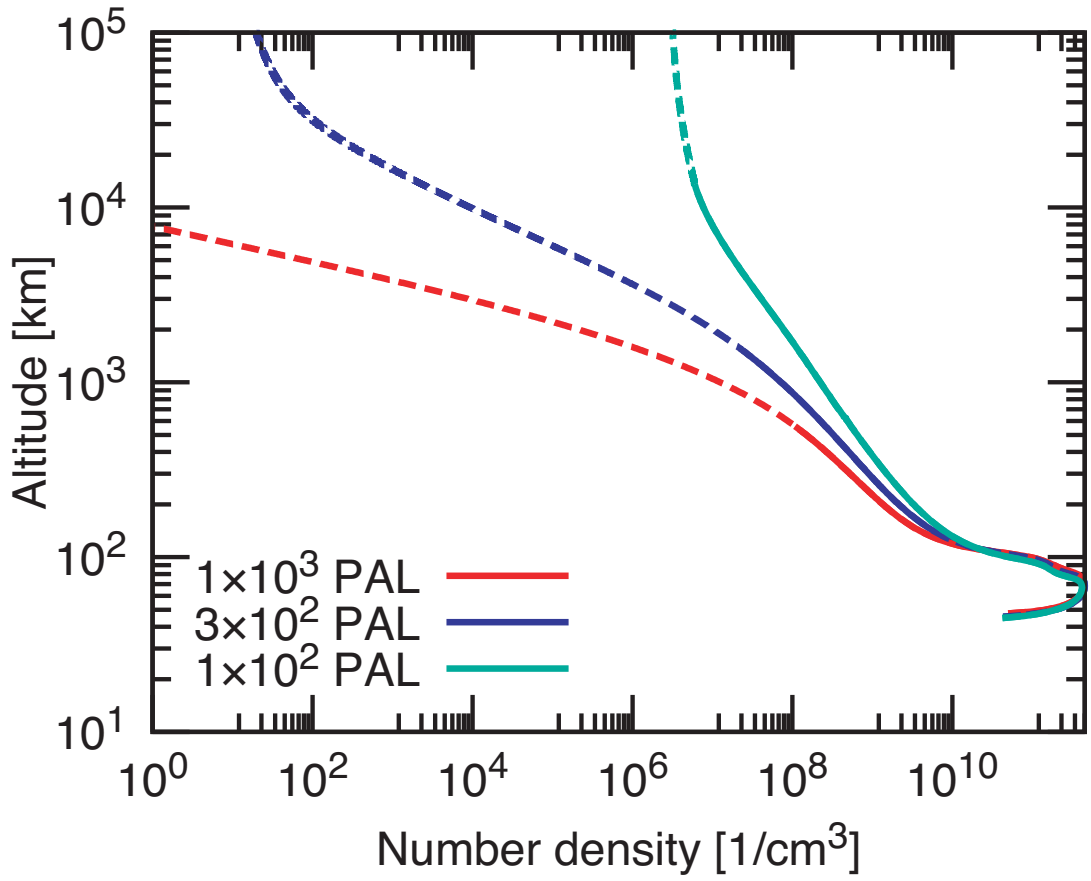

Figure 3.18: Number density profile of oxygen for the planetary masss $M_p = 1M_\oplus$ and different partial pressure of CO_2, P_{CO_2}. The red, blue, and green lines indicate number density profiles for $P_{CO_2} = 1 \times 10^3$ PAL (red), 3×10^2 PAL (blue), and 1×10^2 PAL (green), respectively. Solid lines indicate the profiles derived by the upper atmospheric model. Dashed lines indicate the profiles derived by the oxygen corona model.

width (see Eq.(3.57)). The absorption cross-section at the line center decreases from 7.1×10^{-13} to 1.5×10^{-14} cm^2, as the partial pressure of CO_2 decreases from 1×10^3 to 1×10^2 PAL. However, the oxygen can absorb the emission in a wider wavelength region for larger temperature conditions.

Using the obtained number density profile and absorption cross-section, we show the observable flux of OI lines during the planetary transit, in Fig.3.20. As done above, we plot the observable flux for three different P_{CO_2} in solid lines. The color of lines also correspond to the same conditions shown above. The flux before planetary transit is shown in the black dashed line. The level population of the OI triplet calculated by the exospheric temperature is given in table 3.8. As the partial pressure of CO_2 decreases, the oxygen in the ground state ($^3P_2$)

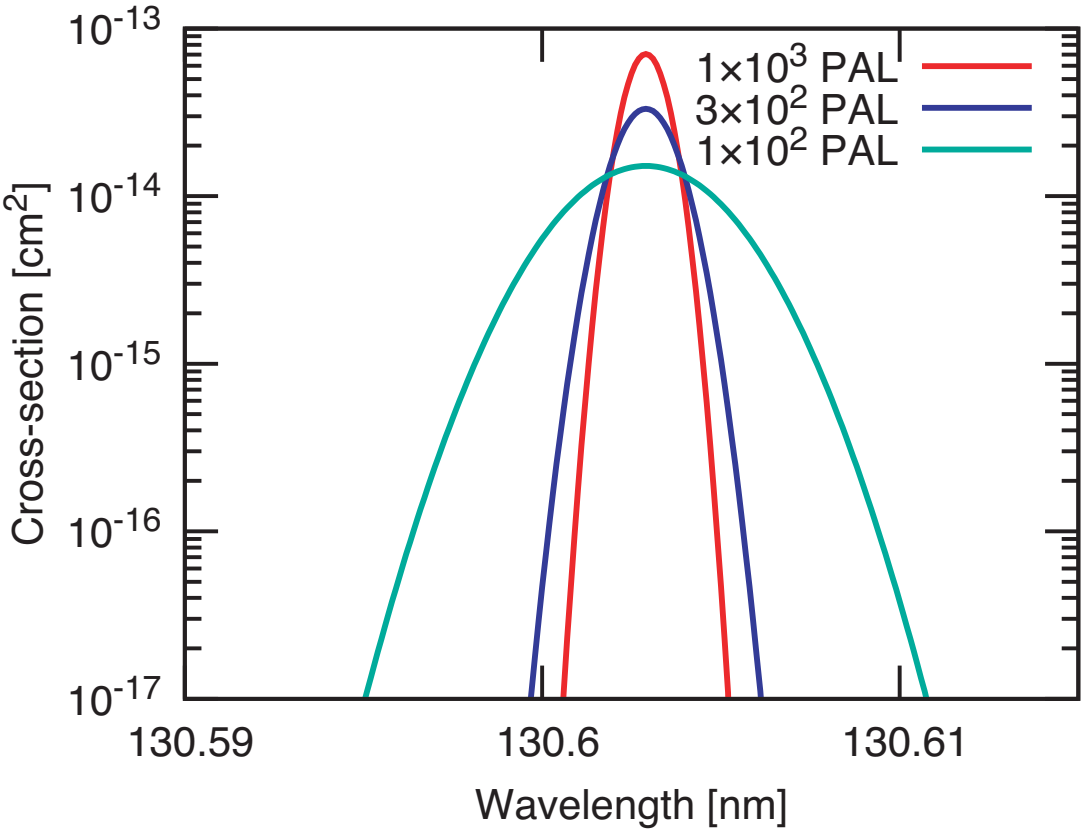

Figure 3.19: Absorption cross-section of OI line around 130.6 nm for the planetray mass $M_{\rm p} = 1M_{\oplus}$ and different partial pressure of CO_2. The red, blue, and green lines mean the cross-section for the exospheric temperature of 3056 K, 6486 K, and 42715 K, respectively.

decrease because higher temperature readily excites the level of the oxygen. However, it is a rather small influence on the transit depth than the effects of the Doppler broadening of absorption cross-section and the expansion of the corona. For $P_{\rm CO_2} = 1 \times 10^3$ PAL, the oxygen corona inefficiently absorbs stellar emission because the geocorna is hardly expanded. The transit depth of the corona corresponds to 1.0×10^{-7} which is much smaller than that in the solid part of the planet (4.3×10^{-3}), even at the line center. For $P_{\rm CO_2} = 3 \times 10^2$ PAL, the oxygen corona can absorb stellar emission around the line center, although the emission at line wings is never absorbed. Thus, for the emission around 130.6 nm, the transit depth at the line center and wavelength integrated transit depth become 2.3×10^{-1} and 4.4×10^{-2}. For $P_{\rm CO_2} = 1 \times 10^2$ PAL, the oxygen corona perfectly absorbs stellar emission in most wavelength region because of expanded corona. The Doppler width of the absorption cross-section is larger than the half width of the stellar emission for the emission around 130.2 nm.

Table 3.8: Level population of OI triplet

Partial pressure of CO_2 (PAL)	$^3P_2$	$^3P_1$	$^3P_0$
1×10^2	5.6×10^{-1}	3.3×10^{-1}	1.1×10^{-1}
3×10^2	5.7×10^{-1}	3.3×10^{-1}	1.0×10^{-1}
1×10^3	5.8×10^{-1}	3.2×10^{-1}	1.0×10^{-1}

Thus, wavelength integrated transit depth also becomes almost unity. On the other hand, the half width of the stellar emission is larger than the Doppler width for the emission around 130.5 and 130.6 nm. Thus, the corona is transparent at the line wing. However, the corona is opaque in most wavelength region: Wavelength integrated transit depths correspond to 9.3×10^{-1} and 9.5×10^{-1} for the emission around 130.5 and 130.6 nm, respectively. The total transit depth integrated from 130.2 to 130.65 nm corresponds to 9.5×10^{-1} for $P_{CO_2} = 1\times10^2$ PAL, which is much larger than 4.3×10^{-3} for $P_{CO_2} = 1\times10^3$ PAL. Thus, the significant difference in the transit depth caused by the difference of CO_2 abundance is the distinguishable feature. We should notice that the interstellar medium affects the observable flux around 130.2 nm because there is abundant oxygen at the ground level. However, other emission lines also show a significant absorption feature and, thus, the absorption of the interstellar medium never affects our conclusion. In our EUV irradiance environment, Abrupt transition of the transit depth for $M_p = 1M_\oplus$ occurs at the partial pressure between 1×10^2 and 3×10^2 PAL, which corresponds to $\sim 1.0\times10^{-1}$ bars. Thus, we can distinguish two extreme climates of ocean planets with massive ocean estimated in Part I because a moderate P_{CO_2} is never achieved. In contrast, equilibrium and warm climate of ocean planet with small ocean masses and low degassing conditions (see Fig. 2.10) have a moderate P_{CO_2}. As shown in Fig. 2.8, in this regime, P_{CO_2} is sensitive to ocean masses, stellar insolation, and degassing rates. For stellar insolation of $1.0S_\odot$, P_{CO_2} is varied over wide range between 2.5×10^{-4} and 2.4×10^{-1} bars. Thus, a variety of transit depth would be observed in this regime and we should discuss their climates carefully to apply actual planets. However, the stellar irradiation is observable and ocean masses would be constrained by another method, discussed in § 3.4.1. Therefore, we would distinguish which climate regime is in from observations.

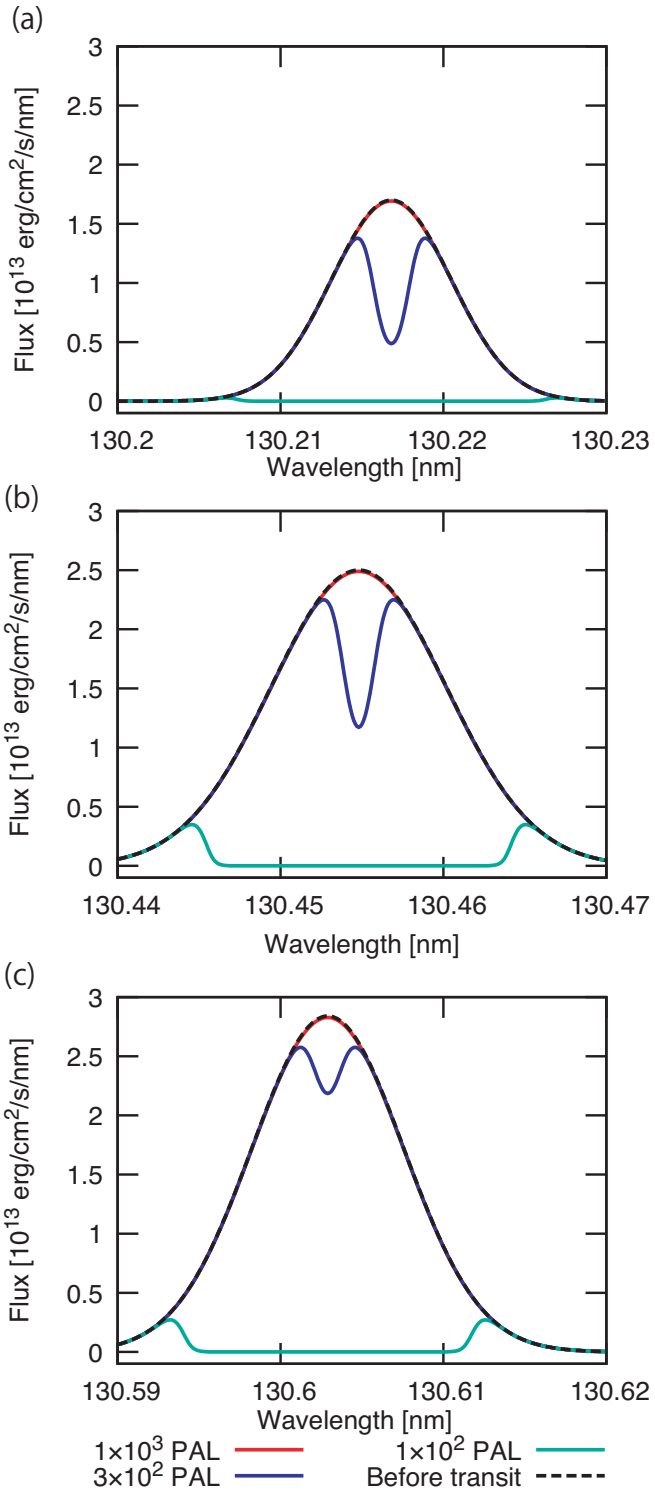

Figure 3.20: Observable flux of OI lines before transit and during transit for three different partial pressure of CO_2, P_{CO_2}. The dashed black line and solid lines indicate the flux before transit and during transit, respectively. Solid lines indicate observable flux for $P_{CO_2} = 1 \times 10^{-3}$ PAL (red), $P_{CO_2} = 3 \times 10^{-2}$ PAL (blue), $P_{CO_2} = 1 \times 10^{-2}$ PAL (green). Panel (a), (b), and (c) show emission lines around 130.2, 130.5, 130.6 nm, respectively. The red solid line mostly overlaps the dashed line.

3.3.2.2 Dependence of planetary mass on transit depth

Finally, we show the dependence of planetary mass. In Fig.3.21, we show the transit depth as a function of P_{CO_2} for four different planetary mass. Solid lines are estimated, using the obtained density structure. We extrapolated the transit depth toward lower partial pressure of CO_2 from the value where hydrodynamics escape is operated (i.e., the Jeans escape parameter becomes unity), as done in Fig.3.17. Extrapolated values are plotted in dashed lines. For planetary mass larger than $M \geq 0.5M_{\oplus}$, hydrostatic structure is achieved in larger P_{CO_2}. For $M = 0.5M_{\oplus}$, hydordynamic escape begin to operate in $P_{CO_2} = 1 \times 10^3$ PAL, which is 10 times that for $M_p = 1M_{\oplus}$, because of low gravity. However, overall trend of transit depth is similar to that for $M_p = 1M_{\oplus}$. For the partial pressure larger than 1×10^3 PAL, transit depth is 3.0×10^{-3}, which is mainly came from the solid part of the planet. For the partial pressure smaller than 1×10^3 PAL, in contrast, transit depth becomes 8.9×10^{-1} because of the extended oxygen corona. Thus, large dependence of P_{CO_2} enables us to distinguish the planetary climate of an ocean planet with $M_p = 0.5M_{\oplus}$. On the other hand, for $M_p \leq 0.2M_{\oplus}$, hydrodynamic escape is operated in all of P_{CO_2}. Thus, the transit depth is insensitive to P_{CO_2} and becomes a large value of approximately 0.8–0.9. In the hydrodynamic escape regime, the smaller transit depth, the small planetary mass is because smaller exospheric temperature leads to smaller Doppler width of absorption cross-section. We further discuss the effect of hydrodynamic escape on the transit depth in § 3.4.2.3. Consequently, we can not distinguish the planetary climate of smaller planetary mass from the absorption of OI lines during the planetary transit because large transit depth would be observed regardless of P_{CO_2} in the EUV irradiation environment used in our model.

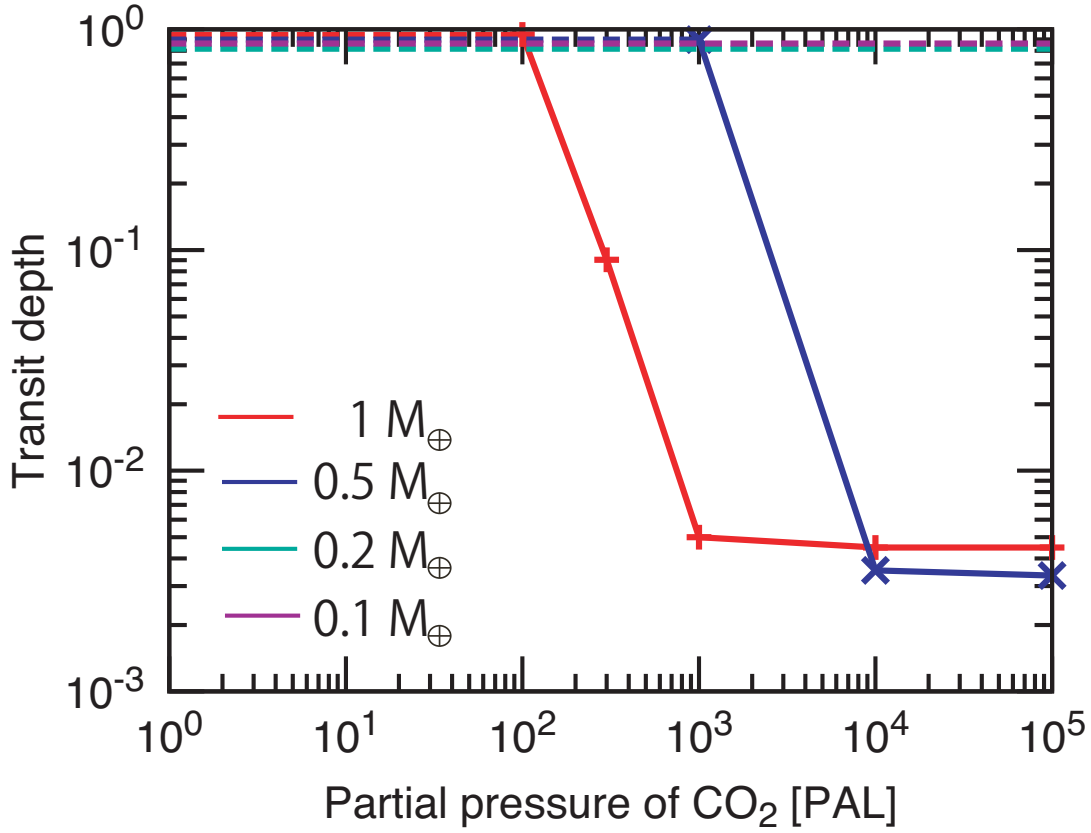

Figure 3.21: Transit depth as a function of partial pressure of CO_2 for four different planetary masses, M_p. The red, blue, green, and purple lines indicate the transit depth for $M_p = 1M_\oplus$, $M_p = 0.5M_\oplus$, $M_p = 0.2M_\oplus$, and $M_p = 0.1M_\oplus$, respectively. Solid lines indicate calculated values. Dashed lines indicate extrapolated values and detailed description is in the main text. Four dashed lines are overlapped and their transit depth correspond to ~ 0.9.

3.4 Discussion

3.4.1 Constraining ocean masses from other method

Our results show that two extreme climates (i.e., CO_2-rich or CO_2-poor atmosphere) of ocean planets around M-type stars in the habitable zone can be distinguished by the transit observation of OI lines. However, the difference of CO_2 abundance in terrestrial planets is also found in the Solar system: The Earth and Venus. The difference in climate between Venus and the Earth would arise from the presence of an ocean and carbon cycle (e.g., Kasting et al., 1984). This reason is very different from why ocean planets become extreme climates, which come from the presence of the HP ice and supply-limit of the seafloor weathering. Thus, the only estimation of abundance of CO_2 never unravels surface environment on the planet. If ocean masses are estimated from another method, we gain a deeper understanding planetary climate of terrestrial planets because ocean mass has a crucial role in the planetary climate of ocean planets. In this section, we discuss the detectability of ocean masses of terrestrial planets.

An increase in ocean masses decreases the planetary mean density because water is lighter than rocks and metals. Thus, massive oceans lead to a significant decrease in the planetary mean density. When the mean density is accurately estimated, ocean mass is constrained by observations. Some of the space telescopes are scheduled in a decade. Next-generation space telescopes provide highly accurate mass and radius determinations. While typical current uncertainty of mean density determination is about 40%, *PLATO*, which will be launched in the mid-2020s, will reduce the uncertainty to about 10% (Rauer et al., 2014).

Using the internal structure model given in § 2.2.1, we derive the relationship between ocean mass and planetary mean density for a given planetary mass. Fig. 3.22 shows the planetary mean density normalized by the mean density of the planet with $1M_{\mathrm{oc},\oplus}$ as a function ocean mass for planetary masses of 0.1, 0.2, 0.5, 1 $M_\oplus$. As a result, the planetary mean density decreases with ocean masses. The small planetary mass, the larger variation of the mean density is because a fraction of the ocean mass to the planet mass is large and compression is weak. For an Earth-mass planet, the planetary mean density decreases by about 9% with an increase in ocean masses to $200M_{\mathrm{oc},\oplus}$. For a Mars-mass planet, the planetary mean density decreases by about 37% with an increase in ocean masses to $200M_{\mathrm{oc},\oplus}$. Considering uncertainty of observation, this figure shows that ocean

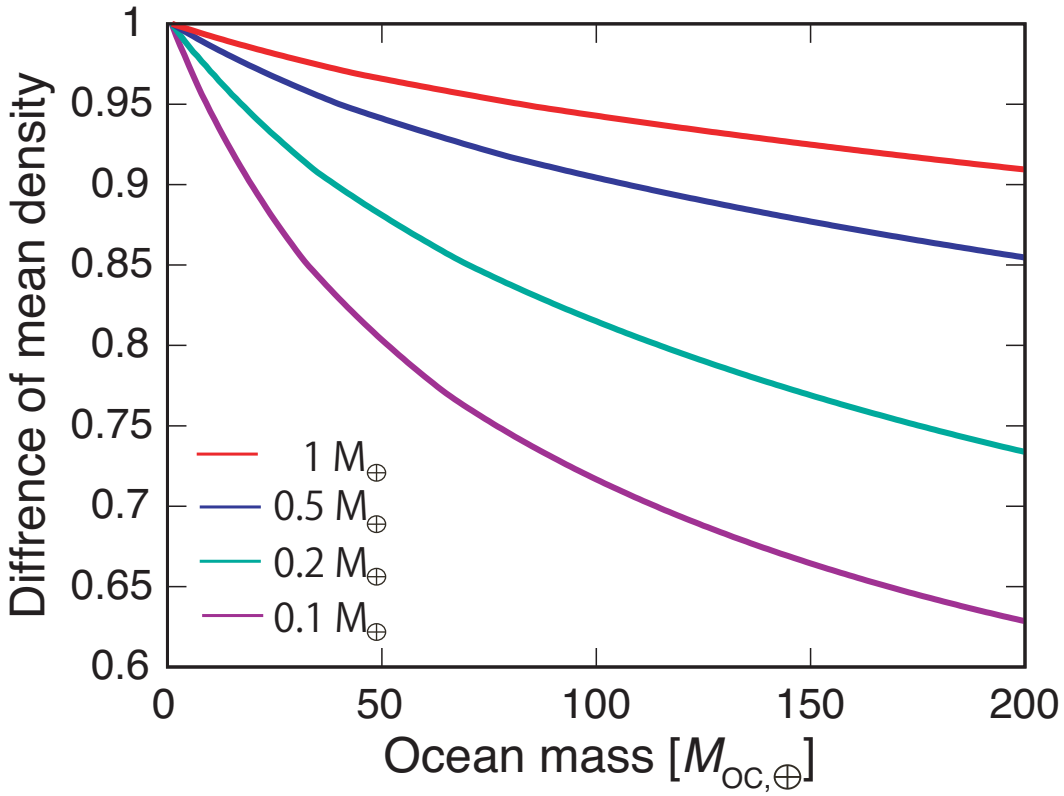

Figure 3.22: The planetary mean density as a function of ocean mass, M_{oc}, for four values of planetary masses, M_p. The planetary mean density is normalized by the mean density of the planet with $M_{oc} = 1M_{oc,\oplus}$, where $M_{oc,\oplus}$ means the Earth's ocean mass. The red, blue, green, and purple lines indicate the planetary mean density for $M_p = 1M_\oplus$, $0.5M_\oplus$, $0.2M_\oplus$, and $0.1M_\oplus$, respectively.

mass would be estimated with an order of $\sim 10M_{oc,\oplus}$ for $M_p \lesssim 0.2M_\oplus$. In contrast, for $M_p \gtrsim 0.5M_\oplus$, ocean mass would be estimated with an order of $\sim 100M_{oc,\oplus}$. Furthermore, the more accurate measurement would be carried out in further future because of the advance in observational technologies. Thus, it can be distinguished whether the planet has massive oceans, even if the planet is Earth mass. Therefore, we would distinguish between the Venus-like planet and an ocean planet with massive oceans from the planetary mean density measurement.

3.4.2 Caveats

In this section, we discuss some caveats of our models. In particular, we discuss the effects of the lower boundary condition, radiative cooling, hydrodynamic escape, partial pressure of O_2, eddy diffusivity, and tidal locking on the upper

atmospheric structure and the transit depth.

3.4.2.1 Temperature inversion at stratosphere

Our results show that the absorption of CO_2 at IR wavelength heats up the lower part of the atmosphere and, then, produces temperature inversion. The temperature inversion due to CO_2 absorption was also found by Kasting et al. (2015). Such heating is effective for M-type stars because the stellar spectrum is red-shifted. In this section, we discuss the temperature inversion at the stratosphere from the points of view about radiative cooling of CO_2 and horizontal heat transport. We only consider strong vibrational bands of $\nu_2 = 1$ and $\nu_3 = 1$ for CO_2 emission. However, Dickinson (1973) showed that local thermal equilibrium (LTE) is achieved above ~ 5 Pa. Thus, emissions at other weak bands are also effective at the stratosphere. In addition, planets with faster rotation rate prospected for a planet around an M-type star have the strong zonal wind at the stratosphere (e.g., Kopparapu et al., 2016). The strong zonal wind would result in efficient horizontal heat transport. Although we need to perform 3-D simulation to resolve this issue, horizontal heat transport also reduces the temperature at the stratosphere.

To clarify the effect of the temperature inversion on the upper atmospheric structure, we perform additional calculations with a higher lower boundary condition. A higher lower boundary condition corresponds to the case with no temperature inversion and isothermal stratosphere of 200 K. For the lower boundary condition, we derive the height of 1 Pa, which corresponds to the Earth's mesopause, from the lower atmospheric model (§ 2.4.3.2). In Fig. 3.23, we show the temperature profile for the lower boundary of 1Pa in the solid line. As a reference, we also plot the temperature profile for the lower boundary of 100 Pa as the dashed line, also shown in Fig. 3.6. Similar temperature profiles are achieved for both cases. However, the height at the exobase for the case of 1 Pa is slightly lower. This is because the temperature inversion at the stratosphere inflates the upper atmosphere. We have confirmed that this effect has a small impact on the transit depth and our conclusion because the temperature structure is mainly determined by the intensity of EUV heating and radiative cooling.

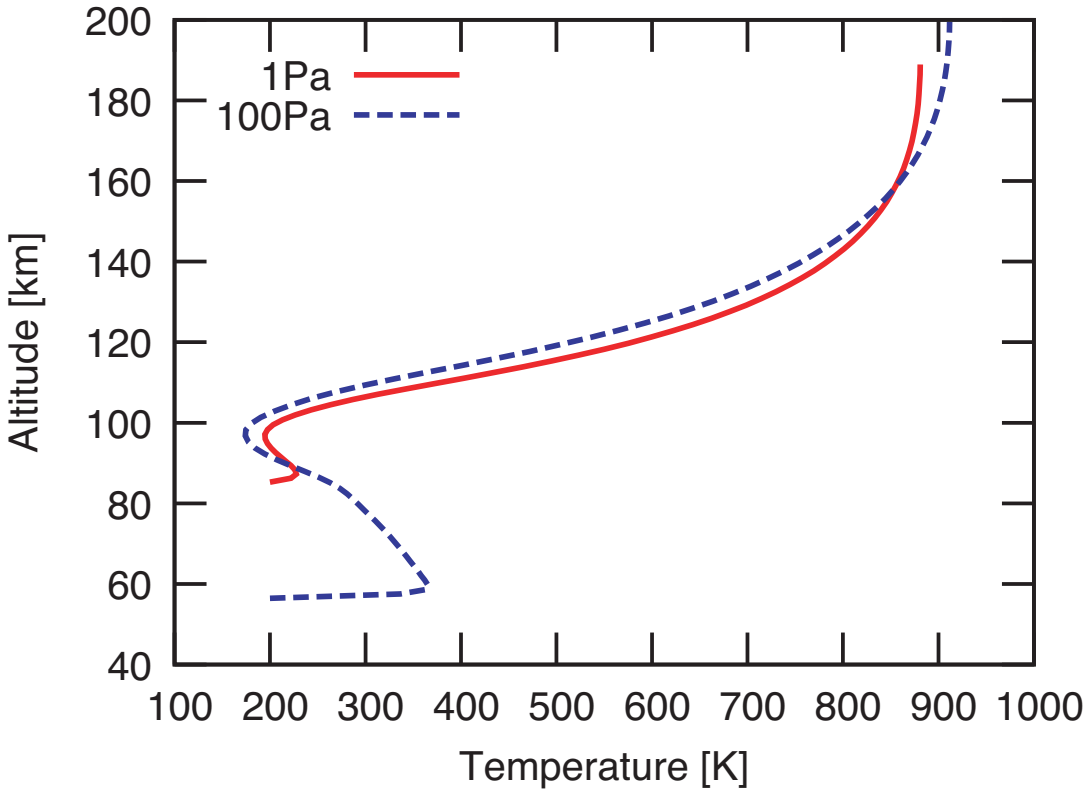

Figure 3.23: Temperature profiles for different boundary conditions. The solid line means that the pressure at the lower boundary is assumed to be 1 Pa. The dashed line means that the pressure at the lower boundary is assumed to be 100 Pa, which is same as our nominal condition.

3.4.2.2 Other radiative coolant

Here, we discuss the uncertainty of the IR cooling, focusing on the CO_2-rich atmosphere. We only consider CO_2 emission at strong bands of 4.3 and 15 μm. However, higher temperature enhances the emission at a shorter wavelength (e.g., 2.7 μm). Furthermore, in the CO_2 dominant atmosphere, CO is produced by the dissociation of CO_2. Indeed, CO abundance is larger than CO_2 abundance for the upper part of the atmosphere (see Fig. 3.10). CO has a strong emission bands at 2.4 and 4.7 μm (e.g., Funke et al., 2012). The emission at 4.7 μm behaves similarly to CO_2 emission at 4.3 μm because excitation temperature is similar. Thus, CO emission would be effective coolant for CO_2-rich atmosphere, Consequently, those emissions would cool the upper atmosphere. Additional cooling strengthens the dependence of the transit depth on CO_2 abundance. Thus, another radiative coolant involving CO_2 has a small influence on our conclusion.

3.4.2.3 Effect of hydrodynamic escape on transit depth

Our results show that hydrodynamic escape proceeds for a low-mass planet. The hydrodynamic escape leads to higher density that of our estimate, for a given radial distance. Thus, our estimate of the absorption depth of OI lines would be underestimated. However, hydrodynamic escape results in the cooling of the upper part of the atmosphere due to the adiabatic cooling (Tian et al., 2008a). This inversely leads to a decrease in the absorption depth because low temperature reduces the Doppler broadening. In this section, we discuss the effect of temperature reduction on transit depth to clarify the absorption of OI lines can be observed when the hydrodynamic escape operates.

We calculate the density structure of the corona and absorption of OI lines, assuming that the exospheric temperature is artificially fixed to 10000 K which is consistent with the hydrodynamical simulation of (Tian et al., 2008a). We use the result of upper atmosphere structure of $M_{\rm p} = 1 M_{\oplus}$ and $P_{\rm CO_2} = 1 \times 10^2$ PAL as the density profile below the exobase. Fig. 3.24 shows the observable flux of the OI line around 130.6 nm. The red solid line indicates the flux that the exospheric temperature is not restricted and 42715 K, as same as the result shown in Fig. 3.20. The blue solid line indicates the flux that the exospheric temperature is restricted to 10000 K. The dashed black line is the flux before planetary transit. The emission around the line center is perfectly absorbed in both cases. The reduction of the temperature, however, significantly affects the absorption at the line wing because the Doppler width becomes about half of that of non-restricted case. Thus, wavelength integrated transit depth reduces to 6.3×10^{-1} from 9.6×10^{-1}. This value is still much larger than that for the planet with high $P_{\rm CO_2}$. In addition, high dispersion observation readily detects the absorption of the line center. Therefore, significant absorption of OI lines is an evidence for the planet with low $P_{\rm CO_2}$ condition, even when hydrodynamic escape proceeds. This result indicates that the hydrodynamic escape has a small influence on our conclusion.

3.4.2.4 Oxygen amount

We have assumed that the partial pressure of O_2, $P_{\rm O_2}$, is the Earth-like constant value of 0.2 bars. The oxygen-rich atmosphere seems to be adequate for ocean planets around M-type stars, even for the lifeless planet. This is because terres-

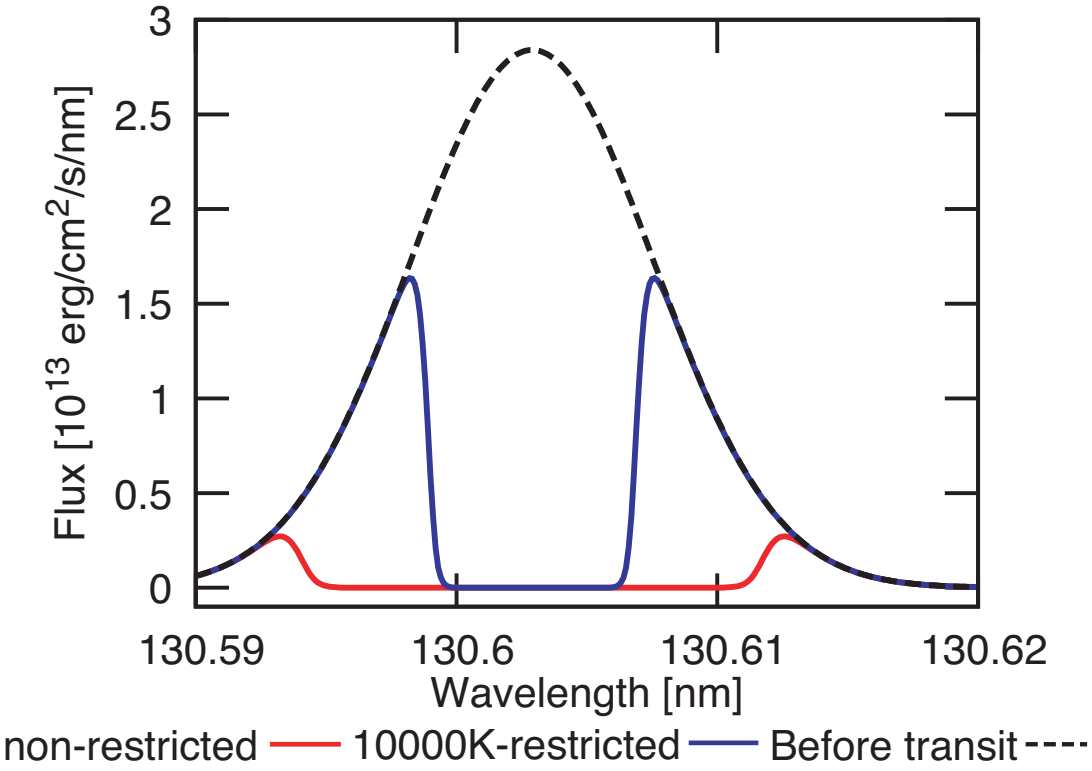

Figure 3.24: Observable flux of OI line around 130.6 nm. In the red line, the exospheric temperature is not restricted, which is same as the green line in Fig. 3.20. In the blue line, the exospheric temperature is restricted to 10000 K. The dashed black line means flux before transit.

trial planets in the habitable zone experienced runaway greenhouse, resulting in significant hydrogen loss and build up of O_2, in brighter stellar pre-main sequence phase (Luger & Barnes, 2015; Schaefer et al., 2016). However, P_{O_2} is varied by several orders of magnitude, even in the Earth (e.g., Lyons et al., 2014). Mass-independent fractionation of sulfur suggests that atmospheric O_2 concentration must have been $< 2.0 \times 10^{-6}$ bars in the Earth before great oxidation event at approximately 2.3 Ga (Pavlov & Kasting, 2002). To discuss the effect of the partial pressure of O_2 on the number density of O in the upper part of the atmosphere, we perform an additional calculation that mixing ratio in lower boundary sets to 10^{-5} PAL. In Fig. 3.25, we show the number density profiles of oxygen compounds (a) and oxygen production rate via photo-chemical reactions (b). The planetary mass and partial pressure of CO_2 are assumed to be $M_p = 1 M_\oplus$ and $P_{CO_2} = 1 \times 10^4$ PAL. which are same as our nominal condition shown in Figs. 3.10 and 3.11. Solid lines indicates that results for $P_{O_2} = 2.0 \times 10^{-6}$ bars. As a reference, we also show the results for $P_{O_2} = 2.0 \times 10^{-1}$ bars in dashed lines.

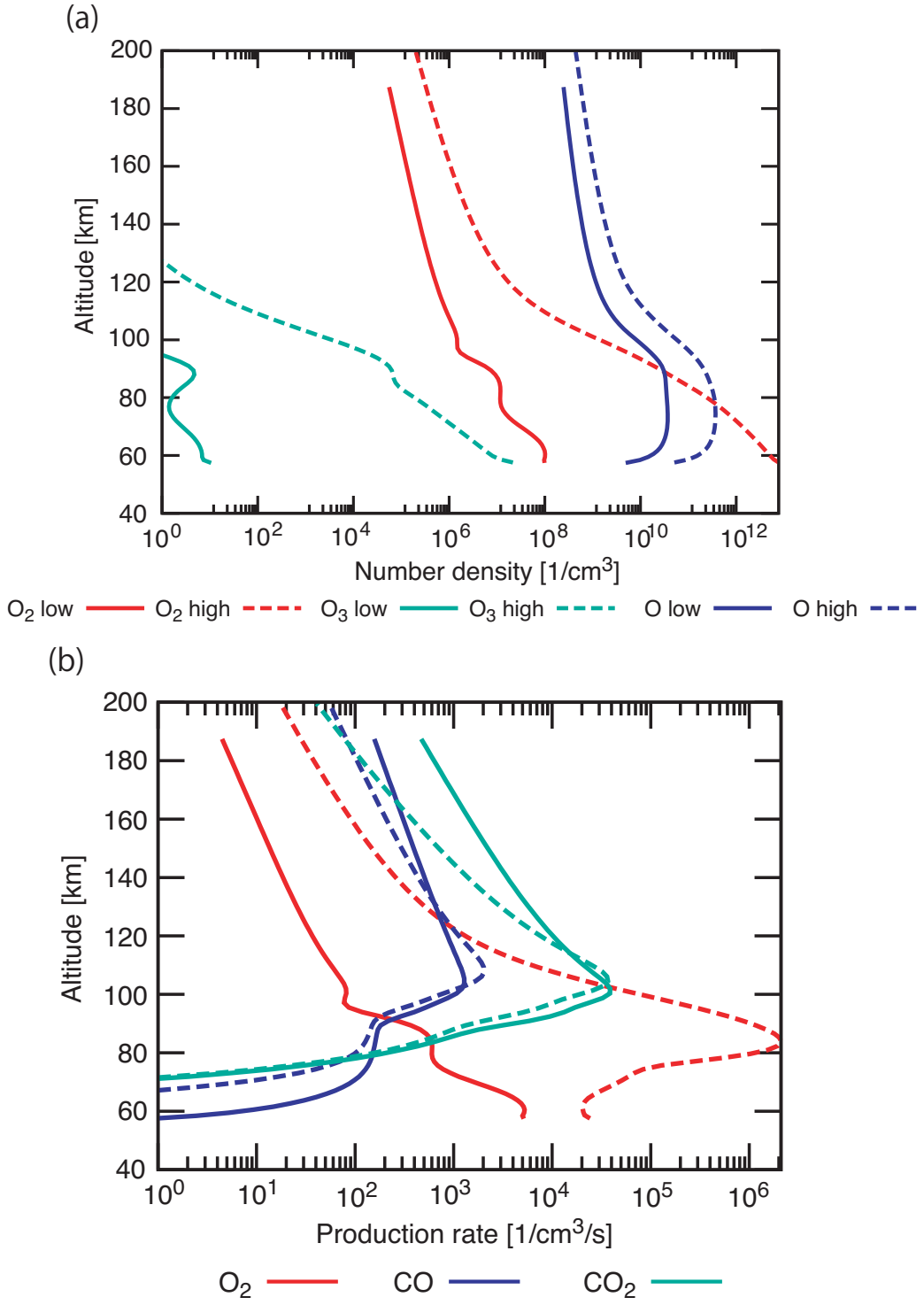

Figure 3.25: Number densities of oxygen compounds (a) and photo-chemically production rate of oxygen (b) as a function of the altitude. In solid lines, the mixing ratio of O_2 at the lower boundary derived from O_2 surface pressure of 2.0×10^{-6} bars. In dashed lines, the mixing ratio of O_2 at the lower boundary derived from O_2 surface pressure of 2.0×10^{-1} bars, which is same as our nominal condition. Panel(a) shows number density profiles of O_2 (red), O (blue), O_3 (green). Panel(b) shows production rate of oxygen via photo-chemical reactions of O_2 (red), CO (blue), CO_2 (green).

Significant differences appear in O_2 and O_3 number densities, in particular in the lower atmosphere. However, the difference of O number density is relatively small and within an order of magnitude in all calculation domain. This is because CO_2 and CO dissociations produce O, instead of O_2. Focusing O production in the upper region near the exobase, O production by CO_2 and CO are superior to that by O_2 in low P_{O_2} condition, while these are comparable in high P_{O_2} condition. Thus, O number density is rather insensitive to the partial pressure of O_2. Reactions of photo-electron result in dissociation and ionization, which also affect O number density. However, these would be small influence on number density of O because ionization via collisions with photo-electrons is comparable or smaller to direct ionization induced by high energy photon in the moderate wavelength range (~ 10 nm) (Solomon & Qian, 2005).

Considering the above uncertainties, the number density of O would decrease by an order of magnitude. Thus, we have calculated the transit depth for the condition where the number density of O artificially decreases by an order of magnitude. We use temperature and number density profiles for $M_p = 1 M_\oplus$ and $P_{CO_2} = 1 \times 10^2$ PAL. Reduction of O number density decreases the transit depth of OI lines integrated over the wavelength between 130.2 to 130.65 nm from 9.5×10^{-1} to 9.1×10^{-1}. Thus, the reduction of O number density is a small influence on our results. This is because the upper atmosphere in the hydrodynamic escape regime is expanded and the oxygen corona is spread over the stellar radius. Consequently, significantly absorption of OI lines is still evidence of the planet with low P_{O_2}.

3.4.2.5 Eddy diffusivity

In this study we have assumed an empirical, Earth-like eddy diffusivity in the thermal and compositional diffusion equations (Dickinson et al., 1984; Roble, 1995). Since the eddy (or turbulent) diffusion mixes gases in the lower atmosphere (e.g., Taylor, 1922), more efficient eddy diffusion brings heavy compounds such as CO_2 to higher altitudes. The gravity wave produced in the surface and troposphere is known to play an essential role in the turbulence in the mesosphere of the Earth (e.g., Houghton, 2002). Thus, ocean planet atmospheres would have different eddy diffusivities from that in the Earth's atmosphere, because its surface topography is significantly different from the Earth's. To resolve such an issue, we need a global 3D simulation of atmospheric dynamics with high

resolutions, which is beyond the scope of this study. Instead, in this section, we evaluate the effect of eddy diffusivity on the upper atmospheric structure.

We calculate additionally the upper atmospheric structure for an eddy diffusivity of 10 % of the fiducial Earth's value. In Fig. 3.26, we show the exospheric temperature as a function of CO_2 partial pressure for the fiducial (red line) and small (blue line) eddy diffusivities, respectively. As in Fig. 3.17, the solid and dashed lines are calculated and extrapolated values, respectively. While overall trends are similar in both cases, the smaller eddy diffusivity results in higher exospheric temperature. This is because inefficient eddy diffusion leads to inefficient mixing of CO_2 and, thus, reduction of the radiative cooling by CO_2. As a result, the transition from the compact atmosphere in the hydrostatic equilibrium regime to the expanded atmosphere in the hydrodynamic escape regime occurs at a large CO_2 partial pressure in the case of a small eddy diffusivity. It is found that an order-of-magnitude decrease in eddy diffusivity brings about an order-of-magnitude increase in the transition CO_2 partial pressure, which causes an abrupt transition in the transit depth. Therefore, the eddy diffusivity turns out to have a great impact on our results. Qualitatively, smaller (larger) eddy diffisivity causes the abrupt transition of the transit depth to be detected for larger (smaller) CO_2 partial pressure and planetary mass. Thus, we suggest that what controls the eddy diffusion and how different it is from planet to planet are future important issues to be addressed for the detectability of the extended upper atmosphere of terrestrial exoplanets with various atmospheric composition and surface topography different from those of the Earth.

3.4.2.6 Tidal locking

We have assumed that the upper atmosphere and the oxygen corona have spherically symmetric structures. In reality, the planet around M-type stars would be tidally locked. The tidal force and the Coriolis force would affect the flow structure of the hydrodynamic escape (e.g., Shaikhislamov et al., 2019). Thus, the atmospheric structure would become spherically asymmetric. In this section, we discuss the effect of tidal locking on the transit depth.

We have no enough knowledge of the effects of the tidal locking because three-dimensional simulations of the hydrodynamic escape of terrestrial planets have not been investigated. Recently, three-dimensional simulations of the atmospheric escape and absorption by various atomic species were performed for

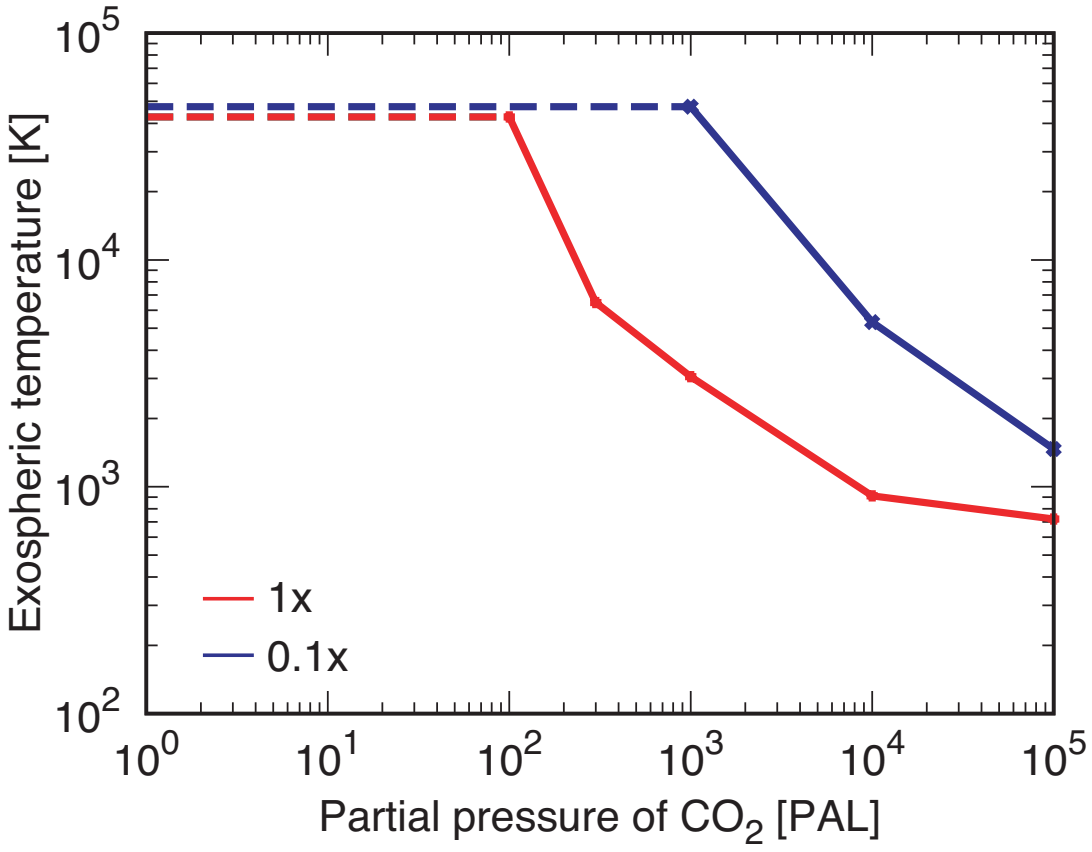

Figure 3.26: Exospheric temperatures as a function of the partial pressure of CO_2 for different eddy diffusivities, A_E (see Eq. (3.21)). The red line corresponds to the result for nominal value of $A_E = 10^8$ which is also shown in Fig. 3.17. The blue line corresponds to the result for $A_E = 10^7$. Solid lines indicate calculated values. Dashed lines indicate extrapolated values toward lower partial pressure of CO_2 because of the hydrodynamic escape. In this calculation, we assume the Earth-mass planet.

hot Jupiter HD209458b which is the planet around the G-type star (Shaikhislamov et al., 2019). In addition to the hydrogen Ly α, absorption of oxygen and carbon lines were detected in its atmosphere (Vidal-Madjar et al., 2003, 2004). Their simulations indicated that tidal force results in flows toward the night side and, thus, the atmosphere on the night side is slightly expanded. However, the oxygen number density profile is almost symmetric structure. Thus, the effects of the tidal lock have a small influence on the number density profile and the transit depth of oxygen.

3.4.3 Effect of EUV intensity on detactability of planetary climate

We use the spectrum of GJ1214 as input irradiation of UV spectrum. However, a large variety of the ratio of soft X-ray to bolometric luminosity for M-type star is detected (e.g., Scalo et al., 2007). This fact implies a large variety of EUV irradiance environments for planets around M-type stars. In this section, we give a brief discussion about the effect of EUV intensity on the detectability of the planetary climate.

The EUV intensity strongly affects the exospheric temperature and, thus, the density profile of the oxygen corona. Eq. (3.68) suggests that the exospheric temperature depends on the EUV intensity with a power of about 1–2, depending on the atmospheric composition. Since our model predicts that the transition from hydrostatic equilibrium regime to hydrodynamics escape regime results in a large difference of the absorption of OI lines (see Fig. 3.21), smaller (larger) planets are promising targets for weaker (stronger) EUV irradiance environments. This is because a weak EUV intensity would cause such a transition in small planets. Thus, planets around quiet M-type stars are promising targets for constraining planetary climate of Earth-size planets, because GJ1214 used in our EUV spectrum model is relatively a quiet M-type star (France et al., 2016).

3.4.4 Impacts of atmospheric escape to loss of ocean

Our results show that hydrodynamic escape proceeds for low-mass planets or low P_{CO_2} condition. Thus, their atmosphere should be blow-off. Furthermore, the hydrodynamic escape also results in loss of ocean (e.g., Kasting & Pollack, 1983). In this section, we discuss the climate evolution and loss of ocean via atmospheric escape.

Ribas et al. (2016b) and Bolmont et al. (2017) estimated the loss rate of oceans via hydrodynamic escape for Earth-sized planets around M-type stars, using energy-limited escape formalism in which the energy of incident EUV flux is converted into the gravitational energy of the lost gas (e.g., Watson et al., 1981). They showed that the loss rate is an order of $M_{\mathrm{oc},\oplus}$/Gyr, although M-type starts is more energetic than the Sun-like stars. The escape rate also depends on the planetary mass because gravitational energy depends on the planetary mass. The difference of mass loss rate between an Earth-mass planet and a Mars-mass planet is, however, by a factor of 2 because the mass loss rate is inversely

proportional to approximately planetary mean density. Thus, the mass loss rate is relatively insensitive to the planetary mass than other effects such as the evolution of EUV intensity. Consequently, the loss of oceans via hydrodynamic escape is a small influence on ocean reservoirs for ocean planets with the massive ocean. Further discussion about atmospheric evolution and loss of ocean via hydrodynamic escape is beyond the scope of this study.

3.5 Summary of Part II

Constraining climates of terrestrial exoplanets observationally is a crucial issue to understand planetary habitability. Carbon dioxide is an important coolant in the terrestrial upper atmosphere and its abundance greatly affects the thermal structure of the upper atmosphere. Based on the cooling effects of CO_2, the previous study showed that the absorption of emission lines of oxygen (OI lines) during planetary transit greatly depends on CO_2 abundance (Tavrov et al., 2018). However, their prediction is inapplicable to planets around M-type stars, which are a primary target in current exoplanetary science. Thus, we have made a detailed investigation on the effect of the CO_2 abundance and the planetary mass on the absorption depth of OI lines for planets around M-type stars. Then, we have explored the detectability of the planetary climate of ocean planets predicted in Part I.

Our upper atmosphere model has shown that the temperature and number density profiles greatly depend on the CO_2 abundance. We have found that the transition from the compact atmosphere with hydrostatic equilibrium to expanded atmosphere with hydrodynamic escape occurs at a moderate partial pressure of CO_2 of 0.1–1 bars for $0.5M_\oplus \leq M_\mathrm{p} \leq 1M_\oplus$, when stellar EUV intensity is comparable to 8.5 times EUV irradiation of the present Sun received by the Earth which is relatively quiet for M-type stars. Atomic oxygen is the major constituent in the upper part of the atmosphere even in the CO_2-rich atmosphere, because photo-dissociation of O_2 and CO_2 produce O. For the same EUV intensity, the upper atmospheres are in a hydrodynamic escape regime for $M_\mathrm{p} \leq 0.2M_\oplus$ regardless of partial pressure of CO_2. Thus, the CO_2 abundance would have a small influence on the atmospheric structure in low-mass planets. However, those predictions may remain to be refined because poorly-constrained eddy diffusivity has been shown to greatly affect the upper atmospheric structure. This exemplifies the importance of better understanding of eddy or turbulent diffusion in the atmospheres of ocean planets beyond the Solar system.

Then, we have performed modeling the absorption of OI lines of stellar radiation during a planetary transit. We have found that the extended atmospheres (or the oxygen coronae) in the hydrodynamic escape regime occult a large portion of stellar cross-section during a planetary transit. Thus, extended atmospheres absorb a large fraction of the stellar emission of OI lines, while

the compact atmospheres in the hydrostatic equilibrium regime provide small or negligible absorption. Since our theoretical model of the planetary climate in Part I predicts that ocean planets with massive oceans have extreme climates of CO_2-poor or CO_2-rich climates, absorption feature of OI lines are observed only in snowball state with CO_2-poor atmosphere. The predicted difference of planetary climate of ocean planets with massive oceans would be distinguishable by next-generation space telescope of the Russian space telescope World Space Observatory—Ultra-violet (WSO-UV) to be launched in 2025.

Chapter 4

Conclusion

What made the Earth habitable? Are there life-supporting planets, like the Earth, beyond the Solar system? Those are fundamental questions for humankind. The presence of oceans is thought to be an important factor for characterizing the Earth because terrestrial life and the geochemical carbon cycle essentially need liquid water or oceans. However, ocean water amount in terrestrial exoplanets must be diverse, given diverse water-supply processes and their stochastic nature. In this thesis, we explore the effect of water amount on the planetary climate of terrestrial planets in the habitable zone, to extend and generalize the comparative theory of planetary habitability for the Solar-system planets toward extra-solar planets.

In order to gain a deeper understanding of the planetary climate and habitability of terrestrial exoplanets, we have theoretically explored the planetary climate of ocean planets in the habitable zone and assessed the verifiability of our theoretical prediction for the planetary climates through near-future observations. To do so, we have developed integrated climate models of ocean planets with plate tectonics for different ocean masses, which include the effects of the carbonate-silicate geochemical carbon cycle and HP ice melting neglected in previous studies. Then, we have classified the planetary climate as a function of ocean masses and planetary degassing rates of CO_2. Furthermore, we have developed upper atmospheric models, which self-consistently include the effects of variations in atmospheric composition and stellar spectrum. Then, we quantify the detectability of the CO_2 partial pressure and planetary climate of terrestrial exoplanets, considering the UV absorption of oxygen during planetary transits.

First, we have found that material circulation (e.g., carbon cycle) will sufficiently occur, even if the planet has a massive ocean and, thus, a high-pressure

ice layer in the deep ocean. This is because plate tectonics produces the horizontal variation in geothermal heat flux and the heat flux from a mid-ocean ridge is too high to be transferred by solid convection, making the HP ice molten and forming a sorbet region, at least, near the mid-ocean ridge. In addition, melting of the high-pressure ice greatly affects the planetary climate of ocean planets. We have found that the climate is destabilized and lapses into a CO_2-poor, extremely cold state, which is called the snowball state. This indicates the existence of a critical ocean mass, beyond which an ocean planet no longer maintains a temperate climate. Also, because of the supply limit of cations, seafloor weathering is ineffective in compensating massive degassing, not achieving equilibrium climates, but yielding extremely hot ones. Consequently, planets with massive oceans with mass larger the critical one never maintain temperate climates without other greenhouse gas than CO_2, even if they are in the habitable zone.

Finally, we have applied our upper atmospheric models to planets around M-type stars. Then, we investigate the effects of the CO_2 abundance and the planetary mass on the absorption depth of OI lines during planetary transits. We have found that hydrodynamic escape proceeds and the expanded atmosphere is formed on the Earth-sized planets with small or moderate CO_2 abundance around quiet M-type stars. Thus, hydrodynamically escaping, expanded atmospheres results in significant absorption of OI lines. Otherwise, CO_2-rich atmospheres achieved with extremely hot climates absorb a small portion of stellar light. Those results suggest that the difference in the predicted climates of ocean planets with massive oceans would be distinguishable with the next-generation space telescope World Space Observatory-UltraViolet (WSO-UV) to be launched in 2025. At the same time, this exemplifies the importance of deeper understanding of the atmospheric properties of ocean planets such as eddy diffusion, to which we have quantified the sensitivity of detectability in this study.

In conclusion, water amount has a crucial role in climate and habitability of terrestrial planets and their diversity, even if the planets have the carbon cycle and plate tectonics similarly with the Earth. Temperate climates are difficult to maintain on ocean planets with massive oceans. This finding provides an insight into why the Earth is habitable and suggests that Earth-like habitable planets may be less common beyond the Solar system, given the frequency of water-rich planets predicted by planet formation theories. To understand what really

makes a planet habitable, it is crucial to observationally constrain the planetary climate of distant exoplanets. The predicted observable climatic features of ocean planets would verify our theory of planetary climates and clarify whether the planet has geochemical carbon cycle and Earth-like plate tectonics. This will mark a significant milestone in exoplanetary science.

Acknowledgements

First, I would like to show my deepest gratitude to my PhD supervisor, Dr. Masahiro Ikoma. He has supported and encouraged me so patiently at any time. Without his advice and instructive comments, I would not be able to complete my thesis and PhD program. He is a respectable scientist for physics and I want to be a researcher like him.

I am also deeply grateful to another PhD supervisor, Dr. Yutaka Abe. He gave me the joy of and approach to planetary science. He is a scientist for planetary and system sciences who is worthy of respect. I will never forget his teaching. I would like to express special thanks to Dr. Takanori Kodama. In addition to fruitful discussions, he has motivated and encouraged me to work on this study. Without his help, I am not able to complete this thesis.

I would like to express my gratitude to the following people. Dr. Singo Kameda gave fruitful discussions regarding modelling transmission during planetary transits. I am grateful to Prof. Hitoshi Fujiwara and Mr. Naoya Osada for kindly providing me their upper atmospheric model. Prof. Naoki Terada and Dr. Kaori Terada greatly help for modelling the upper atmosphere. Dr. Hidenori Genda kindly provided his carbon cycle model. Advice and comments from Prof. Eiichi Tajika, Prof. Masaki Ogawa, Prof. Yoshio Takahashi, Prof. Kanako Seki were great help for improving the model and the discussions.

I would like to thank Prof. H. Nagahara, Prof. S. Sugita, Prof. S. Tachibana, Prof. Y. Sekine, Dr. S. Kasahara, Dr. H. Kawahara, Dr. K. Hamano, and Dr. A. Fukui for fruitful comments and suggestions to this thesis. I am grateful to the members of the research group, Dr. M. Kunitomo, Dr. K. Kurosaki, Dr. S. Kadoya, Mr. Y. Takao, Dr. Y. Ito, Mr. T. Fujita, Mr. S. Fukushima, Dr. Y. Kawashima, Dr. K. Kawauchi, Mr. S. Kurokawa, Mr. A. Nitta, Mr. S. Hirose, Dr. Y. Aoyama, Mr. Y. Shirai, Mr. M. Mitsumoto, Mr. N. Hasegawa, Mr. S. Shibata, Ms. M. Ozawa, Ms. M. Imou, Mr. T. Kimura, Mr. T. Tajiri, and Mr. K. Kikuchi. Without their encouragement, this thesis would not

completed. I also express my appreciation to Prof. R. Tada, Dr. S. Takahashi, Dr. N. Moteki, Dr. K. Kawai, Prof. K. Kuramoto, and Prof. A. Abe-Ouchi for encouragements. I further would like to thank other L-seminer members and members in my student rooms 720 and 721. Finally, I would like to show my heartfelt appreciation to my family for supporting and encouraging me over the years.

Akifumi Nakayama

Appendix

A Characteristic time scales of carbon cycle

Here, we discuss response times against perturbations of surface carbon reservoirs and thermal state of an ocean. Firstly, we discuss the response time of surface of surface carbon reservoirs. We follow the discussion of Tajika & Matsui (1992) who estimated the response time of the surface carbon, τ_C. They assume that degassing flux and regassing flux linearly depend on changes of their reservoirs due to perturbations, because degassing flux and regassing flux linearly depend on the their reservoirs (Eqs. (2.18) and (2.19)). From the mass balance equation of reservoir in the mantle (Eq.(2.16)), τ_C is given by

$$\tau_C \sim (K_D^* + K_R^*)^{-1}, \tag{A.1}$$

$$K_D^* = K_D A_S, \tag{A.2}$$

$$K_R^* = \frac{\beta}{\tau_S}, \tag{A.3}$$

where τ_S is the residence time of the oceanic crust. In most of our simulations, $K_R^* \gg K_D^*$. Thus, the response against perturbations for the surface carbon budget is mainly controlled by regassing. For the Earth like mean mantle heat flow $\bar{q} = 80$ mW m^{-2} and $\beta = 0.4$, τ_C becomes 250 Myr. Thus, an equilibrium state is achieved on a timescale of the order of Gyr. Furthermore, the response of weathering is much faster than the residence time of oceanic crust because weathering flux strongly depends on the surface temperature. Thus, the response time of the atmosphere-ocean system is much shorter than τ_C. Therefore, quasi-steady state of the atmosphere-ocean system is easily achieved in contrast to the geological time scales ($\sim$ Gyr).

Nextly, we show cooling or heating time scales of an ocean against a perturbation of the surface temperature. Neglecting the effect of the latent heat, the

energy balance equation for whole ocean is given by

$$\frac{dT}{dt} = \frac{4\pi R_{\rm p}^2 F_{\rm net}}{C_{\rm P} M_{\rm oc}}, \tag{A.4}$$

where $F_{\rm net}$ is the net heating flux and $C_{\rm P}$ is the specific heat. We use $C_{\rm P} = 4.1 \times 10^3$ J kg^{-1} (at 300 K from Waite et al. (2007)). We also assume Earth's planetary radius. From Eq. (A.4), the response time scale of an ocean, $\tau_{\rm oc}$, is given by

$$\tau_{\rm oc} \sim 3.5 \times 10^6 {\rm yr} \left(\frac{M_{\rm oc}}{100 M_{{\rm oc},\oplus}} \right) \left(\frac{F}{100\ {\rm mW/m^2}} \right)^{-1} \left(\frac{\Delta T}{10{\rm K}} \right). \tag{A.5}$$

For $F_{\rm net}$, we use Earth-like mean mantle heat flow for this analysis. The effect of latent heat does not greatly affect $\tau_{\rm oc}$ because the region causing phase change is relatively small and the latent heat is about 100 times the specific heat (Dunaeva et al., 2010). Although we assume relatively large temperature perturbation, $\tau_{\rm oc}$ is much shorter than the time scale of the carbon cycle. This analysis would be invalid for permanent and large surface temperature rise which prevents the convection in the ocean. However, such events are unlikely in our knowledge. Therefore, the perturbation is relaxed and never affects our results.

B Validation of upper atmospheric model

B.1 Comparison with the present Earth's atmosphere

Here, we examine the validity of the numerical code that we have developed in this study, by comparison with the observed structure of the present Earth's atmosphere. We use the temperature and number density profiles from the empirical model NRLMSISE-00 (Picone et al., 2002) for the day of the 1st January 1990, when the Sun was approximately at the maximum of its activity cycle. For integrating the model atmospheric structure, we use the values of temperature, total number density, and mixing ratios of NRLMSISE-00 at the altitude of 65 km as the lower boundary conditions. In addition, we assume the CO_2 and H_2O mixing ratios of 4×10^{-4} and 6×10^{-6} for reproducing the present Earth's atmosphere, respectively. Those lower boundary conditions are summarized in Table B.1. We also use the EUV spectrum of the present Sun at the maximum of its activity (Claire et al., 2012) shown in Fig. 3.1. The effective temperature for solar infrared irradiation is assumed to be 5777 K.

In Fig. B.1, we show the calculated (solid line) and observed (dashed line) temperature profiles. Comparison shows that our model reproduces the observed profile of the present Earth's atmosphere well; the difference in exospheric temperature, which is of particular interest in this study, is only about 20 K. Although some small differences are found (e.g., the temperature at the mesopause), typical errors are $\lesssim 10\%$.

In Fig. B.2, we show the number density profiles of several neutral species; the solid and dashed lines indicate the model and observed profiles, respectively. Again, it turns out that both profiles are similar to each other. In particular, as for oxygen atoms, O (dark blue lines), which is of special interest in this study, while a relatively large difference in the O number density between the model and observed profiles is found at ~ 100 km, the difference is as small as 4% at the exobase (~ 420 km). Figure B.3 suggests that a large difference at ~ 100 km arises from no O_3 in the lower boundary condition leading to smaller production rate of O. However, such a large difference hardly affects the O abundance in the upper atmosphere, because O production due to O_2 photo-dissociation is predominant in slightly higher altitude. Also, the large differences in abundances of the other species have little influence on the O abundance, because oxygen atoms are produced predominantly from photo-dissociation of oxygen molecules.

Table B.1: Bottom boundary condition

Parameters	Values
Temperature	240 K
Altitude	65 km
Number density of N_2	1.9×10^{15} cm^{-3}
Number density of O_2	5.1×10^{14} cm^{-3}
Number density of Ar	2.3×10^{13} cm^{-3}
Number density of He	1.3×10^{10} cm^{-3}
Number density of CO_2	9.7×10^{11} cm^{-3}
Number density of H_2O	1.5×10^{10} cm^{-3}

In conclusion, such small differences in temperature and abundance of oxygen hardly affect the conclusions of this study. In addition, other upper atmosphere models with detailed treatment of chemical reactions for heat budget (i.e., without assumed heating efficiency) (e.g., Tian et al., 2008a; Johnstone et al., 2018; Smithtro & Sojka, 2005) also show such small differences in temperature and number density from observations. Thus, our model calculates the temperature and number density profiles with reasonable error comparable to other models.

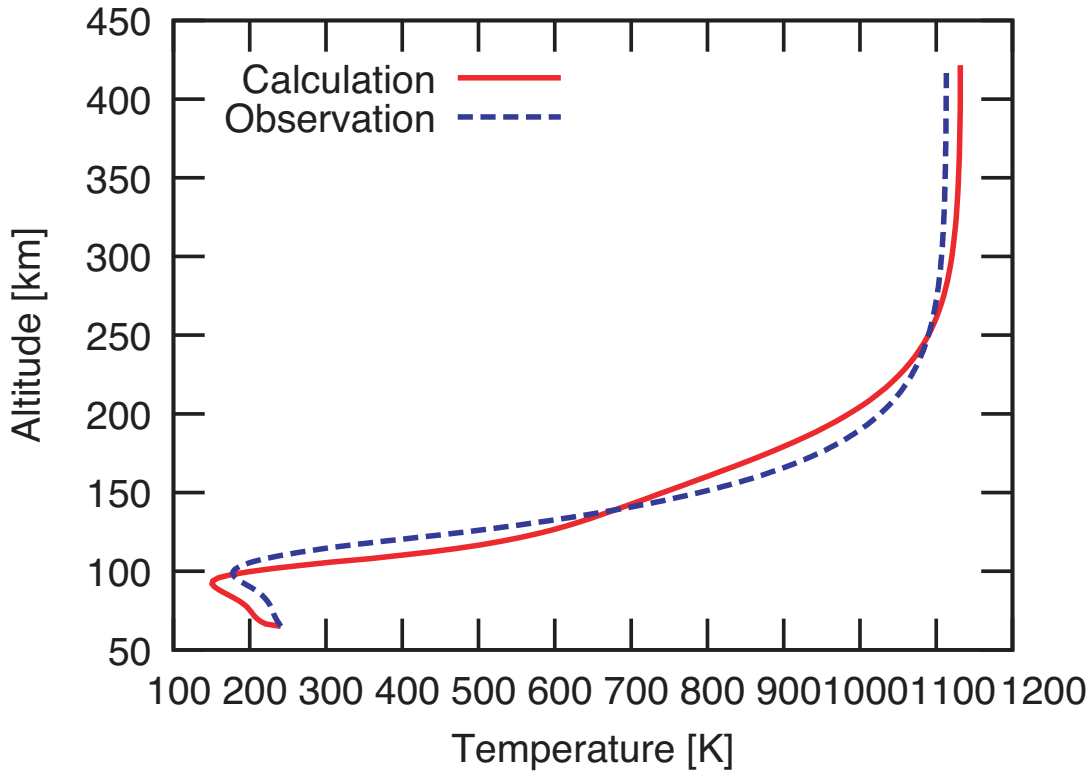

Figure B.1: Temperature profile of the present Earth's atmosphere. The red solid line is one from our upper atmosphere model. The blue dashed line is the observed profile (Picone et al., 2002).

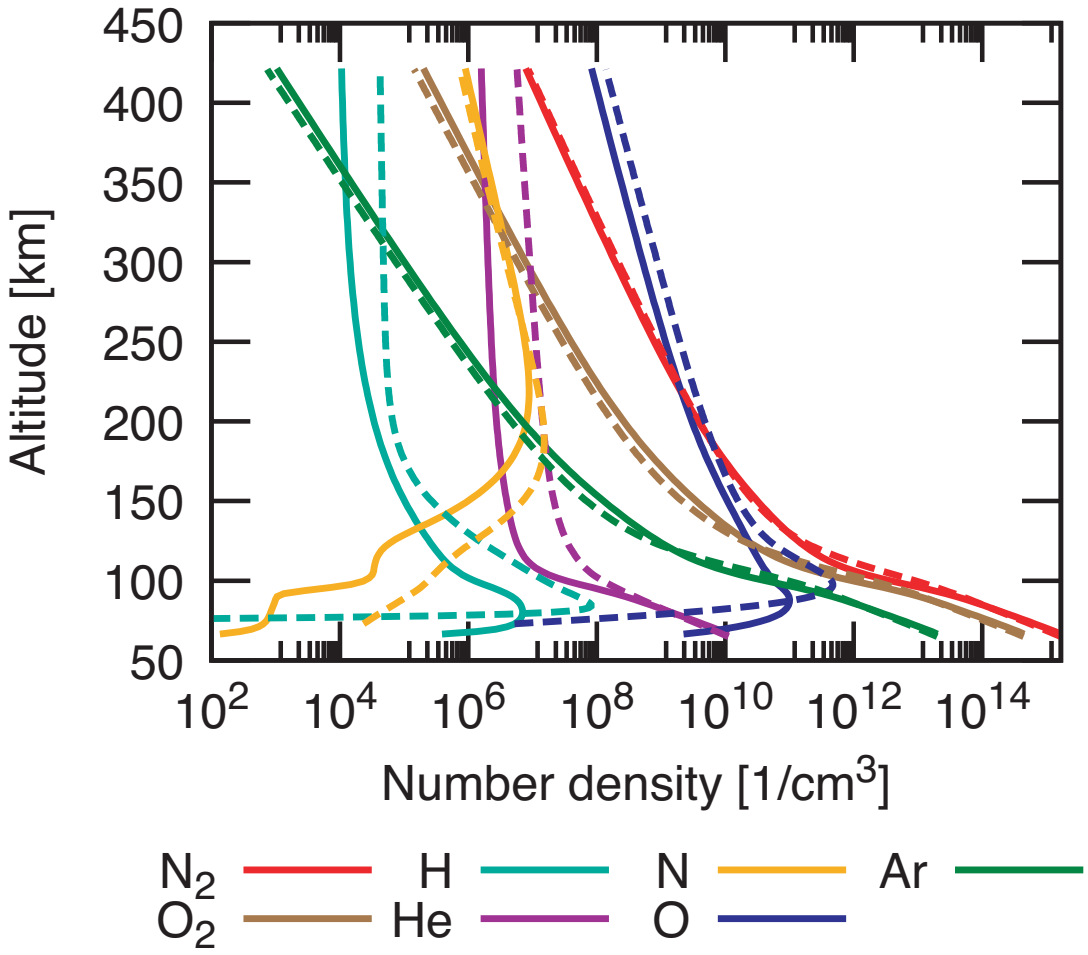

Figure B.2: Number density profiles of several neutral species for the present Earth's atmosphere. The solid lines are profiles from our upper atmosphere model. The dashed lines are the observed profiles (Picone et al., 2002).

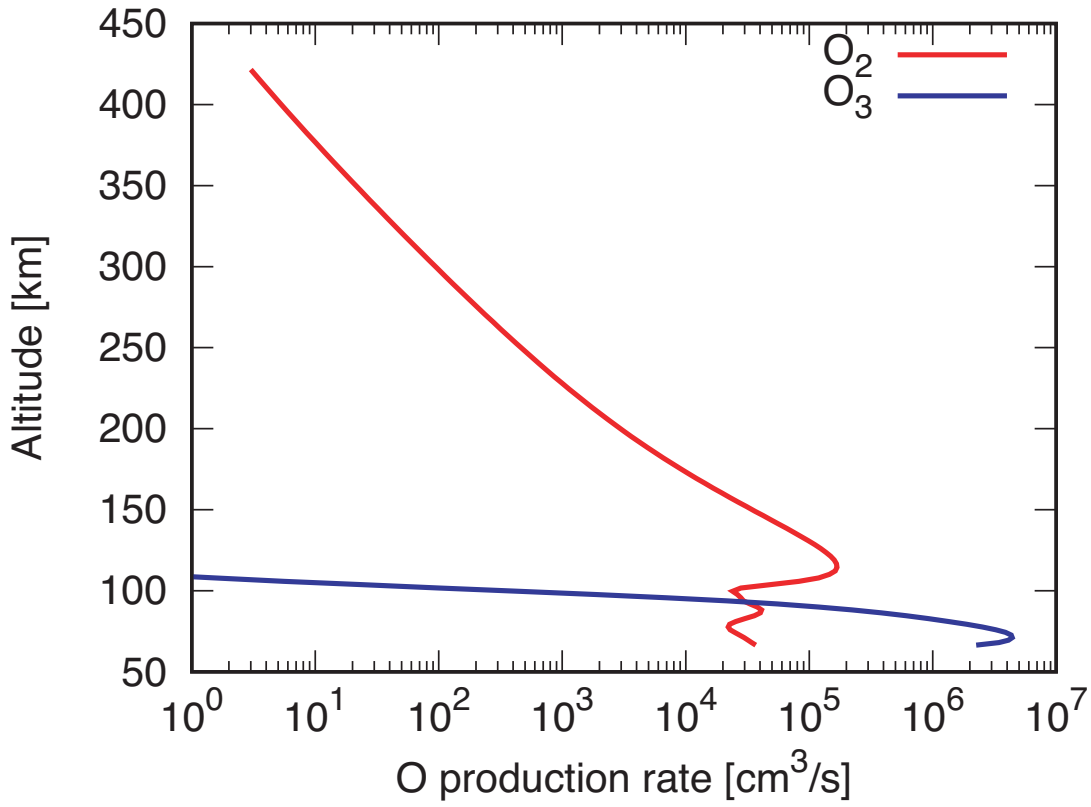

Figure B.3: O production rate as a function of altitude for the present Earth's atmosphere. Each line indicates reactant.

B.2 Comparison with previous study

Here, we compare our upper atmosphere model with the previous one that was also developed to examine the effect of CO_2 on the upper atmosphere structure (Johnstone et al., 2018). Like Johnstone et al. (2018), we use the present Earth's conditions, which are given in Table B.1, at the lower boundary of the atmosphere, expect for the CO_2 abundance. We vary the CO_2 abundance over the range between 1×10^{-2} and 1×10^{3} PAL (PAL = 400 ppm), keeping the total number density unchanged.

In Fig. B.4, we show the temperature structures for different CO_2 abundances. In panel (*a*), we plot only our results. As expected, the CO_2 abundance significantly affects the temperature structure. The exospheric temperature increases from 352 K to 1236 K as the CO_2 abundance decreases from 1×10^{3} PAL to 1×10^{-2} PAL. Likewise, the exobase altitude decreases with increasing CO_2 abundance. In the lower atmosphere ($\lesssim$ 80 km), the thermal inversion induced by absorption of stellar infrared irradiation is found for $P_{CO_2} \geq 1 \times 10^{2}$ PAL.

Panel (*b*) shows a comparison between our models (dashed lines) and Johnstone et al. (2018)'s ones (solid lines; see their Fig. 11). It turns out that the profiles are similar with each other in low-CO_2 cases (i.e., $\leq$ 10 PAL). There are, however, obvious differences in the lower atmosphere for CO_2-rich conditions. This comes from the difference in treatment of absorption of the stellar infrared irradiation (§ 3.2.1.6). To confirm such an interpretation, we integrate the atmospheric structure by a line-by-line (LBL) method in a similar way as Johnstone et al. (2018) in the highest-CO_2 case. Since Johnstone et al. (2018) considered only the stellar radiation absorption in wavelength bins with absorption cross-section larger than 1×10^{-22} cm^2, we also use only such large absorption cross-sections shown in Fig. 3.2. Note that no detailed information of wavelength bins is available in Johnstone et al. (2018), preventing our exact reproduction of their results.

Figure B.5 compares the temperature profiles for $P_{CO_2} = 1 \times 10^{3}$ PAL from the Johnstone et al. (2018)'s LBL model (red dashed line), our LBL model (blue solid line), and our *k*-distribution model (green solid line). By a comparison between the red dashed and blue solid lines, it is confirmed that our model is quite similar to the previous one. This indicates that the obvious difference seen in Fig. B.4 (b) for the high-CO_2 case is not due to computational errors and bugs, but due

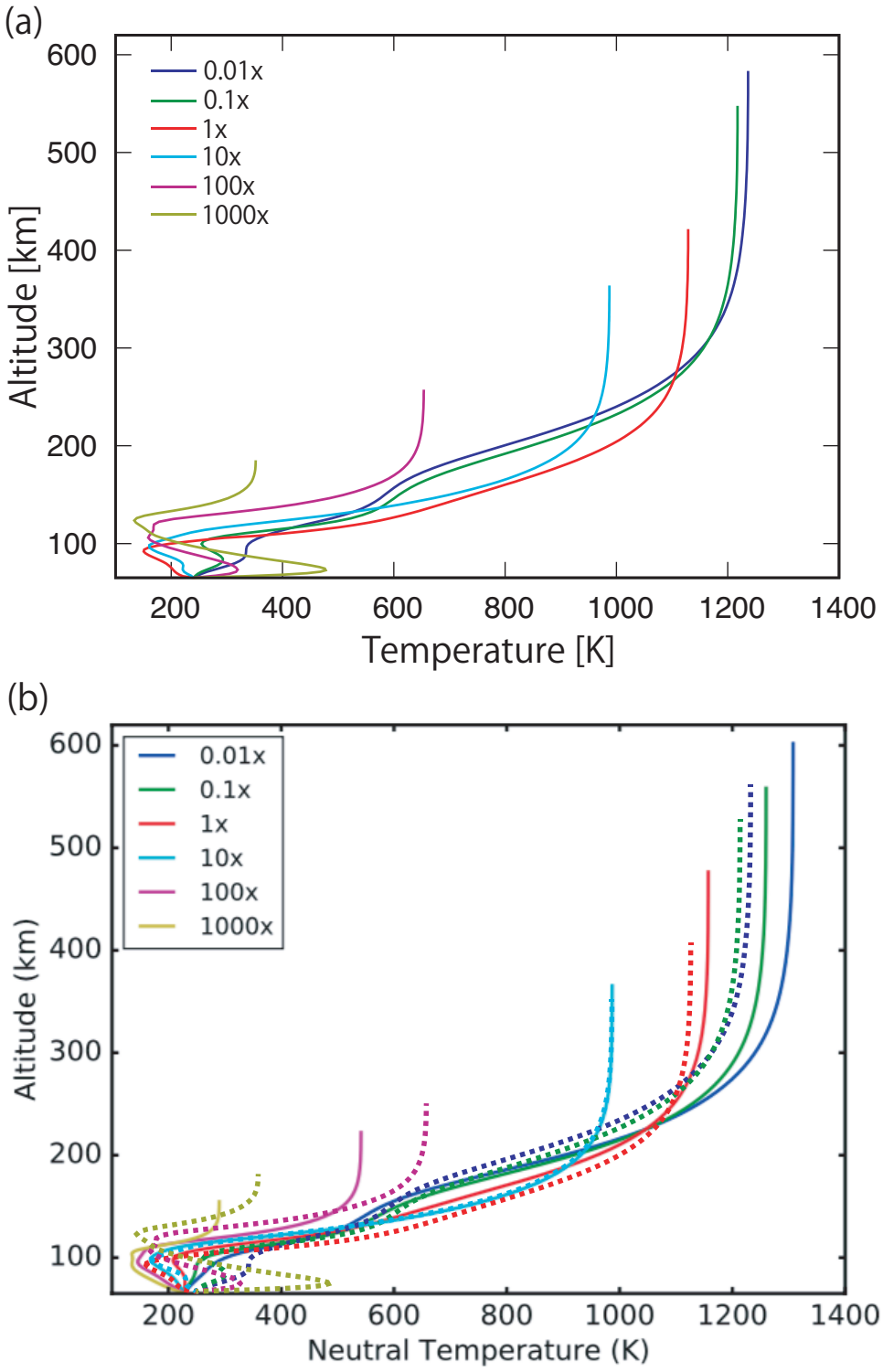

Figure B.4: Temperature as a function of altitude for six different CO_2 abundances: 0.01, 0.1, 1, 10, 100, and 1000 times the value for the present Earth (see the legend for colour-coding). Panel (a) shows temperature profiles calculated by our atmospheric model. Panel (b) compares our profiles with those from Fig. 11 of Johnstone et al. (2018). The solid lines represent the results of Johnstone et al. (2018), while the dashed lines represent the results of our model. In this calculation, we assume the present Earth-like EUV spectrum and the lower boundary conditions given in Table B.1.

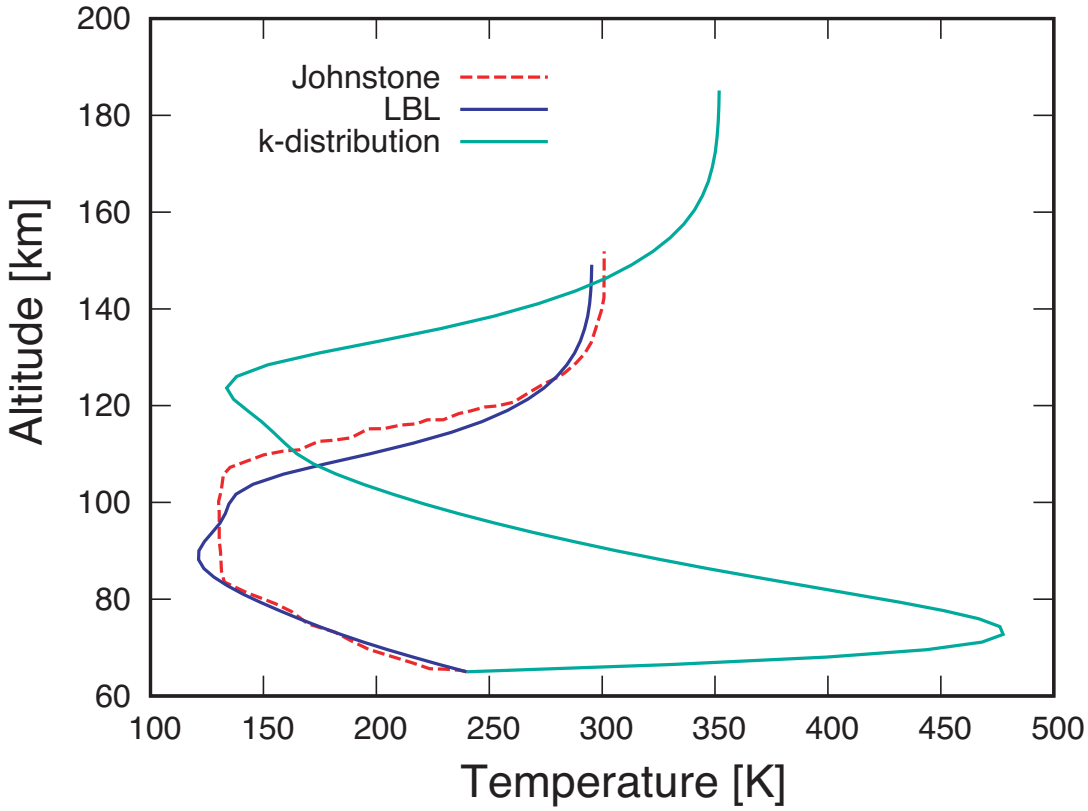

Figure B.5: Temperature as a function of altitude for CO_2 abundance of 1000 times the value for the present Earth. The red dashed line corresponds to the result of Johnstone et al. (2018) by tracing their Figure 10 with the use of the software, PlotDigitizer X. The blue and green solid lines are our model calculations using LBL model and k-distribution model, respectively.

to different treatments of stellar irradiation absorption. Indeed, the calculated heating rates for stellar IR irradiation absorption differ greatly between our *k*-distribution model and the previous LBL model; the former and latter yield 1×10^{22} and 4×10^{20} erg/s, respectively, for $P_{CO_2} = 1 \times 10^3$ PAL. Because of that, the temperature and altitude of the exobase from our *k*-distribution model is higher than those from their model. Some small discrepancies are found around ~ 100 km, which come from difference in wavelength resolution of both LBL models; indeed, we have done the calculation with a higher wavelength resolution and found that the upper atmosphere is hotter because greater amounts of stellar radiation are absorbed around the line center at higher altitudes. Nevertheless, such a difference has a tiny influence on the exobase temperature and thus transit depths for OI lines.

Our models yield colder exospheric temperatures for low CO_2 conditions

than those of Johnstone et al. (2018). Such a difference would arise from the assumption of single temperature among neutrals, ions, and electrons. Johnstone et al. (2018) considered that those species have separate temperatures which result in efficient chemical reactions because of high temperatures of ion and electron species. However, the differences in the temperature and altitude of the exobase between our models and their models are within 100 K (or 10 %). Under higher solar EUV flux conditions, which are of special interest in this study, both models yield similar results (Johnstone et al., 2018).

Finally, we evaluate the impacts of model uncertainties and errors on our conclusions. In Fig. B.6, we show the the transit depth measured at the OI lines as a function of the exobase temperature, $T_{\rm exo}$, for the Earth-mass planet. The red symbols (labeled as M-type) represent our fiducial calculations for planets around M-type stars (e.g., Fig. 3.17); the blue symbols (labeled as M-type eddy) are for planets around M-type stars, but using small eddy diffusivity (Fig. 3.26); the green symbols (labeled as Solar) are for planets around the present Sun (Fig. B.4). Higher exospheric temperatures indicated by the same-colored symbols correspond to smaller partial pressure of CO_2. The transit depth is almost constant ($\sim 4.3 \times 10^{-3}$) for $T_{\rm exo} \lesssim 2000$ K. In this regime, the oxygen corona has little contribution to the transit depth, which is determined by the occultation of the solid part of the planet. Thus, such small differences between models never affect the transit depth in this regime. On the other hand, for $T_{\rm exo} \gtrsim 8000$ K for which the atmosphere has a hydrodynamic structure as suggested by Tian et al. (2008a), the upper atmosphere is significantly expanded. In this regime, the transit depth is rather insensitive to the exospheric temperature and oxygen number density at the exobase shown in § 3.4.2.3 and 3.4.2.4. Thus, small errors induced by our model hardly affect our conclusions. For $2000\ {\rm K} \lesssim T_{\rm exo} \lesssim 8000$ K, the transit depth increases with the exospheric temperature. In this regime, the oxygen corona contributes to the transit depth. The errors in exospheric temperature (typically $\lesssim 100$ K) affects the transit depth, but have a smaller influence on the transit depth than the changes in partial pressure of CO_2 do (see red and blue symbols). Indeed, for the planets around M-type stars (red symbols), the difference in the exospheric temperature between the models with $P_{\rm CO_2}$ of 1×10^3 PAL and 3×10^2 PAL is 3430 K, which is much larger than those induced by model uncertainties and errors. Thus, the uncertainties and errors involved in our model yield no such large difference in transition pressure of CO_2, at which

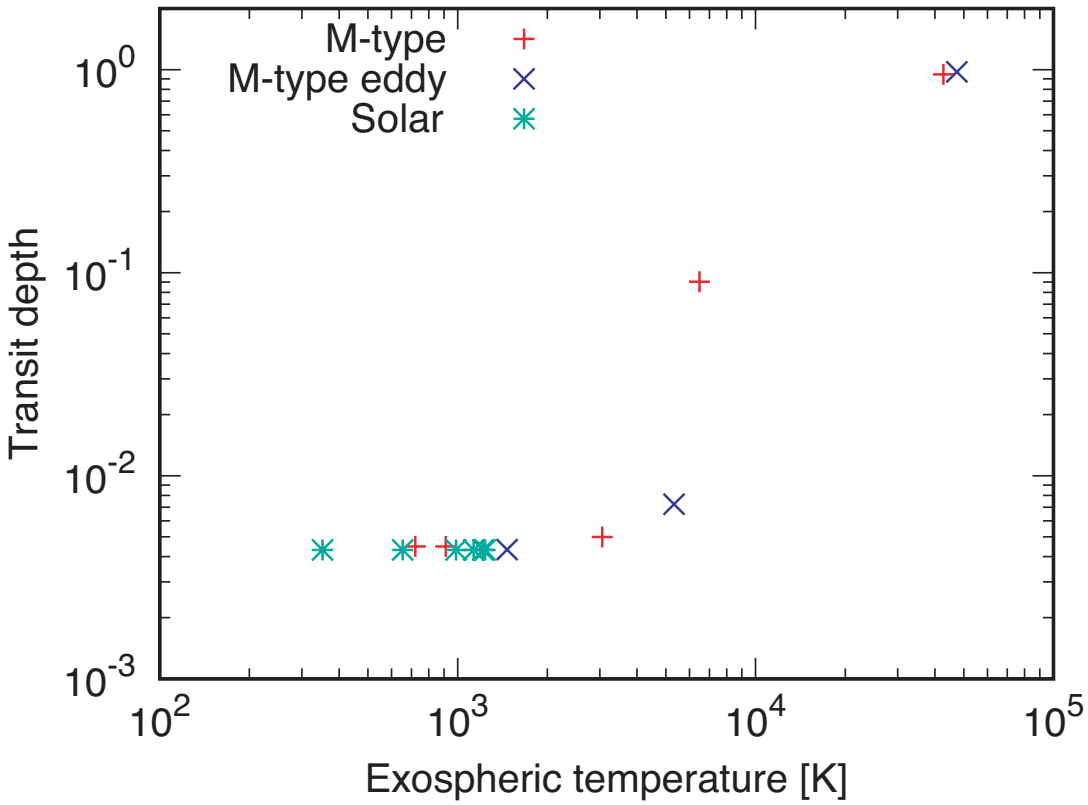

Figure B.6: Transit depth measured at the OI line as a function of the exospheric temperature for the Earth-mass planet. The red symbols (labeled as M-type) are for our fiducial calculations for the planets around M-type stars (e.g., Fig. 3.17); the blue symbols (labeled as M-type eddy) are for the planets around M-type stars, but using small eddy diffusivity (Fig. 3.26); the green symbols (labeled as Solar) are for the planets around the present Sun (Fig. B.4).

the transit depth changes abruptly, that affects our conclusions.

C Chemical reactions

C.1 Neutral reactions

Table C.1: Neutral network

No.	Reaction	Energy (eV)	Rate coefficient
1	$N + O_2 \rightarrow NO + O$	1.40	$1.5 \times 10^{-14} T \exp(-3270.0/T)$
2	$N + NO \rightarrow N_2 + O$	2.68	$4.0 \times 10^{-11} (300.0/T)^{0.2} \exp(-20.0/T)$
3	$N + CO_2 \rightarrow NO + CO$	1.06	1.7×10^{-16}
4	$N + NO_2 \rightarrow N_2O + O$	1.81	3.0×10^{-12}
5	$N + H_2 \rightarrow NH + H$	-1.06	$1.69 \times 10^{-9} \exp(-18095.0/T)$
6	$NO + O + M \rightarrow NO_2 + M$	-	$9.0 \times 10^{-32} (300.0/T)^{1.5}$
7	$NO + O_3 \rightarrow NO_2 + O_2$	2.03	$2.0 \times 10^{-12} \exp(-1400.0/T)$
8	$NO + OH + M \rightarrow HNO_2 + M$	-	$7.0 \times 10^{-31} (300.0/T)^{2.6}$
9	$NO + HO_2 \rightarrow NO_2 + OH$	0.31	$3.7 \times 10^{-12} \exp(250.0/T)$
10	$NO + NO_3 \rightarrow NO_2 + NO_2$	1.34	$1.5 \times 10^{-11} \exp(170.0/T)$
11	$O + O + M \rightarrow O_2 + M$	5.10	$9.59 \times 10^{-34} \exp(480.0/T)$
12	$O + O_2 + M \rightarrow O_3 + M$	1.10	$6.0 \times 10^{-34} (300.0/T)^{2.3}$
13	$O + O_3 \rightarrow O_2 + O_2$	4.06	$8.0 \times 10^{-12} \exp(-2060.0/T)$
14	$O + NO_2 \rightarrow NO + O_2$	2.0	$6.5 \times 10^{-12} \exp(120.0/T)$
15	$O + NO_3 \rightarrow NO_2 + O_2$	2.97	1.0×10^{-11}
16	$O + H_2O \rightarrow OH + OH$	-0.31	$1.85 \times 10^{-11} (300.0/T)^{-0.95} \exp(-52900/T)$

Table C.1: Continued

No.	Reaction	Energy (eV)	Rate coefficient
17	$N(^2D) + O \rightarrow N + O$	2.38	6.90×10^{-13}
18	$N(^2D) + O_2 \rightarrow NO + O(^1D)$	1.84	$9.7 \times 10^{-12} \exp(-185.0/T)$
19	$N(^2D) + O_2 \rightarrow NO + O$	3.76	$5.58 \times 10^{-12} (300.0/T)^{-1.0}$
20	$N(^2D) + NO \rightarrow N_2 + O$	5.63	7×10^{-11}
21	$N(^2D) \rightarrow N$	-	1.06×10^{-5}
22	$N(^2D) + e^- \rightarrow N + e^-$	2.38	$3.86 \times 10^{-10} (300.0/T)^{-0.81}$
23	$N(^2D) + CO_2 \rightarrow NO + CO$	3.41	3.5×10^{-13}
24	$N(^2D) + N_2 \rightarrow N + N_2$	2.38	1.7×10^{-14}
25	$N(^2D) + CO \rightarrow N + CO$	-	1.9×10^{-12}
26	$N(^2D) + H_2 \rightarrow NH + H$	-	$4.2 \times 10^{-11} \exp(-880.0/T)$
27	$O(^1D) + N_2 \rightarrow O + N_2$	1.96	$1.8 \times 10^{-11} \exp(107.0/T)$
28	$O(^1D) \rightarrow O$	-	8.33×10^{-3}
29	$O(^1D) + H_2O \rightarrow OH + OH$	1.23	2.2×10^{-10}
30	$O(^1D) + O_2 \rightarrow O_2(^1\Sigma_g) + O$	0.33	$0.75 \times 3.2 \times 10^{-11} \exp(70.0/T)$
31	$O(^1D) + O_2 \rightarrow O_2 + O$	1.96	$0.25 \times 3.2 \times 10^{-11} \exp(70.0/T)$
32	$O(^1D) + O \rightarrow O + O$	1.96	$6.47 \times 10^{-12} (300.0/T)^{-0.14}$
33	$O(^1D) + H_2 \rightarrow H + OH$	1.88	1.0×10^{-10}
34	$O(^1D) + CO_2 \rightarrow O + CO_2$	1.96	$7.4 \times 10^{-11} \exp(120.0/T)$
35	$O(^1D) + O_3 \rightarrow O_2 + O_2$	6.03	1.2×10^{-10}
36	$O(^1D) + O_3 \rightarrow O_2 + O + O$	0.87	1.2×10^{-10}
37	$O(^1D) + CO \rightarrow O + CO$	-	3.6×10^{-11}
38	$O(^1D) + e^- \rightarrow O + e^-$	-	$2.87 \times 10^{-10} (300/T)^{-0.91}$
39	$O(^1D) + N_2 \rightarrow N_2O$	-	$3.5 \times 10^{-37} (300/T)^{0.6}$
40	$O(^1D) + N_2O \rightarrow N_2 + O_2$	-	4.9×10^{-11}
41	$O(^1D) + N_2O \rightarrow NO + NO$	-	6.7×10^{-11}
42	$H_2O + H_2 \rightarrow H + OH + H_2$	-	$5.8 \times 10^{-9} \exp(-52900/T)$

Table C.1: Continued

No.	Reaction	Energy (eV)	Rate coefficient
43	$OH + N \rightarrow NO + H$	2.10	5.0×10^{-11}
44	$OH + O \rightarrow H + O_2$	0.72	$2.0 \times 10^{-11} \exp(117.0/T)$
45	$OH + CO \rightarrow CO_2 + H$	1.07	1.5×10^{-13}
46	$OH + H_2 \rightarrow H_2O + H$	0.65	$7,7 \times 10^{-12} \exp(-2100.0/T)$
47	$OH + OH \rightarrow H_2O + O$	0.73	$6.2 \times 10^{-14} (300.0/T)^{-2.62} \exp(945.0/T)$
48	$OH + H + M \rightarrow H_2O + M$	5.17	$6.1 \times 10^{-26} T^{-2.0}$
49	$OH + H \rightarrow H_2 + O$	0.08	$1.4 \times 10^{-14} T \exp(-3500.0/T)$
50	$OH + O_3 \rightarrow HO_2 + O_2$	1.73	$1.6 \times 10^{-12} \exp(-940.0/T)$
51	$OH + OH + M \rightarrow H_2O_2 + M$	-	$6.9 \times 10^{-31} (300.0/T)^{0.8}$
52	$OH + NO_2 + M \rightarrow HNO_3 + M$	-	$2.6 \times 10^{-30} (300/T)^{3.2}$
53	$OH + NO_3 \rightarrow NO_2 + HO_2$	0.62	2.2×10^{-11}
54	$OH + HNO_2 \rightarrow NO_2 + H_2O$	-	$1.8 \times 10^{-11} (-390.0/T)$
55	$OH + HNO_3 \rightarrow NO_3 + H_2O$	-	$7.2 \times 10^{-15} \exp(785.0/T)$
56	$CO + O + M \rightarrow CO_2 + M$	5.51	$6.6 \times 10^{-33} \exp(-1103/T)$
57	$H_2 + O(^1D) \rightarrow H + OH$	1.88	1.0×10^{-10}
58	$H_2 + O \rightarrow H + OH$	0.08	$1.6 \times 10^{-11} \exp(-4570.0/T)$
59	$H_2 + M \rightarrow H + H + M$	-4.52	$1.5 \times 10^{-9} \exp(-48000.0/T)$
60	$H_2 + H_2 \rightarrow H + H + H_2$	-2.24	$1.25 \times 10^{-11} \exp(-52000.0/T)$
61	$H_2 + H \rightarrow H + H + H$	0.02	$1.0 \times 10^{-10} \exp(-52000.0/T)$
62	$H + O_2 \rightarrow O + OH$	-0.72	$3.7 \times 10^{-10} \exp(-8450.0/T)$
63	$H + O_3 \rightarrow OH + O_2$	2.004	$1.4 \times 10^{-10} \exp(-470.0/T)$
64	$H + H + M \rightarrow H_2 + M$	4.52	$5.7 \times 10^{-32} (300/T)^{1.6}$
65	$H + H_2O \rightarrow H_2 + OH$	-0.65	$1.5 \times 10^{-10} \exp(-10250.0/T)$
66	$H + O_2 + M \rightarrow HO_2 + M$	2.11	$5.5 \times 10^{-32} (300/T)^{1.6}$
67	$H + H + CO_2 \rightarrow H_2 + CO_2$	-	$1.2 \times 10^{-32} (300/T)^{1.3}$
68	$HO_2 + H \rightarrow H_2O + O$	2.34	$0.02 \times 8.1 \times 10^{-11}$
69	$HO_2 + H \rightarrow H_2 + O_2$	2.41	$0.08 \times 8.1 \times 10^{-11}$
70	$HO_2 + H \rightarrow OH + OH$	1.61	$0.9 \times 8.1 \times 10^{-11}$
71	$HO_2 + OH \rightarrow H_2O + O_2$	3.06	$4.8 \times 10^{-11} \exp(250.0/T)$
72	$HO_2 + O \rightarrow OH + O_2$	2.33	$3.0 \times 10^{-11} \exp(200.0/T)$
73	$HO_2 + O_3 \rightarrow OH + O_2 + O_2$	1.23	$1.1 \times 10^{-14} \exp(-500.0/T)$
74	$HO_2 + HO_2 \rightarrow H_2O_2 + O_2$	1.71	$2.3 \times 10^{-13} \exp(600.0/T)$
75	$H_2O_2 + OH \rightarrow HO_2 + H_2O$	1.35	$2.9 \times 10^{-12} \exp(-160.0/T)$
76	$H_2O_2 + O \rightarrow HO_2 + OH$	3.44	$1.4 \times 10^{-12} \exp(-2000.0/T)$

Table C.1: Continued

No.	Reaction	Energy (eV)	Rate coefficient
77	$O_2(^1\Sigma_g) + N_2 \rightarrow O_2(^1\Delta_g) + N_2$	0.65	2.1×10^{-15}
78	$O_2(^1\Sigma_g) + CO_2 \rightarrow O_2(^1\Delta_g) + CO_2$	0.65	4.2×10^{-13}
79	$O_2(^1\Sigma_g) + O_3 \rightarrow O_2(^1\Delta_g) + O_3$	0.65	2.2×10^{-11}
80	$O_2(^1\Sigma_g) + O \rightarrow O_2(^1\Delta_g) + O$	0.65	8.0×10^{-14}
81	$O_2(^1\Sigma_g) + O_2 \rightarrow O_2(^1\Delta_g) + O_2$	0.65	3.9×10^{-17}
82	$O_2(^1\Sigma_g) \rightarrow O_2$	-	0.085
83	$O_2(^1\Delta_g) + O_2 \rightarrow O_2 + O_2$	0.98	$3.6 \times 10^{-18} \exp(-220.0/T)$
84	$O_2(^1\Delta_g) + N_2 \rightarrow O_2 + N_2$	0.98	1.0×10^{-20}
85	$O_2(^1\Delta_g) + O \rightarrow O_2 + O$	0.98	1.3×10^{-16}
86	$O_2(^1\Delta_g) \rightarrow O_2$	-	2.58×10^{-4}
87	$C + CO_2 \rightarrow CO + CO$	4.53	$7.62 \times 10^{-14} (300/T)^{-0.5} \exp(-3480.0/T)$
88	$C + NO \rightarrow CO + N$	4.67	$7.5 \times 10^{-11} (300/T)^{0.16}$
89	$C + O_2 \rightarrow CO + O$	6.05	$4.9 \times 10^{-11} (300/T)^{0.32}$
90	$NH + H_2 \rightarrow NH_2 + H$	-0.48	$5.96 \times 10^{-11} \exp(-7782.0/T)$
91	$NH + H \rightarrow N + H_2$	1.10	$1.0 \times 10^{-12} T^{0.5} \exp(-2400.0/T)$
92	$N(^2P) + CO_2 \rightarrow N(^2D) + CO_2$	-	2.0×10^{-15}
93	$N(^2P) + CO \rightarrow N(^2D) + CO$	-	6.0×10^{-15}
94	$N(^2P) + O_2 \rightarrow NO + O$	-	$1.03 \times 10^{-12} \exp(-60.0/T)$
95	$N(^2P) + O_2 \rightarrow NO + O(^1D)$	-	$1.03 \times 10^{-12} \exp(-60.0/T)$
96	$N(^2P) + O_2 \rightarrow NO + O(^1S)$	-	$1.03 \times 10^{-12} \exp(-60.0/T)$
97	$N(^2P) + O \rightarrow N(^2D) + O$	-	1.7×10^{-11}
98	$N(^2P) + NO \rightarrow N(^2D) + NO$	-	2.9×10^{-11}
99	$N(^2P) + N_2 \rightarrow N(^2D) + N_2$	-	5.0×10^{-17}
100	$N(^2P) + N \rightarrow N(^2D) + N$	-	6.2×10^{-13}
101	$N(^2P) + H_2 \rightarrow N(^2D) + H_2$	-	2.5×10^{-13}
102	$N(^2P) + e^- \rightarrow N + e^-$	-	$2.04 \times 10^{-10} (300/T)^{-0.85}$
103	$N(^2P) + e^- \rightarrow N(^2D) + e^-$	-	9.5×10^{-9}
104	$N(^2P) \rightarrow N(^2D)$	-	7.9×10^{-2}
105	$N(^2P) \rightarrow N$	-	5.0×10^{-3}

Table C.1: Continued

No.	Reaction	Energy (eV)	Rate coefficient
106	$O(^1S) + CO_2 \rightarrow O(^1D) + CO_2$	-	$2.02 \times 10^{-11} \exp(-1327.0/T)$
107	$O(^1S) + CO_2 \rightarrow O + CO_2$	-	$1.19 \times 10^{-11} \exp(-1327.0/T)$
108	$O(^1S) + O_2 \rightarrow O(^1D) + O_2$	-	$1.36 \times 10^{-12} \exp(-815.0/T)$
109	$O(^1S) + O_2 \rightarrow O + O_2$	-	$3.04 \times 10^{-12} \exp(-815.0/T)$
110	$O(^1S) + O \rightarrow O(^1D) + O$	-	0.0
111	$O(^1S) + N_2 \rightarrow O(^1D) + N_2$	-	5.0×10^{-17}
112	$O(^1S) + CO \rightarrow O(^1D) + CO$	-	$7.4 \times 10^{-14} \exp(-961.0/T)$
113	$O(^1S) + H_2 \rightarrow O(^1D) + H_2$	-	2.86×10^{-16}
114	$O(^1S) + e^- \rightarrow O(^1D) + e^-$	-	8.5×10^{-9}
115	$O(^1S) + e^- \rightarrow O + e^-$	-	$1.56 \times 10^{-10} (300/T)^{-0.94}$
116	$O(^1S) \rightarrow O(^1D)$	-	1.06
117	$O(^1S) \rightarrow O$	-	4.5×10^{-2}
118	$NO_2 + O_3 \rightarrow NO_3 + O_2$	1.0	$1.2 \times 10^{-13} \exp(-2450.0/T)$
119	$NO_2 + H \rightarrow NO + OH$	1.20	$4.0 \times 10^{-10} \exp(-340.0/T)$
120	$NO_3 + NO_3 \rightarrow NO_2 + NO_2 + O_2$	0.39	$8.5 \times 10^{-13} \exp(-2450.0/T)$
121	$Cl + O_3 \rightarrow ClO + O_2$	1.68	$2.9 \times 10^{-11} \exp(-260.0/T)$
122	$ClO + O \rightarrow Cl + O_2$	2.39	$3.0 \times 10^{-11} \exp(70.0/T)$
123	$ClO + NO \rightarrow NO_2 + Cl$	0.37	$6.4 \times 10^{-12} \exp(290.0/T)$
124	$NH_2 + H \rightarrow NH + H_2$	0.47	$1.05 \times 10^{-10} \exp(-4450.0/T)$

C.2 Ion reactions

Table C.2: Ion network

No.	Reaction	Energy (eV)	Rate coefficient
1	$N_2^+ + O_2 \rightarrow O_2^+ + N_2$	3.52	$5.1 \times 10^{-11}(300.0/T)^{1.16}$ $(T \leq 1000\text{K})$
			$1.26 \times 10^{-11}(1000.0/T)^{-0.57}$ $(1000 \leq T \leq 2000\text{K})$
			2.39×10^{-11} $(T \geq 2000\text{K})$
2	$N_2^+ + O \rightarrow NO^+ + N(^2D)$	0.70	$1.33 \times 10^{-10}(300.0/T)^{0.44}$ $(T \leq 1500\text{K})$
			$6.55 \times 10^{-11}(1500.0/T)^{-0.2}$ $(T \geq 1500\text{K})$
3	$N_2^+ + O \rightarrow O^+ + N_2$	1.96	$7.0 \times 10^{-12}(300.0/T)^{0.23}$ $(T \leq 1500\text{K})$
			$4.83 \times 10^{-12}(1500.0/T)^{-0.41}$ $(T \geq 1500\text{K})$
4	$N_2^+ + NO \rightarrow NO^+ + N_2$	6.25	3.6×10^{-10}
5	$N_2^+ + CO_2 \rightarrow CO_2^+ + N_2$	1.81	$3.6 \times 10^{-10}(300.0/T)^{0.28}$
6	$N_2^+ + CO \rightarrow CO^+ + N_2$	1.57	7.40×10^{-11}
7	$N_2^+ + e^- \rightarrow N + N$	5.82	$2.2 \times 10^{-8}(300.0/T)^{0.39}$
8	$N_2^+ + e^- \rightarrow N + N(^2D)$	3.44	$1.98 \times 10^{-7}(300.0/T)^{0.39}$
9	$N_2^+ + N \rightarrow N^+ + N_2$	1.31	1.0×10^{-11}
10	$N_2^+ + Ar \rightarrow Ar^+ + N_2$	-	$1.10 \times 10^{-11}\exp(-2089.0/T)$
11	$N_2^+ + H_2 \rightarrow N_2H^+ + H$	2.60	1.52×10^{-9}
12	$N_2^+ + e^- \rightarrow N(^2D) + N(^2D)$	-	$1.01 \times 10^{-7}(300.0/T)^{0.39}$
13	$N_2^+ + e^- \rightarrow N + N(^2P)$	-	$1.76 \times 10^{-8}(300.0/T)^{0.39}$
14	$N_2^+ + H_2O \rightarrow N_2 + H^+$	3.0	2.2×10^{-9}
15	$N_2^+ + H \rightarrow N_2 + H^+$	2.07	1.2×10^{-10}

Table C.2: Continued

No.	Reaction	Energy (eV)	Rate coefficient
16	$O_2^+ + N_2 \rightarrow NO^+ + NO$	0.93	1.0×10^{-15}
17	$O_2^+ + N \rightarrow NO^+ + O$	4.21	1.0×10^{-10}
18	$O_2^+ + NO \rightarrow NO^+ + O_2$	2.81	4.4×10^{-10}
19	$O_2^+ + e^- \rightarrow O + O$	6.99	$0.22 \times 1.95 \times 10^{-7}(300.0/T)^{0.7}$ $(T \leq 1200\text{K})$
			$0.22 \times 7.38 \times 10^{-8}(1200.0/T)^{0.56}$ $(T \geq 1200\text{K})$
20	$O_2^+ + e^- \rightarrow O + O(^1D)$	5.02	$0.42 \times 1.95 \times 10^{-7}(300.0/T)^{0.7}$ $(T \leq 1200\text{K})$
			$0.32 \times 7.38 \times 10^{-8}(1200.0/T)^{0.56}$ $(T \geq 1200\text{K})$
21	$O_2^+ + e^- \rightarrow O(^1D) + O(^1D)$	3.06	$0.36 \times 1.95 \times 10^{-7}(300.0/T)^{0.7}$ $(T \leq 1200\text{K})$
			$0.36 \times 7.38 \times 10^{-8}(1200.0/T)^{0.56}$ $(T \geq 1200\text{K})$
22	$O_2^+ + N(^2D) \rightarrow NO^+ + O$	-	1.8×10^{-10}
23	$O_2^+ + N(^2D) \rightarrow N^+ + O_2$	-	8.65×10^{-11}
24	$O_2^+ + C \rightarrow CO^+ + O$	4.18	5.0×10^{-11}
25	$O_2^+ + C \rightarrow C^+ + O_2$	0.88	5.0×10^{-11}
26	$O_2^+ + e^- \rightarrow O(^1D) + O(^1S)$	-	$9.75 \times 10^{-9}(300.0/T)^{0.70}$ $(T \leq 1200\text{K})$
			$3.69 \times 10^{-9}(1200.0/T)^{0.56}$ $(T \geq 1200\text{K})$
27	$NO^+ + e^- \rightarrow N + O$	2.75	$8.4 \times 10^{-8}(300.0/T)^{0.85}$
28	$NO^+ + e^- \rightarrow N(^2D) + O$	0.38	$3.36 \times 10^{-7}(300.0/T)^{0.85}$
29	$O^+ + NO \rightarrow NO^+ + O$	4.36	$7.0 \times 10^{-13}(300.0/T)^{0.66}$ $(T \leq 300\text{K})$
			$7.0 \times 10^{-13}(300.0/T)^{-0.87}$ $(T \geq 300\text{K})$
30	$O^+ + CO_2 \rightarrow O_2^+ + CO$	1.20	1.1×10^{-9} $(T \leq 800\text{K})$
			$1.1 \times 10^{-9}(800.0/T)^{0.39}$ $(T \geq 800\text{K})$
31	$O^+ + H_2 \rightarrow OH^+ + H$	0.36	1.65×10^{-9}
32	$O^+ + H \rightarrow H^+ + O$	0.02	$7.26 \times 10^{-11} T^{0.36} \exp(8.6/T)$
33	$O^+ + N_2 \rightarrow NO^+ + N$	1.09	$1.20 \times 10^{-12}(300.0/T)^{0.45}$ $(T \leq 1000\text{K})$
			$7.0 \times 10^{-13}(1000.0/T)^{-2.12}$ $(T \geq 1000\text{K})$
34	$O^+ + O_2 \rightarrow O_2^+ + O$	1.56	$1.6 \times 10^{-11}(300.0/T)^{0.52}$ $(T \leq 900\text{K})$
			$9.0 \times 10^{-12}(900.0/T)^{-0.92}$ $(T \geq 900\text{K})$
35	$O^+ + N(^2D) \rightarrow N^+ + O$	1.45	1.3×10^{-10}
36	$O^+ + e^- \rightarrow O$	-	$3.7 \times 10^{-12}(250.0/T)^{0.7}$
37	$O^+ + C \rightarrow C^+ + O$	-	1.0×10^{-10}
38	$O^+ + H_2O \rightarrow O + H_2O^+$	1.05	$9.54 \times 10^{-10}(0.62 + 2.579(300.0/T)^{0.5})$
39	$O^+ + OH \rightarrow OH^+ + O$	0.69	3.6×10^{-10}
40	$O^+ + OH \rightarrow O_2^+ + H$	2.33	3.6×10^{-10}

Table C.2: Continued

No.	Reaction	Energy (eV)	Rate coefficient
41	$CO_2^+ + O \rightarrow O_2^+ + CO$	1.33	1.6×10^{-10}
42	$CO_2^+ + O \rightarrow O^+ + CO_2$	0.13	1.0×10^{-10}
43	$CO_2^+ + NO \rightarrow NO^+ + CO_2$	4.51	1.2×10^{-10}
44	$CO_2^+ + H \rightarrow H^+ + CO_2$	0.17	2.35×10^{-11}
45	$CO_2^+ + e^- \rightarrow CO + O_2^+$	4.56	$3.5 \times 10^{-7}(300.0/T)^{0.5}$
46	$CO_2^+ + O_2 \rightarrow CO_2 + O_2^+$	1.77	$5.5 \times 10^{-11}(300.0/T)^{0.82}$ $(T \leq 1500\text{K})$
			$1.5 \times 10^{-11}(1500.0/T)^{-0.75}$ $(T \geq 1500\text{K})$
47	$CO_2^+ + N \rightarrow NO + CO^+$	-	3.4×10^{-10}
48	$CO_2^+ + N(^2D) \rightarrow N^+ + CO_2$	-	2.0×10^{-10}
49	$CO_2^+ + H \rightarrow HCO^+ + O$	0.9	4.46×10^{-10}
50	$CO_2^+ + H_2 \rightarrow OCOH^+ + H$	-	$9.5 \times 10^{-10}(300.0/T)^{0.15}$
51	$CO_2^+ + H_2O \rightarrow CO_2 + H_2O^+$	1.2	$5.6648 \times 10^{-10}(0.62 + 2.579(300.0/T)^{0.45})$
52	$CO^+ + O \rightarrow O^+ + CO$	0.39	1.4×10^{-10}
53	$CO^+ + NO \rightarrow NO^+ + CO$	4.75	4.2×10^{-10}
54	$CO^+ + CO_2 \rightarrow CO_2^+ + CO$	0.24	1.1×10^{-9}
55	$CO^+ + O_2 \rightarrow O_2^+ + CO$	2.04	$1.5 \times 10^{-10}(300.0/T)^{1.1}$
56	$CO^+ + H_2 \rightarrow HCO^+ + H$	2.12	7.5×10^{-10}
57	$CO^+ + H \rightarrow H^+ + CO$	0.53	4.0×10^{-10}
58	$CO^+ + N \rightarrow NO^+ + C$	0.26	8.2×10^{-11}
59	$CO^+ + e^- \rightarrow C + O$	-	$1.8 \times 10^{-7}(300.0/T)^{0.55}$
60	$CO^+ + e^- \rightarrow C + O(^1D)$	-	$0.25 \times 10^{-7}(300.0/T)^{0.55}$
61	$CO^+ + H_2O \rightarrow CO + H_2O^+$	1.46	1.7×10^{-9}
62	$CO^+ + H_2O \rightarrow HCO^+ + OH$	1.47	8.84×10^{-10}

Table C.2: Continued

No.	Reaction	Energy (eV)	Rate coefficient
63	$N^+ + O_2 \rightarrow O^+ + NO$	1.28	$4.34 \times 10^{-11}(300.0/T)^{-0.45}$ $(T \leq 1000\text{K})$
			7.53×10^{-11} $(T \geq 1000\text{K})$
64	$N^+ + O_2 \rightarrow O_2^+ + N(^2D)$	0.10	$8.65 \times 10^{-11}(300.0/T)^{-0.45}$ $(T \leq 1000\text{K})$
			1.49×10^{-10} $(T \geq 1000\text{K})$
65	$N^+ + O_2 \rightarrow O_2^+ + N$	2.49	$2.02 \times 10^{-10}(300.0/T)^{-0.45}$ $(T \leq 1000\text{K})$
			3.49×10^{-10} $(T \geq 1000\text{K})$
66	$N^+ + O_2 \rightarrow NO^+ + O$	6.70	$4.32 \times 10^{-11}(300.0/T)^{-0.45}$ $(T \leq 1000\text{K})$
			7.47×10^{-11} $(T \geq 1000\text{K})$
67	$N^+ + O \rightarrow O^+ + N$	0.98	2.2×10^{-12}
68	$N^+ + NO \rightarrow NO^+ + N$	5.29	$4.72 \times 10^{-10}(300.0/T)^{0.24}$
69	$N^+ + CO_2 \rightarrow CO_2^+ + N$	0.78	9.2×10^{-10}
70	$N^+ + CO_2 \rightarrow CO^+ + NO$	1.57	2.0×10^{-10}
71	$N^+ + CO \rightarrow CO^+ + N$	0.54	$4.93 \times 10^{-10}(300.0/T)^{0.5}$
72	$N^+ + H \rightarrow H^+ + N$	0.90	3.6×10^{-12}
73	$N^+ + e^- \rightarrow N$	-	$3.6 \times 10^{-12}(250.0/T)^{0.7}$
74	$N^+ + NO \rightarrow N_2^+ + O$	2.31	$8.33 \times 10^{-10}(300.0/T)^{0.24}$
75	$N^+ + CO \rightarrow NO^+ + C$	0.78	$6.16 \times 10^{-11}(300.0/T)^{0.5}$
76	$N^+ + CO \rightarrow C^+ + NO$	-1.28	$5.60 \times 10^{-12}(300.0/T)^{0.5}$
77	$N^+ + O_2 \rightarrow NO^+ + O(^1D)$	-	$1.75 \times 10^{-10}(300.0/T)^{-0.45}$ $(T \leq 1000\text{K})$
			3.02×10^{-10} $(T \geq 1000\text{K})$
78	$N^+ + H_2 \rightarrow NH^+ + H$	0.071	$8.23 \times 10^{-10}\exp(300.0/T)$
79	$N^+ + H_2O \rightarrow N + H_2O^+$	1.98	2.6×10^{-9}
80	$H^+ + O \rightarrow O^+ + H$	-0.02	5.33×10^{-10}
81	$H^+ + NO \rightarrow NO^+ + H$	4.34	1.9×10^{-9}
82	$H^+ + H_2 \rightarrow H_2^+ + H$	-1.83	$1.0 \times 10^{-9}\exp(-2.19 \times 10^4/T)$
83	$H^+ + e^- \rightarrow H$	-	$4.0 \times 10^{-12}(300.0/T)^{0.64}$
84	$H^+ + CO_2 \rightarrow HCO^+ + O$	0.71	3.8×10^{-9}
85	$H^+ + O_2 \rightarrow O_2^+ + H$	1.61	1.17×10^{-9}
86	$H^+ + He \rightarrow HeH^+$	-	$8.0 \times 10^{-12}(300.0/T)^{-0.24}\exp(-T/4000.0)$
87	$H^+ + H_2O \rightarrow H + H_2O^+$	1.03	$7.3 \times 10^{-9}(300.0/T)^{0.5}$
88	$H^+ + H_2 \rightarrow H + H + H^+$	-2.15	$3.0 \times 10^{-11}(300.0/T)^{-0.5}\exp(-52000.0/T)$
89	$H^+ + OH \rightarrow OH^+ + H$	0.67	2.1×10^{-9}
90	$H^+ + NH \rightarrow NH^+ + H$	0.21	2.1×10^{-9}
91	$H^+ + NH_2 \rightarrow NH_2^+ + H$	2.48	2.9×10^{-9}

Table C.2: Continued

No.	Reaction	Energy (eV)	Rate coefficient
92	$OH^+ + e^- \rightarrow O + H$	8.74	$6.5 \times 10^{-7} T^{-0.5}$
93	$OH^+ + CO \rightarrow HCO^+ + O$	1.19	8.4×10^{-10}
94	$OH^+ + NO \rightarrow NO^+ + OH$	3.82	3.59×10^{-10}
95	$OH^+ + NO \rightarrow HNO^+ + O$	0.53	6.11×10^{-10}
96	$OH^+ + H_2 \rightarrow H_2O^+ + H$	1.08	9.7×10^{-10}
97	$OH^+ + N_2 \rightarrow N_2H^+ + O$	0.1	2.4×10^{-10}
98	$OH^+ + CO_2 \rightarrow OCOH^+ + O$	0.6	1.35×10^{-9}
99	$OH^+ + O_2 \rightarrow O_2^+ + OH$	1.01	3.8×10^{-10}
100	$OH^+ + C \rightarrow CH^+ + O$	1.54	1.2×10^{-9}
101	$OH^+ + N \rightarrow NO^+ + H$	5.92	8.9×10^{-10}
102	$OH^+ + O \rightarrow O_2^+ + H$	1.73	7.1×10^{-10}
103	$OH^+ + e^- \rightarrow O(^1D) + H$	-	$3.94 \times 10^{-8} (300.0/T)^{1.28}$
104	$OH^+ + H_2O \rightarrow OH + H_2O^+$	0.43	1.59×10^{-9}
105	$OH^+ + H_2O \rightarrow H_3O^+ + O$	2.14	1.59×10^{-9}
106	$O^+(^2P) + N_2 \rightarrow N_2^+ + O$	3.02	$2.0 \times 10^{-10} (300.0/T)^{-0.55}$
107	$O^+(^2P) + N_2 \rightarrow N^+ + NO$	0.70	1.0×10^{-10}
108	$O^+(^2P) + O \rightarrow O^+ + O$	5.20	4.0×10^{-10}
109	$O^+(^2P) \rightarrow O^+$	-	0.047
110	$O^+(^2P) \rightarrow O^+(^2D)$	-	0.171
111	$O^+(^2P) + e^- \rightarrow O^+ + e^-$	5.00	$3.03 \times 10^{-8} (300.0/T)^{0.5}$
112	$O^+(^2P) + e^- \rightarrow O^+(^2D) + e^-$	1.69	$1.84 \times 10^{-7} (300.0/T)^{0.5}$
113	$O^+(^2P) + CO_2 \rightarrow CO + O_2^+$	-	6.0×10^{-11}
114	$O^+(^2P) + CO_2 \rightarrow CO_2^+ + O$	-	1.0×10^{-9}
115	$O^+(^2P) + CO \rightarrow CO^+ + O$	-	1.3×10^{-9}
116	$O^+(^2P) + O_2 \rightarrow O^+ + O_2$	-	1.3×10^{-10}
117	$O^+(^2P) + N_2 \rightarrow O^+ + N_2$	-	$6.2 \times 10^{-10} \exp(-340.0/T)$ $(T \leq 4000\text{K})$
118	$O^+(^2P) + N \rightarrow O^+ + N(^2D)$	-	1.0×10^{-11}
119	$O^+(^2P) + NO \rightarrow NO^+ + O$	-	1.2×10^{-9}
120	$O^+(^2P) + H_2 \rightarrow OH^+ + H$	-	8.5×10^{-10}
121	$O^+(^2P) + H_2 \rightarrow H_2^+ + O$	-	$1.01 \times 10^{-9} (300.0/T)^{0.98} \exp(-285.0/T)$
122	$O^+(^2P) + H_2 \rightarrow H^+ + OH$	-	$2.16 \times 10^{-10} (300.0/T)^{0.97} \exp(-292.0/T)$
123	$O^+(^2P) + H_2 \rightarrow H^+ + O + H$	-	$2.16 \times 10^{-10} (300.0/T)^{0.97} \exp(-292.0/T)$
124	$O^+(^2P) + O_2 \rightarrow O_2^+ + O$	-	1.3×10^{-10}

Table C.2: Continued

No.	Reaction	Energy (eV)	Rate coefficient
125	$O^+(^2D) + N_2 \rightarrow O^+ + N_2$	3.31	8.0×10^{-10}
126	$O^+(^2D) + N_2 \rightarrow N_2^+ + O$	1.33	$1.5 \times 10^{-10}(300.0/T)^{-0.55}$
127	$O^+(^2D) + O \rightarrow O^+ + O$	3.31	1.0×10^{-11}
128	$O^+(^2D) + O_2 \rightarrow O_2^+ + O$	4.87	7.0×10^{-10}
129	$O^+(^2D) \rightarrow O^+$	-	4.85×10^{-5}
130	$O^+(^2D) + e^- \rightarrow O^+ + e^-$	3.31	$6.03 \times 10^{-8}(300.0/T)^{0.5}$
131	$O^+(^2D) + CO_2 \rightarrow O_2^+ + CO$	-	6.0×10^{-11}
132	$O^+(^2D) + CO_2 \rightarrow CO_2^+ + O$	-	1.0×10^{-9}
133	$O^+(^2D) + CO \rightarrow CO^+ + O$	-	1.3×10^{-9}
134	$O^+(^2D) + NO \rightarrow NO^+ + O$	-	1.2×10^{-9}
135	$O^+(^2D) + N \rightarrow N^+ + O$	-	1.5×10^{-10}
136	$O^+(^2D) + H_2 \rightarrow OH^+ + H$	-	1.5×10^{-11}
137	$O^+(^2D) + H_2 \rightarrow H_2^+ + O$	-	$1.645 \times 10^{-10}(300.0/T)^{0.98}\exp(-302.4/T)$
138	$O^+(^2D) + H_2 \rightarrow H^+ + OH$	-	$7.2 \times 10^{-11}(300.0/T)^{0.95}\exp(-335.1/T)$
139	$O^+(^2D) + N_2 \rightarrow NO^+ + N$	-	2.5×10^{-11}
140	$H_2^+ + O \rightarrow OH^+ + H$	2.17	1.5×10^{-9}
141	$H_2^+ + H_2 \rightarrow H_3^+ + H$	1.70	$2.24 \times 10^{-9}(300.0/T)^{0.042}\exp(-T/46600.0)$
142	$H_2^+ + H \rightarrow H^+ + H_2$	1.83	6.4×10^{-10}
143	$H_2^+ + e^- \rightarrow H + H$	10.91	$1.75 \times 10^{-8}(300.0/T)^{0.4}$
144	$H_2^+ + CO_2 \rightarrow OCOH^+ + H$	2.94	2.35×10^{-9}
145	$H_2^+ + Ar \rightarrow ArH^+ + H$	-	2.3×10^{-9}
146	$H_2^+ + N_2 \rightarrow N_2H^+ + H$	2.44	2.3×10^{-9}
147	$H_2^+ + CO \rightarrow HCO^+ + H$	3.53	7.65×10^{-10}
148	$H_2^+ + CO \rightarrow CO^+ + H_2$	1.51	6.44×10^{-10}
149	$H_2^+ + O_2 \rightarrow HO_2^+ + H$	1.74	1.53×10^{-9}
150	$H_2^+ + O_2 \rightarrow O_2^+ + H_2$	3.42	4.94×10^{-10}
151	$H_2^+ + C \rightarrow CH^+ + H$	3.89	2.4×10^{-9}
152	$H_2^+ + N \rightarrow NH^+ + H$	0.96	1.9×10^{-9}
153	$H_2^+ + NO \rightarrow NO^+ + H_2$	6.23	1.1×10^{-9}
154	$H_2^+ + H_2O \rightarrow H_2 + H_2O^+$	2.84	3.9×10^{-9}
155	$H_2^+ + He \rightarrow HeH^+ + H$	-	1.30×10^{-10}
156	$H_2^+ + H_2O \rightarrow H_3O^+ + H$	4.48	3.4×10^{-9}
157	$H_2^+ + NH \rightarrow NH^+ + H_2$	2.01	7.6×10^{-10}
158	$H_2^+ + NH \rightarrow NH_2^+ + H$	3.84	7.6×10^{-10}
159	$H_2^+ + NH_2 \rightarrow NH_2^+ + H_2$	4.29	2.1×10^{-9}

Table C.2: Continued

No.	Reaction	Energy (eV)	Rate coefficient
160	$H_3^+ + H \rightarrow H_2^+ + H_2$	-1.70	$2.08 \times 10^{-9} \exp(-19900.0/T)$
161	$H_3^+ + e^- \rightarrow H_2 + H$	9.21	$1.7 \times 10^{-8} (300.0/T)^{0.52}$
162	$H_3^+ + e^- \rightarrow H + H + H$	4.69	$5.1 \times 10^{-8} (300.0/T)^{0.52}$
163	$H_3^+ + N_2 \rightarrow N_2H^+ + H_2$	0.73	1.63×10^{-9}
164	$H_3^+ + O \rightarrow OH^+ + H_2$	0.72	$7.98 \times 10^{-10} (300.0/T)^{0.156} \exp(-1.41/T)$
165	$H_3^+ + O \rightarrow H_2O^+ + H$	1.74	$3.42 \times 10^{-10} (300.0/T)^{0.156} \exp(-1.41/T)$
166	$H_3^+ + O_2 \rightarrow HO_2^+ + H_2$	0.024	6.5×10^{-10}
167	$H_3^+ + CO \rightarrow HCO^+ + H_2$	1.81	$1.36 \times 10^{-9} (300.0/T)^{0.142} \exp(3.41/T)$
168	$H_3^+ + CO_2 \rightarrow OCOH^+ + H_2$	1.23	2.5×10^{-9}
169	$H_3^+ + NO \rightarrow HNO^+ + H_2$	1.16	1.94×10^{-9}
170	$H_3^+ + C \rightarrow CH^+ + H_2$	2.17	2.0×10^{-9}
171	$H_3^+ + H_2O \rightarrow H_3O^+ + H_2$	2.76	5.9×10^{-9}
172	$H_3^+ + OH \rightarrow H_2O^+ + H_2$	1.78	1.3×10^{-9}
173	$H_3^+ + NH \rightarrow NH_2^+ + H_2$	2.12	1.3×10^{-9}
174	$H_2O^+ + H_2 \rightarrow H_3O^+ + H$	1.67	6.1×10^{-10}
175	$H_2O^+ + C \rightarrow CH^+ + OH$	0.43	1.1×10^{-9}
176	$H_2O^+ + CO \rightarrow HCO^+ + OH$	0.07	5.0×10^{-10}
177	$H_2O^+ + H_2O \rightarrow H_3O^+ + OH$	1.02	2.1×10^{-9}
178	$H_2O^+ + e^- \rightarrow O + H + H$	-	$3.53 \times 10^{-6} T^{-0.5}$
179	$H_2O^+ + e^- \rightarrow OH + H$	-	$1.09 \times 10^{-6} T^{-0.5}$
180	$H_2O^+ + e^- \rightarrow O + H_2$	-	$5.72 \times 10^{-7} T^{-0.5}$
181	$H_2O^+ + O \rightarrow O_2^+ + H_2$	0.68	4.0×10^{-11}
182	$H_2O^+ + O_2 \rightarrow O_2^+ + H_2O$	0.58	4.6×10^{-10}
183	$HCO^+ + C \rightarrow CH^+ + CO$	0.46	1.1×10^{-9}
184	$HCO^+ + e^- \rightarrow H + CO$	-	$2.0 \times 10^{-7} (300.0/T)^{1.25}$ $(T \leq 300\text{K})$
			$2.0 \times 10^{-7} (300.0/T)^{1.0}$ $(T \geq 300\text{K})$
185	$HCO^+ + H_2O \rightarrow H_3O^+ + CO$	1.05	2.5×10^{-9}
186	$HCO^+ + OH \rightarrow H_2O^+ + CO$	0.068	6.2×10^{-10}

Table C.2: Continued

No.	Reaction	Energy (eV)	Rate coefficient
187	$C^+ + CO_2 \rightarrow CO^+ + CO$	3.02	1.1×10^{-9}
188	$C^+ + NO \rightarrow NO^+ + C$	2.12	$7.5 \times 10^{-10}(300.0/T)^{0.2}$
189	$C^+ + O_2 \rightarrow O^+ + CO$	3.76	5.22×10^{-10}
190	$C^+ + O_2 \rightarrow CO^+ + O$	3.36	3.48×10^{-10}
191	$C^+ + H_2 \rightarrow CH^+ + H$	-0.27	$7.40 \times 10^{-10}\exp(-4538.0/T)$
192	$C^+ + H_2O \rightarrow C + H_2O^+$	-1.26	2.4×10^{-10}
193	$C^+ + e^- \rightarrow C$	-	$1.43 \times 10^{-10}T^{-0.6}$
194	$C^+ + H_2O \rightarrow HCO^+ + H$	3.72	9.0×10^{-10}
195	$C^+ + OH \rightarrow CO^+ + H$	4.06	7.7×10^{-10}
196	$Ar^+ + CO_2 \rightarrow Ar + CO_2^+$	-	5.0×10^{-10} $(T \leq 700\text{K})$
			$5.0 \times 10^{-10}(700.0/T)$ $(T \geq 700\text{K})$
197	$Ar^+ + O_2 \rightarrow Ar + O_2^+$	-	$4.0 \times 10^{-11}(300.0/T)^{0.78}$ $(T \leq 900\text{K})$
			$2.08 \times 10^{-11}(900.0/T)^{-1.65}$ $(T \geq 900\text{K})$
198	$Ar^+ + CO \rightarrow Ar + CO^+$	-	$3.7 \times 10^{-11}(300.0/T)^{0.43}$ $(T \leq 900\text{K})$
			$2.3 \times 10^{-11}(300.0/T)^{-1.0}$ $(T \geq 900\text{K})$
199	$Ar^+ + N_2 \rightarrow Ar + N_2^+$	-	$1.1 \times 10^{-11}(300.0/T)^{-1.13}$
200	$Ar^+ + NO \rightarrow Ar + NO^+$	-	3.1×10^{-10}
201	$Ar^+ + H_2 \rightarrow Ar + H_2^+$	-	1.78×10^{-11}
202	$Ar^+ + H_2 \rightarrow ArH^+ + H$	-	8.72×10^{-10}
203	$Ar^+ + N_2O \rightarrow Ar + H_2O^+$	-	1.5×10^{-10}
204	$N_2H^+ + CO \rightarrow HCO^+ + N_2$	1.11	8.8×10^{-10}
205	$N_2H^+ + CO_2 \rightarrow OCOH^+ + N_2$	-	1.07×10^{-9}
206	$N_2H^+ + NO \rightarrow HNO^+ + N_2$	0.46	3.4×10^{-10}
207	$N_2H^+ + O \rightarrow OH^+ + N_2$	0.016	$2.4 \times 10^{-10}\exp(-589.0/T)$
208	$N_2H^+ + C \rightarrow CH^+ + N_2$	1.47	1.1×10^{-9}
209	$N_2H^+ + e^- \rightarrow N_2 + H$	-	$2.325 \times 10^{-7}(300.0/T)^{0.84}$
210	$N_2H^+ + e^- \rightarrow NH + N$	-	$1.755 \times 10^{-8}(300.0/T)^{0.84}$
211	$NH^+ + H_2O \rightarrow NH + H_2O^+$	0.90	1.05×10^{-9}
212	$NH^+ + e^- \rightarrow N + H$	-	$7.45 \times 10^{-7}T^{-0.5}$
213	$NH^+ + H_2 \rightarrow H + H_3^+$	0.88	2.25×10^{-10}
214	$NH^+ + H_2 \rightarrow NH_2^+ + H$	1.9	1.28×10^{-8}
215	$CH^+ + H_2 \rightarrow CH_2^+ + H$	0.22	1.2×10^{-9}
216	$CH^+ + O \rightarrow CO^+ + H$	4.41	3.5×10^{-10}
217	$CH^+ + H \rightarrow C^+ + H_2$	0.46	$7.84 \times 10^{-10}(300.0/T)^{0.22}$
218	$CH^+ + CO_2 \rightarrow HCO^+ + CO$	5.42	1.6×10^{-9}
219	$CH^+ + O_2 \rightarrow HCO^+ + O$	5.76	9.2×10^{-10}

Table C.2: Continued

No.	Reaction	Energy (eV)	Rate coefficient
220	$ArH^+ + H_2 \rightarrow N_2H^+ + Ar$	-	6.3×10^{-10}
221	$ArH^+ + N_2 \rightarrow HO_2^+ + Ar$	-	8.0×10^{-10}
222	$ArH^+ + O_2 \rightarrow HCO^+ + Ar$	-	5.05×10^{-10}
223	$ArH^+ + CO \rightarrow HCO^+ + Ar$	-	1.25×10^{-9}
224	$ArH^+ + CO_2 \rightarrow OCOH^+ + Ar$	-	1.1×10^{-9}
225	$ArH^+ + O \rightarrow OH^+ + Ar$	-	5.9×10^{-10}
226	$ArH^+ + C \rightarrow CH^+ + Ar$	-	1.02×10^{-9}
227	$ArH^+ + e^- \rightarrow Ar + H$	-	$1.0 \times 10^{-9}(300.0/T)^{0.5}$
228	$He^+ + CO \rightarrow C^+ + O + He$	2.25	1.6×10^{-9}
229	$He^+ + CO_2 \rightarrow C^+ + O_2 + He$	1.87	2.0×10^{-11}
230	$He^+ + CO_2 \rightarrow CO^+ + O + He$	5.18	7.8×10^{-10}
231	$He^+ + CO_2 \rightarrow O^+ + CO + He$	5.46	1.4×10^{-10}
232	$He^+ + CO_2 \rightarrow CO_2^+ + He$	10.87	5.0×10^{-11}
233	$He^+ + O_2 \rightarrow O^+(^2D) + O + He$	-	2.37×10^{-10}
234	$He^+ + O_2 \rightarrow O^+ + O + He$	5.92	2.39×10^{-11}
235	$He^+ + O_2 \rightarrow O_2^+ + He$	12.57	9.2×10^{-12}
236	$He^+ + O_2 \rightarrow O^+(^2P) + O + He$	-	6.04×10^{-10}
237	$He^+ + O_2 \rightarrow O^+ + O(^1D) + He$	-	4.6×10^{-11}
238	$He^+ + O \rightarrow O^+ + He$	-	1.0×10^{-13}
239	$He^+ + N_2 \rightarrow N^+ + N + He$	0.36	7.8×10^{-10}
240	$He^+ + N_2 \rightarrow N_2^+ + He$	9.07	5.2×10^{-10}
241	$He^+ + NO \rightarrow N^+ + O + He$	3.63	1.35×10^{-9}
242	$He^+ + NO \rightarrow O^+ + N + He$	4.54	1.0×10^{-10}
243	$He^+ + H \rightarrow HeH^+$	-	$4.16 \times 10^{-16}(300.0/T)^{0.37}\exp(-T/4000.0)$
244	$He^+ + H_2 \rightarrow H^+ + He + H$	6.57	8.3×10^{-14}
245	$He^+ + H_2 \rightarrow H_2^+ + He$	-	1.7×10^{-14}
246	$He^+ + H_2 \rightarrow HeH^+ + H$	-	4.2×10^{-13}
247	$He^+ + e^- \rightarrow He$	-	$4.6 \times 10^{-12}(300.0/T)^{0.64}$
248	$He^+ + H_2O \rightarrow He + H_2O^+$	12.00	$9.54 \times 10^{-10}(0.62 + 2.579(300.0/T)^{0.5})$
249	$He^+ + H_2O \rightarrow H^+ + OH + He$	5.92	2.04×10^{-10}
250	$He^+ + H_2O \rightarrow OH^+ + H + He$	6.5	2.86×10^{-10}
251	$He^+ + OH \rightarrow O^+ + H + He$	6.62	1.1×10^{-9}
252	$He^+ + NH \rightarrow N^+ + He + H$	6.72	1.1×10^{-9}
253	$He^+ + NH_2 \rightarrow N^+ + He + H_2$	7.17	8.0×10^{-10}
254	$He^+ + NH_2 \rightarrow NH^+ + He + H$	7.15	8.0×10^{-10}

Table C.2: Continued

No.	Reaction	Energy (eV)	Rate coefficient
255	$OCOH^+ + O \rightarrow HCO^+ + O_2$	0.27	5.8×10^{-10}
256	$OCOH^+ + C \rightarrow CH^+ + CO_2$	0.97	1.0×10^{-9}
257	$OCOH^+ + CO \rightarrow HCO^+ + CO_2$	0.62	7.8×10^{-10}
258	$OCOH^+ + e^- \rightarrow H + O + CO$	-	$2.38 \times 10^{-7}(300.0/T)^{0.5}$
259	$OCOH^+ + e^- \rightarrow H + CO_2$	-	$1.75 \times 10^{-8}(300.0/T)^{0.5}$
260	$OCOH^+ + e^- \rightarrow OH + CO$	-	$9.45 \times 10^{-8}(300.0/T)^{0.5}$
261	$HeH^+ + H_2 \rightarrow H_3^+ + He$	2.56	1.5×10^{-9}
262	$HeH^+ + H \rightarrow H_2^+ + He$	0.91	9.1×10^{-10}
263	$HeH^+ + e^- \rightarrow He + H$	-	$1.0 \times 10^{-8}(300.0/T)^{0.6}$
264	$HNO^+ + CO \rightarrow HCO^+ + NO$	0.69	8.6×10^{-10}
265	$HNO^+ + CO_2 \rightarrow OCOH^+ + NO$	-	9.4×10^{-10}
266	$HNO^+ + C \rightarrow CH^+ + NO$	1.05	1.0×10^{-9}
267	$HNO^+ + N_2 \rightarrow N_2H^+ + NO$	-	$3.4 \times 10^{-10}\exp(-4900.0/T)$
268	$HNO^+ + O \rightarrow NO_2^+ + H$	1.73	1.0×10^{-12}
269	$HNO^+ + e^- \rightarrow NO + H$	-	$3.0 \times 10^{-7}(300.0/T)^{0.5}$
270	$NO_2^+ + e^- \rightarrow O + NO$	-	$3.0 \times 10^{-7}(300.0/T)^{0.5}$
271	$HO_2^+ + CO \rightarrow HCO^+ + O_2$	1.82	8.4×10^{-10}
272	$HO_2^+ + CO_2 \rightarrow OCOH^+ + O_2$	1.24	1.1×10^{-9}
273	$HO_2^+ + NO \rightarrow HNO^+ + O_2$	1.17	7.5×10^{-10}
274	$HO_2^+ + N_2 \rightarrow N_2H^+ + O_2$	0.74	8.0×10^{-10}
275	$HO_2^+ + O \rightarrow OH^+ + O_2$	0.72	6.2×10^{-10}
276	$HO_2^+ + N \rightarrow NO_2^+ + H$	4.23	1.0×10^{-12}
277	$HO_2^+ + C \rightarrow CH^+ + O_2$	2.18	1.0×10^{-9}
278	$HO_2^+ + H_2 \rightarrow H_3^+ + O_2$	0.036	3.3×10^{-10}
279	$HO_2^+ + e^- \rightarrow OH + O$	-	$1.8 \times 10^{-7}(300.0/T)^{0.5}$
280	$HO_2^+ + e^- \rightarrow H + O_2$	-	$6.0 \times 10^{-8}(300.0/T)^{0.5}$
281	$HO_2^+ + e^- \rightarrow H + O + O$	-	$6.0 \times 10^{-8}(300.0/T)^{0.5}$
282	$CH_2^+ + O \rightarrow H + HCO^+$	6.27	7.5×10^{-10}
283	$CH_2^+ + O_2 \rightarrow OH + HCO^+$	5.55	9.1×10^{-10}
284	$CH_2^+ + H \rightarrow H_2 + CH^+$	-0.02	$1.2 \times 10^{-9}\exp(-2700.0/T)$
285	$CH_2^+ + e^- \rightarrow C + H_2$	-	$7.7 \times 10^{-8}(300.0/T)^{0.6}$
286	$CH_2^+ + e^- \rightarrow C + H + H$	-	$4.0 \times 10^{-7}(300.0/T)^{0.6}$

Table C.2: Continued

No.	Reaction	Energy (eV)	Rate coefficient
287	$H_3O^+ + e^- \rightarrow H + H_2O$	-	$1.1 \times 10^{-7}(300.0/T)^{0.5}$
288	$H_3O^+ + e^- \rightarrow OH + H_2$	-	$6.0 \times 10^{-8}(300.0/T)^{0.5}$
289	$H_3O^+ + e^- \rightarrow OH + H + H$	-	$2.6 \times 10^{-7}(300.0/T)^{0.5}$
290	$H_3O^+ + e^- \rightarrow H_2 + O + H$	-	$5.6 \times 10^{-9}(300.0/T)^{0.5}$
291	$H_3O^+ + C \rightarrow HCO^+ + H_2$	5.10	1.0×10^{-11}
292	$NH_2^+ + e^- \rightarrow N + H + H$	-	$1.67 \times 10^{-5}T^{-0.8}$
293	$NH_2^+ + e^- \rightarrow NH + H$	-	$8.65 \times 10^{-6}T^{-0.8}$

C.3 Photo reactions

Table C.3: Photo reaction

No.	Reaction	Critical wavelength (nm)
1	$N + h\nu \rightarrow N^+ + e^-$	85.31
2	$O_2 + h\nu \rightarrow O + O(^1D)$	175.6
3	$O_2 + h\nu \rightarrow O + O$	242.4
4	$O_2 + h\nu \rightarrow O_2^+ + e^-$	175.6
5	$O_2 + h\nu \rightarrow O^+ + O + e^-$	30.40
6	$O_2 + h\nu \rightarrow O(^1S) + O(^1S)$	90.40
7	$NO + h\nu \rightarrow N + O$	191.0
8	$NO + h\nu \rightarrow NO^+ + e^-$	134.0
9	$NO + h\nu \rightarrow O^+ + N + e^-$	61.56
10	$NO + h\nu \rightarrow N^+ + O + e^-$	58.43
11	$O + h\nu \rightarrow O^+ + e^-$	91.04
12	$N_2 + h\nu \rightarrow N + N(^2D)$	127.0
13	$N_2 + h\nu \rightarrow N_2^+ + e^-$	79.50
14	$N_2 + h\nu \rightarrow N^+ + N + e^-$	50.82
15	$O(^1D) + h\nu \rightarrow O^+ + e^-$	79.01
16	$H_2O + h\nu \rightarrow H + OH$	242.5
17	$H_2O + h\nu \rightarrow H_2 + O(^1D)$	143.0
18	$H_2O + h\nu \rightarrow O + H + H$	130.4
19	$H_2O + h\nu \rightarrow OH^+ + H + e^-$	68.00
20	$H_2O + h\nu \rightarrow O^+ + H_2 + e^-$	66.00
21	$H_2O + h\nu \rightarrow H^+ + OH + e^-$	66.00
22	$H_2O + h\nu \rightarrow H_2O^+ + e^-$	97.80

Table C.3: Continued.

No.	Reaction	Critical wavelength (nm)
23	$O^3 + h\nu \rightarrow O_2 + O$	319.0
24	$O^3 + h\nu \rightarrow O_2(^1\Delta_g) + O(^1D)$	1179
25	$CO + h\nu \rightarrow CO^+ + e^-$	88.45
26	$CO + h\nu \rightarrow C^+ + O + e^-$	55.14
27	$CO + h\nu \rightarrow O^+ + C + e^-$	50.02
28	$CO + h\nu \rightarrow C + O$	111.8
29	$CO + h\nu \rightarrow C + O(^1D)$	86.30
30	$CO_2 + h\nu \rightarrow CO + O$	227.5
31	$CO_2 + h\nu \rightarrow CO + O(^1D)$	166.0
32	$CO_2 + h\nu \rightarrow CO_2^+ + e^-$	89.90
33	$CO_2 + h\nu \rightarrow CO^+ + O + e^-$	63.00
34	$CO_2 + h\nu \rightarrow O^+ + CO + e^-$	65.00
35	$H_2 + h\nu \rightarrow H_2^+ + e^-$	80.20
36	$H_2 + h\nu \rightarrow H^+ + H + e^-$	65.00
37	$H + h\nu \rightarrow H^+ + e^-$	91.18
38	$H_2O_2 + h\nu \rightarrow OH + OH$	576.5
39	$C + h\nu \rightarrow C^+ + e^-$	108.3
40	$Ar + h\nu \rightarrow Ar^+ + e^-$	82.49
41	$He + h\nu \rightarrow He^+ + e^-$	51.75
42	$O(^1S) + h\nu \rightarrow O^+ + e^-$	87.92
43	$NO_2 + h\nu \rightarrow NO_2^+ + e^-$	126.0
44	$NO_2 + h\nu \rightarrow NO + O(^1D)$	243.8
45	$NO_2 + h\nu \rightarrow NO + O$	397.8
46	$NO_3 + h\nu \rightarrow NO_2 + O$	589.0
47	$NO_3 + h\nu \rightarrow NO + O_2$	9000
48	$N_2O + h\nu \rightarrow N_2 + O(^1S)$	211.0
49	$N_2O + h\nu \rightarrow N_2 + O(^1D)$	340.7
50	$HNO_3 + h\nu \rightarrow OH + N_2O$	598.0

References

Abbot, D. S., Cowan, N. B., & Ciesla, F. J. 2012, ApJ, 756, 178

Alibert, Y. 2014, Astronomy and Astrophysics, 561, A41

Alibert, Y. & Benz, W. 2017, Astronomy and Astrophysics, 598, L5

Alt, J. C. & Teagle, D. A. H. 1999, Geochimica et Cosmochimica Acta, 63, 1527

Arney, G. N., Meadows, V. S., Domagal-Goldman, S. D., et al. 2017, ApJ, 836, 49

Ayres, T. R. 2010, ApJs, 187, 149

Banks, P. M. & Kockarts, G. 1973, Aeronomy.

Batalha, N. M., Rowe, J. F., Bryson, S. T., et al. 2013, ApJs, 204, 24

Bates, D. R. 1951, Proceedings of the Physical Society B, 64, 805

Bauer, S. J. & Lammer, H. 2004, Planetary aeronomy : atmosphere environments in planetary systems

Bezacier, L., Journaux, B., Perrillat, J.-P., et al. 2014, Journal of Chemical Physics, 141, 104505

Birch, F. 1978, Journal of Geophysical Research, 83, 1257

Blake, R. E., Chang, S. J., & Lepland, A. 2010, Nature, 464, 1029

Bollengier, O., Choukroun, M., Grasset, O., et al. 2013, Geochimica et Cosmochimica Acta, 119, 322

Bolmont, E., Selsis, F., Owen, J. E., et al. 2017, Monthly Notices of the Royal Astronomical Society, 464, 3728

Bougher, S. W. & Dickinson, R. E. 1988, Journal of Geophysical Research, 93, 7325

Boyajian, T. S., von Braun, K., van Belle, G., et al. 2012, ApJ, 757, 112

Brady, P. V. & Gíslason, S. R. 1997, Geochimica et Cosmochimica Acta, 61, 965

Brantley, S. & Olsen, A. 2013, Reaction Kinetics of Primary Rock-Forming Minerals under Ambient Conditions, Vol. 7 (United States: Elsevier Inc.), 69–113

Brown, T. M. 2001, ApJ, 553, 1006

Caldeira, K. 1995, American Journal of Science, 295, 1077

Castle, K. J., Black, L. A., Simione, M. W., & Dodd, J. A. 2012, Journal of Geophysical Research (Space Physics), 117, A04310

Castle, K. J., Kleissas, K. M., Rhinehart, J. M., Hwang, E. S., & Dodd, J. A. 2006, Journal of Geophysical Research (Space Physics), 111, A09303

Cernicharo, J. & Crovisier, J. 2005, Space Science Reviews, 119, 29

Chamberlain, J. W. 1963, Planetary and Space Science, 11, 901

Chapman, S. & Cowling, T. G. 1991, The Mathematical Theory of Non-uniform Gases

Charbonneau, D., Berta, Z. K., Irwin, J., et al. 2009, Nature, 462, 891

Charnay, B., Le Hir, G., Fluteau, F., Forget, F., & Catling, D. C. 2017, Earth and Planetary Science Letters, 474, 97

Checlair, J., Menou, K., & Abbot, D. S. 2017, ApJ, 845, 132

Chen, B., Hsieh, W.-P., Cahill, D. G., Trinkle, D. R., & Li, J. 2011, Physical Review B: Solid State, 83, 132301

Chen, H., Wolf, E. T., Kopparapu, R., Domagal-Goldman, S., & Horton, D. E. 2018, ApJL, 868, L6

Choblet, G., Tobie, G., Sotin, C., Kalousová, K., & Grasset, O. 2017, Icarus, 285, 252

Claire, M. W., Sheets, J., Cohen, M., et al. 2012, ApJ, 757, 95

Coogan, L. A. & Dosso, S. E. 2015, Earth and Planetary Science Letters, 415, 38

Coogan, L. A. & Gillis, K. M. 2018, Annual Review of Earth and Planetary Sciences, 46, 21

Curtis, A. R. & Goody, R. M. 1956, Proceedings of the Royal Society of London Series A, 236, 193

Dickinson, R. E. 1973, Journal of Geophysical Research, 78, 4451

Dickinson, R. E. 1976, Journal of Atmospheric Sciences, 33, 290

Dickinson, R. E., Ridley, E. C., & Roble, R. G. 1984, Journal of Atmospheric Sciences, 41, 205

Dressing, C. D. & Charbonneau, D. 2015, ApJ, 807, 45

Driese, S. G., Jirsa, M. A., Ren, M., et al. 2011, Precambrian Research, 189, 1

Duan, Z. & Sun, R. 2003, Chemical Geology, 193, 257

Duan, Z. & Zhang, Z. 2006, Geochimica et Cosmochimica Acta, 70, 2311

Dumoulin, C., Doin, M.-P., & Fleitout, L. 1999, Journal of Geophysical Research, 104, 12,759

Dunaeva, A. N., Antsyshkin, D. V., & Kuskov, O. L. 2010, Solar System Research, 44, 202

Durham, W. B., Kirby, S. H., & Stern, L. A. 1997, Journal of Geophysical Research, 102, 16293

Edson, A. R., Kasting, J. F., Pollard, D., Lee, S., & Bannon, P. R. 2012, Astrobiology, 12, 562

Ehrenreich, D., Bourrier, V., Wheatley, P. J., et al. 2015, Nature, 522, 459

Eymet, V., Coustet, C., & Piaud, B. 2016, in Journal of Physics Conference Series, Vol. 676, 012005

Fei, Y., Mao, H.-K., & Hemley, R. J. 1993, Journal of Chemical Physics, 99, 5369

Foley, B. J. 2015, ApJ, 812, 812

Forget, F. & Leconte, J. 2014, The Philosophical Transactions of the Royal Society, 372, 20130084

Fox, J. L. 2015, Icarus, 252, 366

France, K., Fleming, B., West, G., et al. 2017, in Society of Photo-Optical Instrumentation Engineers (SPIE) Conference Series, Vol. 10397, Proceedings of the SPIE, 1039713

France, K., Loyd, R. O. P., Youngblood, A., et al. 2016, ApJ, 820, 89

Fu, Q. & Liou, K. N. 1992, Journal of Atmospheric Sciences, 49, 2139

Fu, R., O'Connell, R. J., & Sasselov, D. D. 2010, ApJ, 708, 708

Funke, B., López-Puertas, M., García-Comas, M., et al. 2012, Journal of Quantitative Spectroscopy and Radiative Transfer, 113, 1771

García Muñoz, A. 2007, Planetary and Space Science, 55, 1426

Gillis, K. M. & Coogan, L. A. 2011, Earth and Planetary Science Letters, 302, 385

Gillon, M., Triaud, A. H. M. J., Demory, B.-O., et al. 2017, Nature, 542, 456

Golden, K. M., Ackley, S. F., & Lytle, V. I. 1998, Science, 282, 2238

Gomes, R., Levison, H. F., Tsiganis, K., & Morbidelli, A. 2005, Nature, 435, 466

Grassi, T., Bovino, S., Schleicher, D. R. G., et al. 2014, Monthly Notices of the Royal Astronomical Society, 439, 2386

Gross, S. H. 1972, Journal of Atmospheric Sciences, 29, 214

Gudbrandsson, S., Wolff-Boenisch, D., Gislason, S. R., & Oelkers, E. H. 2011, Geochimica et Cosmochimica Acta, 75, 5496

Guillot, B. & Sator, N. 2011, Geochimica et Cosmochimica Acta, 75, 1829

Haqq-Misra, J., Wolf, E. T., Joshi, M., Zhang, X., & Kopparapu, R. K. 2018, ApJ, 852, 67

Hart, M. H. 1978, Icarus, 33, 23

Hedin, A. E., Niemann, H. B., Kasprzak, W. T., & Seiff, A. 1983, Journal of Geophysical Research, 88, 73

Hindmarsh, A. C. 1983, Scientific computing

Hirschmann, M. M., Tenner, T., Aubaud, C., & Withers, A. C. 2009, Physics of the Earth and Planetary Interiors, 176, 54

Hollenbach, D. & McKee, C. F. 1979, ApJs, 41, 555

Höning, D., Tosi, N., & Spohn, T. 2019, Astronomy and Astrophysics, 627, A48

Houghton, J. 2002, The physics of atmospheres (Cambridge University Press)

Hu, Y. & Yang, J. 2014, Proceedings of the National Academy of Science, 111, 629

Huang, S.-S. 1959, American scientist, 47, 47

Huebner, W. F. & Mukherjee, J. 2015, Planetary and Space Science, 106, 11

Hunten, D. M. 1974, Journal of Geophysical Research, 79, 2533

Ida, S. & Lin, D. N. C. 2004, ApJ, 604, 388

Ikeda-Fukazawa, T., Kawamura, K., & Hondoh, T. 2004, Molecular Simulation, 30, 30

Ikoma, M., Elkins-Tanton, L., Hamano, K., & Suckale, J. 2018, Space Science Reviews, 214, 76

Ikoma, M. & Genda, H. 2006, ApJ, 648, 696

Ingersoll, A. P. 1969, Journal of Atmospheric Sciences, 26, 1191

Inoue, G. & Tsuchiya, S. 1975, Journal of the Physical Society of Japan, 39, 479

Jacchia, L. G. 1977, SAO Special Report, 375

Jackman, C. H., Garvey, R. H., & Green, A. E. S. 1977, Journal of Geophysical Research, 82, 5081

Jarosewich, E. 1990, Meteoritics, 25, 323

Jendrzejewski, N., Trull, T. W., Pineau, F., & Javoy, M. 1997, Chemical Geology, 138, 81

Johnson, R. E., Liu, M., & Tully, C. 2002, Planetary and Space Science, 50, 123

Johnstone, C. P., Güdel, M., Lammer, H., & Kislyakova, K. G. 2018, Astronomy and Astrophysics, 617, A107

Kadoya, S. & Tajika, E. 2014, ApJ, 790, 107

Kalousová, K., Sotin, C., Choblet, G., Tobie, G., & Grasset, O. 2018, Icarus, 299, 133

Kaltenegger, L. 2017, Annual Review of Astronomy and Astrophysics, 55, 433

Kaltenegger, L., Sasselov, D., & Rugheimer, S. 2013, ApJ, 775, L47

Kameda, S., Ikezawa, S., Sato, M., et al. 2017, Geophysical Research Letters, 44, 11,706

Kasting, J. F. 1987, Precambrian Research, 34, 205

Kasting, J. F. 1991, Icarus, 94, 1

Kasting, J. F., Chen, H., & Kopparapu, R. K. 2015, ApJL, 813, L3

Kasting, J. F. & Pollack, J. B. 1983, Icarus, 53, 479

Kasting, J. F., Pollack, J. B., & Ackerman, T. P. 1984, Icarus, 57, 335

Kasting, J. F., Whitmire, D. P., & Reynolds, R. T. 1993, Icarus, 101, 108

Kite, E. S. & Ford, E. B. 2018, ApJ, 864, 75

Kite, E. S., Manga, M., & Gaidos, E. 2009, ApJ, 700, 1732

Kitzmann, D., Alibert, Y., Godolt, M., et al. 2015, Monthly Notices of the Royal Astronomical Society, 452, 3752

Knauth, L. P. & Lowe, D. R. 2003, Geological Society of America Bulletin, 115, 566

Kodama, T., Nitta, A., Genda, H., et al. 2018, Journal of Geophysical Research Planets, 123, 559

Komacek, T. D. & Abbot, D. S. 2019, ApJ, 871, 245

Kopparapu, R. K., Ramirez, R., Kasting, J. F., et al. 2013, ApJ, 765, 131

Kopparapu, R. k., Wolf, E. T., Haqq-Misra, J., et al. 2016, ApJ, 819, 84

Kreidberg, L., Bean, J. L., Désert, J.-M., et al. 2014, Nature, 505, 69

Krissansen-Totton, J., Arney, G. N., & Catling, D. C. 2018a, Proceedings of the National Academy of Science, 115, 4105

Krissansen-Totton, J. & Catling, D. C. 2017, Nature Communications, 8, 15423

Krissansen-Totton, J., Garland, R., Irwin, P., & Catling, D. C. 2018b, The Astronomical Journal, 156, 114

Kuchner, M. J. 2003, ApJ, 596, L105

Kulikov, Y. N., Lammer, H., Lichtenegger, H. I. M., et al. 2007, Space Science Reviews, 129, 207

Kumer, J. B. & James, T. C. 1974, Journal of Geophysical Research, 79, 638

Lammer, H., Bredehöft, J. H., Coustenis, A., et al. 2009, The Astronomy and Astrophysics Review, 17, 181

Léger, A., Selsis, F., Sotin, C., et al. 2004, Icarus, 169, 499

Levi, A., Sasselov, D., & Podolak, M. 2014, ApJ, 792, 125

Linsky, J. L., Fontenla, J., & France, K. 2014, ApJ, 780, 61

Luger, R. & Barnes, R. 2015, Astrobiology, 15, 119

Lustig-Yaeger, J., Meadows, V. S., & Lincowski, A. P. 2019, The Astronomical Journal, 158, 27

Lyons, T. W., Reinhard, C. T., & Planavsky, N. J. 2014, Nature, 506, 307

Machida, R. & Abe, Y. 2010, ApJ, 716, 1252

Manabe, S. & Wetherald, R. T. 1967, Journal of Atmospheric Sciences, 24, 241

Marty, B., Avice, G., Sano, Y., et al. 2016, Earth and Planetary Science Letters, 441, 91

Maruyama, S., Ikoma, M., Genda, H., et al. 2013, Geoscience Frontiers, 4, 4

Mayor, M. & Queloz, D. 1995, Nature, 378, 355

McGovern, P. J. & Schubert, G. 1989, Earth and Planetary Science Letters, 96, 27

Millero, F. J. 1995, Geochimica et Cosmochimica Acta, 59, 661

Millero, F. J., Graham, T. B., Huang, F., Bustos-Serrano, H., & Pierrot, D. 2006, Marine chemistry, 100, 100

Mlawer, E. J., Taubman, S. J., Brown, P. D., Iacono, M. J., & Clough, S. A. 1997, Journal of Geophysical Research, 102, 16,663

Morley, C. V., Kreidberg, L., Rustamkulov, Z., Robinson, T., & Fortney, J. J. 2017, ApJ, 850, 121

Murakami, M., Hirose, K., Kawamura, K., Sata, N., & Ohishi, Y. 2004, Science, 304, 855

Muralidharan, K., Deymier, P., Stimpfl, M., de Leeuw, N. H., & Drake, M. J. 2008, Icarus, 198, 400

Nakajima, S., Hayashi, Y.-Y., & Abe, Y. 1992, Journal of Atmospheric Sciences, 49, 2256

Noack, L., Höning, D., Rivoldini, A., et al. 2016, Icarus, 277, 215

Oberheide, J., Mlynczak, M. G., Mosso, C. N., et al. 2013, Journal of Geophysical Research (Space Physics), 118, 7283

O'Brien, D. P., Izidoro, A., Jacobson, S. A., Raymond, S. N., & Rubie, D. C. 2018, Space Science Reviews, 214, 47

Ogihara, M. & Ida, S. 2009, ApJ, 699, 824

Oka, A., Nakamoto, T., & Ida, S. 2011, ApJ, 738, 141

Öpik, E. J. 1963, Geophysical Journal, 7, 490

Pavlov, A. A. & Kasting, J. F. 2002, Astrobiology, 2, 27

Pavlov, A. A., Kasting, J. F., Brown, L. L., Rages, K. A., & Freedman, R. 2000, Journal of Geophysical Research, 105, 11981

Petigura, E. A., Howard, A. W., & Marcy, G. W. 2013, Proceedings of the National Academy of Science, 110, 19273

Picone, J. M., Hedin, A. E., Drob, D. P., & Aikin, A. C. 2002, Journal of Geophysical Research (Space Physics), 107, 1468

Pierrehumbert, R. T. 2011, ApJ, 726, L8

Quintana, E. V. & Lissauer, J. J. 2014, ApJ, 786, 33

Ramirez, R. M., Kopparapu, R. K., Lindner, V., & Kasting, J. F. 2014, Astrobiology, 14, 714

Rasool, S. I. & de Bergh, C. 1970, Nature, 226, 1037

Rauer, H., Catala, C., Aerts, C., et al. 2014, Experimental Astronomy, 38, 249

Raymond, S. N., Quinn, T., & Lunine, J. I. 2004, Icarus, 168, 1

Raymond, S. N., Quinn, T., & Lunine, J. I. 2007, Astrobiology, 7, 66

Ribas, I., Bolmont, E., Selsis, F., et al. 2016a, Astronomy and Astrophysics, 596, A111

Ribas, I., Bolmont, E., Selsis, F., et al. 2016b, Astronomy and Astrophysics, 596, A111

Ribas, I., Guinan, E. F., Güdel, M., & Audard, M. 2005, ApJ, 622, 680

Roble, R. G. 1995, Washington DC American Geophysical Union Geophysical Monograph Series, 87, 1

Roble, R. G., Ridley, E. C., & Dickinson, R. E. 1987, Journal of Geophysical Research, 92, 8745

Rothman, L. S., Gordon, I. E., Babikov, Y., et al. 2013, Journal of Quantitative Spectroscopy and Radiative Transfer, 130, 4

Rybicki, G. B. & Lightman, A. P. 1986, Radiative Processes in Astrophysics

Rye, R., Kuo, P. H., & Holland, H. D. 1995, Nature, 378, 603

Sagan, C. & Mullen, G. 1972, Science, 177, 52

Sato, T., Okuzumi, S., & Ida, S. 2016, Astronomy and Astrophysics, 589, A15

Sawada, T., Sellin, D. L., & Green, A. E. S. 1972a, Journal of Geophysical Research, 77, 4819

Sawada, T., Strickland, D. J., & Green, A. E. S. 1972b, Journal of Geophysical Research, 77, 4812

Scalo, J., Kaltenegger, L., Segura, A. G., et al. 2007, Astrobiology, 7, 85

Schaefer, L., Wordsworth, R. D., Berta-Thompson, Z., & Sasselov, D. 2016, ApJ, 829, 63

Schunk, R. & Nagy, A. 2000, Space Sci. Ser, 59, 59

Segura, A., Kasting, J. F., Meadows, V., et al. 2005, Astrobiology, 5, 706

Shaikhislamov, I. F., Khodachenko, M. L., Lammer, H., et al. 2019, Monthly Notices of the Royal Astronomical Society, 2804

Shi, G., Xu, N., Wang, B., Dai, T., & Zhao, J. 2009, Journal of Quantitative Spectroscopy and Radiative Transfer, 110, 435

Shields, A. L., Meadows, V. S., Bitz, C. M., et al. 2013a, Astrobiology, 13, 715

Shields, A. L., Meadows, V. S., Bitz, C. M., et al. 2013b, Astrobiology, 13, 715

Shinagawa, H. & Cravens, T. E. 1989, Journal of Geophysical Research, 94, 6506

Siddles, R. M., Wilson, G. J., & Simpson, C. J. S. M. 1994, Journal of Chemical Physics, 189, 779

Sing, D. K., Fortney, J. J., Nikolov, N., et al. 2016, Nature, 529, 59

Sleep, N. H. & Zahnle, K. 2001, Journal of Geophysical Research, 106, 1373

Sleep, N. H., Zahnle, K., & Neuhoff, P. S. 2001, Proceedings of the National Academy of Sciences of the United States of America, 98, 3666

Smithtro, C. G. & Sojka, J. J. 2005, Journal of Geophysical Research (Space Physics), 110, A08305

Smithtro, C. G. & Solomon, S. C. 2008, Journal of Geophysical Research (Space Physics), 113, A08307

Solomon, S. C., Hays, P. B., & Abreu, V. J. 1988, Journal of Geophysical Research, 93, 9867

Solomon, S. C. & Qian, L. 2005, Journal of Geophysical Research (Space Physics), 110, A10306

Staudigel, H., Hart, S. R., Schmincke, H.-U., & Smith, B. M. 1989, Geochimica et Cosmochimica Acta, 53, 3091

Stimpfl, M., Walker, A. M., Drake, M. J., de Leeuw, N. H., & Deymier, P. 2006, Journal of Crystal Growth, 294, 83

Sugimura, E., Iitaka, T., Hirose, K., et al. 2008, Physical Review B: Solid State, 77, 214103

Tajika, E. & Matsui, T. 1990, The evolution of the terrestrial environment., ed. H. E. Newsom & J. H. Jones, 347–370

Tajika, E. & Matsui, T. 1992, Earth and Planetary Science Letters, 113, 251

Tajika, E. & Matsui, T. 1993, Lithos, 30, 267

Tavrov, A., Kameda, S., Yudaev, A., et al. 2018, arXiv e-prints, arXiv:1810.07644

Taylor, G. I. 1922, Proceedings of the london mathematical society, 2, 2

Tian, F. & Ida, S. 2015, Nature Geoscience, 8, 177

Tian, F., Kasting, J. F., Liu, H.-L., & Roble, R. G. 2008a, Journal of Geophysical Research (Planets), 113, E05008

Tian, F., Solomon, S. C., Qian, L., Lei, J., & Roble, R. G. 2008b, Journal of Geophysical Research (Planets), 113, E07005

Tosi, N., Godolt, M., Stracke, B., et al. 2017, Astronomy and Astrophysics, 605, A71

Tsiaras, A., Waldmann, I. P., Tinetti, G., Tennyson, J., & Yurchenko, S. N. 2019, Nature Astronomy, 451

Tully, C. & Johnson, R. E. 2001, Planetary and Space Science, 49, 533

Turbet, M., Bolmont, E., Leconte, J., et al. 2018, Astronomy and Astrophysics, 612, A86

Turbet, M., Leconte, J., Selsis, F., et al. 2016, Astronomy and Astrophysics, 596, A112

Turcotte, D. L. & Schubert, G. 2002, Geodynamics - 2nd Edition

Valencia, D., Sasselov, D. D., & O'Connell, R. J. 2007a, ApJ, 665, 1413

Valencia, D., Sasselov, D. D., & O'Connell, R. J. 2007b, ApJ, 656, 545

Valencia, D., Tan, V. Y. Y., & Zajac, Z. 2018, ApJ, 857, 106

Vance, S., Harnmeijer, J., Kimura, J., et al. 2007, Astrobiology, 7, 987

Vidal-Madjar, A., Désert, J. M., Lecavelier des Etangs, A., et al. 2004, ApJL, 604, L69

Vidal-Madjar, A., Lecavelier des Etangs, A., Désert, J. M., et al. 2003, Nature, 422, 143

Vinet, P., Rose, J. H., Ferrante, J., & Smith, J. R. 1989, Journal of Physics: Condensed Matter, 1, 1941

Waite, W. F., Stern, L. A., Kirby, S. H., Winters, W. J., & Mason, D. H. 2007, Geophysical Journal International, 169, 767

Walker, J. C. G., Hays, P. B., & Kasting, J. F. 1981, Journal of Geophysical Research, 86, 9776

Watson, A. J., Donahue, T. M., & Walker, J. C. G. 1981, Icarus, 48, 150

Weiss, R. 1974, Marine chemistry, 2, 2

Wolf, E. T. & Toon, O. B. 2013, Astrobiology, 13, 656

Wolf, E. T. & Toon, O. B. 2015, Journal of Geophysical Research Atmospheres, 120, 5775

Wordsworth, R. D. & Pierrehumbert, R. T. 2013, ApJ, 778, 154

Yang, J., Abbot, D. S., Koll, D. D. B., Hu, Y., & Showman, A. P. 2019, ApJ, 871, 29

Yang, J., Boué, G., Fabrycky, D. C., & Abbot, D. S. 2014, ApJL, 787, L2

Zahnle, K. J., Gacesa, M., & Catling, D. C. 2019, Geochimica et Cosmochimica Acta, 244, 56

Zeebe, R. E. & Wolf-Gladrow, D. 2001, CO2 in seawater: equilibrium, kinetics, isotopes No. 65 (Gulf Professional Publishing)

Zhang, H., Nakajima, T., Shi, G., Suzuki, T., & Imasu, R. 2003, Journal of Geophysical Research (Atmospheres), 108, 4641